Influence of sulfur on metallic glass forming Zr-Ti-Ni-Cu alloys

UNIVERSITÄT
DES
SAARLANDES

Dissertation

zur Erlangung des Grades des
Doktors der Ingenieurswissenschaften (Dr.-Ing.)

der Naturwissenschaftlich-Technischen Fakultät
Universität des Saarlandes

vorgelegt von
Bastian Adam

Saarbrücken
2025

Tag des Kolloquiums:	11.12.2025
Dekan:	Prof. Dr.-Ing. Dirk Bähre
Berichterstatter:	Prof. Dr. Ralf Busch Prof. Dr. mont. Christian Motz
Vorsitz:	Prof. Dr. Karen Lienkamp
Akad. Mitglied:	Dr.-Ing. Christoph Pauly

Statement of academic honesty

I hereby declare the academic authenticity and authorship of the following work, furthermore i declare that all used sources and foreign materials are marked as such.

Location, date

Bastian Adam

Abstract

This work investigates the influence of sulfur on the key materials properties of a metallic glass-forming Zr-Ti-Ni-Cu alloy. Alloys of varying S-infusion were synthesized and characterized, and a rise in glass forming ability from 0.25 mm to 6 mm was found; the origin of this was explored with in-depth analysis and the alloy was further refined by alloy development.

Several advanced characterization methods were employed to investigate the Bulk metallic glasses in depth, from electron microscopy, X-ray diffraction and calorimetry to parabolic flight based viscosity measurements in microgravity and in-situ container less levitation melting.

The influence of S on the structure of the alloy's liquid and solid phases was explored, and significant local atomic arrangement disordering was found for both states. The disordering could be determined by Ornstein-Zernike analysis and direct comparison of the S-free and S-infused alloys' structure during reduced pair distribution function analysis.

Excellent yield strength, ductility in compression and three-point bending testing, as well as a high fracture toughness of 104 $MPa\sqrt{m}$ could be determined for the $(Zr50)S3$ alloy, making it a formidable Zr-based BMG. The alloy also proves to be astonishingly resilient towards oxygen contamination in terms of both GFA as well as mechanical properties. The potential BMG alloy is discussed in detail against the state of the art, and an outlook on the application is presented.

Zusammenfassung

Diese Arbeit beschäftigt sich mit dem Einfluss von Schwefel auf die grundlegenden Materialeigenschaften Glas-bildender Zr-Ti-Ni-Cu Legierungen. Verschiedene Gehälter an Schwefel wurden hergestellt und charakterisiert, hierbei wurde ein steiler Anstieg in der Glasbildungsfähigkeit von 0.25 mm auf 6 mm kritischer Dicke der Legierungen festgestellt. Die Hintergründe dieser Beobachtung wurden erforscht und die Legierung wurde durch Legierungsentwicklung optimiert.
Der Einsatz fortschrittlicher Methoden erlaubte eine tiefgreifende Untersuchung der erzeugten metallischen Massivgläser wobei unter anderem Elektronenmikroskopie, Röntgenbeugung, Kalorimetrie bis hin zu Parabelflügen und auf hochenergetischer Synchrotron-Strahlung basierende in-situ Experimente eingesetzt wurde.
Der Einfluss des Schwefels insbesondere auf die Struktur der Schmelze und des Glases wurde untersucht und eine signifikante Erhöhung der lokalen atomaren Unordnung konnte in beiden Zuständen festgestellt werden. Hier wurde ein Vergleich der Strukturen mit und ohne Schwefel in der Legierung mittels Paar-Verteilung-Funktion-analyse genutzt.
Ausgezeichnete Festigkeiten und Duktilität unter Druck- und Biegebeanspruchung, sowie eine hohe Bruch Zähigkeit von 104 $MPa\sqrt{m}$ konnte für die $(Zr50)S3$ Legierung gemessen werden, was die Legierung zu einem hervorragenden Zr-basierten metallischen Massivglas macht. Des Weiteren zeigte sich die Legierung überaus resilient gegen Sauerstoffverunreinigung.

Acknowledgments

This section is dedicated to all the people who supported me and my work during the journey of the PhD. First and foremost, I want to thank my supervisor, Prof. Dr. rer-nat. Ralf Busch, who enabled me to conduct my research at the chair of metallic materials, and whose constant support and constructive feedback made the success of this work possible. The fruitful discussions and the given academic freedom to pursue the encountered scientific questions to the very end deserve my utmost gratitude.

Furthermore, I want to thank Dr. Oliver Gross for the constructive cooperation in the joint projects and exploration of the limits of metallic glass manufacturing technology. His constant innovative ideas contribute to this work in the form of many little improvements that I could adapt in the sense of continuous improvement of good scientific practice and application-minded iterative approaches.

My current and former colleagues who accompanied me on my scientific journey also deserve my gratitude, as without them the journey would have been not only less successful but also less enjoyable. Especially Lucas Matthias Ruschel, Nico Neuber, and Maximillian Frey deserve my thanks for the countless discussions, joint experiments, and the time spent in the control hutches of DESY facilities. Also, I want to thank Dr. Christoph Pauly for the FIB preparation and conductance of the TEM experiments in this work, as well as for the fruitful discussion of the observed phenomena. My gratitude also goes to Dr. Oliver Janka for the collection of data stemming from the numerous X-ray diffraction measurements in this work. My former senior colleagues, Prof. Isabella Gallino and Dr. Frank Aubertin, also deserve my thanks for the stimulating discussions and joint scientific work.

My thanks are also directed towards my current and former colleagues at the LMW, Oliver Kruse, Valeria Lemkova, Amirhossein Ghavimi, Thomas Luke Jamieson, Ziyu Ling, Maryam Rahimi Chegeni, Haoran Jiang, Alexander Kuball, Benedikt Bochtler, Sascha Riegler, Benedikt Schmidt, and Fabian Vollmers.

I also want to thank my team of current and former scientific assistants who supported my work in the laboratories with their motivated and excellent work: Dima Esho, Oliver Kruse, Christoph Köhl, Finn Lambert, Tobias Betz, Thalia

Menzel, and Joe Posner.
The technicians of our laboratory, Jörg Eiden and Herrmann Altmeyer, also deserve huge thanks for the support in all questions relating to technical problems and the construction of prototype devices to the needs of my work, even on pressing schedules, without whom many experiments would not have been as successful as they were. Furthermore, I want to thank Martian Stemmler for the support with the SEM measurements and the preparation and operation of the many X-ray diffraction measurements contributing to this work.
My deep gratitude goes to my Family and Friends who supported me throughout the highs and lows of the PhD journey, especially to my Mum Kirsten, my Dad Hans-Josef, as well as their spouses Nic and Ingrid, for their joint support throughout my student life and PhD. I also want to thank my Brothers, Christopher and Patrick, and my sister Anja for their friendly faces and open ears, as well as the encouragement to advance beyond my own limits.
I want to explicitly thank my friends and colleagues who have accompanied me from the bachelor studies over the master studies and throughout my PhD, especially David, who is my dear friend since the early days of school, and although careers drove us apart, I still enjoy visits and visiting Düsseldorf. Moreover i want to express my gratitude for my new-found, unexpected bestie Lamia, for inspiring and encouraging me during my final year and the time spent together as well as the fun moments and early early morning workouts. My close college friends Oliver, Sarah, and Mirko deserve a lot of thanks too, I am grateful for the time spent learning and crunching together for the exams, struggling and pushing onward together. To the friends that i found outside of college at various places, I want to thank especially Michelle, Kim, Mario and Jessi for the fun times spend together and the shared moments that were a fun and light-hearted contrast to my work in academic life.
And to the friends that became acquaintances again along the journey i want to say thank you for the time shared and appreciated, although not being in my life i hold dear memories of you all.

Publications and Contributions

Peer-reviewed publications as first author

- **B. Adam**, O. Kruse, L. M. Ruschel, N. Neuber, M. Frey, O. Gross, H.-R. Jiang, B. Li, B. Gludovatz, J. J. Kruzic, R. Busch (2025), Introduction of sulfur into an eutectic of the Zr-Ti-Ni-Cu system: Alloy development and characterization of the (Zr50Ti16.6Ni18.3Cu15)100-xSx bulk metallic glasses, Journal of Alloys and Compounds 1025, 180307.

  doi:10.1016/j.jallcom.2025.180307.

- **B. Adam**, T. Hall, L. M. Ruschel, F. Schäfer, C. Pauly, D. Bähre, R. Busch, (2024). How to achieve nanometer flat surfaces: Pulsed Electrochemical Machining of Bulk Metallic Glass, Journal of Materials Research and Technology, 12, 5.

  doi.org/10.1016/j.jmrt.2024.07.130

- **B. Adam**, A. Kuball, L. M. Ruschel, N. Neuber, M. Frey, R. Busch, (2024). Sulphuric precipitates in novel titanium-based, sulphur-bearing bulk metallic glass – a BMG composite?, PhilosophicalMagazine Letters, 104, 1.

  doi.org/10.1080/09500839.2024.2376614

Peer-reviewed publications as Co-author

- M. Frey, N. Neuber, S.S. Riegler, A. Cornet, Y. Chushkin, F. Zontone, L.M. Ruschel, **B. Adam**, M. Nabahat, F. Yang, J. Shen, F. Westermeier, M. Sprung, D. Cangialosi, V. Di Lisio, I. Gallino, R. Busch, B. Ruta, E. Pineda (2025), Liquid-like versus stress-driven dynamics in a metallic glass former observed by temperature scanning X-ray photon correlation spectroscopy, Nat. Commun. 16 4429.

  doi.org/10.1038/s41467-025-59767-2.

- B. Li, L. M. Ruschel, K. Nomoto, O. Gross, **B. Adam**, N. Neuber, M. Frey, S. P. Ringer, B. Gludovatz, R. Busch, J. J. Kruzic, (2025). Fracture behavior of NiNb and NiNbP bulk metallic glasses, Journal of Alloys Compounds, 1010, 177369.

  doi.org/10.1016/j.jallcom.2024.177369

- M. Frey, J. Wegner, L. M. Ruschel, E. S. Barreto, S. S. Riegler, **B. Adam**, N. Ellendt, S. Kleszczynski, Ralf Busch (2025). Additive manufacturing of Ni62Nb38 metallic glass via laser powder bed fusion. Prog Addit Manuf (2025).

  doi.org/10.1007/s40964-025-01007-6

- T. Jamieson, P. Decker, A. Yasinskiy, R. Düssel, G. Gunnarsson, J. Magnusson, **B. Adam**, R. Busch, I. Gallino, (2025). On the Alloy Development of Ni–Fe–Cu Inert Anodes for Sustainable, CO2-Free Aluminium Electrolysis. In: Edwards, L. (eds) Light Metals 2025. TMS 2025. The Minerals, Metals & Materials Series. Springer, Cham.

  doi.org/10.1007/978-3-031-80676-6_105

- L. M. Ruschel, S. Jakovlev, O. Gross, N. Neuber, **B. Adam**, M. Frey, B. Schmidt, B. Bochtler, R. Busch, (2024). Unraveling the role of relaxation and rejuvenation on the structure and deformation behavior of the Zr-based bulkmetallic glass Vit105, Materials Today Advances, 23, 100522.

doi.org/10.1016/j.mtadv.2024.100522

- L. M. Ruschel, A. Kuball, **B. Adam**, M. Frey, R. Busch, (2024). Viscosity and surface tension of the Zr56.5Ti13.3Ni13.6Cu9.6S7 bulk metallic glass-forming liquid, AIP Advances, 14, 3.

  doi.org/10.1063/5.0192705

- L. M. Ruschel, O. Gross, B. Bochtler, B. Li, **B. Adam**, N. Neuber, M. Frey, S. Jakovlev, F. Yang, H. Jiang, B. Gludovatz, J. J. Kruzic, R. Busch, (2023). Ni-Nb-P-based bulk glass-forming alloys: Superior material properties combined in one alloy family. ActaMaterialia, 253, 118968.

  doi.org/10.1016/j.actamat.2023.118968

- L. M. Ruschel, **B. Adam**, O. Gross, N. Neuber, M. Frey, H.-J. Wachter, R. Busch, (2023). Development and optimization of novel sulfur-containing Ti-based bulk metallic glasses and the correlation between primarily crystallizing phases, thermal stability and mechanical properties, Journal of Alloys Compounds, 960, 170614.

  doi.org/10.1016/j.jallcom.2023.170614

- M. Frey, J.Wegner, E. S. Barreto, L. M. Ruschel, N. Neuber, **B. Adam**, S. S. Riegler, H. Jiang, G.Witt, N. Ellendt, V. Uhlenwinkel, S. Kleszczynski, R. Busch, (2023). Laser powder bed fusion of Cu-Ti-Zr-Ni bulk metallic glasses in the Vit101 alloy system. AdditiveManufacturing, 66, 103467.

  doi.org/10.1016/j.addma.2023.103467

- N. Neuber, M. Sadeghilaridjani, N. Ghodki, O. Gross, **B. Adam**, L.M. Ruschel, M. Frey, S. Muskeri, M. Blankenburg, I. Gallino, R. Busch, S. Mukherjee, (2022). Effect of composition and thermal history on deformation behavior and cluster connections in model bulk metallic glasses. Scientific Reports, 12(1), 17133.

  doi.org/10.1038/s41598-022-20938-6

- M. Becker, A. Kuball, A. Ghavimi, **B. Adam**, R. Busch, I. Gallino, F. Balle (2022), Solid State Joining of a Cold Rolled Zr-Based Bulk Metallic Glass to a Wrought Aluminum Alloy by Power Ultrasonics, Materials (Basel). 15, 1–15.

  doi.org/10.3390/ma15217673

- L. Thorsson, M. Unosson, M. Teresa Pérez-Prado, X. Jin, P. Tiberto, G. Barrera, **B. Adam**, N. Neuber, A. Ghavimi, M. Frey, R. Busch, I. Gallino (2022) Selective laser melting of a Fe-Si-Cr-B-C-based complex-shaped amorphous soft-magnetic electric motor rotor with record dimensions, Mater. Des. 215, 110483.

  doi.org/10.1016/j.matdes.2022.110483.

- J. Wegner, M. Frey, M. Piechotta, N. Neuber, **B. Adam**, S. Platt, L. Ruschel, N. Schnell, S.S. Riegler, H.R. Jiang, G. Witt, R. Busch, S. Kleszczynski (2021), Influence of powder characteristics on the structural and the mechanical properties of additively manufactured Zr-based bulk metallic glass, Mater. Des. 209, 109976.

  doi.org/10.1016/j.matdes.2021.109976.

- M. Frey, J. Wegner, N. Neuber, B. Reiplinger, B. Bochtler, **B. Adam**, L. M. Ruschel, S. S. Riegler, H. Jiang, S. Kleszczynski, G. Witt, R. Busch, (2021). Thermoplastic forming of additively manufactured Zr-based bulk metallic glass: A processing route for surface finishing of complex structures. Materials & Design, 198, 109368.

  doi.org/10.1016/j.matdes.2020.109368

- H.-R. Jiang, J. Tseng, N. Neuber, J. Barrirero, **B. Adam**, M. Frey, A.C. Dippel, S. Banerjee, I. Gallino, A.H. Feng, G. Wang, F. Mücklich, R. Busch, J. Shen (2022). On the devitrification of Cu–Zr–Al alloys: Solving the apparent contradiction between polymorphic liquid-liquid transition and phase separation, Acta Materialia, 226, 117668.

  https://doi.org/10.1016/j.actamat.2022.117668.

- H.-R. Jiang, J. Hu, N. Neuber, B. Bochtler, **B. Adam**, S. S. Riegler, M. Frey, L. M. Ruschel, W. Lu, A. Feng, R. Busch, J. Shen, (2021). Effect of sulfur on the glass-forming ability, phase transformation, and thermal stability of Cu-Zr-Al bulk metallic glass. Acta Materialia, 212, 116923.

  doi.org/10.1016/j.actamat.2021.116923

- O. Gross, L. M. Ruschel, A. Kuball, B. Bochtler, **B. Adam**, R. Busch, (2020). Bulk metallic glass formation in the (Ti,Zr)-(Ni,Cu)-S system. Journal of Physics: CondensedMatter, 84(20), 4029–4031.

  doi.org/10.1088/1361-648X/ab7c15

- A. Kuball, O. Gross, B. Bochtler, **B. Adam**, L.M. Ruschel, M. Zamanzade, R. Busch, (2019). Development and characterization of titanium-based bulk metallic glasses. Journal of Alloys and Compounds, 790, 337–346.

  doi.org/10.1016/j.jallcom.2019.03.001

Conference contributions

- 16. – 21.03.2025: DPG-Frühjahrstagung, Fachverband Metall- und Materialphysik 2025, Regensburg, Germany, oral presentation: Influence of sulfur on the amorphous structure, high temperature viscosity and solidification of Zr-based bulk metallic glass formers
- 01. – 06.12.2024: Materials Research Society (MRS) Fall Meeting & Exhibit 2024, Boston, USA, oral presentation: Introduction of sulfur into the (Zr3Ti)2(Ni,Cu) system—characterization of a new group of Zr based BMG containing sulfur
- 17. – 22.03.2024: 87. Jahrestagung der DPG und DPG-Frühjahrstagung der Sektion Kondensierte Materie (SKM) 2024, Berlin, Germany, oral presentation: Introduction of sulfur into the (Zr3Ti)2(NiCu)1 system – characterization of a new group of (A2B)100-xSx Zr-based BMGs
- 20. – 25.08.2023: Joint conference: 17th Rapidly Quenched and Metastable Materials (RQ 17) and 27th International Symposium on Metastable, Amorphous and Nanostructured Materials (ISMANAM 27), Warsaw, Poland, poster contribution: Introduction of sulfur in the Zr-Ti-Ni-Cu Bulk Metallic Glass forming system
- 26. – 30.08.2019: 17th International Conference on Liquid and Amorphous-Metals (LAM17), Lyon, France, oral presentation: Characterization of a novel titanium based bulk metallic glass in the quaternary TiZrCuS-system

Managed projects

- 2019 – 2022: Industry research project with Heraeus Deutschland AMLOY Technologies GmbH & Co. KG, Alloy development and optimization of amorphous alloys
- 2019 – 2023: Industry research project with Heraeus Deutschland AMLOY Technologies GmbH & Co. KG, Process development of amorphous alloys

Successful scientific proposals

PETRA III

- Deutsches Elektronen Synchrotron (DESY) beamtime I-20250256 in 2025 (72 h), PETRA III, P21.2; , W. Zhou, **B. Adam**, Y. Li, R. Busch; Revealing the structural origin of the memory effect in metallic glasses.

- Deutsches Elektronen Synchrotron (DESY) beamtime I-20250673 in 2025 (72 h), PETRA III, P21.2; A. Ghavimi, **B. Adam**, L.M. Ruschel, M.T. Perez-Prado, E. Ferrara, P. Tiberto, I. Gallino, R. Busch; Structural investigation during stress relief, relaxation and nano-crystallization of cast and 3D-printed Fe-based soft magnetic bulk metallic glasses (BMG).

- Deutsches Elektronen Synchrotron (DESY) beamtime I-20231426 in 2024 (72 h), PETRA III, P21.2; **B. Adam**, N.Neuber,M. Frey, L.M. Ruschel, A. Ghavimi, V. Lemkova and R. Busch; Structural investigation of devitrification, supercooled liquid structure and nano crystallization behavior of BulkMetallic Glass forming alloys.

- Deutsches Elektronen Synchrotron (DESY) beamtime I-20210883 in 2021 (144 h), PETRA III, P21.1; N. Neuber, L.M. Ruschel, D. Holland-Moritz, F. Yang, **B. Adam**, N. Grund and R. Busch; Study of the influence of metalloid addition on the structure and crystallization behavior of Ni-Nb based metallic liquids by combination of In-situ X-ray diffraction with electrostatic levitation.

- Deutsches Elektronen Synchrotron (DESY) beamtime I-20210781 in 2021 (108 h), PETRA III, P21.1; L. M. Ruschel, **B. Adam**, N. Neuber and R. Busch; Structural investigation of an anomalous exothermic event in the supercooled liquid region of refractory Ni-Nb-P-based amorphous alloys.

- Deutsches Elektronen Synchrotron (DESY) beamtime I-20200684 in 2020 (96 h), PETRA III, P21.2; **B. Adam**, A. Kuball, O. Gross, Ralf Busch; In-situ structural investigation of sulfuric precipitates and intermetallic nanocrystallization in novel sulfur bearing Bulk Metallic Glass formers.

TEMPUS

- 2024 (5 parabolas); **B. Adam**, L.M. Ruschel, R. Busch; TEMPUS experiment proposal (Idea I-2024-03726): “High temperature viscosity and surface tension in the liquid state of the Zr50Ti16.6Ni18.3Cu15 bulk glass forming alloy.”
- 2024 (5 parabolas); A. Ghavimi, L. M. Ruschel, **B. Adam**, R. Busch; TEMPUS experiment proposal (Idea I-2024-03580): “Viscosity and surface tension in the liquid state of a bulk glass forming composition Fe72Si7.68B16.32Nb4 for 3D printing application.”
- 2023 (5 parabolas); **B. Adam**, L.M. Ruschel, R. Busch; TEMPUS experiment proposal (Idea I-2023-02333): “High temperature viscosity and surface tension in the liquid state of the (Zr50Ti16.6Ni18.3Cu15)97S3 bulk glass forming alloy”
- 2023 (10 parabolas); L.M. Ruschel, **B. Adam**, R. Busch, F. Yang; TEMPUS experiment proposal (Idea I-2023-02109): “Viscosity and surface tension in the liquid state of a bulk glass forming composition Ni59.2Nb38.8P2”
- 2022 (10 parabolas); L.M. Ruschel, **B. Adam**, R. Busch, F. Yang; TEMPUS experiment proposal (Idea I-2022-01413): “Viscosity and surface tension in the liquid state of a bulk glass forming composition Ni59.2Nb38.8P2
- 2022 (10 parabolas); N. Neuber, L. M. Ruschel, **B. Adam**, R. Busch, F. Yang; TEMPUS experiment proposal (Idea I-2022-01720): “Viscosity and surface tension in the liquid state of an ultra-fragile bulk glass forming composition Pd58Ni12Se30”

Education

Supervised works

- Master thesis, Dima Esho, High load thermoplastic forming and alloy optimization of thermoplastic-formability, Saarland University, Oct. 2025
- Master thesis, Oliver Kruse, Development of a novel Sulfur bearing Zirconium based Bulk Metallic Glass, Saarland University, Dec. 2021
- Master thesis, Oriol Bosch, Alloy development, processing and characterization of Fe-based BMGs made from Ferroalloys, Saarland University, Dec. 2021

Contents

List of Figures

List of Tables

List of Abbreviations

3PBB	3-Point Beam Bending
AMZ4	Amorphous Zirconium Alloy 4-components $Zr_{59.3}Cu_{28.8}Al_{10.4}Nb_{1.5}$
BMG	Bulk Metallic Glass
BSE	Backscattering Electron
D_c	Critical Casting Thickness
DESY	German Electron Synchrotron
DSC	Differential Scanning Calorimetry
DTA	Differential Thermal Analysis
EBSD	Electron Backscattering Diffraction
ECP	Efficient Cluster Packing Model
EDS	Energy Dispersive X-ray Spectroscopy
ESL	Electrostatic Levitation
FSDP	First Sharp Diffraction Peak
FST	Fragile-to-Strong Transition
GFA	Glass-Forming Ability
HAADF	High Angle Annular Dark Field
HEA	High Entropy Alloy
HE-XRD	High Energy X-ray Diffraction
ISRO	Icosahedral Short-Range Order
KWW	Kohlrausch-Williams-Watts
LRO	Long-Range Order
MEMS	Micro-Electro-Mechanical-Systems
MG	Metallic Glass Former
MRO	Medium-Range Order
MYEGA	Mauro, Yue, Ellison, Gupta, and Allan

PETRA	Positron-Elektron-Tandem-Ring-Anlage
PID	Proportional-Integral-Differential Regulator
PDF	reduced Pair Distribution Function
SAED	Selected Area Electron Diffraction
SCL	Supercooled Liquid
SCLR	Supercooled Liquid Region
SE	Secondary Electron
SEM	Scanning Electron Microscopy
SENB	Single Edge Notched Beam
SLM	Selective Laser Melting
SRO	Short-Range Order
SSDP	Second Sharp Diffraction Peak
STEM	Scanning Transmission Electron Microscope
STZ	Shear Transformation Zone
TEM	Transmission Electron Microscope
TEMPUS	Containerless Electromagnetic Processing in Microgravity
Vit101	Vitreloy 101 $Cu_{47}Ti_{34}Ni_8Zr_{11}$
Vit105	Vitreloy 105 $Zr_{52.5}Ti_5Ni_{14.6}Cu_{17.9}Al_{10}$
Vit106	Vitreloy 106 $Zr_{57}Cu_{15.4}Ni_{12.6}Al_{10}Nb_5$
Vit106a	Vitreloy 106a $Zr_{58.5}Cu_{15.6}Ni_{12.8}Al_{10.3}Nb_{2.8}$
$(Zr50)$ *alloy*	$Zr_{50}Ti_{16.6}Ni_{18.3}Cu_{15}$
$(Zr50)Sx$ *alloy*	$(Zr_{50}Ti_{16.6}Ni_{18.3}Cu_{15})_{100-x}S_x$

List of Symbols

Symbol	Description
D^*	fragility parameter
E	Young's modulus
$G(r)$	reduced pair distribution function
$G_l(T)$	Gibbs free energy of the liquid phase
$G_x(T)$	Gibbs free energy of the crystalline phase
$H_l(T)$	enthalpy of the liquid phase
$H_x(T)$	enthalpy of the crystalline phase
$I(Q)$	corrected scattering intensity
K_Q	provisional fracture toughness
K_{IC}	plane strain fracture toughness
Q	scattering wave vector
R	heating rate
R_c	critical cooling rate
$S(Q)$	total scattering structure function
$S_l(T)$	entropy of the liquid phase
$S_x(T)$	entropy of the crystalline phase
T_0	VFT temperature
T_f	temperature of fusion
T_g^{onset}	onset temperature of the glass transition
T_K	Kauzmann temperature
T_l	liquidus temperature
T_m	melting temperature
T_s	solidus temperature
T_u	supercooling temperature

T_x	onset temperature of crystallization
d_c	critical casting thickness
$\Delta G_{l,x}(T)$	driving force for crystallization
$\Delta G_u(T)$	difference in Gibbs free energy due to supercooling
ΔH_f	enthalpy of fusion
ΔS_f	entropy of fusion
$\Delta S_u(T)$	difference in entropy of the solid and liquid phase due to supercooling
η_0	viscosity limit at infinite temperature
$\eta(T)$	dynamic viscosity
ϵ_{total}	total strain to failure
$\gamma_{l,x}$	interfacial energy between the crystal and the liquid
ν	Poisson ratio
ρ	density
σ	surface tension
$\sigma_{\max}$	total flexural strength
$\sigma_{\text{Rp 0.2}}$	0.2 % offset yield strength
T_{rg}	reduced glass transition temperature
r	distance in real space

1 Introduction

The world of material science and engineering is a discipline that seeks insight into the resulting material behaviors and properties based on the structure of the micro- and nano-scales throughout a vast variety of materials. This work focuses on metallic materials as it is performed within the vicinity of the chair of metallic materials at Saarland University. Here, we focus on a specific subsection of metallic materials that is rather 'young' in the history of a few thousand years of metallurgy to date, the amorphous metals - metallic materials that are non-crystalline solids. In a regular crystalline metallic material, the atom's position is determined by the interaction with its nearest neighbors - the most basic structural unit that repeats periodically throughout a greater volume of the solid, called the elementary cell. The regular repetition in all dimensions of the elementary cell makes up the crystal lattice that largely dictates the macroscopic properties of the solid metallic material. In contrast, this regular periodic order is missing in metallic liquids where the mobility and movement of the atoms are so high that the liquid does not possess a shape despite its strong binding forces between the atoms in the liquid so that they possess fluidity [1]. The structure of the amorphous solid is similar to that of the liquid phase, although metallic glasses possess a much lower mobility of the atoms in their solid state. The structure of the amorphous solid contains increased disorder compared to the crystalline material since it contains no regularly ordered crystal lattice but a characteristic randomness of the long-range order (LRO) yet it is characterized by a medium-range order (MRO) in the range of up to 10 Å and the short-range order (SRO) in the range of 2-3 Å. The difference in structure is sketched exemplarily in Figure 1.1, where a simplified metallic glass microstructure and a simplified crystalline microstructure are depicted.
To achieve the formation of metallic glass from the liquid metal, it must therefore be cooled down from the liquid state to a solid state with low mobility and also by-

pass the occurring formation of crystalline structures - although counter intuitive, under certain conditions a lot of substances can be cooled into a glass state [2]. The amorphous metals or metallic glasses were discovered during splat quenching studies of the Au-Si system back in 1960 within experiments at the California Institute of Technology under Pol Duwez [3]. Here, a 25 $at\%$ Si Au-Si alloy was quenched rapidly from 1573 K to room temperature, and an X-ray diffraction (XRD) spectrum of the flake sample showed no crystalline diffraction behavior [3].

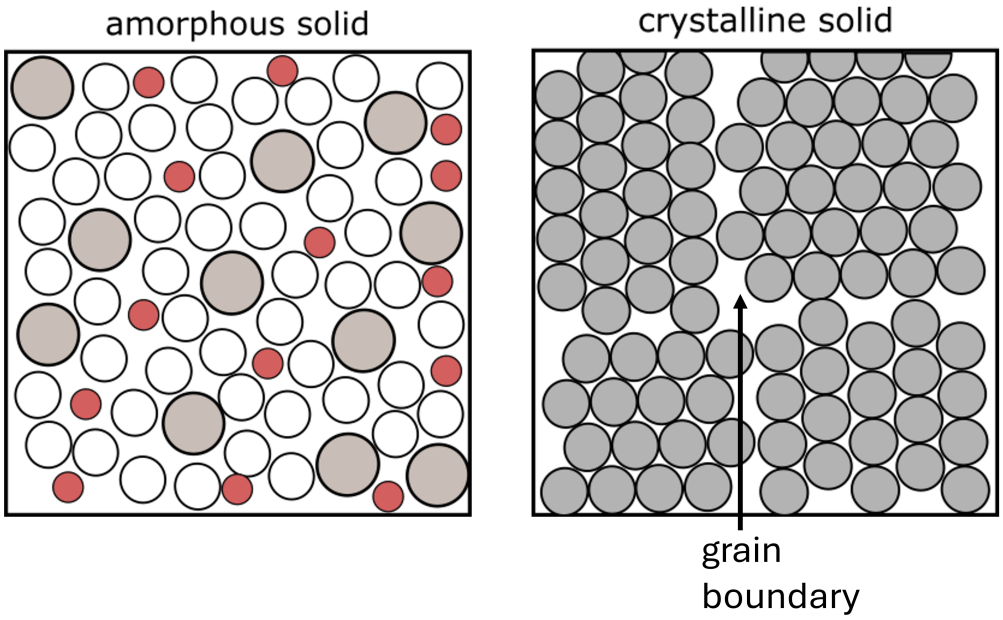

Figure 1.1: Schematic drawing of the atomic arrangements in amorphous and crystalline solids.

Although this had not been reported for metallic materials before, it only marked the beginning in this field of metallurgy, since then numerous discoveries of glass forming systems and even glass forming elements like Ta or V have been reported [4], while recent studies could demonstrate that even Au could be quenched into the amorphous state at cooling rates of $10^{13} K/s$ [5]. Over the course of the last 60 years, the known glass forming systems quickly expanded into ternary and quaternary systems, with modern glass forming alloys for the application usually being quite complex alloys of 4 components or more. With the discovery of the

massive glass forming in the Pd-Ni-P system that ultimately reached a GFA of 80 mm after employing a fluxing technique, the bulk metallic glasses reached the current peak in casting size for water quenched samples [6].
With the discovery of the Vitreloy 1 alloy in 1993 the first commercially available Zr-based bulk metallic glass was successfully developed by Peker and Johnson [7] that saw application especially in injection casting applications for the high performance sports applications, electronic housings and research projects in the defense sector under a start-up founded from the California Institute of Technology, the Liquid Metal Technologies Inc. [8].

Since their discovery in the 1990's bulk metallic glasses have been expanded from only a few to numerous compositions that have been successfully produced in the amorphous state, with numbers of systems being estimated in 2017 of about 10^3 discovered systems and the numbers have been increasing in the past years due to still ongoing research activities in this sector. The number of potentially existing, practical BMG alloys is estimated to be much larger at about 3 million systems in total [9]. Within the chair of metallic materials, a novel group of metallic glass formers was discovered in 2017 by Kuball [10], due to the introduction of sulfur into a Pd- and Ti-based alloy system. This sparked research activities on these new systems within the chair of metallic materials, and the research following this initial discovery of sulfur as an alloying element for the metallic glass formation added quite a few systems to the list of bulk metallic glass formers. Further works on the Ti-based system led to the discovery of Ti-Zr-Cu-S BMGs in 2019 [11] and Ti-Ni-Zr-Cu-S BMGs in 2020 [12]. The introduction into Ni- and Cu-based systems yielded the Ni-Nb-S [10] and Cu-Zr-Al-S bulk glasses [13]. The additions of sulfur that lead to beneficial effects on glass forming ability (GFA) and stability of the supercooled liquid region (SCLR) can vary for the different systems. Glass forming ability is maximized at additions of sulfur from less than 1 $at\%$ in Cu-Zr-Al and up to 27 $at\%$ in the Pd-Ni-S system. For well-known BMG alloys like Vitreloy 105 ($Zr_{52.5}Ti_5Ni_{17.9}Cu_{14.6}Al_{10}$) [14] and Vitreloy 101 ($Cu_{47}Ti_{34}Ni_8Zr_{11}$) [15] the influence of minor additions of sulfur was investigated by Bochtler [16] which provided an insight into the effect of those on GFA and especially SCLR. Here the minor additions ability to retard the primary crystallization from the SCLR was

highlighted [16].

Alloy development efforts in cooperation with industry partners led to the discovery of the $Ti_{40}Zr_{35}Cu_{17}S_8$ alloy that showed good glass forming ability paired with high corrosion resistance and resilience against impurities, making the alloy a promising candidate for structural applications [11]. Within the same efforts, the $Zr_{56}Ti_{13.3}Ni_{13.6}Cu_{9.6}S_7$ alloy was developed that showed a GFA of about 1 mm paired with a large supercooled liquid region and promising mechanical properties, both alloys mentioned showed fracture strengths up to twice as high as crystalline Ti6Al4V [11].
Preceding this work the previously reported alloy of $Ti_{40}Zr_{35}Cu_{17}S_8$ was characterized [17] and further investigated. Here, the role of sulfuric precipitates enabled a deeper understanding of the sulfur's effect on the primary phase formation in Ti-Zr-Cu that was beneficial in further alloy development studies [18]. The Ti-rich BMGs were then further optimized by Ruschel et al., where a strong correlation between the primary phases, thermal stability, and mechanical properties was established [19].

In the present work, the influence of sulfur on a specific section of the Zr-Ti-Ni-Cu system is investigated. The section with a fixed ratio of Ti and Zr in relation to Ni and Cu can be presented as $(Zr, Ti)_2(Cu, Ni)$. The system spans a compositional space between the four intermetallic compounds Ti_2Ni, Ti_2Cu, Zr_2Cu, and Zr_2Ni, where two eutectic points can be found and concentration ranges for amorphous alloys with a critical cooling rate of 10^3 - 10^4 K/s have been reported [20]. The alloy $Zr_{50}Ti_{16.6}Ni_{18.3}Cu_{15}$ was described as the composition with the highest glass-forming ability in the study and Molokanov et al. showed during the following studies that they could melt-jet quench the alloy into the bulk glass, also postulating a temperature overheating range for these intermetallic alloys that ensures a homogeneous melt [21].
The work in the following investigates the influence of sulfur on the $Zr_{50}Ti_{16.6}Ni_{18.3}$ Cu_{15} -which is referred to in the following as '$Zr50$' alloy- in-depth and characterizes the system $(Zr_{50}Ti_{16.6}Ni_{18.3}Cu_{15})_{100-x}S_x$ (with increment $x = 0...8$) that is referred to as '$(Zr50)Sx$' and was in part published in reference [22].
First, the influence of sulfur on the glass-forming ability and the thermophysical

properties of the $Zr50$ alloy is investigated in detail. This includes the determination of critical casting thickness, characterization of the characteristic temperatures of the alloys, as well as the recording of time-temperature-transformation diagrams (TTT) for the different sulfur contents, determined from isothermal calorimetric experiments.
The investigation is supported by structural investigations during in-situ synchrotron X-ray scattering experiments at the German electron synchrotron (DESY) in Hamburg, where the influence of sulfur on the amorphous structure, as well as the structure of the undercooled and stable liquid, was determined, as well as the occurring crystallization and devitrification processes.
With the help of two successful TEMPUS (containerless electromagnetic melting processing under microgravity) experiments during the 41^{st} and 43^{rd} parabolic flight campaign by the German aerospace center (DLR) a precise determination of the sulfur's impact on high temperature viscosity and fragility of the liquid could be obtained as well as the influence on the high temperature liquid's surface tension of the alloy.
Secondly, the in-depth investigation of the $(Zr50)Sx$ system, the most promising alloys of the series are evaluated regarding industrial applicability, and mechanical characterizations are presented, accompanied by reference materials synthesized in industrial quality. Here, the characterization utilizes conventional compression testing, three-point beam bending, and fracture toughness testing, as well as micro-hardness mapping, which was performed in cooperation with the group of Professor Jay Kruzic of the University of New South Wales.
The alloy system is subjected to further alloy development strategies, and the applicability of the alloy was tested by employing the alloy in arc-melting injection casting at Amorphous Metal Solutions GmbH and determining processing parameter windows that allow the production of low porosity, high-quality castings. The achieved properties of this system are evaluated against the state of the art, and possible applications of the material are highlighted and discussed.

2 Theoretical foundation of metallic glasses

2.1 Thermodynamic consideration

Before the discussion of the bulk metallic glasses, the necessary concepts and theoretical background shall be explained in this chapter, starting with the concept of different states of the system. The thermodynamic classification of the different states that a system can occupy is coupled to the description of those systems using well-defined thermodynamic quantities. The first description necessary for this approach is the basic law of the conservation of energy, which is referred to as the first law of thermodynamics. The law can be expressed by equation (2.1) where the difference in internal energy of the system dU is given as:

$$dU = \delta Q \ + \delta W \tag{2.1}$$

where δQ and δW are the changes in internal heat Q and performed work W of the system, respectively [23].
For an isolated system with no transfer of mass and heat transfer being possible between the inside and surroundings of the system, this means that the difference in work equals the difference in heat transfer for this system, which can be expressed utilizing $\delta Q = -\delta W$. For a closed system, the interchange of energy is possible, but the mass of the system stays constant. The basic instrument of a thermometer and its principle of function comes to mind as a prime example of a closed thermodynamic system that is able to exchange heat with its surroundings and expand the indicator liquid accordingly, thereby performing an equal amount of work through expansion. Once the volume V of the system itself is introduced

with its respective pressure p, the combination is described by the enthalpy H of the system. It's is given mathematically in equation (2.2) in its differential form dH as:

$$dH = dU + d(p \cdot V) \tag{2.2}$$

where $d(p \cdot V)$ is the total differential of pressure and volume of the system.
The more detailed and widely used description of the state of a system, however, is the Gibbs free energy of the system that can be described with equation (2.3) by G as:

$$G = H - T \cdot S \tag{2.3}$$

where the product of entropy S and temperature T is subtracted to account for the entropic part of the Gibbs free energy.
The absolute Gibbs free energy can not be accessed directly by experimental means easily, therefore, the difference in Gibbs free energy is often determined relative to a well-known reference state or material. Its differential form is embodied by equation (2.4) as dG :

$$dG = dH - (T \cdot dS + S \cdot dT) = V dp - S dT \tag{2.4}$$

that can be simplified and expressed as a differential in dependence on pressure and temperature.
The Gibbs-Helmholtz relation that is given in equation (2.5) for the difference in Gibbs free energy ΔG:

$$\Delta G = \Delta H - T\Delta S \tag{2.5}$$

is used when it comes to the description of the differences in energetic state between glasses and crystals. The Gibbs Helmholtz relation is also useful to estimate the driving forces that a glass experiences towards its equilibrium state, which is an important factor to consider in the design of metallic glasses [24].
This driving force plays a vital role in the determination of origin of the glass forming ability, as it is one of the key motivations of a system to reduce its energy

state from glass or liquid -depending on the temperature- by forming a crystalline phase and the estimation of these driving forces can therefore allow to estimate the glass forming ability and compare between different systems.
For this work, the conditions of the encountered systems are mostly isobaric, as the pressure does not deviate from the regular atmospheric pressure except for the protective atmospheres during synthesis. The differential of work dW on the system is therefore considered negligible throughout this work.

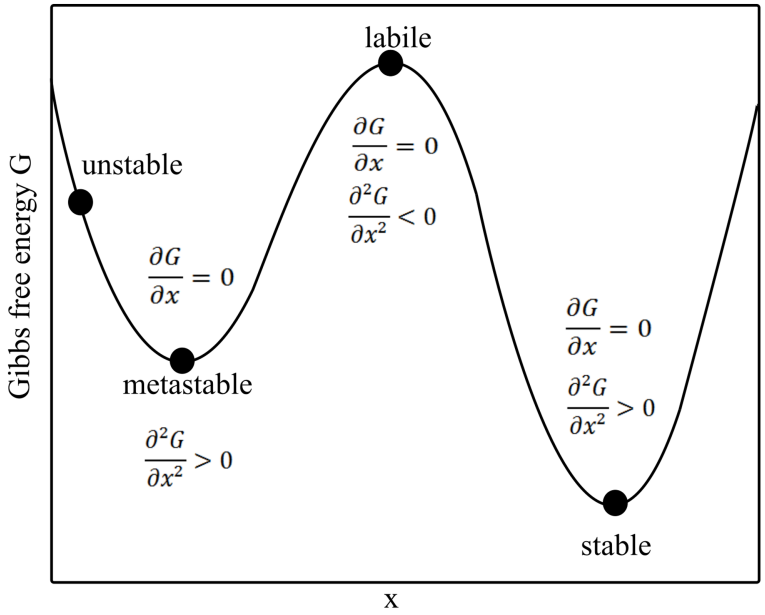

Figure 2.1: Schematic drawing of the energetic landscape of a system, displaying the most prominent energy states of a system and their relations to the specific conditions of the Gibbs free energy function of the system [17].

In Figure 2.1, the different states of the system are shown exemplarily, where the conditionals of the Gibbs free energy are given at the respective states. The figure shows the concepts of the unstable state and labile state, which can change rapidly on their own or upon small excitation, respectively. The metastable state is characterized by a local minimum of the Gibbs free energy, which means the system will remain in the given state without external excitement. This is the state of the supercooled liquid region, as it is the local minimum in the energy

landscape, and to form a crystal, a certain energy barrier needs to be overcome to form a new surface within the existing liquid phase.

For a regular metallic system, the stable equilibrium state at room temperature is the crystalline state. This state is the global minimum of the Gibbs free energy function for the system. As the system prefers to minimize the energy of the system, all other states of the system experience a certain driving force towards this state of matter. Depending on the energetic barrier that needs to be overcome for the system to be able to move into that energetic state, the energetic pathway of the respective transition of states is determined. For this consideration, dynamic effects are not included yet, but will be discussed in the following section in depth.

For bulk metallic glass formers, this consideration is especially important as the driving forces between the supercooled liquid and the crystal play a pivotal role in the glass-forming ability of the alloys. Here, the Turnbull approximation of the Gibbs free energy for undercooled liquids has proven to be a successful approach in linearization of the difference between the liquid's Gibbs free energy and the Gibbs free energy of the crystal, which is expressed by ΔG^{l-x}. The liquid state is the stable state above the liquidus temperature T_l and in the zone between T_m and T_l, a two-phase region is encountered where the liquid and solid phases are in an equilibrium state, albeit in different concentrations. Upon cooling, the Gibbs free energy of the liquid increases at a faster rate than that of the crystal and surpasses the Gibbs free energy needed to form a crystal from the liquid below T_l. Therefore, with progressive undercooling, the energetic gain by forming the crystalline phase is increased significantly with lowering temperature of the system.

The enthalpy or the equivalent volume as a function of the temperature for a glass-forming system is given in Figure 2.2 for two glasses that experience different cooling rates R_{c1} and R_{c2} into the glassy state, where the glass 1 is being cooled faster with the higher cooling rate $R_{c1} > R_{c2}$. Both cooling rates are sufficient to bypass the crystallization pathway that is sketched with a dashed line and would occur at T_m(T_s under ideally slow cooling as described by the equilibrium phase diagram. When kinetic effects and non-equilibrium conditions dominate the system, like in the case of bulk glass formers, the behavior deviates significantly from the equilibrium solidification pathway.

The crystalline state is sketched as a baseline due to simplification, as in most bulk glass forming systems, there exists a mixture of crystalline phases. The temperature range where the glass transitions from supercooled liquid into the solid state is indicated by the tangents that allow for comparison of the respective onset of the glass transition temperature T_g.

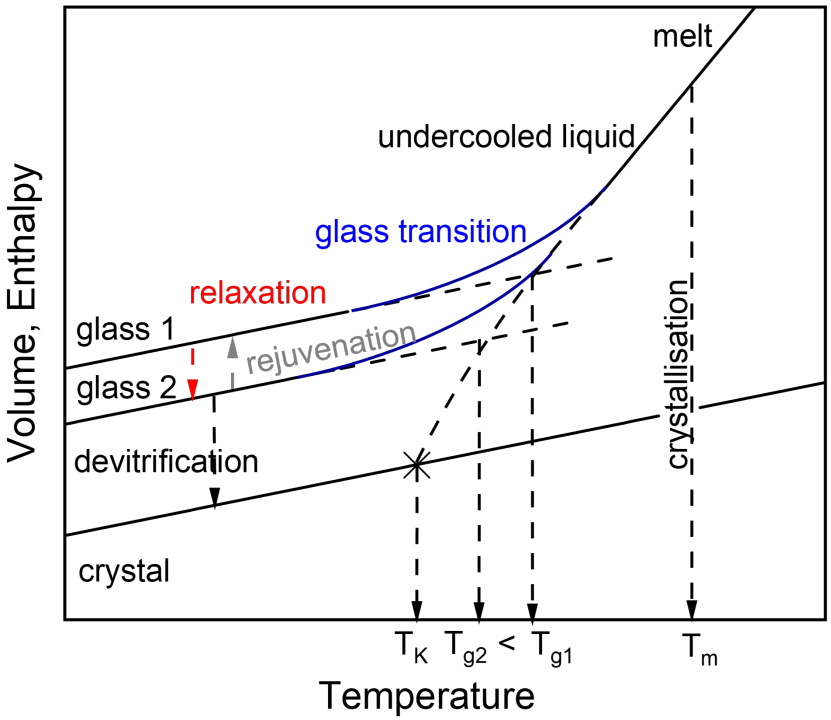

Figure 2.2: Schematic display of the volume or enthalpy as a function of the temperature for a glass forming system, the glass 1 experiences a cooling rate R_{c1} that is higher than the rate R_{c2} of the glass 2, taken from [17].

Here the difference in enthalpic states resulting from the different cooling rates can be observed as the system is given less time to position itself closer to its equilibrium state before solidification, so that the enthalpic difference between the glass 1 and the crystalline state is greater than the difference between glass 2 and the crystalline state, as it was cooled slower. For metallic glasses, the transition

between glassy states towards a lower enthalpy in the glass is known as the relaxation of the system and is headed towards its nearest local minimum of Gibbs free energy, the supercooled liquid state.
The reversal of this effect or the increase in enthalpy of the glassy state is known as the rejuvenation of the glass, which can be performed by procedures altering the thermo-mechanical history of the glass by bringing energy into the system, as in thermal treatment procedures, for example [25]. These effects play a crucial role in the post-processing treatment of both direct casting of BMG as well as additive manufacturing. For both routes, the rapid cooling conditions and inhomogeneous distribution of the resulting temperature gradients in the BMG parts impact the mechanical properties of the materials, as those are coupled to the enthalpic state of the system.

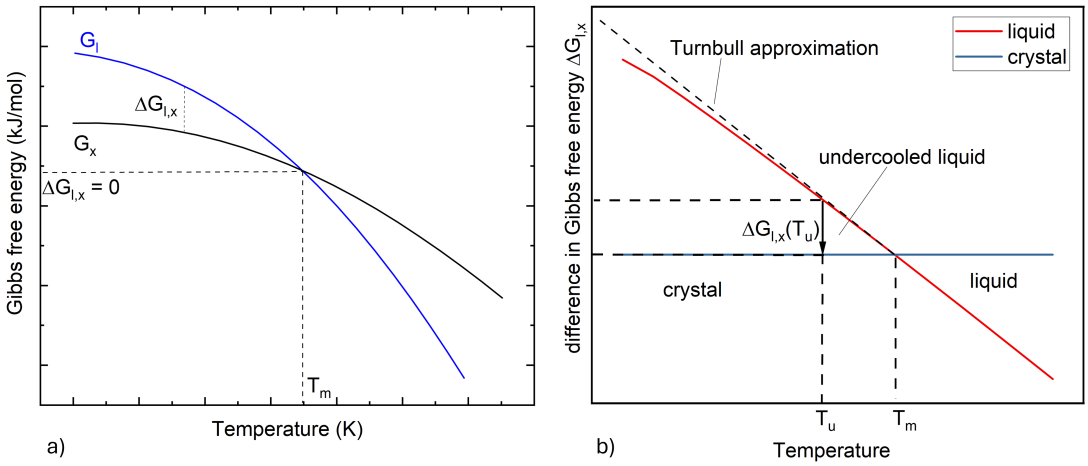

Figure 2.3: a) Schematic of the Gibbs free energy curves of liquid and crystalline state with b) sketch of the linearization of the difference in Gibbs free energy $\Delta G_{l,x}(T_u) = \Delta G_u$ included, for small supercooling states that was postulated by Turnbull, taken from [17].

The driving force for the crystallization pathway is a function of the supercooling of the liquid, as the Gibbs free energy curves are not linear and their differences grow with rising supercooling. A sketch of those curves G_{liquid} (G_l) and $G_{crystalline}$ (G_x) is given in Figure 2.3 a). For a small supercooling, the difference in Gibbs free energy between the liquid and the crystal $\Delta G_{l,x}$ can be assumed as a linear de-

pendence of the supercooling as shown in Figure 2.3 b), according to the Turnbull approximation [26], which is expressed in equation (2.6) for $\Delta G_{l,x}$ as:

$$\Delta G_{l,x} = -(S_l - S_x) \cdot (T_l - T_u) \approx -\Delta S_f \cdot \Delta T_u \tag{2.6}$$

that linearizes the relation for small supercoolings.

The linearization allows the equation to be approximated with the term of equation (2.7) for $\Delta G_{l,x}$ as:

$$\Delta G_{l,x} = -\Delta S_f \cdot \Delta T_u \approx -\frac{\Delta H_f}{T_f} \cdot \Delta T_u \tag{2.7}$$

and thereby to be expressed as a function of the system's enthalpy of fusion ΔH_f. The supercooling ΔT_u and the temperature of fusion T_f can be utilized to approximate the driving force between the crystal phase and the liquid phase without actually calculating the respective Gibbs free energy curves.

While the thermodynamic consideration locates the start of the crystallization at T_l, the reality of complex systems shows a variety of undercooling ranges that depend both on the external conditions of the liquid as well as the kinetic aspects of the cooling rate and energetic barrier of the nucleation that result in the supercooled temperature $T_u < T_l$ at which the system finally solidifies.

For the supercooling at T_u, the Figure 2.4 shows the entropy S that deviates from the entropy of the liquid S_l and approaches the entropy of the solid S_x with progressing undercooling. When cooled towards a temperature where the entropy of the undercooled liquid, in theory, approaches the entropy of the crystalline phase, this temperature is referred to as the Kauzmann temperature T_K [27]. However, the system should not be able to reach the Kauzmann temperature as the point where the entropy of the disordered liquid is lower than the ordered crystal would be a paradox [27].

The contributions to the Gibbs free energy at the undercooling T_u can be described by the equations (2.8) and (2.9) as $\Delta G_{l,x}(T_u)$:

$$\Delta H_{l,x}(T_u) = \Delta H_f - \int_{T_u}^{T_l} \Delta C_p^{l,x}(T)\, dT, \tag{2.8}$$

$$\Delta S_{l,x}(T_u) = \Delta S_f - \int_{T_u}^{T_l} \frac{\Delta C_p^{l,x}(T)}{T}\, dT, \tag{2.9}$$

here, the enthalpy of fusion ΔH_f and entropy of fusion ΔS_f as well as the difference in isobaric heat capacity C_p between the liquid phase and the solid phase, play a crucial role in the total Gibbs free energy.

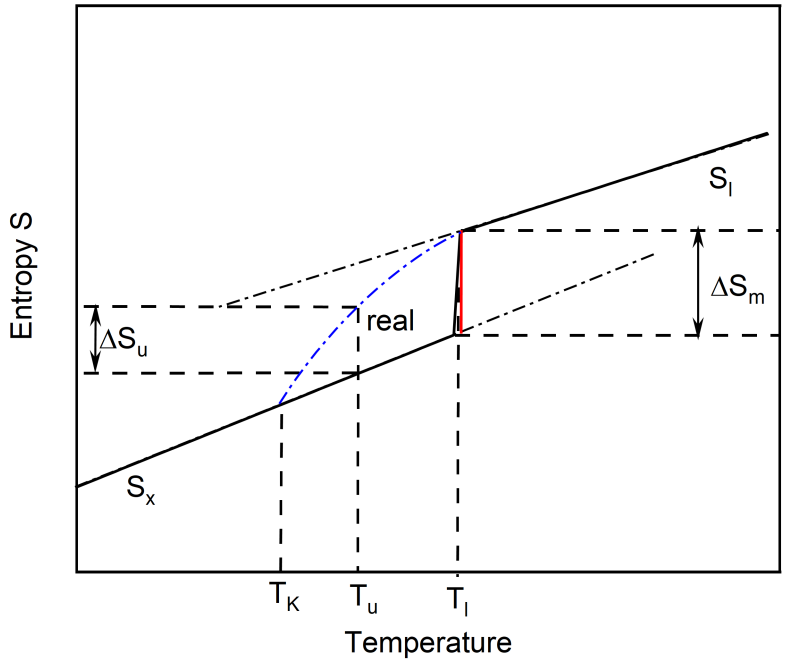

Figure 2.4: Schematic display of the entropy as a function of the temperature for a glass forming system, the point where the entropy of the liquid equals the solid phase was described by Kauzmann and is therefore labeled T_K, where the difference in entropy between liquid and solid ΔS_u is minimal.

The isobaric heat capacity can be determined through DSC measurements utilizing the Kubaschewski equations [28] for the liquid as C_p^l and the crystal as C_p^x:

$$C_p^l(T) = 3R + aT + bT^{-2} \tag{2.10}$$

$$C_p^x(T) = 3R + cT + dT^2 \tag{2.11}$$

with R being the universal gas constant ($8.314\ J/(mol \cdot K)$) and the fitting parame-

ters a, b, c, and d. During fast cooling from the liquid to bypass the crystallization, the heat capacity of the super cooled liquid increases until the glass transition is reached, this increase in the isobaric heat capacity is coupled to the decrease of the entropy during undercooling as well as the decrease in volume, as shown in Figure 2.2 that also contributes to the increase of C_p. When the system transforms into the glass, the heat capacity declines rapidly to a value that is still larger than the corresponding crystalline phase, due to the degree of disorder in the glass that is 'frozen' within the glassy structure.

2.2 Nucleation and growth of crystalline phases

The initial stage of a limited region of atoms in the liquid phase ordering into the structure of the crystalline phase below T_m defines a nucleus. According to Hollomon, the temperature where the nucleation occurs, T_u, is very close to T_m for pure metals, when no impurities are present [29]. For larger systems of liquid under conditions close to industrial application, however, the experimental evidence appears to be decisive that initial nucleation happens on existing container surfaces or particles inside the liquid according to Turnbull [30]. This study also implicates that the thermal history of overheating beyond a certain overheating threshold is significant for depth of the possible undercooling, shown exemplarily on gallium, and it was found that the supercooling temperature T_u 'is generally characteristic of the highest temperature attained' during superheating of the system [30].
The energetic consideration of the nucleation process is characterized by two contributions: the reduction in Gibbs free energy due to the system's change from the liquid phase into the crystalline phase and the increase in Gibbs free energy due to the new interface of the nucleus. The consideration is given in equation (2.12) for ΔG_{nuc}:

$$\Delta G_{nuc} = \Delta G_s + \Delta G_v = 4\pi r^2 \cdot \gamma_{sur} - \frac{4}{3}\pi r^3 \cdot \Delta g_V \tag{2.12}$$

that sums up the contribution of Gibbs free energy of the formed nucleus to the system during supercooling of the liquid phase. The contribution of the volume specific transition energy Δg_V and the constant describing the surface energy γ_{sur} are employed.
The equation can be visualized schematically as it is displayed in Figure 2.5, where the resulting curve of ΔG_{nuc} as well as its individual contributions ΔG_s and ΔG_v are given as a function of the nucleus radius r. The resulting curve describes an distorted parabola with a maximum at the point of r^*, the critical nuclei radius, from this point on each increase in size stabilizes the nucleus energetically so that growth of the nucleus is energetically favored in contrast to nuclei with $r < r^*$ that dissolve into the liquid again as they are not stable compared to the liquid phase.

In the graphic there is already included the influence of the heterogeneous and homogeneous nucleation mechanism on the resulting $\Delta G_{nuc}(r)$ curve, the energetic barrier to nucleation is reduced in the case of heterogeneous nucleation as $\Delta G_{nuc}^{homo}(r) > \Delta G_{nuc}^{hetero}(r)$.

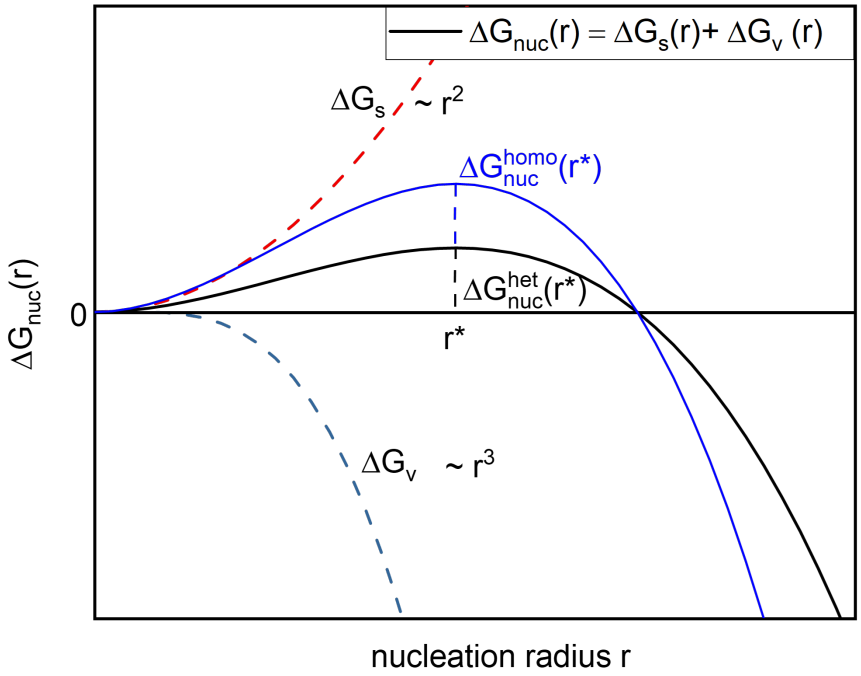

Figure 2.5: The energetic barrier to form a nucleus as a function of two Gibbs free energy functions, the difference in Gibbs free Energy needed for the creation of the surface of the nucleus ΔG_S and the energy gained from the creation of the crystalline volume from the undercooled liquid ΔG_V. The maximum of the resulting function ΔG_{nuc} defines the critical nuclei radius r^*, taken from [17].

The determination of the critical nucleus radius r^* can be seen to be the same for both mechanisms and by curve discussion means it can be calculated from the maximum of the $\Delta G_{nuc}(r)$ curve by determining the zero point of the first derivative in equation (2.13) given for the $\frac{\delta G_{nuc}(r^*)}{\delta r}$ as:

$$\frac{\delta G_{nuc}(r^*)}{\delta r} = 0 = 8\pi(r^*)\gamma_{sur} - 4\pi(r^*)^2\Delta g_V \tag{2.13}$$

which results in the form of equation (2.14) for the critical radius r^*:

$$r^* = \frac{2\gamma_{sur}}{\Delta g_V} \tag{2.14}$$

The resulting energetic barrier to the critical nucleus formation can also be determined by inserting the result from equation (2.14) into equation (2.12), which leads to equation (2.15) that gives $\Delta G_{nuc}(r^*)$ as:

$$\Delta G_{nuc}(r^*) = \frac{16}{3}\frac{(\gamma_{sur})^3}{(\Delta g_V)^2} \tag{2.15}$$

where the critical nucleus radius and the resulting $\Delta G_{nuc}(r^*) = \Delta G^*$ are characteristic for the system and play a pivotal role in the solidification pathway as they embody the nucleation barrier. When the Turnbull approximation of equation (2.7) is used to approximate Δg_V as $\frac{\Delta H_f}{T_f} \cdot \Delta T_u$ the equation can be expressed as equation (2.16) where:

$$\Delta G^* = \frac{16}{3}\frac{(\gamma_{sur})^3 \cdot (T_f)^2}{(\Delta H_f)^2} \cdot \frac{1}{(\Delta T_u)^2} \tag{2.16}$$

the ΔG^* can be seen to be coupled to the supercooling with a $1/x^2$ relation.

However, the dominant mechanism in the application is still the heterogeneous nucleation mechanism. For this mechanism, the material combination of the crucible walls or particles in the melt and the liquid is decisive for the wetting angle of the liquid on the surface of the crucible wall or particle surface. Figure 2.6 displays 3 different wetting behaviors that are characterized by their wetting angle and have a significant influence on the solidification.

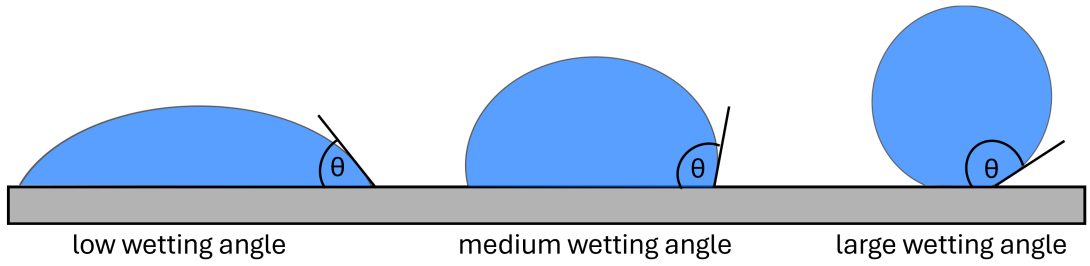

Figure 2.6: Schematic showing the influence of the wetting angle θ on the ratio of surface to volume of the nucleus, the wetting angle is determined by the material combination as well as the nature of the nucleation process, whether the nucleation happens homogeneous in the liquid or heterogeneous on an existing surface, taken from [17].

The impact on the time-temperature-transformation diagram of the three different wetting behaviors is sketched in Figure 2.7 for a solidification into glass by cooling from the melt. The wetting angle significantly influences the crystallization time t_x. The lower the wetting angle Θ is, the smaller is the contribution of the surface term ΔG_s to $\Delta G_{nuc}(r^*)$, which lowers the amount of energy needed to form an energetically stable nucleus significantly, this can be expressed by equation (2.17) for $\Delta G_{nuc}^{hetero}(r)$ as:

$$\Delta G_{nuc}^{hetero}(r) = \Delta G_{nuc}^{homo}(r) \cdot f(\theta) \tag{2.17}$$

here $f(\Theta)$ is the description of the proportionality as a function of the wetting angle given in equation (2.18) according to [30, 31] as:

$$f(\theta) = \frac{(2 + cos(\theta))(1 - cos(\Theta))^2}{4} \tag{2.18}$$

where a wetting angle of 10° lowers the activation energy of the nucleation barrier by 4 orders of magnitude compared to the homogeneous mechanism [32]. This underlines the importance of wetting behavior to crucible walls and impurities for the actual casting processes, as the dominant mechanism is the heterogeneous nucleation in the application of casting processes. This means that especially alloys that have high wetting angles at the crucible wall or the particles within the supercooled liquid can form bulk glass easily in comparison to alloys that show a

low wetting angle and a subsequently low crystallization time t_x.

The size of the critical nucleus, however, is not dependent on the ΔG^*_{nuc} but rather on the ratio from equation (2.14). This depends strongly on the supercooling as the inverse proportionality with Δg_V suggests, as the energetic gain per volume increases with deeper supercooling.

For the number of stable crystallites that can form, however, this depends on the energetic barrier ΔG_{nuc} and the relation can be expressed by an Arrhenius-like function, given in equation (2.19) that describes N^*_r according to Turnbull [30] as:

$$N^*_r = N_0 \; exp(\frac{-\Delta G^*_{nuc}}{k_B T}) \tag{2.19}$$

where the number of stable nuclei increases with a decrease in $\Delta G_{nuc}(r^*)$.

The nucleation rate I(T) defines the number of formed nuclei per second as a function of the temperature, which is given in (2.20) as:

$$I(T) = A \; \nu(T) \cdot exp(\frac{-\Delta G^*_{nuc}}{k_B \cdot T}) \tag{2.20}$$

here, the atomic jump frequency $\nu(T)$ and the Boltzmann constant k_B as well as a constant pre-factor A, contribute to the equation. The atomic jump frequency is connected to the average atomic diffusivity coefficient D by equation (2.21) :

$$D(T) = a_0^2 \; \nu(T) \tag{2.21}$$

with a_0 being the atomic diameter of the respective atomic species.

A critical nucleus that has been formed can then further be described in its growth with equation (2.22) that gives the crystal growth rate u (T):

$$u(T) = A \; D(T)(1 - exp(\frac{-\Delta G^*}{R \cdot T})) \tag{2.22}$$

which describes the growth after nucleation. Both the nucleation rate as well as the growth rate contain a thermodynamic contribution and a kinetic contribution in the form of the atomic diffusivity.

The combination of both nucleation rate $I(T)$ and growth rate $u(T)$ describes the crystallization processes during supercooling the liquid. The situation is being

displayed in Figure 2.8 where the nucleation rate I(T) and the growth rate u(T) are being displayed for both a good glass former, as well as a bad glass former.

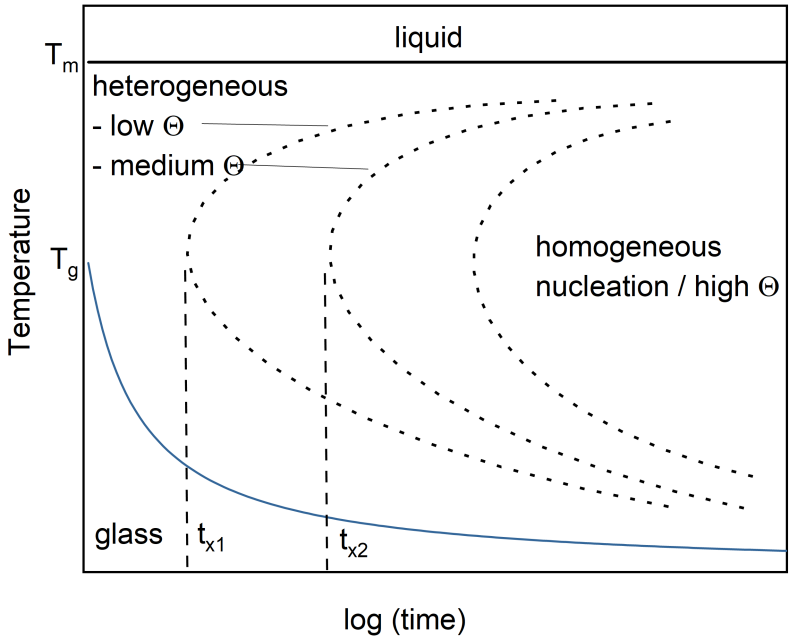

Figure 2.7: Time-temperature-transformation diagram that embodies the influence of the nucleation mechanism expressed by a variation of the wetting angle Θ, where the impact on the crystallization times t_x can be observed.

The marked area between the curves indicates the area where both nucleation as well as growth are significant, so that this area in principle makes up the crystallization nose. The Johnson-Mehl-Avrami-Kumogorov (JMAK) equation combines the two into equation (2.23) [33] where X(t) is given as:

$$X(t) = 1 - exp(\frac{\pi}{3} I(T)(u(T))^3 t^4) \tag{2.23}$$

and the equation describes the shape of the crystallization in the TTT-diagram. Just below T_m, the growth rate is high and dominates the process. Whereas at low temperatures, the low mobility limits the growth rate despite the high driving force that triggers the nucleation and initial crystallization.
The shape of this crystallization 'nose' and the different growth and nucleation contributions to the crystallization process lead to the microstructure's dependence

on the cooling rate that the system experiences during solidification, as Turnbull already described for Gallium [30]. When the cooling rate is low and the system is cooled in conditions similar to sand casting, the melt stays close to T_m for a while where very little stable nuclei form, although once they form the crystallization then is dominated by the slow growth of those nuclei, leading to a coarse and globular microstructure. In contrast, when the cooling rate is high, as it is in copper mold casting, the amount of stable nuclei is high, and a finer, often orientated microstructure results, which contains nucleation and growth dominated zones of numerous fine crystals and a rapid crystal growth zone, respectively, resulting in characteristic microstructures.

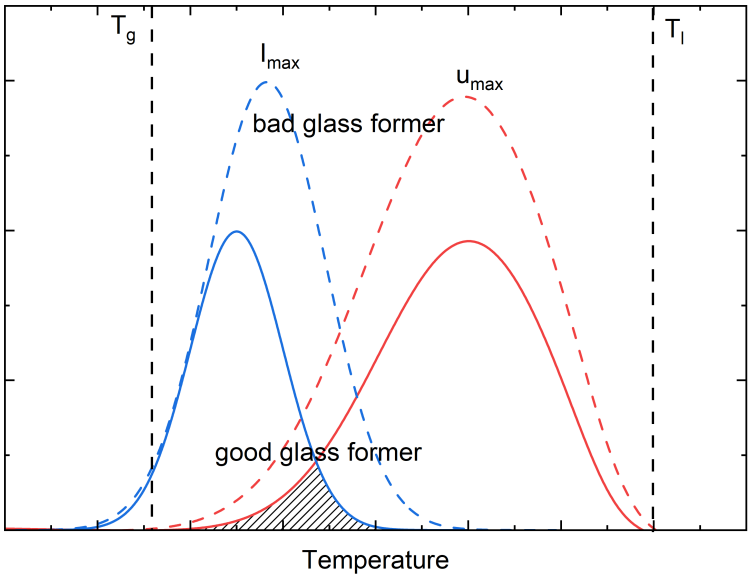

Figure 2.8: Schematic display of the nucleation rate and growth rate as a function of the temperature for both a good glass former and a bad glass former, the region where I(T) and u(T) overlap is unfavorable for the glass formation and the goal of alloy development can be interpreted to reduce the Area between the two curves.

2.3 Viscosity and fragility concept

The atomic mobility mentioned in the previous section is represented in the glass forming systems on an macroscopic scale by the viscosity of the liquid and supercooled liquid region. The diffusion coefficient is also connected to the viscosity of the system via the Stokes-Einstein relation given in equation (2.24) that describes $D(T)$:

$$D(T) = \frac{k_B T}{6\pi\eta(T)a_0} \tag{2.24}$$

where k_B denotes the Boltzmann constant, a_0 is the atomic diameter, and T is the absolute temperature.

The absolute viscosity and the change in viscosity during cooling, in combination with the previously discussed thermodynamic considerations, present the fundamental quantities defining the glass-forming ability of a metallic glass former. The viscosity is the quantity that is intertwined inverse proportional with the atomic mobility, which can be accessed the easiest in the laboratory and is therefore often the favorite characterization method of choice [16]. The viscosity is given in $Pa \cdot s$ and describes the resistance of a liquid to the resulting internal shearing of liquid layers, thereby precisely phrased, the dynamic viscosity η, and is meant to demarcate against the kinematic viscosity. The viscosity can also be understood as a measure of the internal friction of the system during its flow.

However, the behavior of deeply supercooled liquids can deviate from this behavior where a 'decoupling' of translational diffusion from the viscosity occurs when structured domains start appearing in the liquid, as it can happen in deeply supercooled liquids approaching the glass transition temperature [34]. For their study of supercooled o-terphenyl, Cicerone et al. argue that structured domains less than 2.5 nm in size form near the glass transition temperature [35], where Tarjus et al. point out that even small clusters can induce a huge increase in relaxation time, causing a significant increase in viscosity as it is proportional to stress-relaxation time [34]. This emphasizes the deviation from Stokes-Einstein behavior that can be caused by structured domains in the liquid. For bulk metallic glass formers, a similar finding was reported by Geyer et al. for the $Zr_{46.7}Ti_{8.3}Cu_{7.5}Ni_{10}Be_{27.5}$

alloy, where rather a cooperative diffusion mechanism is indicated at the glass transition temperature [36].
The Maxwell relation in equation (2.25) links the viscosity η to the alpha relaxation τ_α:

$$\eta = G_\infty \tau_\alpha \tag{2.25}$$

with G_∞ being the high frequency shear modulus and τ_α being the time atoms in the liquid need to rearrange while being in the equilibrium liquid state above T_g [37, 38]. The α -relaxation is characterized by non-Arrhenius behavior that shows an increasing activation energy with decreasing temperature that can be described well with a Vogel-Fulcher-Tamman (VFT) type equation [38]. The VFT model consists of the iterative contributions of Vogel [39], Fulcher [40] and Tammann [41] to the description of the behavior of viscosity as a function of the temperature and can be seen in the equation (2.26) that describes $\eta(T)$ as:

$$\eta(T) = \eta_0 \; exp(\frac{D^* \cdot T_0}{T - T_0}) \tag{2.26}$$

here, the fragility parameter D^* is introduced, which is quite useful to quantify the behavior of the viscosity and classify the different behaviors of viscosity in the different metallic liquids. The T_0 is the so-called VFT-temperature where the viscosity of the liquid approaches infinity, meaning that the T_0 is the lowest possible glass transition temperature, and amorphous alloys have to transform into the supercooled liquid for each $T > T_0$ independently of the heating rate [42]. The pre-factor η_0, however, marks the other fixed point of the equation as it describes the viscosity of the liquid at an infinite temperature. According to Nemilov [43] the theoretical value can be calculated with equation (2.27) for η_0 as:

$$\eta_0 = N_A \frac{h}{V} \tag{2.27}$$

with the N_A being the Avogadro's constant, h being the Planck's constant, and V the molar volume of the alloy. The value is often situated close to $10^{-5}\ Pa \cdot s$ [32, 44].
The schematic viscosity behavior for a metallic glass forming system can be ob-

served in Figure 2.9, where the typical steep increase of viscosity towards the glass transition temperature is encountered and the transition into a glass is sketched at a viscosity of $10^{12} Pa \cdot s$. To visualize the VFT parameters that were discussed previously, the parameters can be found with their respective limits being drawn as dashed lines into this schematic plot of the viscosity. The display in this kind of figure directly depicts viscosity as a function of temperature; though the depiction in this form is not optimal for comparing the behaviors of liquids with different fragility. The difference in behavior can be quite striking despite the optical difference between the directly depicted viscosities being small. Angell investigated the formation of glasses from liquids and classified liquid behavior during cooling into 'strong' and 'fragile' liquids depending on their fragility and found a convenient way of display that is henceforth called 'Angell-plot' [45].

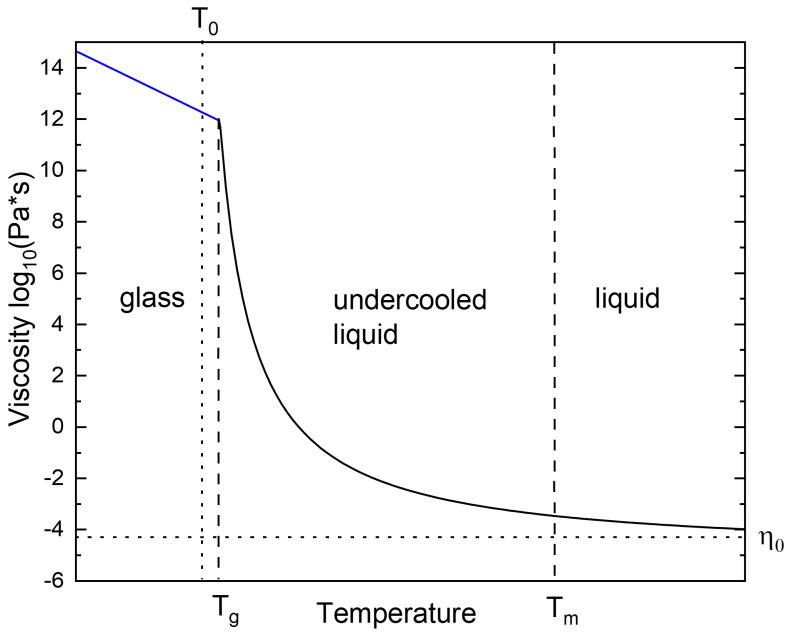

Figure 2.9: Viscosity displayed schematically as a function of the temperature for a glass forming system, the slope of the viscosity is expressed by the fragility, namely the m-fragility, which is the resulting slope at T_g.

The schematic Angell plot for liquids of metallic glass formers is given Figure

2.10, the typical range of fragility parameter D^* range from intermediate 10 to 26 for bulk metallic glass formers [46], whereas fragile liquids are typically showing a D^* below 10 and tend to be only marginal metallic glass formers [47]. The 'strong' metallic glass formers with a high fragility parameter show Arrhenius-like behavior as they have a high viscosity at the melting point and tend to form stable glasses [44].

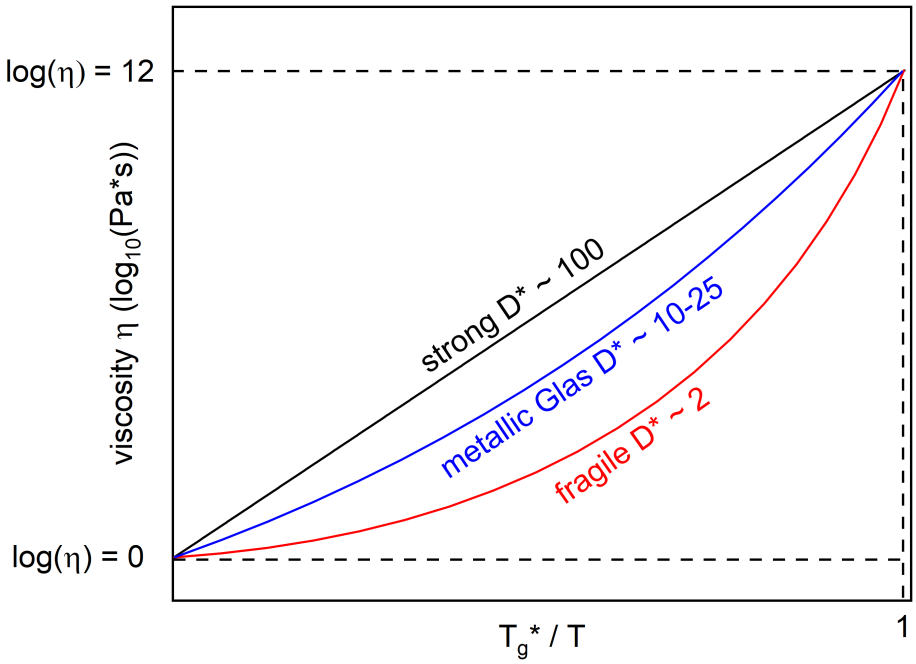

Figure 2.10: The logarithmic viscosity as a function of the inverse temperature, which is named Angell-plot after Austen Angell, is frequently used to display differences in fragility between liquids in a well comparable graphic.

The fragility index m is also commonly used in the description of the viscosity's behavior, with m given by equation (2.28) as:

$$m = \frac{d\ \log_{10}(\eta)}{d\ (T_g^*/T)}\bigg|_{T=T_g^*} \tag{2.28}$$

here, the m-fragility describes the slope of the logharithmic viscosity-curve at T_g^*, the kinetic glass transition temperature, where the viscosity equals $10^{12}\ Pa \cdot s$ [48, 49].

The VFT-model describes the behavior of a multitude of glass-forming liquids, however, it is an empirical model, and there are liquid behaviors that are not well described by the VFT-model. Especially in bulk glass forming liquids, as in the case of the $Fe_{43}Cr_{16}Mo_{16}C_{15}B_{10}$ where the viscosity in the high temperature liquid phase and the low temperature supercooled liquid state was investigated by Bochtler et al. and found to transition from a fragile to a strong behavior during cooling from the equilibrium liquid [50], which is also observed in a variety of other bulk glass forming liquids [16]. An example in the form of Fe-based BMG can be seen in Figure 2.11 where the behavior of a strong low-temperature liquid in TMA analysis and a fragile high temperature liquid behavior in TEMPUS can be observed, that results in two different fragility parameters D^*, indicating a transition in the intermediate region [50].

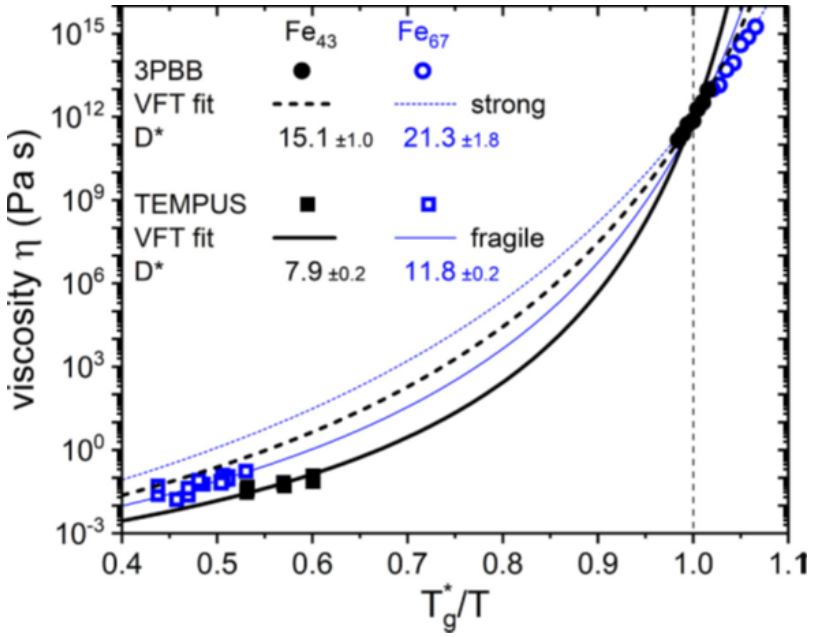

Figure 2.11: Low temperature viscosity data from TMA and high temperature viscosity from TEMPUS of $Fe_{43}Cr_{16}Mo_{16}C_{15}B_{10}$ and $Fe_{67}Cr_{3.5}Mo_6C_{5.5}P_{12}B_{2.5}$, where both alloys show fragile high temperature behavior and strong low temperature behavior with the respective VFT-fits, taken from [50].

This is a commonly observed phenomenon in bulk metallic glasses, especially in Zr-based metallic glasses. Various reports on the matter can be found in the

literature [45, 51–55]. The precise mechanism of this transition is debated in the literature for BMG forming melts with the degree of order in the liquid state, as the higher medium-range ordered liquid should also behave stronger, while strong short-range order is thought to lead to a decrease in fragility parameter [53, 56]. A more recent, yet also empirical model was therefore proposed by Mauro, Yue, Ellison, Gupta and Allan, referred to as the MYEGA-model, given in equation (2.29) [57] that describes $\eta(T)$ as:

$$\eta(T) = \eta_0 \; exp[ln(10)\frac{B}{T}exp(\frac{C}{T})] \tag{2.29}$$

here, the parameters B and C function as fitting parameters for the MYEGA-model, and η_0 has quite the same meaning as in equation (2.26) and denotes the viscosity limit at an infinite temperature.

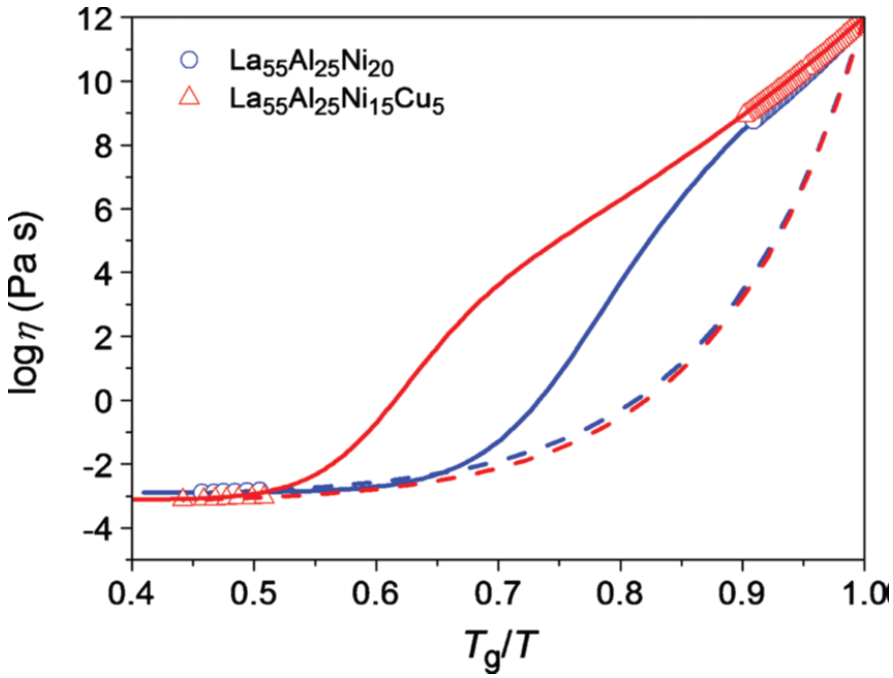

Figure 2.12: Lanthanum-based bulk metallic glasses exhibit a fragile to strong transition that can be described well with the extended MYEGA model, drawn in solid lines and not with the regular MYEGA fit that is drawn in dashed lines, for the two BMGs, taken from [58].

The MYEGA-model can be extended, as it was shown by Mauro et al. to accom-

modate for fragile to strong transitions by accommodating the different scaling of dynamics across the strong regime and fragile regime by weighting factors [58].
The problem becomes apparent when the MYEGA-model is applied exclusively to the high temperature region, as the dashed lines in Figure 2.12 indicate, for two metallic glass forming liquids, the low temperature data cannot be easily accounted for in the standard MYEGA-expression with its three parameters.
The extended MYEGA-model that was used by Zhang et al. [58] to describe the fragile to strong transition can be found in equation (2.30) where it describes η by:

$$\log(\eta) = \log(\eta_\infty) + \frac{1}{T\left[W_1 \exp\left(-\frac{C_1}{T}\right) + W_2 \exp\left(-\frac{C_2}{T}\right)\right]}. \tag{2.30}$$

where two constraints C_1 and C_2 with their respective normalized weigthing factors W_1 and W_2 that account for two different mechanisms controlling the dynamic behavior of the liquids, this enables the model to describe both the low temperature viscosity and the high temperature viscosity and 'capture the full range of viscosities' [58].
The fragile-to-strong transition was implied by Zhang et al. to be intrinsic to strong liquid systems [58]; however, when sulfur is involved, this is not necessarily the case, as the data stemming from Kuball [59], Ruschel et al. [60] and the results of this work on the S-infused liquid's viscosity demonstrate.

2.4 Glass forming criteria for Bulk metallic glasses

Critical cooling rate and reduced glass transition temperature

As previously mentioned, the glass formation of alloy systems depends on both thermodynamic as well as kinetic aspects, like the nucleation and growth behavior of crystalline phases. The ability to form a glass is labeled the glass forming ability (GFA) of the alloy, and it describes simply the rapid solidification of the alloy at a temperature below the glass transition temperature T_g. The alloy is considered to be a glass by the generally accepted criterion of a total crystalline volume fraction below 10^{-6} [44]. Therefore, the critical cooling rate R_c is defined by that volume fraction and is itself an alloy-specific property that depends on the composition of the alloy. For the critical volume fraction the corresponding R_c can be expressed in dependence of the previously mentioned factors influencing the glass transition, which is the nucleation rate I(T), the growth rate u(T) of the crystalline phase as well as the liquidus temperature T_l, the glass transition temperature T_g and the cooling rate T' that the liquid experiences which, according to Suryanarayana [44] , in combination results in equation (2.31) that describes R_c as:

$$(R_c)^4 = \frac{4\pi}{3 \cdot 10^{-6}} \int_{T_l}^{T_g} I(T') \left[\int_{T''}^{T_g} u(T'')dT'' \right]^3 dT' \tag{2.31}$$

The concept of the critical cooling rate can best be explained with the help of Time-Temperature-Transformation (TTT) diagrams. The schematic of Figure 2.13 highlights the difference between the classes of metallic glass, bulk metallic glass, and regular pure metals by their difference in critical cooling rate. Pure metals typically require a high R_c of $> 10^{10-12}$ K/s, which is only available under rather extreme conditions that cannot be achieved by simple solidification means [44, 61]. One possibility is the laser ablation of a glass-forming alloy submerged in coolant, as demonstrated by Tong et al. that demonstrated synthesis of amorphous Au [5]. Once another atomic species is being introduced into the system, the critical cooling rate can typically become as small as 10^4 - 10^6 K/s [44]. The impact of added elements can have a significant effect on the position of the crystallization nose

time t_x in the T-T-T diagram, as it is well known from classical metallurgy systems like aluminum alloys where the alloying elements cause significantly different nose times depending on their interaction with the primary phases of the system, whether they are being favored or hindered in their formation by the alloying element [62]. As the number of components increases, the R_c decreases further as multi-component alloys can reach down to 10^2 K/s, whereas bulk metallic glasses typically can reach as low as 10 K/s and in extreme cases even below 1 K/s [63]. For those systems with a large number of alloying elements, the crystallization nose is shifted to longer times to the right of the TTT-diagram in Figure 2.13.

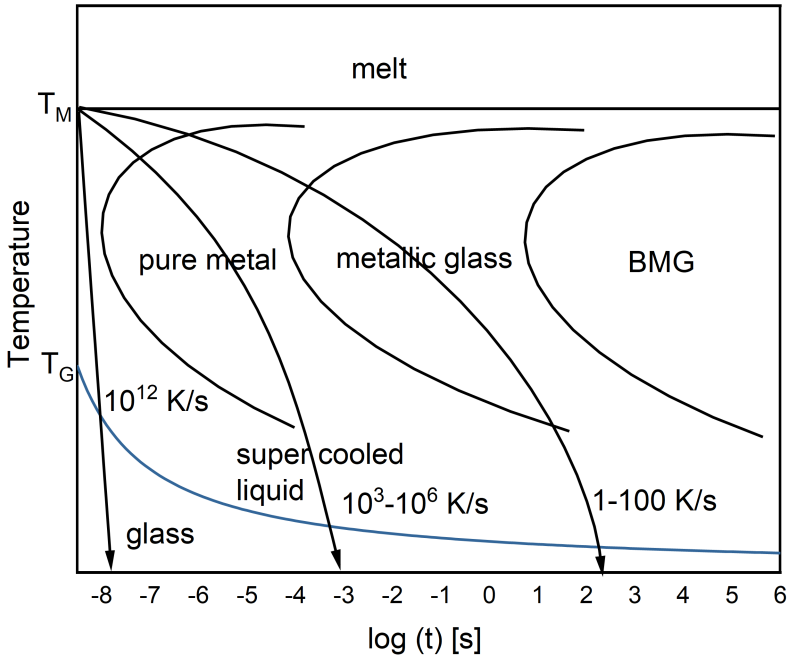

Figure 2.13: The different classes of metallic glass formers displayed in a TTT diagram, where metallic glasses refers to the material class that possesses critical cooling rates situated between 10^3 to 10^6 K/s.

Here, the reduced glass transition temperature T_{rg} given in equation (2.32) as:

$$T_{rg} = \frac{T_g}{T_l} \tag{2.32}$$

can be understood as a related glass forming criterion to the critical cooling rate, as the glass forming tendency should increase with a decrease of the difference

between T_g and T_l [44].

Due to the fact that I, u, and η vary throughout the whole temperature range, the T_{rg} provides a good estimation measure for the rather difficult accessible R_c. The concept was proposed by Turnbull based on the classical nucleation theory, where for $T_{rg} \geq \frac{2}{3}$ the homogeneous nucleation is completely suppressed, from the majority of reported investigations there is a typical lower limit of 0.4 for T_{rg} that was found as minimum required value for alloys to be able to form a glass [44].

Regarding the different types of phase diagrams that are encountered in the investigation of the Zr-Ti-Ni-Cu-S system, the basic types are to be explained in the following section. Figure 2.14 a) shows the basic ideally miscible system where the components can form both a mixed crystal as well as a liquid phase. This is the base type of system that is encountered for the Ni-Cu system where especially the similar chemistry and near identical atomic diameter contribute to the systems behavior, although more recent studies report a miscibility gap for nanolayered thin films within the cubic face centered phase with a maximum at 780 K [64].

The second type of phase diagram that is crucial to this work is shown as a sketch in 2.14 b) that shows an ideal binary eutectic system. For systems that show an eutectic behavior, the solidification reaction of $L \longrightarrow \alpha + \beta$ dominates the systems behavior and the composition at the eutectic point where the liquidus temperature equals the eutectic temperature is pre-destined to result in the highest T_{rg} value, which correlates with the fact that bulk glass formers can typically be found close to deep eutectics, making them an ideal starting point for the search of BMG [65].

The remaining phase diagrams in 2.14 c) come in the form of a complete miscibility gap in both solid as well as liquid states, which appears in binary systems where two elements with a strong positive enthalpy of mixing are involved. This system behavior is unfavorable for the design of glass forming systems, as the homogeneous liquid is often only encountered at very high superheatings that are not easily achievable by regular melt quenching techniques. For a partial miscibility gap in the liquid state, like sketched in Figure 2.14 d), however, the situation is different; the phase separation of liquid into $l_A + l_B$ does not rule out bulk glass forming. There have been reported phase-separated glasses that show a certain degree of local chemical inhomogeneity with an attractive influence on the macro-

scopic behavior of the alloys due to a hierarchical microstructure [66]. Regarding the phase-separated BMG stemming from a type d) phase diagram, for Zr-based phase-separated BMGs, there have been reports of exceptional ductility in those systems, in the case of $Zr_{62}Cu_{18}Ni_{10.4}Al_8Fe_{1.6}$, the reported ductility in compression testing reaches up to a stunning 32.6 % [67].

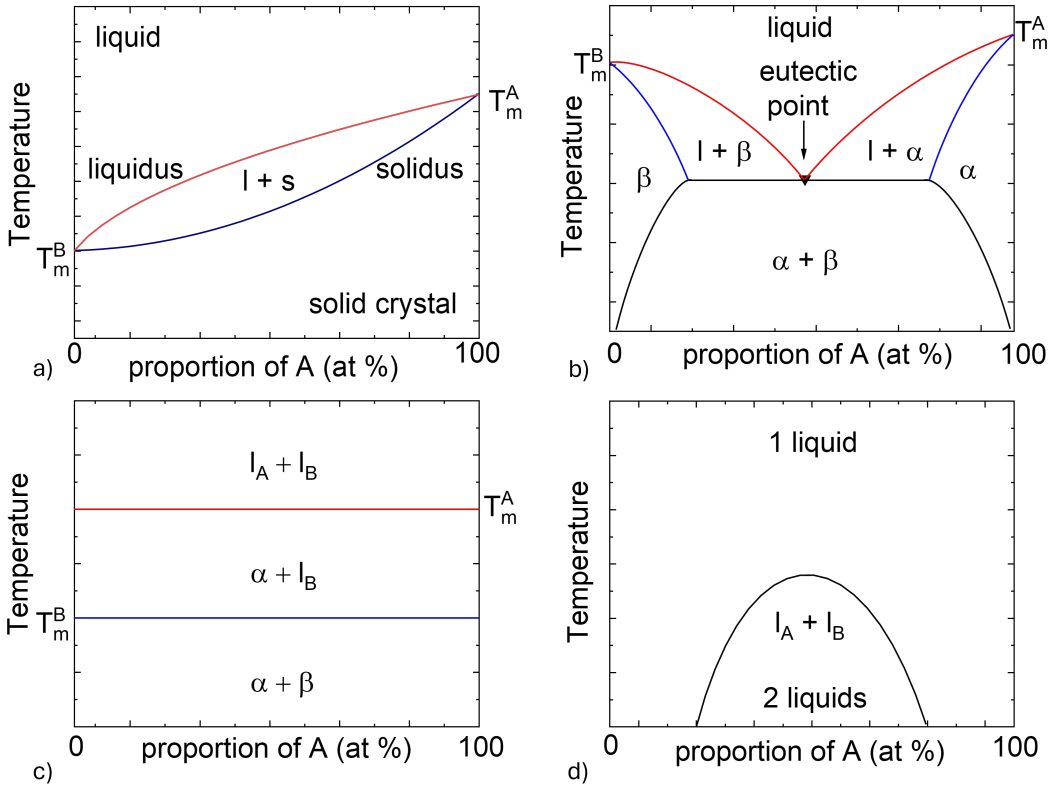

Figure 2.14: Types of phasediagrams for the different types of binary systems for a) an ideal miscibility of the two elements like it is found e.g. in Ti-Zr b) a simple eutectic system where a reaction of $L \rightarrow \alpha + \beta$ dominates the phasediagram, like it is found in a more complex variant in the Zr-Cu system c) a complete miscibility gap for the system exists, like found in Fe-Pb below 2000 K and d) a miscibility gap in the liquid phase exists that leads to spinodal decomposition of the liquid during cooling like it is found in the Cu-S system for both low and high content of sulfur in the system.

As a consequence, the implication is that T_{rg} rises with the increase of solute con-

tent and nears its respective maximum at the eutectic composition for systems that show eutectic behavior. This is sketched in Figure 2.15, where a glass forming ability for this eutectic system is given, and the value for the respective T_g is sketched that varies only slightly as a function of the composition. The reduced glass transition temperature, however, behaves inversely to the liquidus temperature, which is strongly dependent on the composition, so that T_{rg}, which is drawn as a dashed purple line, shows a maximum at the eutectic point. Since the introduction of the T_{rg} concept, there have been numerous further glass forming criteria parameters introduced, which will be discussed in the at the end of the chapter.

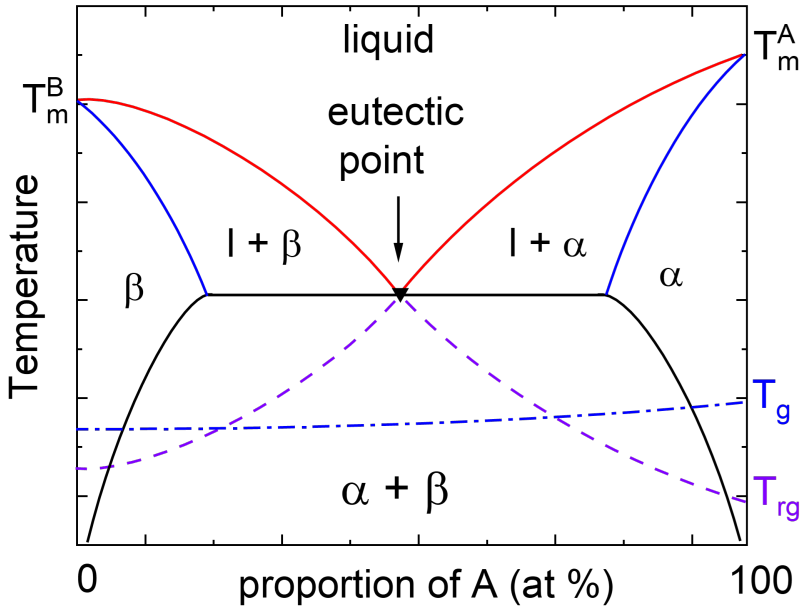

Figure 2.15: Previously mentioned eutectic system where the glass transition temperature T_g is given in a blue dashed point-line and the reduced glass transition temperature is sketched in a dashed purple line.

2.4.1 T_0 concept

For the description diffusionless phase transformations Kaufman and Cohen proposed the concept of the T_0 temperature [68]. The concept is especially interesting for the Bulk Metallic Glasses since their rapid quenching and high viscosity melts in combination do not allow for much diffusion during solidification. For the T_0 concept a temperature T_0 is defined where the Gibbs free energy of the parent phase is equal to atleast one product phase and have the same composition [69]. The T_0 concept is utilizes the chemical potential to describe the Gibbs free energy, that can be defined for a multicomponent system according to equation (2.33):

$$\mu_i = \left(\frac{\partial G}{\partial n_i}\right)_{T,P,n_{j\neq i}} \tag{2.33}$$

where the system is comprised of a number of individual components i that possess a chemical potential μ_i that refers to the change in Gibbs free energy due to changes in the concentration of the component i, this can be expressed by the partial derivation at constant pressure P, constant temperature T and constant remaining molar quantity n_j for $j \neq i$ of all other components except component i [70].
G relates here again to the Gibbs free energy of the system. The chemical potential relates to the mixture of components according to the concept of a regular solution that accommodates interactions between different atomic species and mixing effects [71]. The sum of all chemical potentials in the system comprises the total Gibbs free energy of the system, expressed by equation (2.34) for G as:

$$G = \sum_i \mu_i n_i. \tag{2.34}$$

making it a function of the composition [70].
In a binary eutectic system, as mentioned before, the three phases of liquid, solid phase α, and solid phase β are present. Accordingly each phase has an individual Gibbs free energy that is expressed by the chemical potential for component A in the liquid μ_A^L, for component A in the solid phase α μ_A^α and for component A in the solid phase β μ_A^β with the corresponding complementary molar fractions n_A and n_B and the same denomination analog for the component B in the three phases.

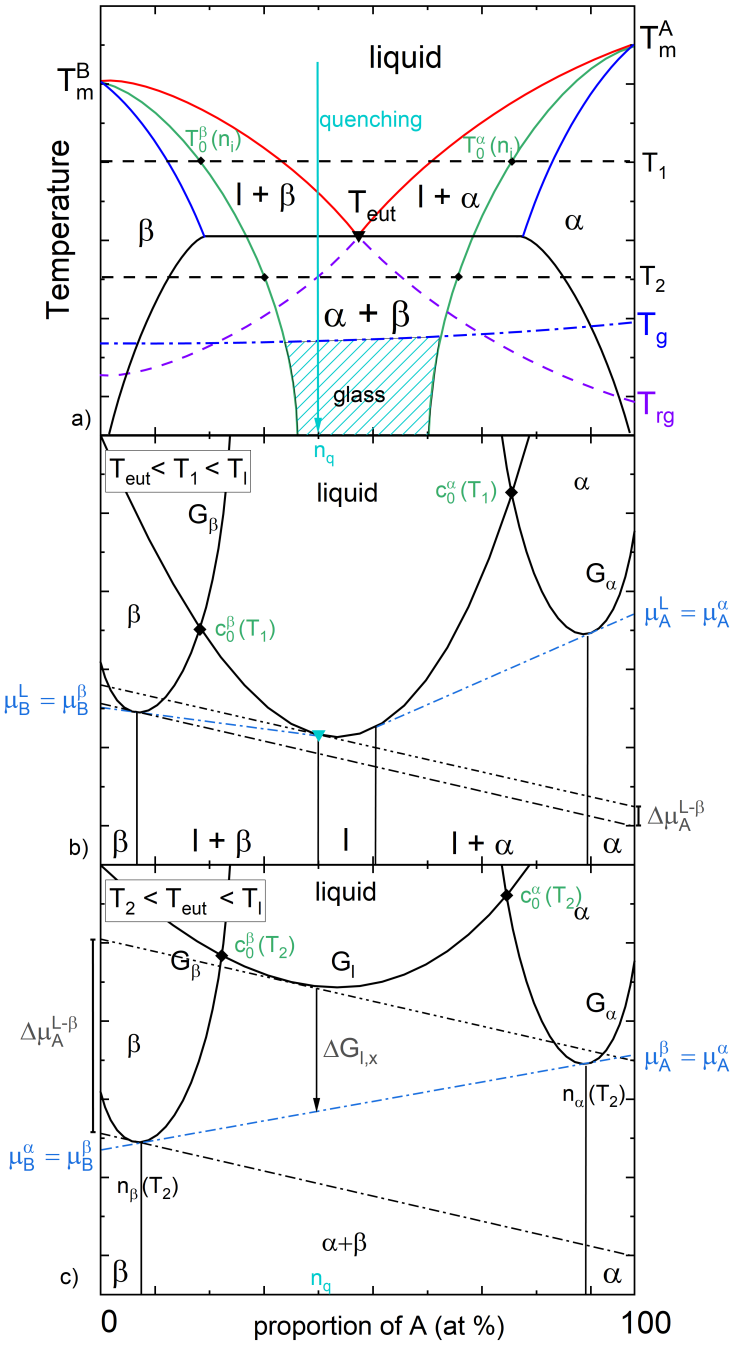

Figure 2.16: a) Phase diagram of a binary eutectic system, the green lines are the T_0 lines that embody the intersection of solid and liquid phase Gibbs free energy b) and c) show the Gibbs free energy curves for two different temperatures, the region between the T_0 lines favors glass formation when being quenched below T_g.

The double tangent to the lowest Gibbs free energy at a given temperature determines which phase is the most stable phase in the equilibrium state of the system. For those systems, regions of the phase diagram exist, where multiple phases are present at a given temperature. If the difference in chemical potential is small, the tangent to the respective Gibbs free energy curve is the graphic representation of the chemical potential.

The concept is sketched in Figure 2.16 a)-c) for two reference temperatures $T_l > T_1 > T_2$. For the sketched quenching composition n_q the difference in Gibbs free energy between the eutectic $\alpha+\beta$ 2-phase region is given by the difference between the Gibbs free energy curve of the liquid and the blue point-dashed tangent in Figure 2.16 c), this represents the thermodynamic driving force for crystallization of the liquid. The difference in chemical potential $\Delta\mu_i^{l-x}$ is the driving force for the component i towards crystallization. Here for a composition n_α the $\Delta\mu_B^{l-\beta}$ stands for the chemical potential of the component B to form the β phase from the liquid and $\Delta\mu_A^{l-\beta}$ describes the same for component A. For multi-component systems, the chemical potential of all components and appearing phases gets more complex with each added element, so that complete phase diagrams with the data on the chemical potential are rarely found for complex systems such as bulk metallic glass formers. The driving force for crystallization is more easily accessible from calorimetric approaches to approximate $\Delta G_{l,x}$.

The T_0 curves allow to assess the region of the phase diagram where the mixture of $\alpha + \beta$ is the most stable phase according to the thermodynamics of the system and the crystallization mechanism is diffusion controlled [72]. Those areas can be quenched into the glassy state if the cooling rate is fast enough to avoid the chemical separation preceding the eutectic crystallization. This can be favored by stabilizing the liquid phase against chemical separation, as then the liquid can be cooled further towards the glassy region, which reduces the driving force towards the eutectic mixture. The T_0 curves show the composition-dependent point where the Gibbs free energy of liquid and crystal is equal, and for two different temperatures, the resulting Gibbs free energy curves are sketched in Figure 2.16 b) and c). In the outlying section of the T_0 lines, the α or β phase can crystallize and form a solid solution that requires no diffusion to form and can easily intersect the

glass formation. Therefore, alloy development measures aim to slow down melt dynamics and position the composition near a deep eutectic where the driving force for crystallization is low.

2.4.2 Empirical glass formation criteria

There are multiple empirical models, of which the most prominent are to be mentioned in the following section, excluding strictly theoretical models.
Early on in the beginning of the 1990s the so called 'confusion principle' was formulated by A. Greer as 'the more elements involved, the lower the chance that the alloy can select viable crystal structures, and the greater the chance of glass formation' [73] meaning that a low chance of a viable crystal structure diminishes both nucleation and growth of the crystals and thereby enables a higher chance of glass formation. The atomic species with the most impact on 'confusing' the systems are those that differ significantly in size from the other elements of the alloy, discussed on the example of the role that Be plays for the Zr-Ti-Ni-Cu-Be system. Here the Be is the element that enables a large increase in GFA due to the introduction of a large quantity of the very small element into the Vitreloy 1 alloy of Johnson and Peker that 'confuses' the alloy and prevents formation of the crystalline phase [7, 73].
In 1997 A. Inoue postulated three empirical rules as guidelines in designing BMG alloys to maximize the glass forming ability and ensure a large supercooled liquid region, based on experimental observation as well as on kinetic theories: (1) the system should consist of more than three elements, (2) the atomic size ratios of the included elements should differ by about 12 % and (3) overall there should be a negative heat of mixing between the constituents of the system [74]. The satisfaction of the three empirical rules gave rise to a higher degree of dense random packing that makes atomic rearrangement on the long-range scale more difficult and subsequently hinders crystal growth and also increases the solid-liquid interfacial energy [74].
Since then a multitude of glass forming criteria have been reported, accompanied by 'glass forming parameters', one being the topological approach of the δ parameter that describes the mismatch in atomic size within an alloy according to [75]

that is given in equation (2.35) that gives δ as:

$$\delta = \sqrt{\sum_{i=1}^{N} c_i \left[1 - r_i/(\sum_{i=1}^{N} c_i r_i)\right]^2} \tag{2.35}$$

where r_i being the covalent atomic radius of the element i and c_i the concentration of element i in the alloy.
This parameter can be utilized to calculate the overall 'confusion' in the alloy and allocate the alloy in the groups of characteristic atomic size mismatch ranging from high entropy alloys (HEA) over intermetallic alloys to amorphous alloys with rising δ parameter and yield strength [75]. The δ parameter is quite useful for the discussion of the impact of sulfur on the structure of glass and liquid in chapter 5, and the atomic radii utilized for the calculation can be found in reference [76].
Further glass forming criteria that involve the different characteristic temperatures of the glass forming systems to be mentioned briefly are listed in Table 2.4.2, as reported in the oversight table of Long et al. [77].

Table 2.1: Ten established GFA criteria from the literature in chronological order.

No.	**GFA parameter**	**Formula**	**Year**	**Ref.**
1	ΔT_x	$T_x - T_g$	1991	[78]
2	T_{rg}	T_g/T_l	2000	[79]
3	γ	$T_g/(T_g + T_l)$	2002	[80]
4	ΔT_{rg}	$(T_x - T_g)/(T_l - T_g)$	2004	[81]
5	α	T_x/T_l	2005	[82]
6	β	$T_g/T_l + T_g/T_l$	2005	[82]
7	δ	$T_g/(T_l - T_g)$	2005	[83]
8	γ_m	$(2T_x - T_g)/T_l$	2007	[84]
9	ϕ	$T_g/T_l(\Delta T_x/T_l)^{0.1543}$	2007	[85]
10	ξ	$T_g/T_l + \Delta T_x/T_l$	2008	[86]

The problem of those criteria correlating the characteristic temperatures with glass forming ability is that they are being arbitrary in their complexity of calculation, like the recently reported parameter χ given in equation 2.36 as:

$$\chi = \left(\frac{T_x - T_g}{T_l - T_x}\right) \times \left(\frac{T_x}{T_l - T_x}\right)^a \tag{2.36}$$

demonstrates by introducing more parameters and complicating the calculation utilizing the same characteristic temperatures [77]. Despite their difference in mathematical formula, those parameters still show very similar trends across the different parameters. The approach to correlate the GFA across a large range of systems of metallic glass forming systems with a general glass forming criterion including the crystallization temperature T_x is especially problematic for systems that involve metastable or quasi-crystalline phases, here the criteria often show no direct correlation with the experimentally observed glass forming ability of the alloys. When considering the T_0-concept and the change in chemical potential at different temperatures it becomes apparent why the dominant phase in the section just below the solidus temperature T_s and in the section above T_x is not necessarily the same for complex alloys. Therefore, except for T_{rg} and the topological δ parameter, the interpretation and discussion of the glass forming criteria from table 2.4.2 was not an expedient measure for the Zr-Ti-Ni-Cu-S system.

2.4.3 The Zr-Ti-Ni-Cu system

The Zr-Cu system is a classical example of the previously mentioned good glass-forming systems that are located near eutectic points of the respective system. For a certain region of the binary Zr-Cu phase diagram, even binary bulk glass formation has been reported near the deepest eutectic point of the system located at 38.2 $at\%$ Zr and with a T_{eut} of 1.158 K (885 $°C$) [87]. The systems of Zr-Ni, Ti-Cu, and Ti-Ni are very similar to Zr-Cu as they all share the same base type of phase diagram and show multiple eutectic points and intermetallic phases. Especially the congruent melting phases are interesting for metallic glass development with the previously discussed T_{rg} criterion in mind, which are especially A_2B type and AB type alloys for the $A = (Ti, Zr)$ and $B = (Ni, Cu)$. This work focuses on the A_2B section of the phase diagram, where in all 4 binary systems, a congruently melting stoichiometric intermetallic phase can be encountered.

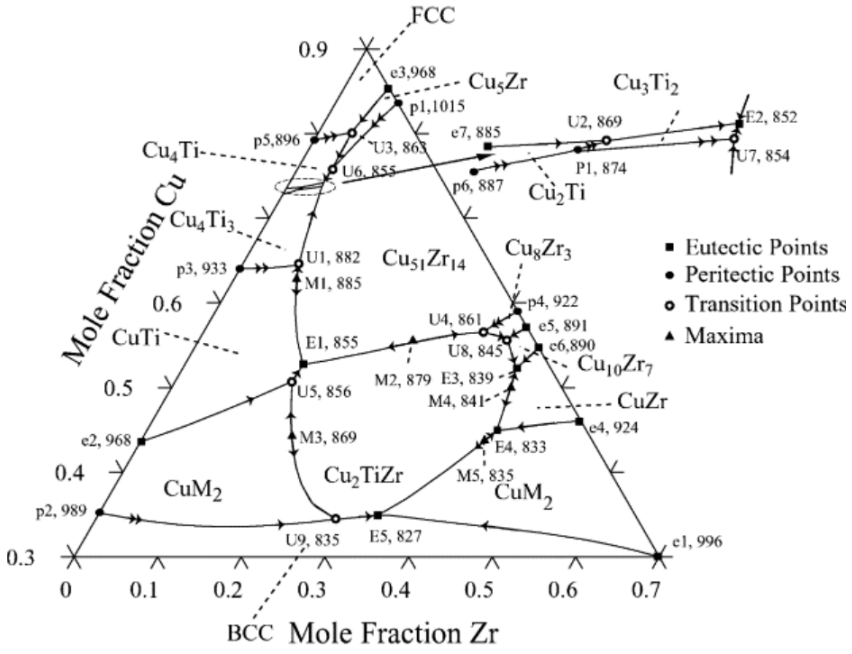

Figure 2.17: Ternary system showing the solidification temperatures of Ti-Zr-Cu in $°C$ with important points marked out in the compositional space, especially the eutectic point 5 ($E5$) is important for the alloys developed in this work as it describes $L \longrightarrow CuTi_2 + Cu_2TiZr + CuZr_2$. Taken from reference [88].

In total (Zr, Ti, Cu, Ni) mixtures show different eutectic points throughout the binary, ternary and quarternary systems with a prominent eutectic located at the composition of $Zr_{33.3}Ti_{33.3}Cu_{33.3}$, where the minimum in liquidus temperature is reached in regions of the pseudo-binary system of (Ti, Zr)-(Cu) where $X_{(Ti,Zr)} = X_{Cu}$ as in those central regions the respective binary interaction energies reach their minimum and the entropy of mixing is maximized, simliar to the base concept of HEA alloys [88]. The liquidus projection of the ternary Ti-Zr-Cu system is displayed in Figure 2.17. This eutectic point is especially interesting as it is exactly equi-molar, and the $T_{eut}(E5)$ at 1.100 K is even lower than the previously mentioned Zr-Cu eutectic point that can form binary bulk glass. The E5 eutectic alloy is explored in reference [19] and can be understood as the logical predecessor to the quaternary BMG alloy.

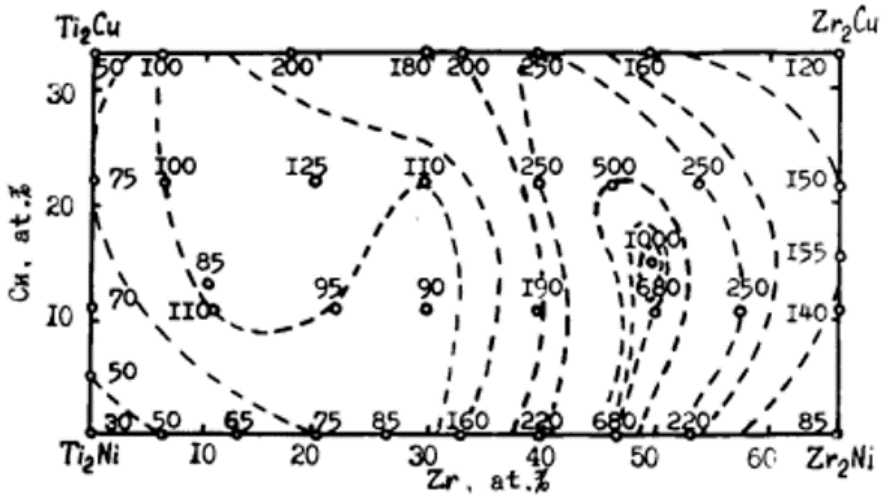

Figure 2.18: Depiction of the glass forming ability in μm as a function of the composition as a quarternary map between the four intermetallic compounds of A_2B with A = (Zr, Ti) and B = (Ni, Cu), taken from reference [20].

The Zr-Ti-Ni-Cu quaternary system was investigated by Molokanov and Chebotnikov in 1990, where mixtures of the intermetallic compounds were investigated regarding their thermophysical properties, and multiple composition-property graphs were published. The glass-forming ability of the system as a compositional map is shown in Figure 2.18, it displays the critical casting thickness that could be

obtained with melt spinning or jet melt quenching in μm as a function of the composition with dashed lines marking out regions of similar GFA. The publication also lists the glass forming factors for the individual binary compositions as well as the ZrTiNi ternary Laves phase with a minimum cooling rate of 2×10^5 K/s [20]. From the GFA map the peak in glass forming ability can be located at the composition of $Zr_{50}Ti_{16.6}Ni_{18.3}Cu_{15}$, with a GFA of 1000 μm assigned to it and the critical cooling rate R_c was estimated to be 3×10^3 K/s [20]. Which is close to 300 μm critical casting thickness, according to the Johnson formula discussed in the methodology section, that correlates quite well with the copper crucible casting setup employed by the chair of metallic materials. This point is later chosen as the starting point for the alloy development that was performed in this work, as it is a very promising candidate of the Zr-based metallic glasses that contains neither aluminum nor metalloid additions and is still able to form a bulk glass, although only via the melt jet quenching technique.

Later in 1999, the system was investigated thoroughly by Molokanov et al. regarding the crystallization sequences and encountered phases in the bulk material they were able to produce by the jet melt quenching technique. Here, a difference in microstructure depending on the undercooling of the melt was observed [21]. For a better understanding of the hypothesis based on the reported findings, the schematic of the publications is reprinted in Figure 2.19.
Molokanov et al. describe a hypothetical phase separation in a system that is the mixture of two glass forming components A (e.g. Ti_2Cu) and B (e.g. Zr_2Cu) into two different liquids above the liquidus temperature as in the $Zr_{50}Ti_{16.6}Ni_{18.3}Cu_{15}$ the undercooling of the melt and the crystallization product depends on the superheating of the liquid [21]. The product resulting from a low overheating threshold can be a metastable intermetallic compound A_xB_y in f.c.c. structure. For the $Zr_{50}Ti_{16.6}Ni_{18.3}Cu_{15}$ a metastable f.c.c. type Ti_2Ni phase was experimentally observed, in addition to the expected Zr_2Cu, Zr_2Ni and $ZrTi(Ni, Cu)$ Laves phases, whereas heating above region II results in 'primary dendrites and eutectics' [21]. The report also elaborates that eutectic microstructures without the metastable f.c.c. phase can be found for a higher overheating threshold that is marked as region II in Figure 2.19 b).

The explanation given by the Molokanov et al. is that quenching from the low overheated melt results in a polyhedral intermetallic solid solution phase, based on the A_2B compound with an f.c.c. structure, which cannot be formed by an eutectic reaction and therefore the metastable phase could potentially form during a syntectic reaction from a phase separated liquid region or in the case of a suppression of the metastable phase from an alternative crystallization product like tetrahedral Zr_2Ni by polymorphic crystallization, since the composition is close to the compound [21].

During the course of this work however we found an alternative crystallization path from the supercooled liquid in the system that involves an icosahedral quasicrystalline phase, that precedes the formation of the intermetallic compound and possesses no difference in composition compared to the liquid or amorphous structure and can act as a nucleation site for the intermetallic compound as well as for the metastable f.c.c Zr_2Ni phase.

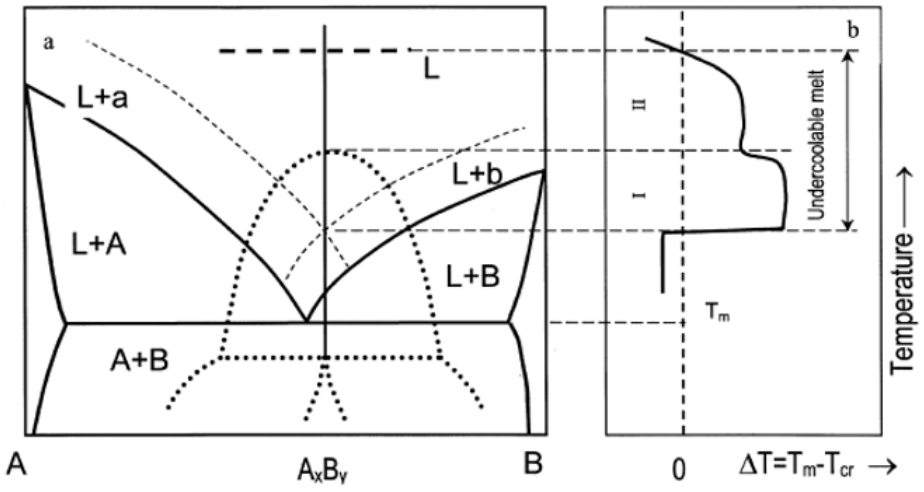

Figure 2.19: a) phase diagram for the mixture of two glass forming compounds A (e.g. Ti_2Cu) and B (e.g. Zr_2Cu), the dotted lines mark the hypothetical diagram for the metastable cubic A_xB_y compound, quenched from a low overheated melt I, where syntectic reaction from phase separated liquid region could take place and b) typical dependence of the undercooling behavior on the overheating threshold of a melt near eutectic composition where phase separation is encountered in region I, taken from reference [21].

This is not uncommon, as for example in Vitreloy 101, which is also Ti-Zr-Ni-Cu, Hays et al. reported a significant dependence of the achieved undercooling on the respective superheating in electrostatic levitation [89] and Mukherjee et al. reported similar for Zr-based systems that need a certain overheating threshold to supercool properly and form glass without showing a recalescence during electrostatic levitation experiments [90].

2.5 Sulfur as alloying element

Sulfur was not an element that was actively considered for alloy development in the field of bulk metallic glasses until Kuball et al. started experimenting on utilizing the element in alloy synthesis of Pd-Ni-S and Ti-Ni-S alloys, finding a new family of bulk metallic glass formers bearing S [10]. The addition of sulfur to the Ti-Ni system increased the glass forming ability from some 30 μm in the binary Ti-Ni to 500 μm in Ti-Ni-S, which marks a significant increase in glass forming by the added 8 $at\%$ of S [10].

Starting from this system, multiple investigations by the members of the Busch group led to several feasible glass forming systems that profited from the addition of sulfur to the system. The Ti-Zr-Cu system was one of the more promising systems, that was further developed from the initial systems explored by Kuball and co-authors, here a significant increase in GFA up to 3 mm paired with promising mechanical properties and a good resistance to electrochemical corrosion was reported in the $Ti_{40}Zr_{35}Cu_{17}S_8$ alloy [11].

The whole family of the developed sulfur-bearing bulk metallic glasses was patented by the Saarland University under grant WO2019038415A1, as they hold significant industrial interest, which is also why the Heraeus Amloy Technologies GmbH acquired licences to produce those BMGs exclusively.

Parallel Gross and co-workers developed bulk glasses in the (Ti, Zr)-(Ni, Cu)-S system [12]. Here, the content of titanium was significantly higher, and the alloys were based on quaternary systems. Those systems however were off-eutectic systems and their overall glass forming was limited, especially on the Zr-rich side of the system, the found bulk glass of $Zr_{56}Ti_{13.3}Ni_{13.6}Cu_{9.6}S_7$ that was developed by

Kuball [59] was limited to about 1 mm in GFA. Later on, the system was characterized in-depth by Ruschel et al. regarding the high temperature viscosity and fragility of the liquid phase [60]. The works were followed up by developments near the eutectic points of Ti-Cu-Ni and Ti-Zr-Cu where an introduction of sulfur into the ternary eutectic E5 was performed by the Ruschel et al. which after some alloy development received potent Ti-based glass formers like the $Ti_{36}Zr_{33.5}Cu_{24.5}S_6$ alloy [19].
Furthermore, the Zr-Cu-Al [13] and the Zr-Cu system [91] were investigated by Jiang et al., where a significant increase in the glass forming ability was found, and the stability of the supercooled liquid could be enhanced. The Ni-Nb system also benefited from the introduction of sulfur into the system as shown in the initial study on the new family of sulfur bearing alloys [10] and later on investigated in depth by Grund et al., where the rise in glass forming ability was attributed to the geometrical frustration of the crystal nucleation due to the influence of sulfur [92]. The optimal amount of sulfur addition to those systems spans a vast range in absolute amount of S introduced into the system, it varies from being as small as 1% in the case of Cu-Zr-Al [13] and ranges up to a significant amount of 27 $at\%$ as in the case of Pd-Ni-S [10]. Therefore, the approach of the screening of S-content during early stages of alloy development of new alloys is still subject to further research regarding the influence of sulfur on the respective BMGs' glass forming ability, mechanical properties, and supercooled liquid behavior.
Regarding the behavior of the undercooled liquid, the sulfur shows a tendency to increase the alloys fragility parameter in comparison to non sulfur bearing alloys as the alloy $Zr_{56}Ti_{13.3}Ni_{13.6}Cu_{9.6}S_7$ shows a high temperature fragility parameter of $D^* = 19.6$ and a viscosity that is twice as high as it is found in other Zr-based BMG formers like Vit105 [60]. Additionally, the study found sulfur to reduce the surface tension in the liquid state significantly compared to other Zr-based bulk glass forming systems, similar to effects reported for oxygen [60].

2.6 Structure of the amorphous phase

2.6.1 Efficient cluster packing model

To describe the structural changes due to the introduction of sulfur into the alloy, the changes in the structure of the glass will be described relative to the sulfur free state of the glass. Therefore it is important to understand the structure of the Zr-Ti-Ni-Cu glass and the model utilized to describe it on the local atomic scale within clusters as well as on the medium range order of cluster connection.

The local structure of crystalline materials is given by their crystalline lattice and elementary cell, this basic unit can be used to describe the structure of the crystal over a large volume, as the same atomic arrangement is encountered periodically throughout the respective volume according to the symmetries of the respective lattice. The whole picture on a realistic crystalline material's microstructure includes of course a lot more phenomena like the existence of grain boundaries, voids, stacking faults, dislocations and lattice deformations, although those faults play a crucial role for the behavior of crystalline material they are only to be mentioned as a side note in this work.

In contrast, metallic glasses contain no such periodic long-range order (LRO), they do, however, contain a certain short-range order of the clusters (SRO) as well as a certain degree of inter-cluster ordering beyond the first shells of nearest neighbor coordination, the so-called medium range order (MRO). The details of the structural order in metallic glasses are still an actively researched topic among the recent investigations in the field of the bulk metallic glasses, examples can be found both in the experimental field [93] as well as in the theoretical description of the structure of metallic glasses [94], still after 65 years since their initial discovery.

The structural model D. Miracle proposed in 2004 extends beyond the nearest neighbor shell in the glass and focuses on efficiently packed atomic clusters that center around a solute atom [95]. The model Miracle proposed abstracts the clusters themselves as spheres, and the idea is to fill the space efficiently with the abstracted clusters, which results preferentially in face centered cubic (f.c.c.) or hexagonal closest packed (h.c.p.) arrangement as they can fill space most efficiently [96]. The model is referred to as the efficient cluster packing model (ECP)

and contains just three topologically distinct solute atomic species, irrespective of the chemically distinct atomic species [44]. The main aspect of the model can be understood by the sketched structure in Figure 2.20, where the cluster packing structure of an exemplary metallic glass comprised of 3 atomic species is given. The atomic arrangements are labeled α for the f.c.c. arranged clusters and β for the octahedral sites within those arrangements of the α-clusters. The clusters centered around an α-solute atom share their solvent Ω atoms that are sketched as hollow black circles and form relaxed icosahedra around the α-atom [44].
For the example of Vitreloy 1 Miracle proposes the coordination number of α is $N_\alpha = 12$, for β it is $N_\beta = 10$ and for the tetrahedral sites γ (not in the sketch) it is $N_\gamma = 9$, resulting in a $< 12\ 10\ 9 >$ glass for Zr-Ti-(Ni,Cu)-Be that present a very good agreement with the actual structure found for both Vitreloy 1 and Vitreloy 4 [95].

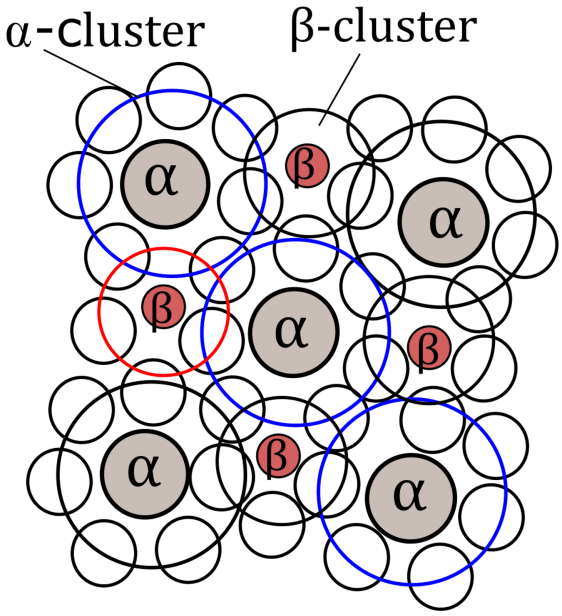

Figure 2.20: Schematic image of structural order in a 3 atomic species glass in efficient cluster packing, where the clusters interpenetrate and the randomness of solvent atoms as well as the ordering of solute atoms is displayed, drawn after [97].

If all tetrahedral sites are filled with α Atoms too, a resulting $\Omega_2\alpha$ composition

remains [44]. The icosahedral clusters have no orientational order among each other so that no LRO exist within the model, furthermore the model predicts Zr-Ti-(Ni,Cu) as $< 12\ 10 >$ glasses according to Miracle where both Zr and Ti are coordinated in icosahedral clusters yet those clusters themselves still occupy random positions in the structure of the glass which distinguishes the structure from quasi-crystalline icosahedral phases [95].
The 3D arrangement of those clusters with their respective octahedral β and tetrahedral γ sites is shown in Figure 2.21. The structure contains a Zr-Ti-(Ni, Cu)-Be alloy the (Ni, Cu) on the octahedral sites sketched in purple, and the small Be atoms sit on the tetrahedral sites drawn in orange.

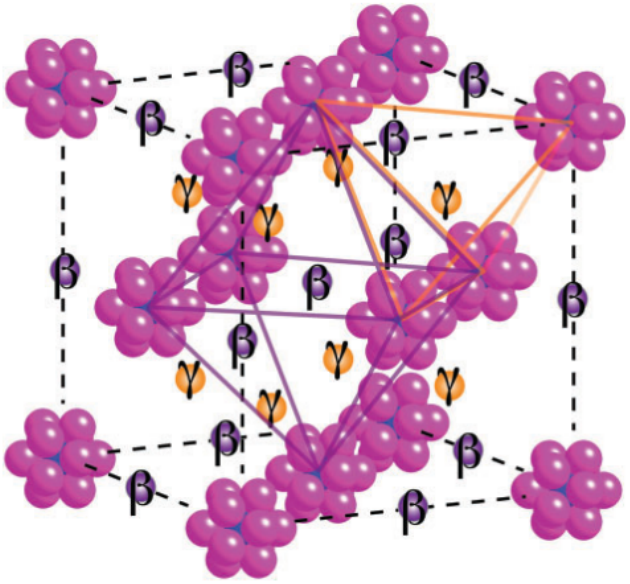

Figure 2.21: 3D schematic image of a bulk metallic glass with 4 topologically different atomic species glass in efficient cluster packing, where the clusters interpenetrate and the tetrahedral and octahedral sites for solute atoms are displayed, the distances between atoms are exaggerated for the sake of visibility- reprinted with permission from [98].

As Miracle and co-workers reported in 2015 the model does not attribute to the direct impact of chemistry on the structure as for example Cu and Ni are considered to be topologically equivalent yet Zr-Ni forms no bulk glass in contrast to Zr-Cu,

so that the impact of chemistry has to be considered separate from the ECP model and a direct impact on GFA is to be expected [99]. Therefore, the impact of the chemical aspects of alloying the Zr-Ti-Ni-Cu with sulfur will be discussed separately from the structural impact according to a model of hard spheres, which is discussed along structural type of the Miracle <12 10 9> glass, as found in Zr-Ti-Ni-Cu-Be.

2.7 Mechanical properties of BMG

From their difference in local atomic structure, which comprises SRO and MRO, results a significantly different mechanical behavior that differs from the commonly attributed properties of a 'metallic solid' as it is commonly known. First, the macroscopic observed behavior is described in the following, which is then followed by an explanation of the local atomic scale mechanisms in the amorphous 'microstructure'. Bulk metallic glasses show remarkable mechanical strengths that regularly exceed the strength of common steels or titanium alloys easily. M. Telford published a generalized overview of the mechanical properties found in bulk glass forming alloys in 2004, which is reprinted in Figure 2.22 as a display of yield strength in dependence on elastic limit of the materials. The figure highlights the distinct material behavior for steels, titanium alloys, and polymers by their characteristic material properties of elasticity and yield strength. This sketch is meant to emphasize the general characteristics of the materials, although there are certainly exceptions to the commonly found behavior. Polymers exhibit a low strength paired with a high elastic limit, whereas common titanium alloys show intermediate strength and a moderate elastic limit. Steels, in contrast, show a rather low elasticity in combination with a high strength range. Wood and Silica are also listed in the figure, where Silica and Wood hold little strength, while Wood shows a decent elasticity, Silica shows the least desirable mechanical properties for structural engineering applications. As mentioned before, the local structure of metallic glasses is quite different from classic crystalline alloys, while containing a certain similarity to amorphous polymers, the characteristics they exhibit of both metallic alloys and polymers result in a combination of high strength and high

elastic limit, which makes the class of material an uncommon blend of the two well known material classes of metallic materials and polymers [8].
The strength of bulk metallic glasses is typically composition dependent and ranges from about 1.8-1.9 GPa in Zr-based BMGs [8, 65] to a yield strength of 3 GPa in Ni-Nb based BMGs [100] and can reach up to 6 GPa in the case of Co-based BMG [101]. The hardness of the amorphous materials is typically also astonishingly high in the cast state of the material, which spans from a Vickers hardness of about 500 HV in Zr-based BMGs [102] to over 1000 HV in Ni-Nb alloys [100] and up to 1500 HV in Fe-based alloys [103].

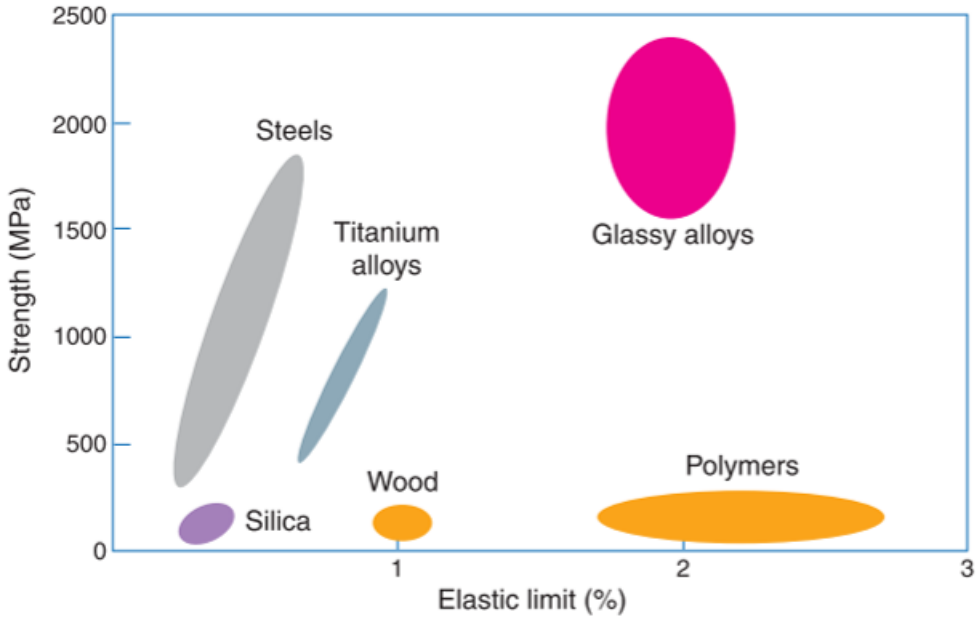

Figure 2.22: Schematic of characteristic strength and elastic limit ranges of common material families and amorphous metallic alloys, reprinted with permission from [8].

The combination of the mentioned properties in one material is unique, and therefore, it draws the interest of industrial applicants to take advantage of this combination of properties. The absence of the typical crystalline microstructure's features, however, is also responsible for a different plastic deformation behavior of the metallic glasses and results in very different local processes in the glass that enable plastic deformation.

In the case of bulk metallic glasses, the deformation mechanisms can be separated into two different behaviors above and below T_g respectively. Here, we take a look at the low-temperature region where the glass behaves like a solid. The plastic deformation happens quite differently in comparison to the crystalline materials, as the significant difference in the local atomic structure and the lack of a regular deformation mechanism by dislocation movement is not given in amorphous metals. Still, the deformation that can be observed experimentally has to be connected to the local rearrangement of the atoms. In Figure 2.23, two possible local atomic deformation mechanisms are sketched.

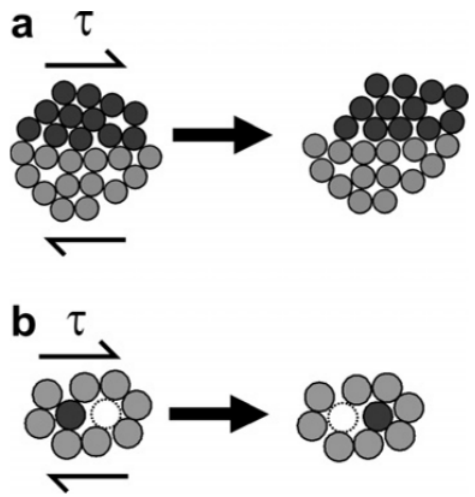

Figure 2.23: Schematics of possible local atomic rearrangement in the deformation mechanism a) by shear transformation zones as proposed by Argon [104] and b) by local atomic jumps as proposed by Spaepen [105], reprinted with permission from [106].

In Figure 2.23 a) the shear transformation zone (STZ) model is shown, which describes a coordinated movement of a 'flow defect' under local shear stress symbolized as τ where a shear transformation zone can be understood as a local cluster that undergoes an inelastic shear distortion [106]. The details of size, structure, and energy scale are believed by Schuh et al. to vary between the different metallic glasses, yet the STZs are found to be 'common to deformation of all amorphous metals' [106].

In Figure 2.23 b) the alternative to the STZ model is depicted, where the deformation of the metallic glass is coupled with the free volume model by Cohen and Turnbull [107], here the model is applied to the deformation of metallic glasses as done by Spaepen [105]. In this case, the deformation can be understood as a series of atomic jumps in the glass structure, which occur more often in regions with higher free volume throughout the structure. The model does not accommodate shear strain according to Schuh, however, it is quite useful as the development of constitutive laws based on the creation and annihilation of the existing free volume within the glass structure influences the mechanical properties of the glass [106].

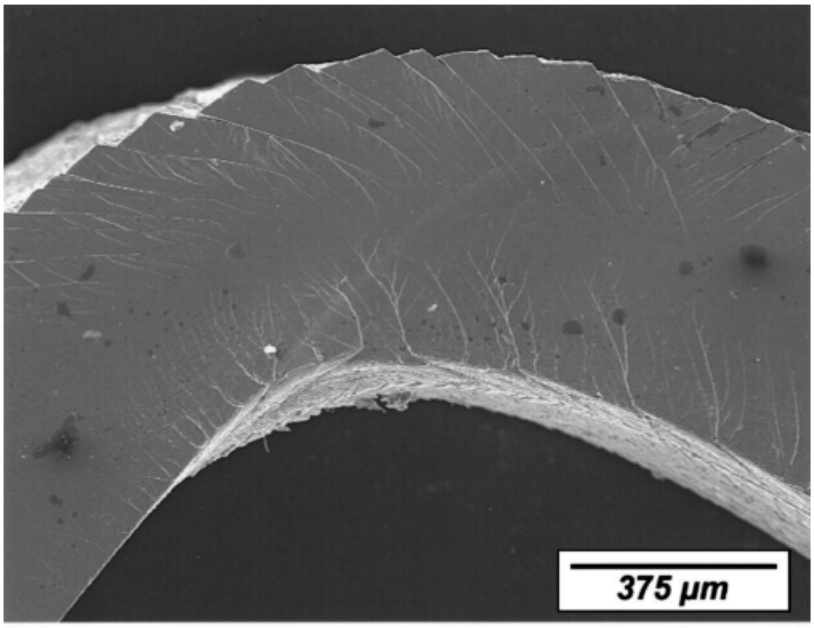

Figure 2.24: Beam bending sample of Vit106 ($Zr_{57}Cu_{15.4}Ni_{12.6}Al_{10}Nb_5$) in the scanning electron microscope after deformation, the slips of material are visible and associated with the occurrence of shear bands in the material, reprinted with permission from [108].

The surface artifacts of a bent beam of metallic glass shown in Figure 2.24 are a commonly observed feature that is associated with the formation of shear bands in the material that were not critical for the sample to fail catastrophically. These slip steps were first encountered as a macroscopic observation, and from then on, further investigations of the shear bands were performed [109]. The shear induced

slip steps can even be observed directly in the laboratory with the bare eye, when a highly ductile BMG like the AMZ4 ($Zr_{59.3}Cu_{28.8}Al_{10.4}Nb_{1.5}$) is massively deformed during cold rolling of a 1.75 mm strip down to sheet metal with a 250 μm final thickness.

The previously described deformation of the BMGs can be understood as inhomogeneous deformation which is quite different from the deformation that can take place for elevated temperatures near T_g, this deformation is referred to as homogeneous deformation where the mobility in the glassy structure is high enough to enable the local movement of not only the STZ, that moves along under the shear stress, but the whole glassy structure-resembling the viscous behavior of the deeply supercooled liquid.

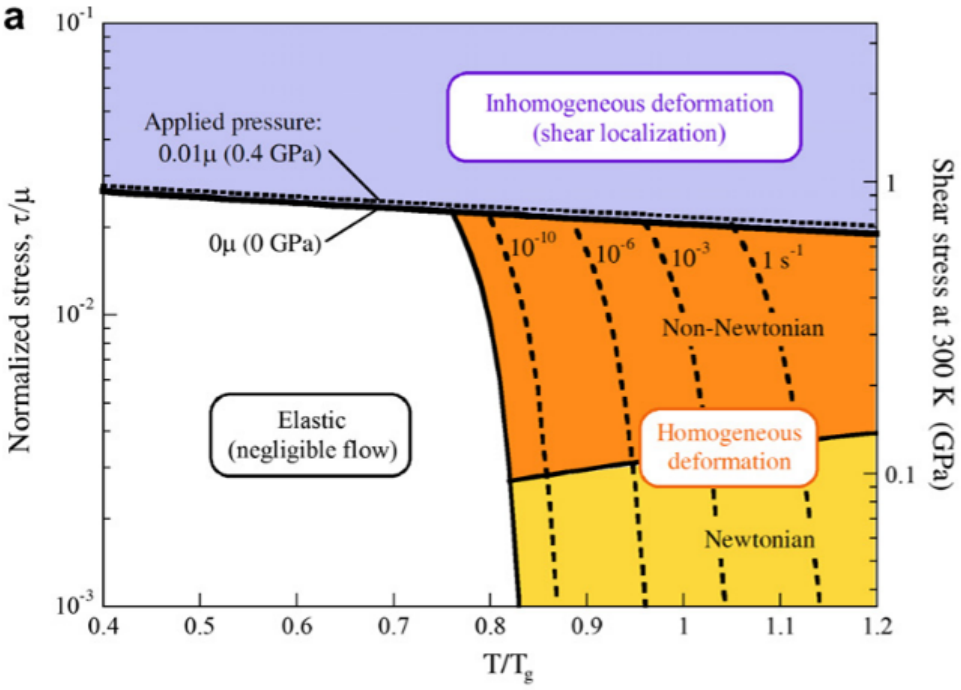

Figure 2.25: Stress-temperature-deformation map that mainly divides the deformation mechanism into homogenous and inhomogeneous deformation (shear localization) typically at lower temperatures and higher stresses or strain rates for the $Zr_{41.2}Ti_{13.8}Cu_{12.5}Ni_{10}Be_{22.5}$ alloy [106].

In Figure 2.25, the stress-temperature-deformation map is shown for the Vitreloy 1 BMG that incorporates the originally constructed map of Spaepen [105], where the

stresses are presented as fractions of the shear modulus, and the values in brackets give the absolute amount of shear stress. The homogeneous deformation consists of three different subsections, where the elastic regime is easily understandable as a region of no plastic flow, and the border of elastic deformation is defined at a strain rate of ($10^{-12}s^{-1}$). As Schuh elaborates, the map also shows that at high temperatures it is possible to observe not only both modes of Newtonian flow and non-Newtonian flow behavior but also inhomogeneous flow by shear localization, if the strain rate is high enough that is -meaning that the deformation is induced faster than even the supercooled liquid's structure atomic rearrangement can accommodate for the deformation [106].

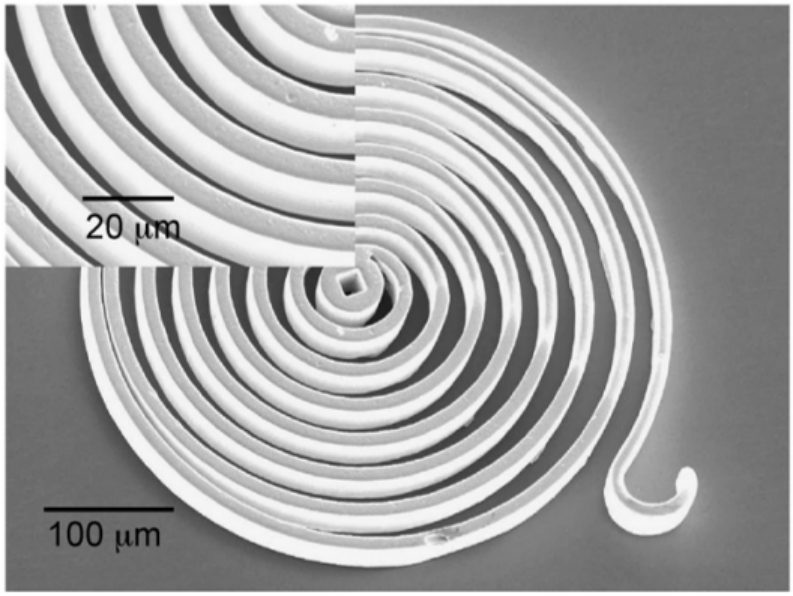

Figure 2.26: TPF manufactured micrometer-sized flat-coil spiral spring that utilizes the elastic properties of the BMG to the fullest, reprinted with permission from [110].

The homogeneous flow ability in the supercooled liquid region (SCLR) enables the BMGs to be shaped freely without any constraints of the microstructure during the process of thermoplastic forming (TPF), where a BMG is heated into the SCLR regime to be thermoplastically deformed and then quenched into the desired glassy state again. Utilizing this technique, even the smallest details can be replicated in the BMG surface from the tools used during the thermoplastic forming Kumar

et al. showed that the process can replicate even nano-scale features as well as an atomically smooth surface, adding a 'versatile toolbox for nanofabriction' to the manufacturing capabilities of BMGs [111].
In Figure 2.26, the capabilities of this manufacturing technology are demonstrated by TPF forming of parts for Micro-Electro-Mechanical-Systems (MEMS) as parts for mechatronic systems that can benefit from the unique mechanical properties combination and find use in diverse applications that require device robustness in harsh environments [110].

3 Methodology

3.1 Alloy synthesis

The synthesis of the alloys that were investigated in this work was consistent with the methodology employed by the numerous works that precede this work at the chair of metallic materials. The alloys were synthesized from manually cut elemental metals and metalloid elements, and later on, as well, from industrial-grade alloys of Zr and Ti. The typical appearance of these elements can be seen in Figure 3.1, where some of the elemental ingredients for the alloy Vitreloy 105 are shown.

Figure 3.1: Typical raw materials for the synthesis in the Zr-Ni-Cu-Al alloys, the appearance is typical for the high-purity metallic elements employed in the synthesis.

The sulfur-bearing alloys incorporate another ingredient that carries the sulfur,

which is the Cu_2S compound that was synthesized in the laboratory of the chair of metallic materials itself. The dark blue appearance of the synthesized highly pure Cu_2S can be seen in Figure 3.2. The compound was crafted from elemental Cu granules that were obtained from HMW Hauner GmbH and S pellets bought from Onyxmet (Poland).

The sulfur was mixed with the Cu granules and the mixture was filled in fused silica tubes - commonly known as quartz glass- with an outer diameter of 19 mm and a wall thickness of 1.5 mm, by sliding a solid cylinder of fused silica with a diameter of 10 mm on top of the mixture with a distance of approximately 20 cm between the Cu+S mixture and the quartz cylinder. A vacuum pump was then attached to the tube and the mixture was sealed in a vacuum of approximately 10^{-2} $mbar$ by heating with an acetylene flame that fused the solid quartz cylinder with the quartz tube as the vacuum wrapped the tube around the cylinder, the resulting vacuum tight quartz plug can be seen in Figure 3.2 c).

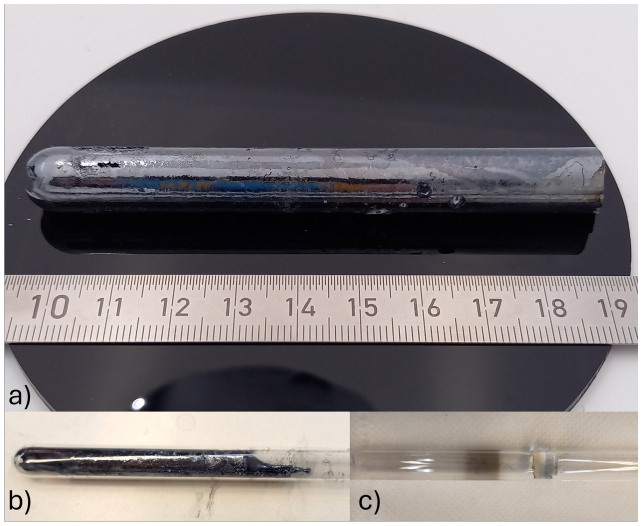

Figure 3.2: a) Synthesized Cu_2S that was crafted from elemental Cu and S by mixing, sealing 50 h at 1473 K to achieve α-chalcogenide b) encapsulated Cu+S after heating and c) sealed quartz plug, fused with the capsule.

This was performed to ensure that all of the sulfur that inevitably turns into liquid and then gas during initial heating of the mixture up to 1473 K stays in the hot zone of the vertical furnace that is used to hold the capsule at 1473 K for 12 h

to ensure a homogeneous liquid phase that is then cooled into the stoichiometric α-chalcogenide ($\alpha - Cu_2S$) compound.
The Cu_2S compound is needed as the alloy synthesis is performed with a water-cooled electric arc furnace, which is schematically shown in Figure 3.3. The essential advantage of this furnace being the ability to operate under protective Ar gas atmosphere (99.999 Vol %) that is further cleaned by melting ASTM grade 2 Ti, thereby entrapping remaining impurities in the atmosphere within the molten Ti that analog to a simple ion getter pump, therefore being referred to as 'Ti-getter'. The furnace can easily reach temperatures beyond 3000 $°C$. The chamber of the Arc-melter can be evacuated by the attached rotary vane pump down to a vacuum of $3 \cdot 10^{-3}$ $mBar$.

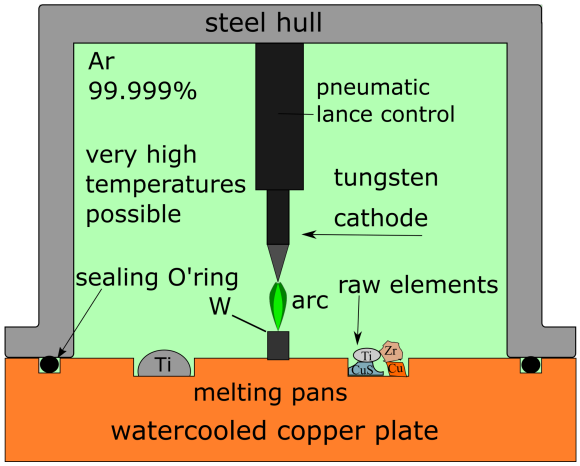

Figure 3.3: Arc-melting furnace shown as a schematic, embodying all the key aspects of the furnace. The metal is molten in pure Ar 5N (99.999 $vol\%$) and sits on a water-cooled copper plate so that no contamination of crucible material spilling into the alloy is possible. The ingots can be flipped via a manually operated manipulator that is not part of the schematic, taken from [17].

The heat is brought into the material by direct Joule heating and the current is being transferred by the arc from a water-cooled tungsten tip into the material sitting in the copper molds. The Arc-melter, however, instills a large temperature gradient in the material as the copper plate does not heat up beyond about 50 $°C$. Therefore, the buttons need to be flipped and the alloys homogenized at least 5

times due to the possibility of segregation of denser, higher melting elements in the bottom of the so-called master alloy button. For this purpose, the furnace is equipped with two hand-operated manipulators, equipped with shovels on the front end. The tungsten lance itself is operated via a pneumatic system to rise or lower the lance, which also operates on Ar to prevent contamination from the pneumatic system into the hull of the Arc-melter.

3.2 From master-alloy to amorphous material

The resulting master-alloy has yet to be reheated and then vitrified, as the cooling rate of free cooling on the water-cooled copper plate is not sufficient for the alloys used within this work to solidify without crystallization. The determining factor here is the critical cooling rate R_c that describes the minimum necessary cooling rate that has to be applied to a liquid to be supercooled deeply enough and without crystallization occurring, to vitrify into a glass.

3.2.1 Meltspinning

Initially melt-spinning technique was used to examine the GFA of the sulfur-free alloys from the literature and the initial sulfur addition experiments- to test the influence of sulfur with the same applied cooling rate, identical to earlier studies of Molokanov and Chebotnikov, that also utilized the melt-spinning technique and melt-jet quenching for the Zr-Ti-Ni-Cu alloys. The working principle of the melt-spinner is depicted in Figure 3.4. The machine consists of a rotating copper wheel with a large diameter, that is used to rapidly solidify a liquid melt jet that is being ejected with Ar gas from a quartz tube through a quartz nozzle. The melt solidifies upon contact with the copper wheel, and the resulting ribbon is ejected into a flight tube through the centrifugal force, where the ribbon can later be retrieved by the operator after the chamber is brought to atmospheric pressure again. The resulting cooling rate that can be achieved with this method varies in dependence on the machine parameters and is typically reported to be about $10^3 - 10^6\ K/s$ [7].
The width and thickness of the ribbon is determined by the parameters of the

setup, including wheel speed, wheel diameter, nozzle to wheel distance, Ar pressure for the ejection procedure, mass of the alloy and overheating of the alloy during melting the correlation of the aforementioned setup parameters can be found very well within the literature on the early days of metallic glass production [112, 113].

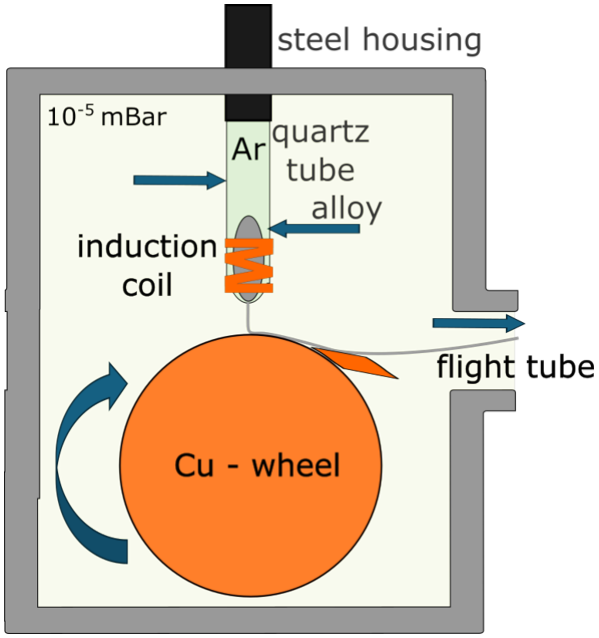

Figure 3.4: Schematic drawing of the meltspinner, the indicated induction coil was supplied with an Eldec HF-Generator of up to 10 kW and a quartz tube nozzle diameter of 0.8 mm.

For this work, a parameter set was employed that was optimized for the very setup within the laboratories of the chair of metallic materials utilizing AMZ4 ($Zr_{59.3}Cu_{28.8}Al_{10.4}Nb_{1.5}$) alloy [114]. The meltspinner was operated in a vacuum, and the alloy was molted by induction heating. The procedure utilized a rotation speed v of 2700 U/min and an Ar pressure of 0.1 bar that was released rapidly from a solenoid valve upon sufficient overheating of the melt.

3.2.2 Arcmelting suction and injection casting

Upon completion of the initial investigation of the glass forming ability of the Zr-Ti-Ni-Cu system, the sample production was performed by water-cooled copper mold casting. The standard apparatus for this procedure was the suction casting machine, which is in principle a small Arc-melter and a copper plate that houses a removable crucible that is sitting in a cavity that can be evacuated, thereby creating a pressure difference between the chamber on top of the melt and the cavity under the melt, so that the melt is 'sucked' into the copper crucible where the melt then solidifies in the shape of the respective crucible during a successful casting.

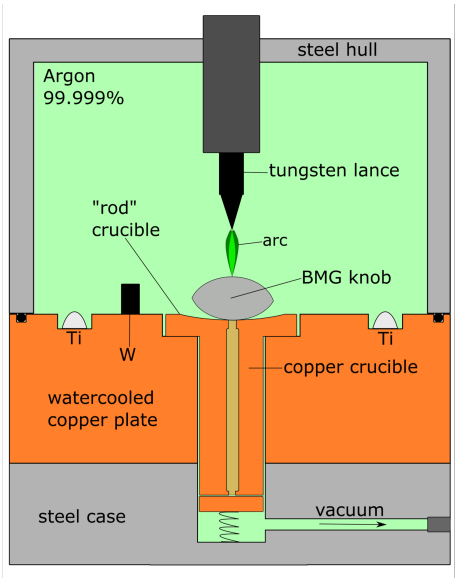

Figure 3.5: Suction casting machine used in the laboratory to melt master-alloys and quench them into copper molds by applying an under pressure over a valve that is sitting between the cavity and the vacuum pump, taken from [17].

The setup is shown in Figure 3.5 for an exemplary casting setup, designed for casting cylindrical rods, as it was used frequently during the GFA determination experiments. The majority of castings for this work were rods with a length of 55 mm. The diameters of the castings ranged from 2 mm to 10 mm and were consecutively increased with rising glass forming ability that was being probed.

The suction casting machine possesses the advantages of the arc technology that allows for greater and reliable overheating. This is especially important for alloys that do not melt eutectic or congruent and therefore show a larger spread of liquidus temperature T_l and solidus temperature T_s. For the overheating threshold, the relevant temperature is not T_s but T_l due to the critical nuclei that remain in the liquid beyond T_l, it is the temperature that needs to be sufficiently surpassed. Therefore, the suction casting has proven to be a robust technique to achieve reproducible casting results. The speed of the volume exiting the chamber through the cavity was tracked by a flow-meter and adjusted for each rod size to minimize cavity formation and inhomogeneous, turbulent flow behavior.

A derived BMG production method with an improved, more controllable casting procedure was developed within the laboratories of the chair of metallic materials in 2018 and patented in Germany under grant DE102018115815A1, and a later worldwide patent application was filed. This procedure uses an electric arc to liquefy and overheat a melt properly within a few seconds and then inject the melt with a previously lowered shell and stamp system, which enables putting sufficient pressure on the liquid while injecting to fill even the smallest cavities. The drawings from the filed patent application and crucial steps of the procedure are shown in Figure 3.6 a) to c).
The cooling rate of the method correlates well with the empirical equation (3.1) that gives R_c as:

$$\begin{aligned} &R_c = 1/(D_c)^2 \\ &with\ [R_c] = K/s\ and\ [Dc] = cm \end{aligned} \tag{3.1}$$

which is referred to as a rule of thumb formula for the inverse correlation between critical cooling rate R_c and critical casting thickness D_c [115].

A more precise estimation would have to be composed of a more complex formula with a setup specific factor that has to incorporate the sample mass, the overheating of the melt [90], the temperature of the water cooling system (WCS) [116] and of course the geometry of the actual copper mold in case it is not a rod shape.

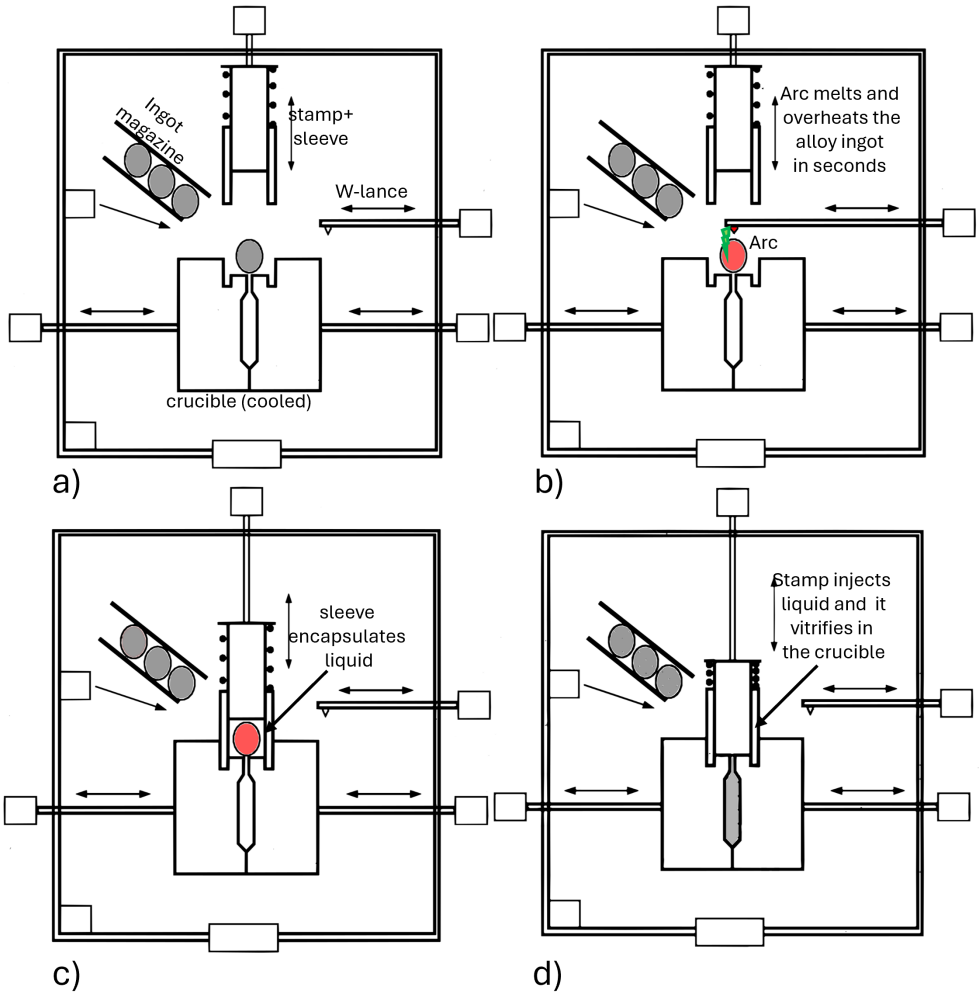

Figure 3.6: Injection casting procedure of the Amorphous Metal Solution GmbH (AMS) as drawings from the patent with the crucial components numbered, a) placing and melting of the alloy, b) tube encapsulating the melt, c) injection by the stamp, taken from patent DE102018115815A1 [117].

Therefore, empirical casting and structural analysis are still the well-versed, reliable, and reproducible techniques of choice to determine the glass forming ability of the respective alloy. A consequence of this approach, however, is the slow acquisition of GFA data as each composition has to be handcrafted and cast, as well as analyzed thoroughly.

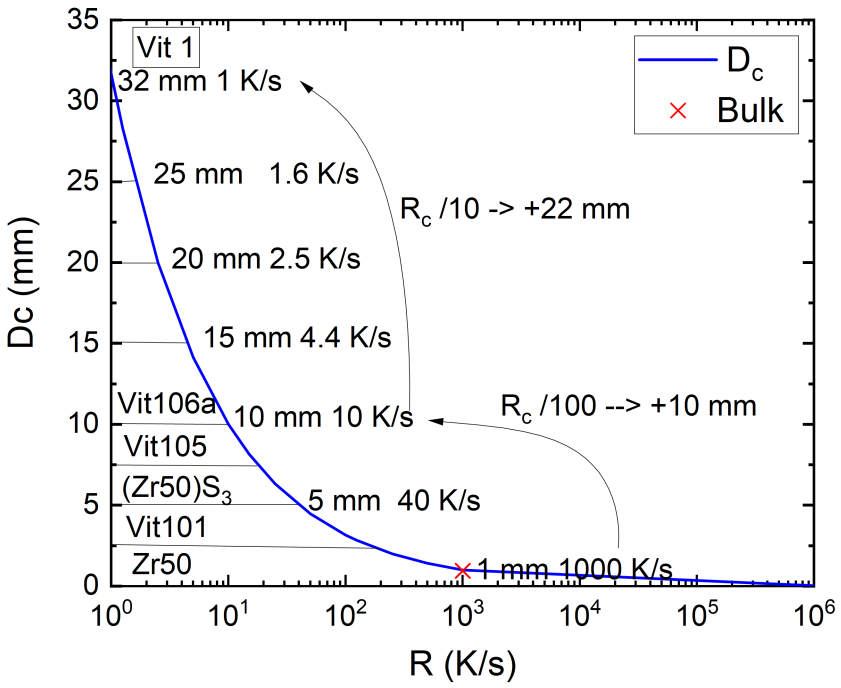

Figure 3.7: Relation between critical casting thickness D_c and the critical cooling rate R_c visualized and supported with commonly known examples of the different BMG families, it is noteworthy that one order of magnitude improval of the critical cooling rate of the BMG former can have a quite different effect in the resulting D_c gain.

The R_c is a material-specific property, and the maximum cooling rate that a production method can achieve, R_{max}, depends primarily on the amount and shape of the liquid that is being quenched. The approximate cooling rates for the typical alloys used in the laboratories of the chair of metallic materials are presented schematically in Figure 3.7. Here, the correlation of R_c and D_c can be seen to be not linear, and a reduction of the R_c by a factor of 10 can have quite a different impact on the absolute D_c as illustrated by the example in the figure.
Recently high high-throughput characterization methods have been developed and reported that can be utilized to craft compositional libraries crafted by gas-phase deposition. Luwdig et al. reported a magnetron sputtering deposition process that can deposit binary, ternary, and quaternary combinatorial composition libraries in the form of thin films for the efficient screening of material properties of Ti-Ni-X shape memory alloys for MEMS applications [118]. The same principle was applied

by Tsai and Flores to characterize compositional trends in both GFA and mechanical properties for ternary alloy systems utilizing a laser additive manufacturing process by variation of powder and laser travel speed to achieve different Ti-Zr-Cu compositions, retaining 144 discrete compositions that could be probed for GFA and hardness [119]. The techniques have the potential to rapidly accelerate the search for new promising BMG alloys, however, there may still be a significant difference in structure and properties of metallic glasses cast from the liquid or synthesized from the vapor phase [120, 121].

3.2.3 Metallographic preparation

The samples that were cast by suction casting or AMS injection casting were analyzed to confirm their structure routinely with X-ray diffraction and calorimetry. Therefore, selected parts of the rods were cut from the sample with a Mecatome T202 precision saw. This metallographic saw was equipped with an ultra-thin wheel (UTW) made from SiC grains that were bound in a polymer resin as an abrasive cutting wheel, or with a diamond abrasive cutting wheel with diamonds bound in a metallic alloy. The cutting process was performed under constant flood water cooling, and a maximum velocity of 1000 rpm was used to ensure that the microstructure is protected from the thermal influence of the cutting procedure.
The samples were then prepared for the individual analysis methods as follows: the DSC samples were cut so that at least one flat side resulted, and then sanded to a dull surface finish with grit 600 SiC sanding paper to allow proper thermal contact to the Aluminum pans in the DSC. For the XRD samples two plan-parallel cuts were performed that resulted in a slice with a typical thickness of 1 mm for the further analysis, here the bottom one side that was to be placed on the zero diffraction plate was only roughly sanded to a grit 120 finish, while the side designated for the XRD measurement was brought to a surface finish of grit 1200 sandpaper. For the electron microscopy methods, the preparation was performed analog, yet after the grit 600 sandpaper, the samples were embedded in DemoTec 35 polymer resin. The following preparation was then performed on a PRESI mecatech 250 polishing machine.
Here, the samples were treated with a sanding program that was developed for

Zr-based BMGs on the machine, which was found to suit all the prepared samples well. The complete machine was cleaned thoroughly between the preparation steps with finer and finer sanding paper, and images of the surface preparation were taken with a stereoscopic lens to control and document the surface quality. The surfaces were sanded until the scratch marks from the previous preparation step were no longer visible under the stereoscopic lens. Although no preparation step exceeded 300 s, the coarser sandpapers needed to be renewed after about 90 s already. Sanding operations were performed with 3-step force profiles that started with an individual force of 1.5 dN, went up to 2.5 dN after 60 s, and decreased the force applied to 1 dN again after 60 s. This was performed under constant flood-cooling in combination with a clockwise turning grinding table and counterclockwise turning rotor head, to achieve the maximum material removal rate. After the grit 4000 sandpaper was used, which contains abrasive particles of 3 to 5 μm[122], a diamond suspension polishing with diamonds suspended in lubricant in combination with soft polishing cloths was used. Thorough cleaning in-between each of the polishing steps was performed for 3 μm, 1 μm diamond suspension and the final preparation step was polishing with a 0.05 μm SiO_2 particle solution that was followed by 120 s of polishing only with the fine polishing cloth and flood cooling of water to remove the smallest particles remaining on the surface from the sample.

3.2.4 Ion beam preparation

For the advanced electron microscopy techniques like the electron back scattering diffraction (EBSD), the preparation was improved even further by utilizing broad ion beam polishing methods. This technique was employed to remove a thin layer of material without mechanical forces to ensure that no residual deformation in the microstructure interfered with the EBSD measurement. Therefore, the surface of the samples was removed by accelerated Ar ions as the ion source emits a beam of ions with an energy in the range of 0.5 to 2 keV. The schematic of the procedure can be seen in Figure 3.8. The polishing was performed under an angle θ of 10 ° and a constant rotation of the sample on the axis that was perpendicular to the surface to ensure a homogeneous material removal. The material is removed by the Ar ions as the atoms of the material are emitted in the collision cascade that ensues upon entry of the Ar ions into the surface of the material. Each EBSD sample was ion polished for 120 min.

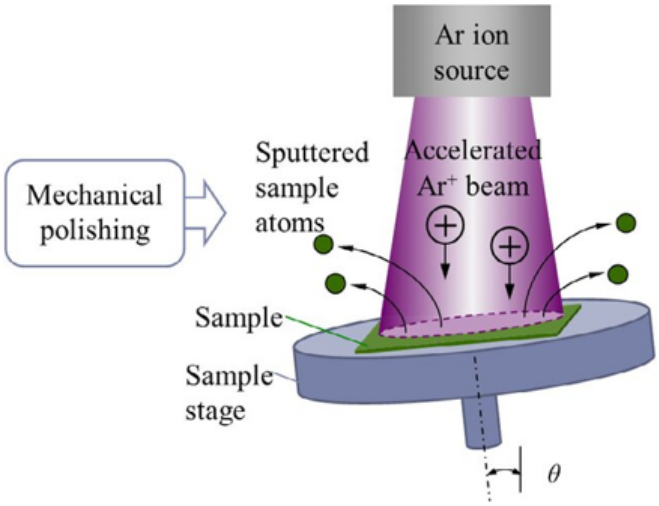

Figure 3.8: Schematic setup of the ion polishing that was used before the EBSD analysis, image taken from ref [123] redistributed under copyright license CC BY-NC-ND 4.0.

Focused Ion beam machining (FIB) was utilized to craft thin lamellae from the surfaces of samples by the lift-out procedure, which were designated for further analysis by transmission electron microscopy (TEM). For this method, the mate-

rial needs to be thin enough to be electron transparent, as the analysis utilizes transmission geometry. Before the FIB operation with Ga ions, the surface of the samples is covered with a platinum protective layer that is being deposited from the gas phase with the help of a gas injector system to protect the surface of the sample while a later on performed thinning operation is performed.

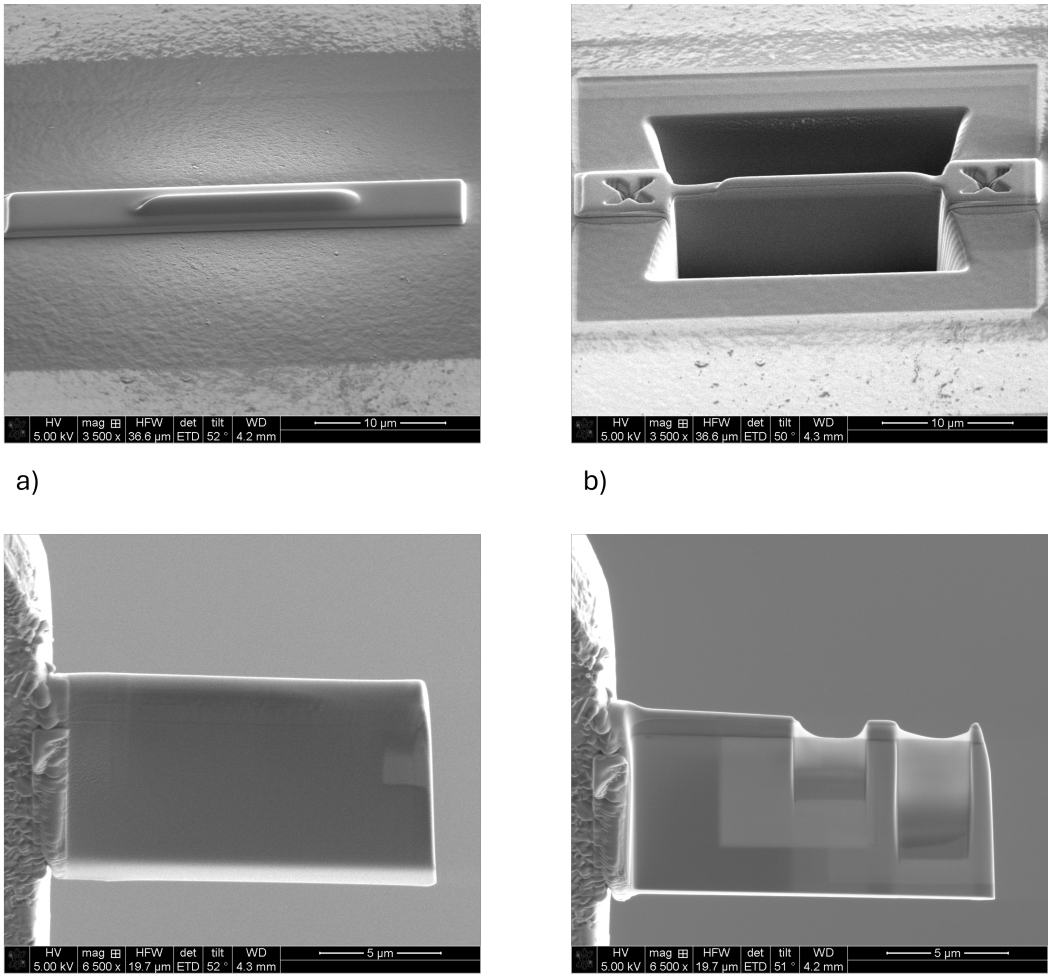

Figure 3.9: a) Sample surface prepared with a Pt cover layer, b) wedge cut into the surface of the sample from both sides, where the lamella that is still attached to the surrounding material remains. c) lifted out lamellae attached to the copper holder with a Pt deposit at the connection, d) final resulting lamellae with two regions of interest that were thinned to electron transparency.

The procedure is visualized in Figure 3.9, in image a), the deposited Pt can be seen before the operation, which is applied in two layers, to protect the surface further along the FIB process, where later on, thinning of the lamellae ensues. The focused ion beam is used to cut a wedge shape into the surface of the material from 2 sides, as can be seen in Figure 3.9 b). The lamellae are then welded to an OmniProbe nano-manipulator and cut free from the sample material with the FIB and lifted out in-situ. The lifted out lamella is shown in Figure 3.9 c) where it is attached to the sample holder on the left-hand side of the image. The lamellae after the thinning operation can be seen in Figure 3.9 d), where on the right-hand side of the lamellae, two regions of interest for the transmission electron microscope can be seen. For scanning transmission electron microscopy (STEM) imaging and the STEM-EDS mappings that were performed during the precipitate phase analysis, the lamella had to be thinned even more, and therefore, the sample was processed with a NanoMill ion mill to thin the lamella beyond the capabilities of the FIB.

3.3 Characterization of the materials

3.3.1 Thermophysical Characterization

Differential scanning calorimetry (DSC)

The calorimetric analysis of the glass transition, relaxation of the glass, and behavior of the glass in the super-cooled liquid regime was probed with a Perkin-Elmer DSC 8000. The DSC 8000 operates with a power-compensated measurement principle, utilizing a $> 90\ wt\%$ Pt-alloy as furnace material to allow operation without protective gas $> 600°C$ and combustion cleaning of the furnaces [124]. The furnaces are equipped with two Pt-thermocouples, one each for the sample and the reference oven. Power-compensated DSC measurements keep both furnaces at the same temperature, which follows the measurement program, while recording the consumed electrical power that is needed to keep the temperature of the actual furnaces aligned with the programmed heating program. The furnaces themselves are thermally isolated, and the furnace setup is flushed continuously with high-purity argon (6N) at 20 mL/min to prevent the influence of oxygen on the measurement results. Schematics of the setup can be seen in Figure 3.10.

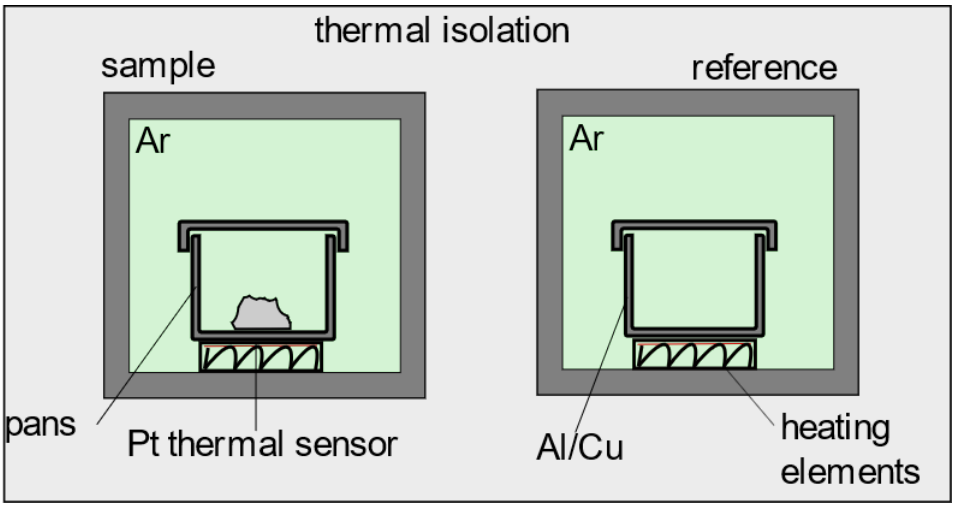

Figure 3.10: Schematic setup of the power-compensated DSC 8000 from Perkin Elmer, the DSC is equipped with thermally insulated Pt-alloy furnaces and utilizes Al or Cu-pans depending on the temperature range of the experiments [17].

The standard scanning program utilizing the temperature scanning method is depicted in Figure 3.11 a) to visualize the procedure. Isothermal measurements were an essential part of the characterization of the alloy's crystallization behavior during Time-Temperature-Transformation (TTT) measurements. The standard procedure is depicted in Figure 3.11 b) where the amount of time for the measurement was adjusted for each alloy, respectively, to guarantee that the crystallization is completed a following baseline measurement was performed for the isothermal procedure. The second measurement of the crystallized samples serves as a baseline measurement that only contains the device-specific information that is included in the data of the sample measurement and is deducted from the data of the sample in the Pyris data analysis software.

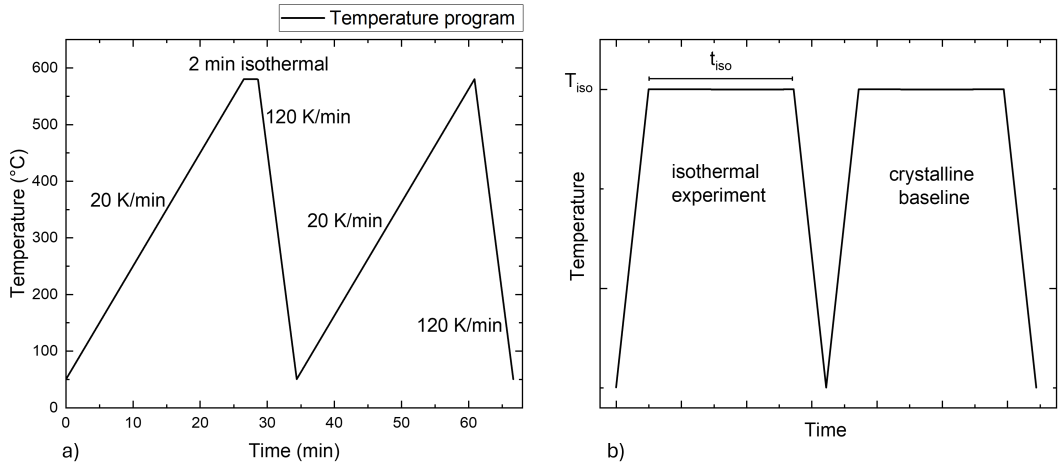

Figure 3.11: a) Schematic of the temperature program that was employed as a 'standard scan' for the work, where the second measurement serves as a baseline measurement of the crystalline sample, and b) schematic temperature program for the isothermal experiments, utilized to characterize the time-temperature-transformation diagrams.

Differential thermal analysis (DTA)

The melting experiments were performed in a Netzsch Jupiter STA 449 that which was equipped with a rhodium furnace that allows experiments at a temperature of up to 1650 °. The furnace was evacuated and afterwards constantly flushed with

Ar 6N at a rate of 50 mL/min to protect the alloys from oxidation during the experiments. The setup can be seen in Figure 3.12, it consists of a heat-flux bridge equipped with thermoelements and graphite crucibles that were covered in yttrium-oxide coating to prevent crucible reactions of Zr and carbon. Melting experiments were also performed in a Netzsch DSC 404, which was similarly equipped with yttria-coated carbon crucibles. The experiments were conducted at a heating rate of 20 K/min, and the data correction and baseline subtraction were performed with the help of the Origin Pro software.

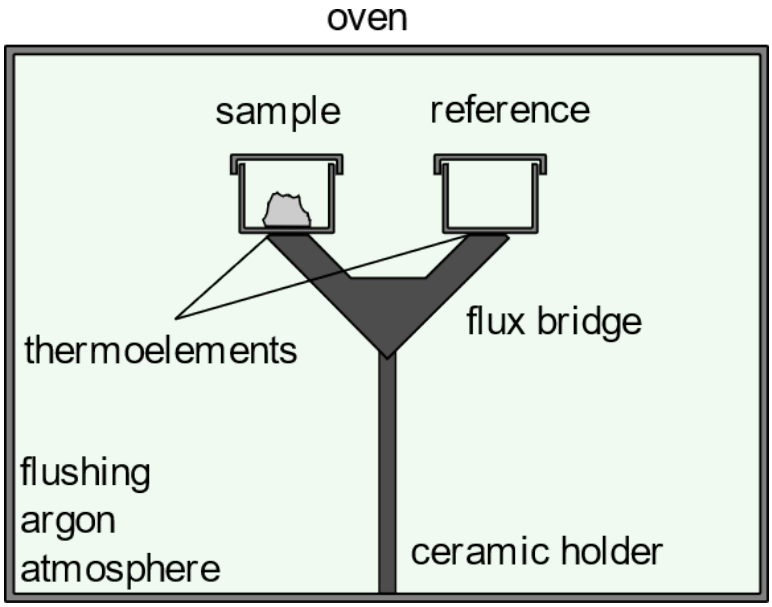

Figure 3.12: Schematic depiction of the differential thermal analysis setup of the Netzsch Jupiter STA 449 that was used to characterize the melting behavior and the characteristic thermophysical properties of the alloys [17].

The samples were molten and overheated in the first heating run, and cooled down and solidified again before the second heating run was performed. The data of the second heating was analyzed as the initial heating run from the amorphous sample material differs from the second heating run, the initial sample tends to melt at a lower temperature due the unique microstructure that forms during devitrification while heating the amorphous material from the glass through the SCLR into the first crystallization event and following intermetallic crystallization.

This crystallization sequence differs from the equilibrium crystallization at a slower cooled solidification, and the quenched alloys tend to form metastable phases with different melting points. The observed second heating effect is well described by Bochtler as well as the effect of the yttrium oxide coating on the measurement result [16].

The exemplary data set in Figure 3.13 shows the characteristic temperature determined for the system which are the solidus temperature T_s, the liquidus temperature T_l and the temperature of fusion T_f.

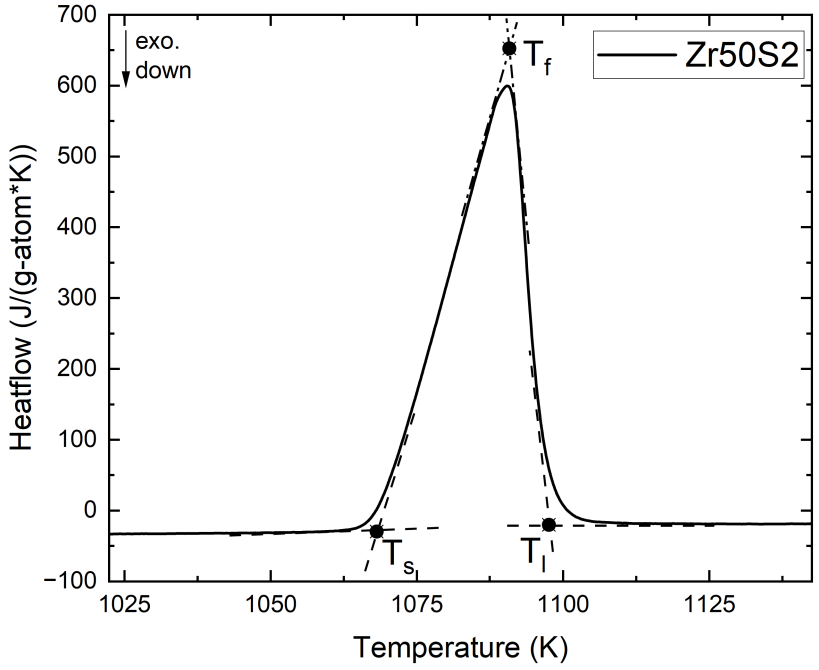

Figure 3.13: Example curve from the (Zr50)S2 alloy, showing the melting event in detail and the characteristic temperatures.

Thermo-mechanical analysis (TMA)

The thermo-mechanical analysis was performed using a Netzsch TMA 402 F3 Hyperion thermo-mechanical analyzer (TMA) with a three-point beam bending setup made from quartz, the schematic of the setup can be seen in Figure 3.14. The TMA was equipped with a steel furnace that allows heating ramps up to 1000 °C with a maximum heating rate of 50 K/min. The experiments were performed under a protective Argon Atmosphere with an Ar 99.999 Vol % purity.

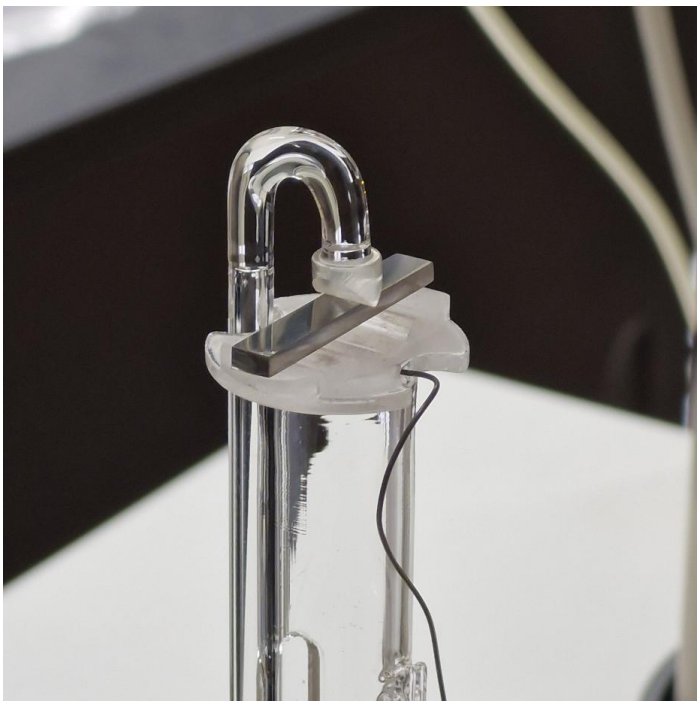

Figure 3.14: Setup of the Netzsch Hyperion TMA that was equipped with a quartz three-point beam bending setup for the analysis of the low temperature viscosity.

The specimen in the form of rectangular beams was loaded in the center with a Force of 0.1 N, and the deflection of the sample as a function of temperature and time was recorded. The analogy between elastic and viscous deflection rate is given through the relation described by equation (3.2), where η:

$$\eta = -\frac{g \cdot L^3}{144 \cdot I_c \cdot \nu}(M + \left[\frac{\rho \cdot A \cdot L}{1.6}\right]) \tag{3.2}$$

is the viscosity of the sample, L being the support width, M being the loading mass, g the gravitational constant, I_c being the cross-sectional moment of inertia, A being the area of the samples cross-section and ρ being the density of the glass as postulated by Hagy [125]. The scanning experiments were performed with a heating rate of 0.33 K/s.

Isothermal thermo-mechanical experiments were performed to investigate the relaxation behavior of the glass towards the equilibrium supercooled liquid, and the isothermal behavior can be described by the Kohlrausch-William-Watts (KWW) equation that is given by equation (3.3) [126] that gives $\eta(t)$ as:

$$\eta(t) = \eta_g + \eta_{eq-g}(1 - exp\left[(-t/\tau)^{\beta}\right]) \tag{3.3}$$

where τ refers to the relaxation time, β is the stretch exponent and η_g is the initial viscosity in the as cast state that is unrelaxed.

The data collected by the Hyperion TMA can be seen in Figure 3.15 for the (Zr50)S7 alloy that shows a stable super cooled liquid region.

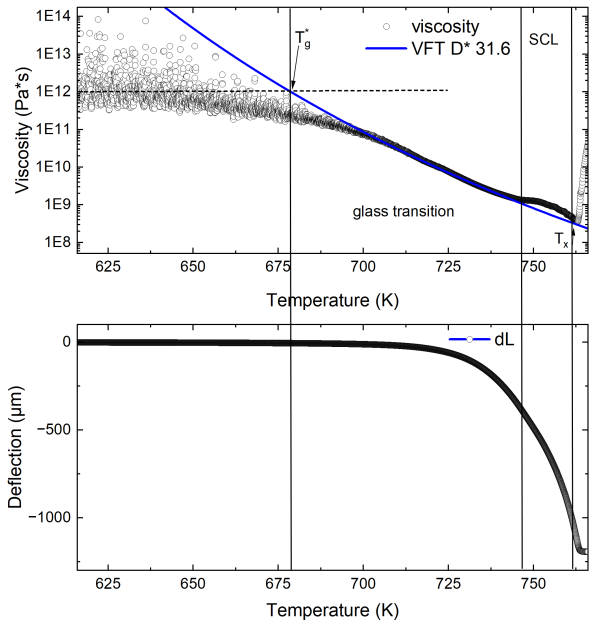

Figure 3.15: Example of the recorded deflection data from the Hyperion TMA viscosity, for a scan measurement of (Zr50)S7 with a heating rate of 20 K/min showing the deflection and the viscosity.

Container-less electromagnetic processing in micro-gravity (TEMPUS)

The viscosity in the high temperature region of the glass forming alloys liquid was measured in cooperation with the German aerospace center (DLR) within the 41^{st} and 43^{rd} campaign of container-less electromagnetic processing in micro-gravity TEMPUS (Tiegelfreies-elektromagnetisches-Prozessieren-unter-Schwerelosigkeit) during scientific parabolic flight campaigns. The parabolic flights were performed in Bordeaux by Novespace, aboard the Airbus A310-300 'Air Zero G'. The airplane has a historic background as it was previously known as the 'Konrad-Adenauer' of the German Air Force, where it served both German chancellors Helmut Kohl and Angela Merkel. The temperatures for the liquid state during these experiments were situated between 1000 K and 1873 K, the temperature was measured by a pyrometer that was integrated into the sample environment of the TEMPUS device. The sample was heated by induction heat transfer with a specifically developed coil system, which contains an integrated positioning coil as well as a separate heating coil arrangement [127]. This allows the TEMPUS device to operate the positioning of the sample separately from the heating pulses, which increases the stability of the positioning in the micro-gravity phase. In addition to free cooling, the ESL device was equipped with the possibility to do He gas quenching for a higher cooling rate during the micro-gravity phase. The metallic sample is positioned by a magnetic quadruple field and heated with a dipole field with a separate rf current supply, each [127]. This allows for rapid heating of the sample while also decoupling heating and positioning units, resulting in a completely liquefied and massively superheated sample in less than 10 s during the parabola.

The excitation of the droplet was performed by pulses from the heater, and a brief overview of the experiment configuration within the TEMPUS device can be seen in Figure 3.16 a). The metallic liquid was excited by pulses from the heater coil system, and the radius r of the droplet was analyzed after being derived from the recorded video frames.

The parabolic flight maneuver is sketched in Figure 3.16 b) and consists of 5 phases during the flight. Initially the aircraft flies at an altitude of about 6000 m with a velocity of about 228 m/s, when the 'Pull-Up' maneuver is performed, the pilot ascends 1600 m and gradually changes the climbing angle of the plane towards

50°, during this phase hyper-gravity of 1.8 g is experienced inside the airplane. At the 'injection point', the velocity is reduced to 105 m/s and the airplane climbs a parabola of an additional 900 m where micro-gravity of 0 g is experienced inside the airplane.

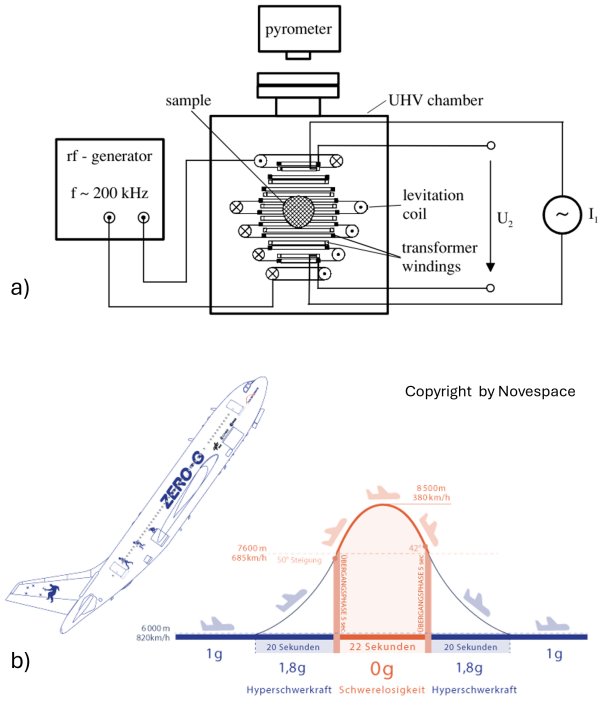

Figure 3.16: a) Schematic setup of the TEMPUS facility utilized to measure the high temperature viscosity data, taken from [128] b) image of the A310 Zero G ascending into the parabola at an angle of 50° as well as a schematic of velocities and gravitational forces experienced during a parabola, taken from [127].

The 'Pull-Out' maneuver then brings the airplane back into the horizontal flight path at an altitude of 6000 m, and during this maneuver, the hyper-gravity is experienced again for about 20 s before the parabolic flight maneuver ends back at the regular gravitational acceleration of 1 g.
The oscillations can be described as a function of time as given in equation (3.4) [129] for the radius of the droplet r(t):

$$r(t) = r_0 + A\ cos(\omega t)\ exp(-\Gamma t) \tag{3.4}$$

by a damped cosine function as given . In this formula, γ is the surface tension and m is the mass of the droplet.

The oscillating drop method also describes the viscosity of the liquid via the dampening constant according to equation (3.5), which is based on Kelvin's work as described by Egry [129], which gives Γ as:

$$\Gamma = \frac{20\pi}{3} \frac{\eta\ R_0}{m} \tag{3.5}$$

where R_0 is the quiescent radius of the droplet, m the mass of the sample and η is the viscosity of the liquid that is being excited by the pulse and thereby oscillated. However, these equations are valid only when external gravitational fields are negligibly small, as is the case when performing such experiments under micro-gravity [129].

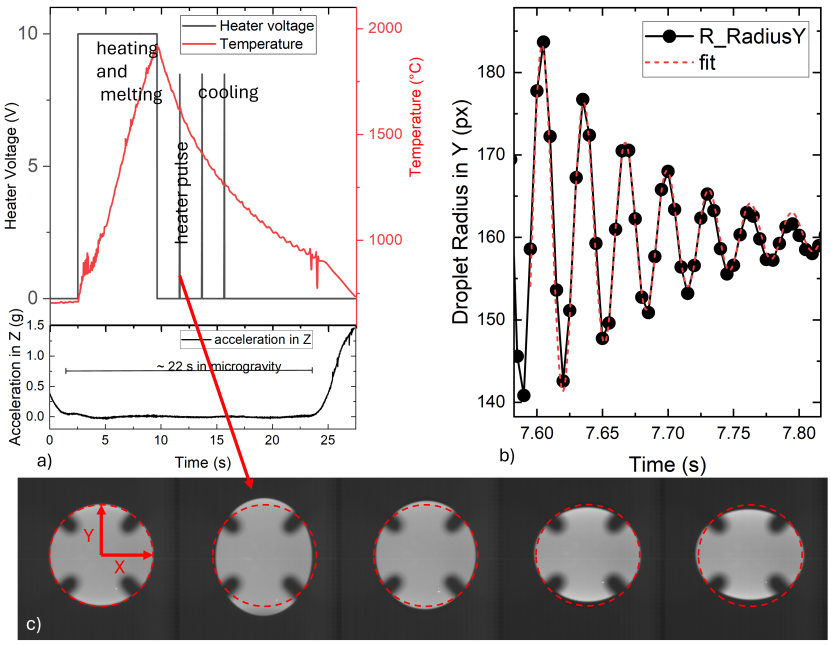

Figure 3.17: Cycle of heating, cooling, and oscillation during the processing of a $(Zr50)S3$ sample by TEMPUS, the exciting pulses are induced by the heating coil. The measured resulting acceleration of the gravitational force throughout the experiment can be seen in the lower half of the graphic. The images below the graphs portray an exciting pulse and the experienced deflection of the liquid droplet.

This equation can only be applied for a harmonic oscillation that results from the excited droplet and is not superposed by other modes of oscillation, therefore, the liquid droplet has to levitate stably without much rotation or movement resulting from the initial heating the micro-gravity. To guaranty this, a certain resting time after the initial heating is given in the program of the TEMPUS facility for the melt to stabilize in the micro-gravity before the first pulse is applied.
The data received from TEMPUS was evaluated utilizing the TEVI software that was specifically developed by the DLR's micro-gravity user support center department (DLR-MUSC) due to the high-demanding video frequency and data rate requirements [130]. The software allows for the determination of the radius of the droplet as a function of time, which can then be evaluated with Origin(Pro), 2024 (OriginLab Corporation, Northampton, MA, USA), where damped wave functions are available by default in the Origin fitting tools.
The experimental data from the 43^{rd} parabolic flight campaign is displayed per example in Figure 3.17 a) where the recorded temperature profile of the measurement is displayed together with the voltage of the heating coil and the recorded acceleration in the vertical direction Z along the radius of the earth that is experienced within the plane. The oscillation of the liquid droplet due to the stimulation of the heating coil impulse can be seen in the lower part of Figure 3.17 c), the quiescent radius of the droplet is marked in red, and the deflection can be seen quite clearly in the recorded images. The derived radius in the Y direction of the recorded images and the fit of the data can be seen in Figure 3.17 b) as a dashed red line.

3.3.2 Structural analysis by X-ray diffraction (XRD)

The structures of the sample specimen were analyzed by utilizing Saarland University's center for X-ray diffraction, which is led by Dr. Oliver Janka. The structural analysis was performed on a Bruker D8-Advance diffractometer that was configured in Bragg-Brentano $\theta - \theta$ geometry (goniometer radius 280 mm) with Cu-K_α-radiation (λ = 154 pm). The measurement principle is shown schematically in Figure 3.18.

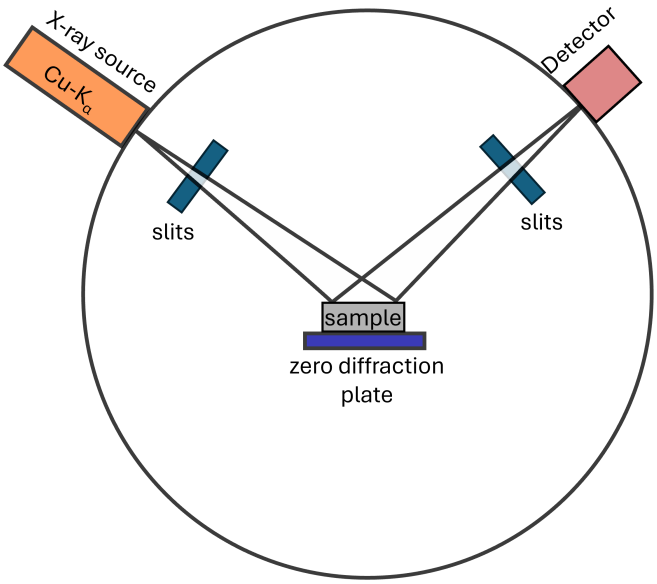

Figure 3.18: Setup of the Bragg-Brentano $\theta - \theta$ geometry that was used for the in-house laboratory XRD experiments, the image is a sketch, and the actual setup was equipped with a Ni-filter and collimator.

A 12 μm Ni foil working as K_β filter and a variable divergence slit were mounted at the primary beam side. A LYNXEYE detector with 192 channels was used at the secondary beam side. Experiments were carried out in a 2θ range of 20° to 80° to cover the significant part of the diffraction spectrum [22]. The samples were mounted on zero-diffraction plates acquired from the company Siltronix (France) which are single crystal silicon wafers that are cut under a defined angle to the crystal's main crystallographic orientation that results in a wafer that shows no background reflexes or noise in a range between 20° and 120° 2θ for Cu-K_α ra-

diation. Exemplary XRD measurements with the described setup can be seen in Figure 3.19.

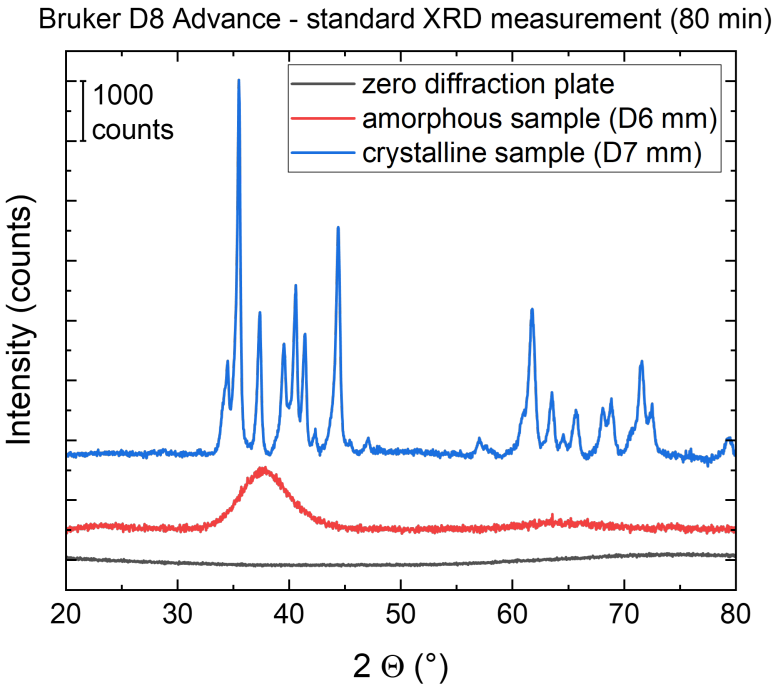

Figure 3.19: Comparison of the diffraction spectra resulting from the zero diffraction silicon wafer as well as an amorphous, 6 mm diameter rod and a crystalline diameter 7 mm rod slice that were all measured with the same setup on the Bruker D8 Advance.

The spectrum that results from the zero diffraction plate alone contains no Bragg-reflexes and shows only a slight curvature. An amorphous sample mounted on the zero diffraction plate can also be seen above the spectrum of the zero diffraction plate, the spectrum typically shows a broad peak, in this case between 32° and 44° 2θ and a second, less significant halo between 58° and 72° which is the resulting spectrum of an amorphous sample. The third spectrum belongs to a crystalline sample where the casting thickness exceeded the critical casting thickness and therefore contains a significant amount of crystalline phase. Those samples typically yield a much higher diffracted intensity due to the strong scattering behavior. The figure is given in absolute counts to show the difference exemplarily, in the

following chapters, the spectra will be normalized to the maximum intensity when being shown comparatively in a waterfall plot.

3.3.3 Mechanical characterization

Within this work, the samples were characterized by three-point beam bending (3PBB) testing after being suction cast into 1.8 mm x 3 mm (h x w) and then sanded with SiC sandpaper until sandpaper of grit 1200 was reached to ensure a proper surface for the mechanical testing. The bending tests were performed on a Shimadzu universal testing machine with a support span L of 20 mm and a displacement rate of 0.3 mm/m, deflection D was recorded, as well as the applied force F measured with a load cell, as described in [22].

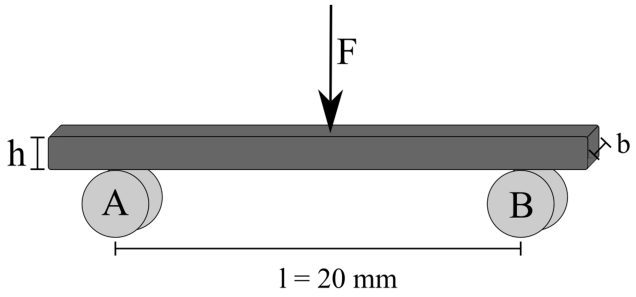

Figure 3.20: Schematic of the three-point beam bending setup on the Shimadzu universal testing machine, taken from [17].

The maximum stress σ and strain ϵ on the surface were calculated according to equation (3.6) and (3.7) respectively, as:

$$\sigma = \frac{3FL}{2wh^2} \tag{3.6}$$

$$\epsilon = \frac{6Dh}{L^2} \tag{3.7}$$

where the Force F and the length of the support span L as well as the sample width w, sample height h and deflection D, the setup is being sketched in Figure 3.20.

The hardness of the samples was measured using a Wolpert Wilson 930 N universal hardness tester with a load of 49 N and a diamond Vickers indenter with a pyramid of 136° top angle and a resting time of 15 s in the material. The testing principle is sketched in Figure 3.21. The indents remaining in the material after indentation and plastic deformation are investigated with an optical microscope to determine the diagonal lengths d of the remaining indent in the material, and the Vickers hardness is calculated according to equation (3.8) as:

$$HV = 0.189 \cdot \frac{F}{((d_1 + d_2)/2)^2} \tag{3.8}$$

where d is the diagonal of the indent.
For each sample, results of 10 individual indents were averaged, and the standard deviation was calculated to improve the statistical aspect of the hardness measurements, as the hardness can vary throughout the surface of the sample due to the hardness being closely tied to the cooling conditions that the alloy experiences.

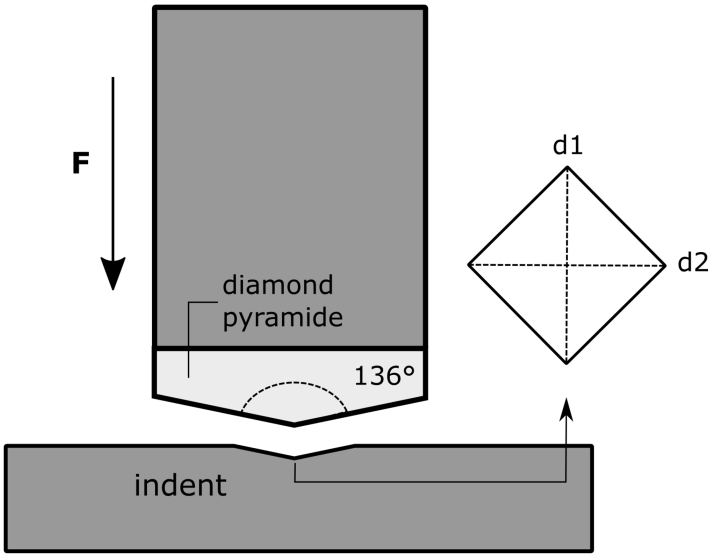

Figure 3.21: Schematic of the Vickers indentation measurement, taken from [17].

Additionally single single-edge notched beam bending samples with a cross-section of 2 mm x 4 mm (B x W) were used to determine the fracture toughness of the sample material. The surface of each sample was sanded to a 4000 grit finish and

polished to a 0.1 μm surface finish. Notches with a radius of about 150 μm were instilled with a diamond blade, followed by the sliding of a razor blade across the diamond blade notch. The resulting micro notch was then created with a root radius of 20 μm. Fatigue pre-cracking was performed by cyclic loading with a frequency of 10 Hz sine wave with a ratio of minimum to maximum load of $R = P_{min}/P_{max} = 0.1$ by a servo-hydraulic testing machine (Instron Model 8872, Instron Corporation, USA) with a 25 kN load cell. Stresses of $\Delta K = K_{max} - K_{min}$ between 6-8 $MPa\sqrt{m}$ were applied for the pre-cracking and the three point beam bending fracture tests were performed with a support span of 16 mm on an Instron 8872 dynamic test machine with a 25 kN load cell and a constant displacement rate of 1 $\mu m/s$. As no test samples met the sample dimensions required by ASTM E399 for valid plane strain measurements given in equation (3.9) for K_{IC} as:

$$B, a, b \geq 2.5 \left(\frac{K_Q}{\sigma}\right)^2 \tag{3.9}$$

$$K_J = \sqrt{\frac{E(J_{el} + J_{pl})}{1 - \nu^2}} \tag{3.10}$$

Here $b = W - a$ and instead of K_{IC}, K_Q and K_J are determined as no plane strain fracture toughness K_{IC} can be derived from the alloy set, as:

$$J_{el} = (K_Q)^2(1 - \nu^2)/E \tag{3.11}$$

$$J_{pl} = \eta_{pl} A_{pl}/Bb \tag{3.12}$$

here the parameter $\eta_{pl} = 1.9$, A_{pl} is the area under the force vs displacement curve, E is the elastic modulus of the glass, and ν is the Poisson ratio of the glass.

Compression tests were performed in addition to investigate the properties of the 2 mm x 4 mm beam samples that were also used for the determination of fracture toughness. Here, samples of 2 mm x 2 mm x 4 mm were cut from the testing beams and carefully sanded to be plan-parallel. Here, the samples were tested on tungsten carbide plates that were coated with dry lubricant of MoS_2 based lubricant to minimize the influence of friction during the testing procedure. The

displacement rate was 0.83 $\mu m/s$ and details on the method can be found in reference [22].
Additionally hardness mapping was utilized to characterize the distribution of hardness in the microstructure and therefore Vickers HV0.05 indentations with a force of 0.49 N were measured with a Struers Durascan 80 and a minimum spacing of 40 μm in between the indents, similar to previous works in cooperation with the UNSW [131].

3.3.4 Optical microscopy (OM)

Regular metallographic microscopy methods were used routinely to check the sample preparation as well as to measure the size of the indents during hardness determination. Therefore, an Olympus BH-2 metallographic microscope equipped with a digital camera was utilized. Modern optical microscopy reaches a magnification range of 400-1000 times of the original object size [132]. The optical microscope was employed to measure the width of the Vickers' hardness indents diagonally and document those. For images of crystalline samples, the polarization contrast mode was preferentially used.

3.3.5 Electron microscopy

Scanning Electron microscopy (SEM)

The electron microscope was used preferentially to investigate the microstructure of the cast samples since the appearing crystalline phases were quite small and the contrast of the optical microscope was not sufficient to investigate the microstructure adequately. In contrast to optical microscopy, the magnification of modern SEM systems can reach up to 300.000 times magnification of the original size of the objects [132]. The electron microscope utilizes no direct imaging in comparison to conventional microscopy, the surface of the sample is rather excited by an electron beam, and the emission of the sample is analyzed by the respective detectors. The source of the electron beam can be a heated cathode made from tungsten or LaB_6, while newer electron guns use a field emission gun (FEG) that supports the emission of electrons through a high voltage field that is applied to the cath-

ode [133]. The FEG-SEM has several advantages over the conventional SEM that operates on W-filament, as the spatial resolution is significantly increased over the conventional electron gun [133].
The different interactions of the electron beam with the sample are drawn schematically in Figure 3.22. Primary electrons thereby refer to electrons that are being elastically scattered at the sample materials atoms, images from the back-scattered primary electron detector contain a significant materials contrast as the amount of back-scattered electrons is proportional to the atom's amount of protons in the core, as they yield the positive charge that is being responsible for the amount of back-scattered electrons.

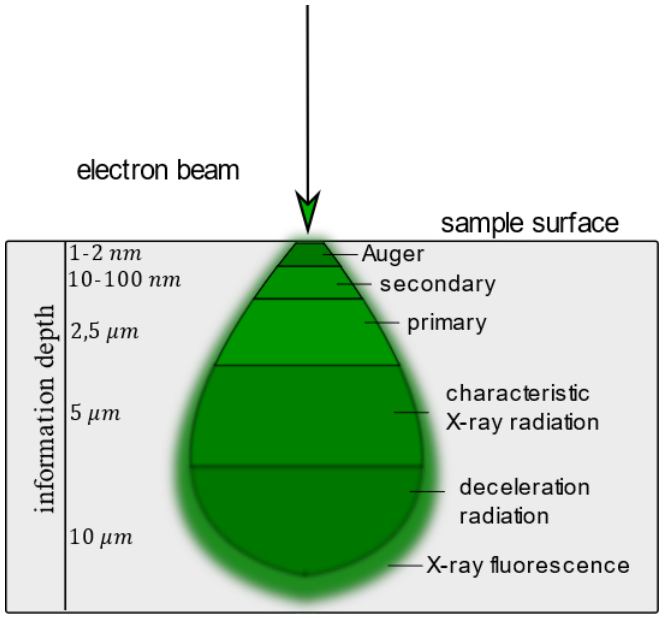

Figure 3.22: Schematic of the interaction zone of electron beam and the surface material with the zones of interaction drawn and labeled, the information depth is dependent on the acceleration voltage of the gun, each interaction of the electron beam with the material contains information about the material that can be detected by the individual detectors, taken from [17].

Although the back-scattered electrons also contain topology information, in this work, the majority of the samples that were investigated with the back-scattering contrast were flat samples, so that the major contribution to the contrast of the

back-scattered electrons was materials contrast, the detector is mounted on the very bottom of the column of the FEG-SEM. The angle-selective back-scattering detector (AsB) was primarily used in this work for the back-scattering electron (BSE) images.
Secondary electrons (SE) refer to indirectly scattered electrons that do not move in a backwards orientated vector but exit the surface randomly orientated from a low depth of the upper material layers of the sample, therefore, they contain mostly topology information.
The detector for the SE2 information is the Everhart Thornley Detector that utilizes a plastic scintillator, which attracts the SE2 electrons with a housing that has a positive bias of 50-300 V [134]. The images constructed from the signal of the SE2 detector are amplified by a photo-multiplier, and the amplification is controllable by the voltage applied to the photo-multiplier and is often integrated into the SEM-control to adjust the contrast of the SE2 images.
In the following, a multitude of measuring techniques that were employed in this work are discussed and elaborated. The scanning electron microscope that was used for the characterizations in this work was a Zeiss Sigma VP FEG-SEM, equipped with an Oxford-Instruments EBSD/EDS system at the chair of experimental methodology of materials science (MWW). Scanning electron microscopy uses scanning coils for the discrete movement of the electron beam in the X and Y axes on the sample surface in the form of straight lines, that form the pixel grid of the resulting image [132]. While the beam is manipulated by the scanning coils to move over the sample in a defined grid, each pixel is assigned a certain dwell time spent at the position, exciting the respective point on the sample. The images contain pixels that are recorded individually and processed digitally after amplification to reconstruct images from the position in the scanning grid and the respective detector signal recorded for the pixel. For the angle-sensitive back-scattering detector (AsB) that was primarily used in this work, a grey-scale of the image results that is directly proportional to the atomic number of the excited atoms results.

Energy-dispersive X-ray diffraction (EDS)

The analysis of the emitted characteristic X-rays is utilized in the energy-dispersive X-ray spectroscopy (EDS). This technique analyzes the emitted spectrum, which is a superposition of all the excited atoms' photon emissions. The Oxford Instruments AzTec software is used to quantify the elemental composition of the samples. An example of a spectrum and the resulting analysis can be seen in Figure 3.23. The spectrum contains the information on the individual contributions of the 5 elements superposed in the sum spectrum, as well as the Au that was sputtered on the sample.

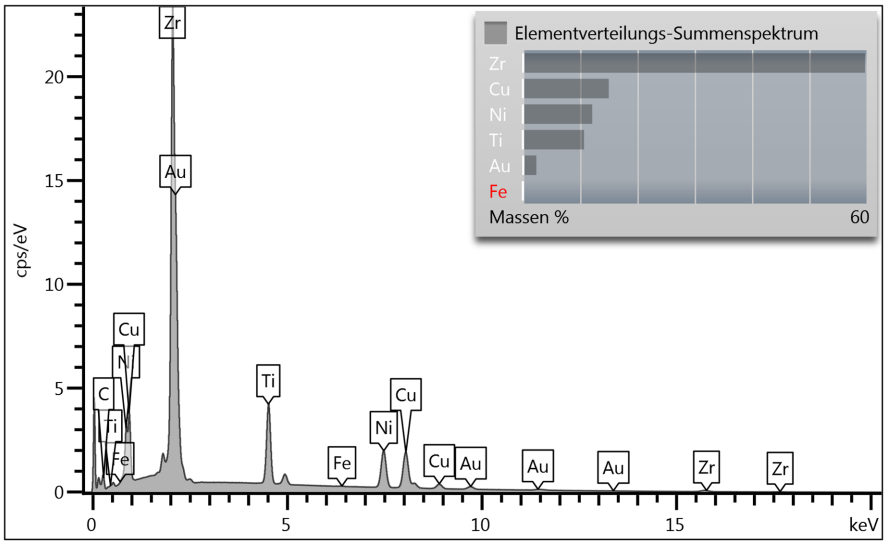

Figure 3.23: The spectrum of a $Zr_{50}Ti_{16.6}Ni_{18.3}Cu_{15}$ sample and the respective quantification of its elements calculated to mass%, including the sputtered Au atoms that were situated on the surface.

Electron back-scattering diffraction (EBSD)

Electron back-scattering diffraction (EBSD) is a technique that provides crystallographic information in the SEM, the surface preparation, however, is quite time-consuming, as the surface needs to be perfectly flat and without mechanical deformation of the microstructure [135]. In comparison to the rather simple to prepare X-ray diffraction analysis, this is used for in-depth characterization of samples, the combination with the EDS results in a local characterization comprised

of information on both local chemistry and structure of the crystalline phases. The spatial resolution that can be achieved with the EBSD in modern FEG-SEM devices is about 20 nm and the depth of information that the Kikuchi pattern results from is dependent on the acceleration voltage, as well as the incident angle under which the electron beam enters the sample surface, for a regular SEM configured at 40 keV and an angle of entry spanning 20° it lies well between 10 nm and 40 nm [136]. It is therefore considered a standard tool for orientation and texture analysis of poly-crystalline materials at grain-specific levels of micro-structural analysis [136].

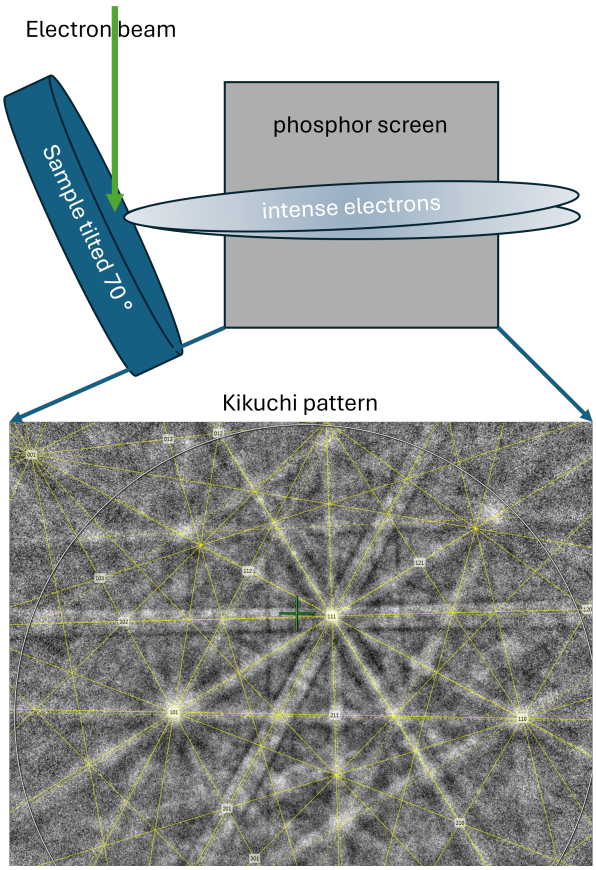

Figure 3.24: Schematic setup of the electron back-scattering diffraction, the under 70° emitted cones of high intensity electrons form lines on the phosphorous screen, which are referred to as Kikuchi lines that, in total, form the Kikuchi pattern.

The electron back-scattering technique was utilized in the analysis of the crystalline

phases to verify the structures that were encountered in the samples originating from the in-situ electrostatic levitation experiments. For the suction cast samples, the quality of the received Kikuchi patterns was very poor, so that only the slow cooling rates of the ESL setup could be evaluated. The setup of the measurement is shown schematically in Figure 3.24, where an indexed example of a Kikuchi pattern resulting from a sample that was processed in the electrostatic levitation environment can be seen.

The analysis was performed against standard crystallographic phases of the database included in the Oxford Instruments software, due to the deviation of the local chemistry in these multi-component glass forming alloys, the statistical requirements for positive identification of the structures were lowered to reasonable standards within the parameters of the solver program. A Hough space resolution of 40 nm and a minimum band recognition of 6 bands were required for the positive identification of the phases. The selection of possible phases was based on the respective phase diagrams that were available from the 2-component systems, as well as the phases that were found during X-ray diffraction in the laboratory or during the in-situ campaigns at the synchrotron.

Transmission electron microscopy (TEM)

Transmission electron microscopy (TEM) is a specialized sub-category of electron microscopy that emerged in the early 1940s [137]. The technique works with very thin specimens, referred to as lamellae, which need to be electron transparent as the setup is in transmission geometry, like the name of the technique already suggests. The electron transparent thickness is not independent from the material that is being investigated, as for aluminum alloys 1 μm would suffice to be electron transparent, for steel however it would be some hundred nanometers, still the axiom for transmission electron microscopy experiments is 'the thinner the better' [138]. The TEM can achieve sub-nanometer resolution thanks to the very small wavelength of the electron beam compared to a photon beam, for example [137].

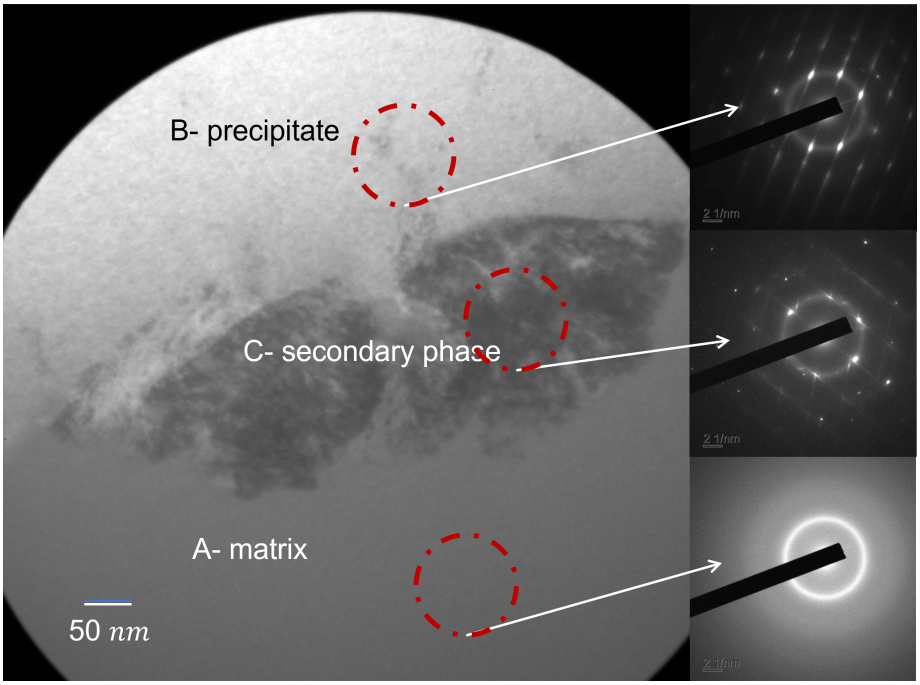

Figure 3.25: Example of a bright field TEM image taken on a specimen of a sulfuric precipitate in an amorphous matrix of a $Ti_{40}Zr_{35}Cu_{17}S_8$ casting, with the corresponding locations marked out in red where the selected area diffraction images displayed on the right hand side on the image are taken from [18].

There are multiple variants of the TEM in practice in material science today, and

within this work, only regular TEM and scanning transmission electron microscopy (STEM) were applied, therefore, this section is limited to those two techniques. In contrast to the back-scattered electron in the SEM, when performing TEM, the interest lies mainly on the forward-scattered electrons that have been interacting with the specimen; those are contained within $\pm$ 5° of the central beam [138].
In the TEM, it is also possible to analyze the composition of the sample by quantifying the energy of the X-rays emitted by the interaction of the electron beam and the specimen, similar to the EDS in the SEM. Due to the interaction zone being a lot smaller in the TEM (typical modern electron beam diameters being $< 5\ nm$) the spatial resolution that can be achieved with the EDS technique in TEM is of course significantly higher due to the reduced size of the excited volume that emits the characteristic X-rays [138].
The TEM also provides another imaging mode utilizing the electron diffraction capability in transmission mode, which takes place when the electrons pass through the thin specimen. The selected area electron diffraction (SAED) imaging is a highly valuable tool for material scientists, as it allows them to characterize the crystal structure as well as potential defects [138]. From those diffraction images, a complete crystal-symmetry analysis is possible.

3.3.6 Synchrotron-based scattering experiments

Within the scope of this work, multiple proposed experiments of our group were funded by the German Electron Synchrotron (DESY) located in Hamburg, Bahrenfeld. The majority of the beamtime was granted at the Swedish Material Science Beamline P21.1 for high-energy X-ray diffraction as well as the beamline P21.2 for diffraction, scattering, and imaging. In cooperation with the German Aerospace Center (DLR), a measurement campaign utilizing an electrostatic levitation environment (ESL) was employed at the P21.1 beamline for in-situ diffraction experiments. The electron storage ring of PETRA III (positron electron tandem ring accelerator) has a circumference of 2.3 km and supplies 6 GeV at a current of nominal 100 mA, which results in a brilliance approaching the 10^{20} ph / ($s\ mm^2\ mrad^2$ 0.1% BW) range [139]. The aerial view of the Bahrenfeld campus where PETRA III is situated can be seen in Figure 3.26 a), where the scale of the

storage ring can be understood quite clearly. The fundamental parts of PETRA III are shown schematically in Figure 3.26 b), and an enlarged section of the Max von Laue and Ada-Yonath Halls are depicted in 3.26 c) to give an idea of the different beamlines arrangement that are attached to the facility of PETRA III.

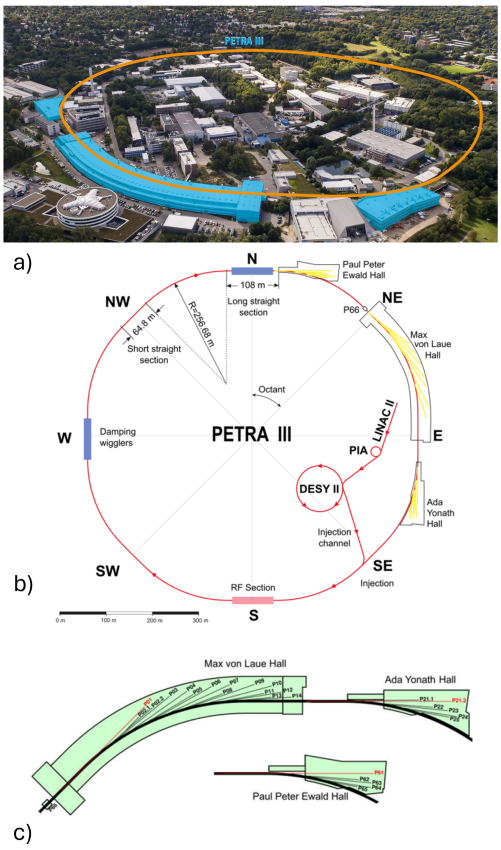

Figure 3.26: a) Aerial view of the PETRA III facility with the experimental halls marked out in blue b) schematic of most important components of the synchrotron and their arrangement on the Bahrenfeld campus c) magnified sketch of the Max von Laue and Ada-Yonath Hall with the arrangement of the different beamlines, taken from [140] and [141].

The synchrotron-based scattering experiments were utilized to characterize the structure of the materials in dependence on temperature and time. Therefore different sample environments were employed, which were the previously mentioned ESL, as well as two LINKAM furnaces, the THMS-600 furnace that consisted

of a silver block equipped with a heater, controlled by a Pt-100 thermoelement and a proportional-integral-differential regulator (PID). The furnace is housed in a water-cooled aluminum case, that allowed atmospheric control of the sample environment. Argon protective gas with a 6N (99.9999 Vol %) purity rating, was flushed at a constant rate to prevent oxidation of the highly reactive Zr-based samples. For in-situ melting experiments, another LINKAM furnace was employed, the TS-1500, which was equipped with an alumina crucible, fitted with custom-made tungsten sample carriers that were coated in yttrium oxide to prevent the highly reactive melt from alloying itself to the sample carrier. The setups can be seen in Figure 3.27 a) where the THMS-600 is depicted that was used mainly for standard scanning experiments with a rate of 20 K/min as well as isothermal holding experiments and in Figure 3.27 b) the high temperature furnace TS-1500 is depicted that was primarily used for melting and solidification experiments within this work.

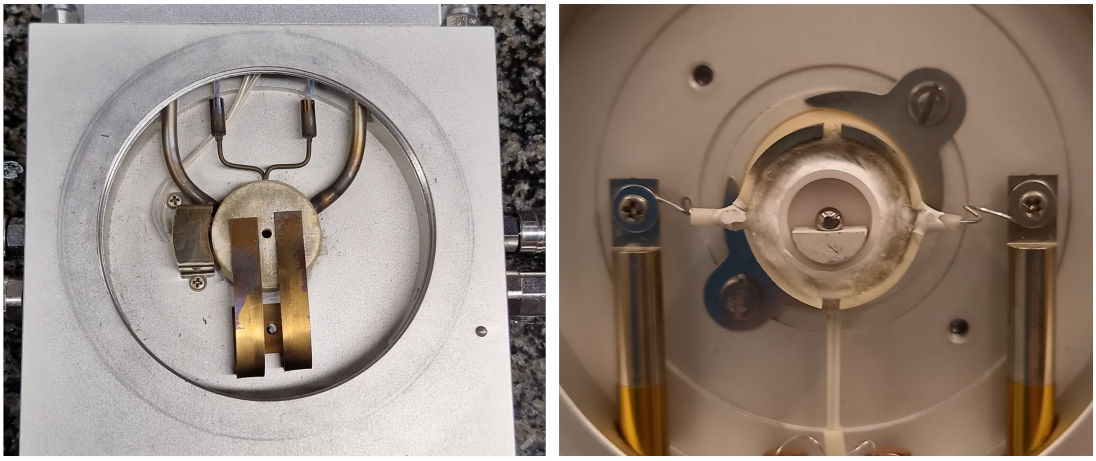

a) b)

Figure 3.27: a) LINKAM THMS-600 furnace equipped with an Ag-block heater and a custom made steel clip that attaches flat samples to the silver block and ensures proper thermal contact to the block b) LINKAM TS-1500 furnace equipped with a tungsten sample holder as well as a ball sample placed inside the furnace, these were molten under inert Argon atmosphere with a temperature of up to 1773 K. (copyright B. Adam)

In-situ wide angle X-ray scattering (WAXS)

The X-ray scattering experiments were performed utilizing hard X-rays with an energy of 60 keV in the case of the P21.2 beamline and 100 keV in the case of the P21.1 beamline. These high energy levels allow for a different experimental setup than the earlier described Bragg-Brentano geometry used in the laboratory X-ray diffraction setup. Here, the high energy of the X-rays coupled with the high brilliance of the beam allows a transmission diffraction setup with a suitable temporal resolution of 1 s per diffraction pattern, despite the sample dimensions being up to 3 mm in thickness.

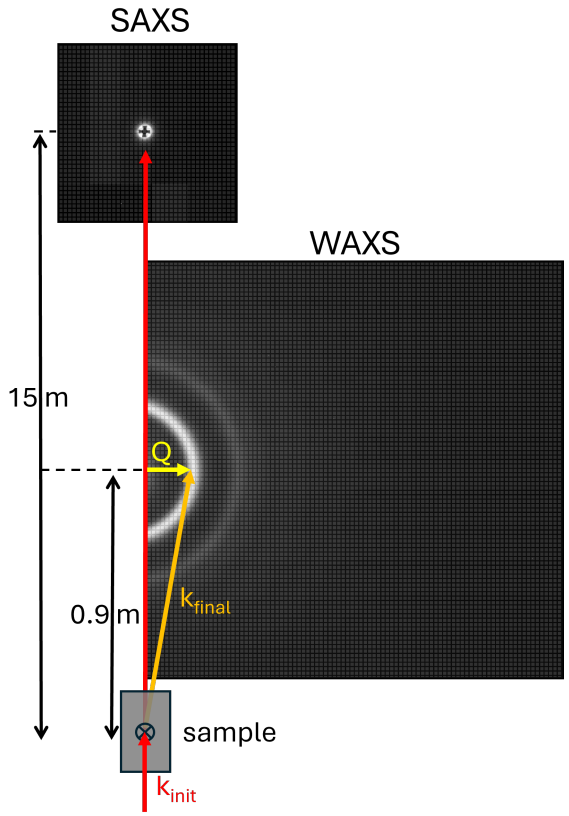

Figure 3.28: Schematic of the experiment and detector setup on the beamline P21.2 for the two proposed LINKAM THMS-600 in-situ structural characterization experiments during heating scans.

The scattered intensity is recorded with a Varex 2D flat panel detector (XRD4343

CT) that contains 2880 x 2880 individual pixels with a single pixel being 150 micrometers in length and width. The data from the flat panel detector was azimuthally integrated with the Python Fast-Azimuthal-Integrator (pyFAI) software to reduce the detector images into two-dimensional diffraction spectra [142]. The setup of the P21.2 beamline with the involved detector is sketched and shown in Figure 3.28, the beamline has a unique setup with a long vacuum flight tube that enables a sample detector distance of 15 m in total for the recording of short angle data and multiple freely positionable Varex detectors for the wide angle data. The data recorded with the detector was corrected regarding background intensities and intensity variations during the Top-Up operation of the PETRA III electron storage ring with the OriginPro 2023 software before further processing.
The theoretical background in this section was described by Egami and Billinge and was centered around equation (3.13) for $\Psi(Q)$ that defines the scattering amplitude [143] as:

$$\Psi(Q) = \frac{1}{< b >} \sum_{v}^{\infty} b_v \; e^{iQR_v} \tag{3.13}$$

where the diffraction vector is defined as Q according to equation (3.14) as:

$$Q = k_{init} - k_{final} \tag{3.14}$$

and the wavevector of the incoming beam is labeled as k_{init} and the wavevector of the scattered beam is labeled as k_{final} [143].
The expression R_v describes in (3.13) the position of the v^{th} atom, and b_v is the respective scattering amplitude of the atom v, which in itself is a measure for the strength of the scattering.
In equation (3.15), that describes the wave vector Q as:

$$|Q| = 2k \; sin(\theta) = \frac{4 \; \pi \; sin\theta}{\lambda} \tag{3.15}$$

the wave-vector of the incoming beam k_{init} is considered to be elastically scattered, thereby it is defined by $|k_{init}| = |k_{final}|$ [143].
The scattering amplitude $\Psi(Q)$ contains the information of the structure in the material, however, the only quantity that can be directly measured is the intensity

$I(Q)$ of the scattered wave [143]. The intensity of the scattered beam's amplitude can be expressed as shown in equation (3.16) according to Egami and Billinge [143], that gives $I(Q)$ as:

$$I(Q) = \frac{< b >^2}{N}|\Psi(Q)|^2 + < b >^2 - < b^2 > \tag{3.16}$$

Furthermore, the total scattering structure function S(Q) is essential for the understanding of the structure encountered in the metallic glasses. It is defined according to equation (3.17) as:

$$S(Q) = \frac{I(Q)}{< b >^2} \tag{3.17}$$

and is calculated from the experimentally acquired diffraction pattern that results from the synchrotron-based scattering experiments. Those diffraction images can be converted into the intensity I(Q) by azimuthal integration and correction of container scattering and subtraction of the detector's dark image current.

The reduced pair distribution function (PDF) G(r) can be acquired from the structure function S(Q) by a 'straightforward numerical Fourier transform' of the total scattering function according to equation (3.18) by:

$$G(r) = 4\pi r\rho_0(g(r) - 1) = \frac{2}{\pi}\int_0^\infty Q[S(Q) - 1]sin(Qr)dQ \tag{3.18}$$

which also contains the radial distribution function g(r) from which the structure of a crystal for example can be directly determined [143].

The results of the 4 steps performed with the acquired diffraction images, that were processed according to the previously described data treatment procedure, are displayed in Figure 3.29 for an exemplary demonstration. The calculations beyond the correction of the intensity I (Q) into the structure function S(Q) and the reduced pair distribution function G(r) were performed with PDFgetX2 software [144].

It is important to remember during pair distribution function analysis of multicomponent systems that all atomic binding pairs contribute to the PDF and that the G(r) function is the superposition of the contributions of all the dominant atomic pairs. The function gives the probability of finding atoms at a certain

distance from the central atom, however, this does not contain information about the atomic species that is found at this position. This means that for two atomic species α and β the pair's scattering amplitude $< b_{\alpha\beta} >^2 = c_\alpha c_\beta b_\alpha b_\beta$ according to the Faber-Ziman definition [143]. This results in equation 3.19:

$$G(r) = \sum_{\alpha\beta} \frac{c_\alpha c_\beta b_\alpha b_\beta}{\langle b \rangle^2} G_{\alpha\beta}(r) \tag{3.19}$$

which means that the total PDF is the weighted sum of the partial PDFs, multiplied by their respective concentrations c_α and c_β.

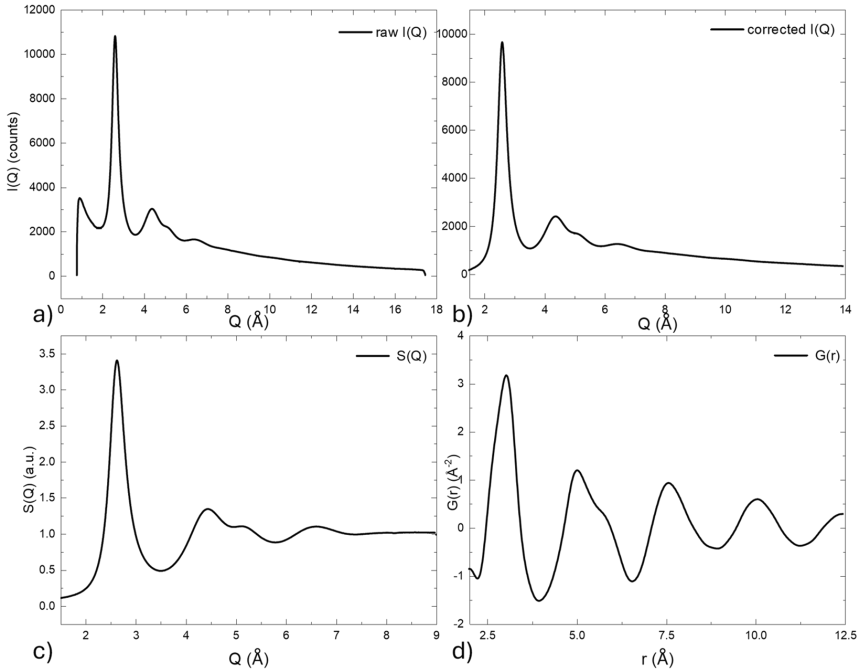

Figure 3.29: Exemplaric display of the data acquired at the P21.2 from amorphous Vitreloy105 alloy where in a) the azimuthally integrated raw data, b) the corrected Intensity I(Q) data, c) the derived total scattering structure function, d) the Fourier transformed data as the reduced pair distribution function (PDF) G(r).

However the total PDF is not the exact weighted sum of the partial PDFs as there is still a Q-dependence of the f(Q), in practice this can be approximated by the Morningstar-Warren approximation [145] that separates the absolute value and

the Q-dependence of the scattering amplitude, so that the Faber-Ziman weighting factors $w_{\alpha,\beta}$ are described as slowly varying function of Q [143].

In-situ small angle X-ray scattering (SAXS)

Small-angle X-ray scattering (SAXS) covers the diffraction that is situated at the low angles near the primary beam. This diffraction technique is mostly utilized by the polymer community. The small-angle scattering provides the possibility to study submicroscopic heterogeneity in the scattering sample [146]. Recent studies utilize SAXS in the investigation of polymorphic crystallization under different thermal histories, to differentiate structurally similar compounds [147]. The technique was applied to amorphous alloys before, and for example, in Fe-P-C alloys, SAXS was utilized to determine electron density fluctuations in the amorphous solid after aging for short periods on a range of particles sized between 0.8 nm and 2.4 nm in Fe-based metallic glasses by Osamura et al. [148]. Here the intensity distribution of the scattering is analyzed for different stages of aging and crystallization. This can be observed quite clearly in the SAXS data due to a rise in scattering intensity or formation of an interference peak that can be observed in the case of distributed heterogeneous structures like reported for Mg-based BMGs [149]. In bulk metallic glasses, the technique can be used to investigate early crystallization stages and growth mechanisms, as it is performed in the literature by Kündig et al. to determine the particle diameters as a function of the annealing time in Vitreloy 105 [150]. The SAXS technique is also utilized to study nano-crystallization in BMG and to detect regions of decomposition and their respective size before crystallization, as well as to gain insights into the growth kinetics of the nanocrystals [151]. The simultaneous SAXS and WAXS technique allows for to gain of information on the shape, size, and pair distance distributions of nanometer-sized aggregates in the analyzed volume, making it a versatile approach to a holistic in-situ structural analysis [152].

In-situ electrostatic levitation wide angle angular diffraction (ESL-WAXS)

In cooperation with the German Aerospace Center (DLR), the chair of metallic materials was able to acquire funding from DESY under proposal I-20210883

for a joint measurement campaign to study the influence of metalloid addition on the structure and crystallization behavior of metallic liquids in container-less electromagnetic levitation. Therefore, a specialized ESL sample environment was integrated into the diffraction setup of the beamline P21.1 at Petra III. Thereby it was possible to study the structure of the metallic liquids of $Zr_{50}Ti_{16.6}Ni_{18.3}Cu_{15}$ as well as $(Zr_{50}Ti_{16.6}Ni_{18.3}Cu_{15})_{97}S_3$ and their respective crystallization behavior from the high temperature equilibrium liquid.

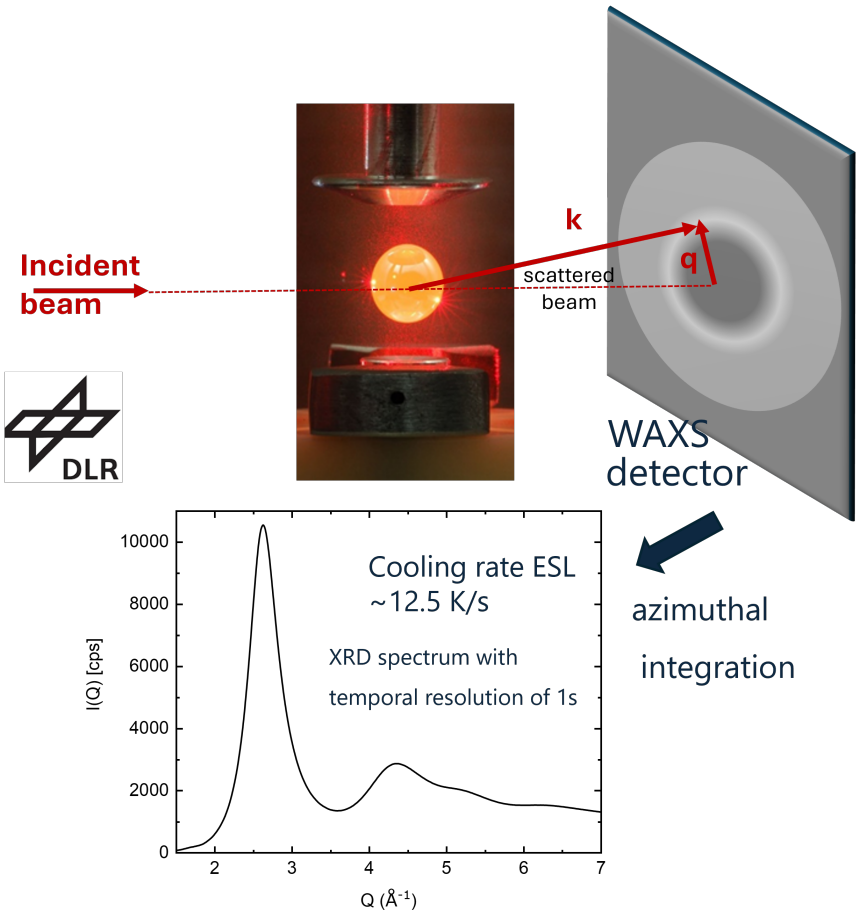

Figure 3.30: Experimental setup of the electrostatic levitation device that was used as a sample environment in the P21.1 beamline setup that was operated in cooperation with the German Aerospace Center (DLR).

For the levitation, the electrodes of the ESL are positioned inside an ultra-high vacuum chamber, which can be evacuated to a pressure of about 10^{-8} mbar [153].

The position of the sample is tracked by illumination of two crossed laser beams, where the sample's shadows are tracked by 2D photo-detectors [153]. The laser beams are being expanded by beam expanders for a homogeneous illumination of the sample [154]. A PID controller adjusts the high voltages of the positioning system (4-20 kV) on a millisecond time-scale [153]. The heating was decoupled from the positioning system, in contrast to electromagnetic levitation systems, by utilizing heating lasers to melt the sample.
At the beamline, the ESL environment was modified with aluminum windows with an integrated beamstop in the form of a tungsten cylinder, instead of the regular quartz windows, to reduce the influence of quartz on the signal quality. The scattering of the aluminum was adjusted to a minimum by positioning the ESL chamber in the beam, and the remaining diffracted intensity of the aluminum was removed from the data during background correction with PDFgetX2. The principal setup of the experiment can be seen in Figure 3.30, the employed WAXS detector was a Perkin Elmer XRD1621 CsI bonded amorphous silicon detector (2048 x 2048 pixel).
The temperature was measured optically utilizing a pyrometer, and the heat was brought into the sample with a fiber laser during the electrostatic levitation. The samples were levitated and then heated slowly and carefully into the liquid state where the beam shutters were opened and once a fully amorphous structure without any observable Bragg peaks in the diffraction spectrum was achieved, the laser was switched off and the sample experienced free cooling during which structural data with a temporal resolution of 1 s was recorded until the sample solidified. The average cooling rate was about 12.5 K/s for the Zr-based samples.

Pair distribution function analysis

The analysis of the BMG's structure relies on the ECP structural model introduced in section 2.6, the analysis of a non-periodic structure that is characterized by MRO and SRO is not as easily accessible as that of regular crystalline materials. For crystalline materials, the existing measurement methods in the laboratory are well established in the form of methods like powder X-ray diffraction, as it uses exactly the characteristic LRO of crystalline phases to determine their structure from the characteristic symmetries of their diffraction spectrum. For bulk metallic glasses, however, the structural analysis is rather similar to that of metallic liquids.

An example of the typical radial distribution function in a metallic liquid can be seen in Figure 3.31 a), where the radial distribution function of Ta liquid and Ta glass is shown in comparison. Here, the structure of the random hard spheres of Ta is sketched, and in Figure 3.31 b), the different connections between the cluster polyhedra are sketched for improved visualization. In the rPDF, the first peak describing the first shell around the central atom is referred to as r_1 and is typically located between 2.5 Å and 4 Å. The second peak in the pair distribution function contains information about the second nearest neighbor shell of coordination, where the inter-cluster connections, beginning with the 4-atom connection at the lower r values and ending with the more distant 1-atom connections of the cluster. The cluster connections are mathematically expressed as 2 r_1 for the 1-atom connection, $\sqrt{3}r_1$ for the 2-atom connection, $\sqrt{8/3}\ r_1$ for the 3-atom connection and $\sqrt{2}\ r_1$ for the 4-atom connection with r_1 being the center of the pair distribution functions first significant peak, embodying the primary atom interaction of the glass [155, 156].

The type of cluster of connections that dominates the distribution of structural motifs found in the glass is very important for the macroscopic properties of the glass. The amount of a certain cluster connection type, as well as the ratios between them and their shift during modification of the glass chemistry or thermal history, have been studied before in the literature [155] and within our group [25, 157, 158]. Especially the influence of compositional variation on Pt-Pd-P based glasses, as $Pt_{42.5-x}Pd_xCu_{27}Ni_{9.5}P_{21}$ is a model system where the variation of the dominance of 3-atom connection motifs can be seen to consistently reduce

with exchanged Pd for Pt. Instead the other connections, the 1-atom and 2-atom connections become more important- which also reflects the macroscopic very different behavior of the brittle Pd-P and ductile Pt-P glasses [159].

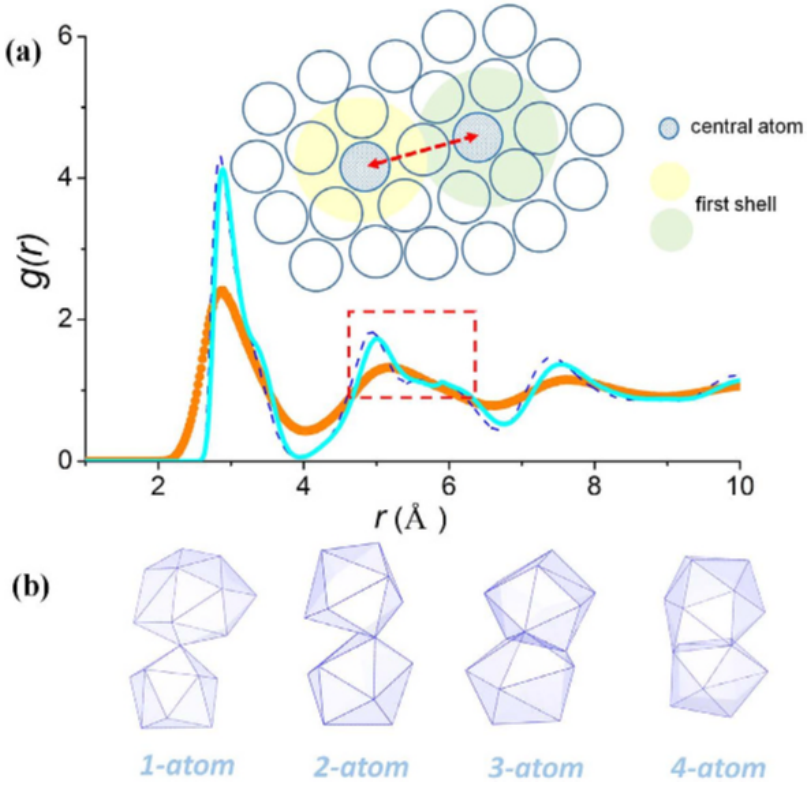

Figure 3.31: Radial distribution of Ta at 3300K (orange) and in the glass at 300K (blue dashed line), the inset illustrates atomic order at the second shell (nearest neighbor shell) of coordination and b) schematics of the four different connection schemes for polyhedra coordination in clusters, taken from [155].

Additionally to the compositional dependence of the connection schemes distribution in the glass structure it depends on the thermal history of the glass as the effects of relaxation and rejuvenation govern the mechanical properties of metallic glasses during thermo-mechanical treatments. Those can also impact the encountered distribution of structural motifs, as both bulk elasticity as well as local stiffness and local stability may have their origin in the local structure [160, 161]. For the Vit105 alloy, Ruschel et al. demonstrated this effect in a study where the

structural data obtained was correlated with the fictive temperature instilled in the glass by the thermal treatment and the corresponding mechanical properties. Especially the ductility of the alloy in its different structural and thermophysical states shows a strong inverse correlation with the 3-atom connection in the Vit105, where an increase in the Zr-Zr bond quantity was observed with progression of the relaxation and where more 3-atom connection could be seen to accompany a more brittle mechanical behavior [25].
The basis for those PDF calculations is the atomic radii of the elements in a metallic glass, here, the reference values reported by Miracle et al. are used throughout this work, which were part of the efficient cluster forming model [76]. The relevant elements as well as the calculated bond lengths for the most important atomic pairs for the $Zr50S3$ alloy are given in Table 3.1.

Table 3.1: Table of the elements atomic radii in metallic glass after Miracle [76] and the calculated inter-atomic distances used in the analysis of the pair distribution functions in chapter 5.

Element	S	Ni	Cu	Zr	Ti
Atomic radius (pm)	100	128	127	158	146
Atomic pair	Cu-Cu	Zr-S	Zr-Ti	Zr-Cu	Zr-Zr
Interatomic length (Å)	2.54	2.58	2.92	2.85	3.16

4 Alloy development of Zr-Ti-Ni-Cu-S

4.1 Critical casting thickness determination

4.1.1 Addition of sulfur and alloy optimization

To reproduce and confirm the glass forming ability of the system, a series of melt-spinning experiments including the base alloy $Zr_{50}Ti_{16.6}Ni_{18.3}Cu_{15}$ as well as two sulfur infused variants with 4 $at\%$ and 8 $at\%$ were conducted.

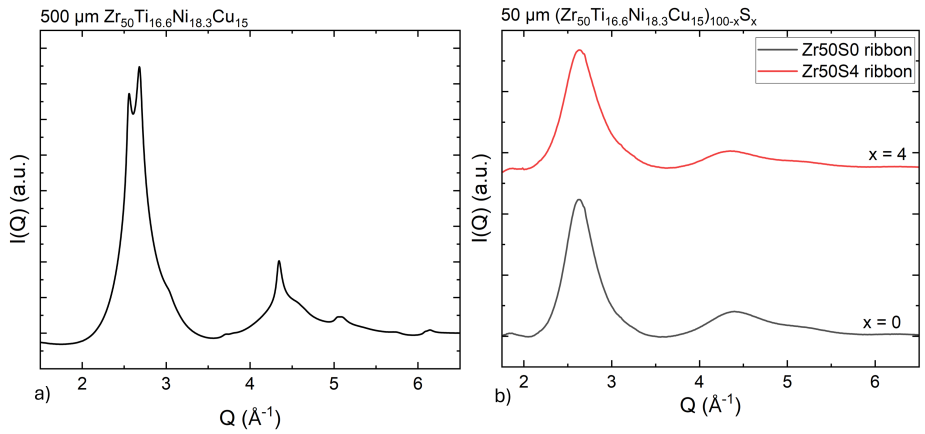

Figure 4.1: a) HE-XRD of the first probed casting thickness in the laboratory, a 0.5 mm thick plate specimen that contains icosahedral phase, b) HE-XRD of ribbon specimen of the initial alloy and the first alloy that was infused with 4 $at\%$ of S.

In the case of the base alloy as well as in the case of the 4 $at\%$ S addition the as-prepared ribbons were found to be X-ray amorphous with the laboratory XRD

and later the amorphous structure was also verified with synchrotron diffraction experiments, the results of the synchrotron experiments can be seen in Figure 4.1 b).

The initial casting series of 500 μm plates from $Zr_{50}Ti_{16.6}Ni_{18.3}Cu_{15}$ contained mostly amorphous phase as well as icosahedral phase, which was not distinguishable by the regular laboratory XRD results. The further determination of the critical casting thickness in this system started based on the assumption that the glass forming alloys published by Molokanov et al. were able to solidify amorphous in copper crucible castings of small plates ranging from 0.25 mm to 0.75 mm in plate thickness, based on the critical cooling rates that were determined by the authors [20].

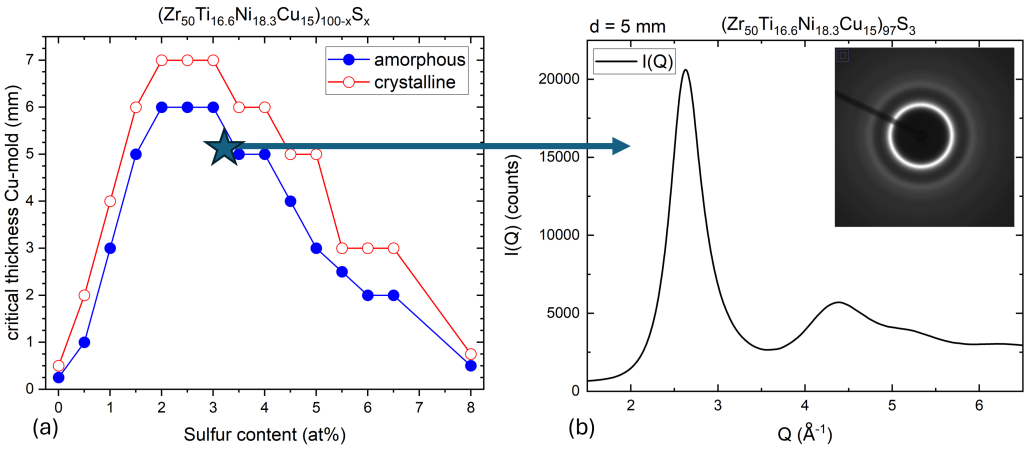

Figure 4.2: a) Summary of the probed casting thickness in the laboratory, b) HE-XRD from PETRA III, diffraction spectrum from an amorphous 5 mm $Zr50S3$ rod, the small inset shows the original detector image.

With initial S-introduction into the system the positive effect of S on the GFA became apparent quickly as in the series of 750 μm plates the S-infused alloy's GFA surpassed the initial alloy on a large range of S-contents varying from 2 $at\%$ to 6 $at\%$, the resulting diffraction spectra can be seen in Appendix Figure 8.3. Throughout the suction casting experiment series, the casting sizes were continuously increased, and the resulting structures were determined by X-ray diffraction. The summary of the found GFA limit for the $(Zr_{50}Ti_{16.6}Ni_{18.3}Cu_{15})_{100-x}S_x$ is dis-

played in Figure 4.2 a). For the most promising alloy of the development, the $Zr50S3$ alloy, a 5 mm diameter rod was probed with the HE-XRD, which was found to display a completely amorphous spectrum, and the original diffraction image is depicted as an inset of Figure 4.2 b). The glass forming ability shows a steep rise from 0.25 mm of the initial alloy to 6 mm for an addition of 2 $at\%$ to 4 $at\%$ and then decreases again from this plateau with a smaller slope, until it fades back to 0.5 mm at an addition of 8 $at\%$.

This steep increase in GFA by a factor of 20, means that the critical cooling rate R_c of the system decreases from an initial cooling rate of about $4 \cdot 10^3$ K/s down to $4 \cdot 10^1$ K/s due to the influence of the S, when determining the cooling rates according to equation (3.1). The origin of this significant reduction of the critical cooling rate of 2 orders of magnitude can hardly be explained with the common GFA criteria or the structural models based on hard spheres.

The S-addition increases the mismatch in atomic size of the system due to being significantly smaller with an atomic radius of 102 pm [76] than the other elements in the alloy. The increased 'confusion' of the alloy might explain the increase in GFA, the further course of the GFA as a function of the S-content, though, cannot be explained by this alone, as the alloys mismatch of atomic size would rise in direct proportion with the amount of S added to the alloy. Since the GFA drops beyond the 3 $at\%$ addition of S to the alloy, the explanation needs to look deeper into the matter of the influence of the S on the alloy's liquid properties.

The maximum of the casting thickness that was achieved can be observed in Figure 4.3 where in part a) a series of 6 mm rods display amorphous structure from 2 $at\%$ to 4 $at\%$ and a partially crystalline structure for both 1 $at\%$ and 5 $at\%$. In part b) of Figure 4.3, the clear surpassing of the GFA limit in copper mold casting is displayed by the castings of the 7 mm rod series, where no fully amorphous sample could be obtained as only spectra of partially crystalline structures were found, none the less the results imply that the glass forming for the 3 $at\%$ and 3.5 $at\%$ is slightly higher than that of the 2 $at\%$ and 2.5 $at\%$ since the amount of crystalline structural signal appears to be lower in the diffraction spectrum of the 3 $at\%$ of S containing 7 mm rod sample.

For the cast 6 mm rod of the $(Zr_{50}Ti_{16.6}Ni_{18.3}Cu_{15})_{97}S_3$ alloy a closer investi-

gation, utilizing electron microscopy methods, of the local microstructure was performed, in Figure 4.4 a high magnification TEM image with the corresponding SAED diffraction image of the illuminated area from the left image can be seen, that contains a minor presence of nanocrystalline phases. This marks the critical limit of the GFA for the S-addition into the system.

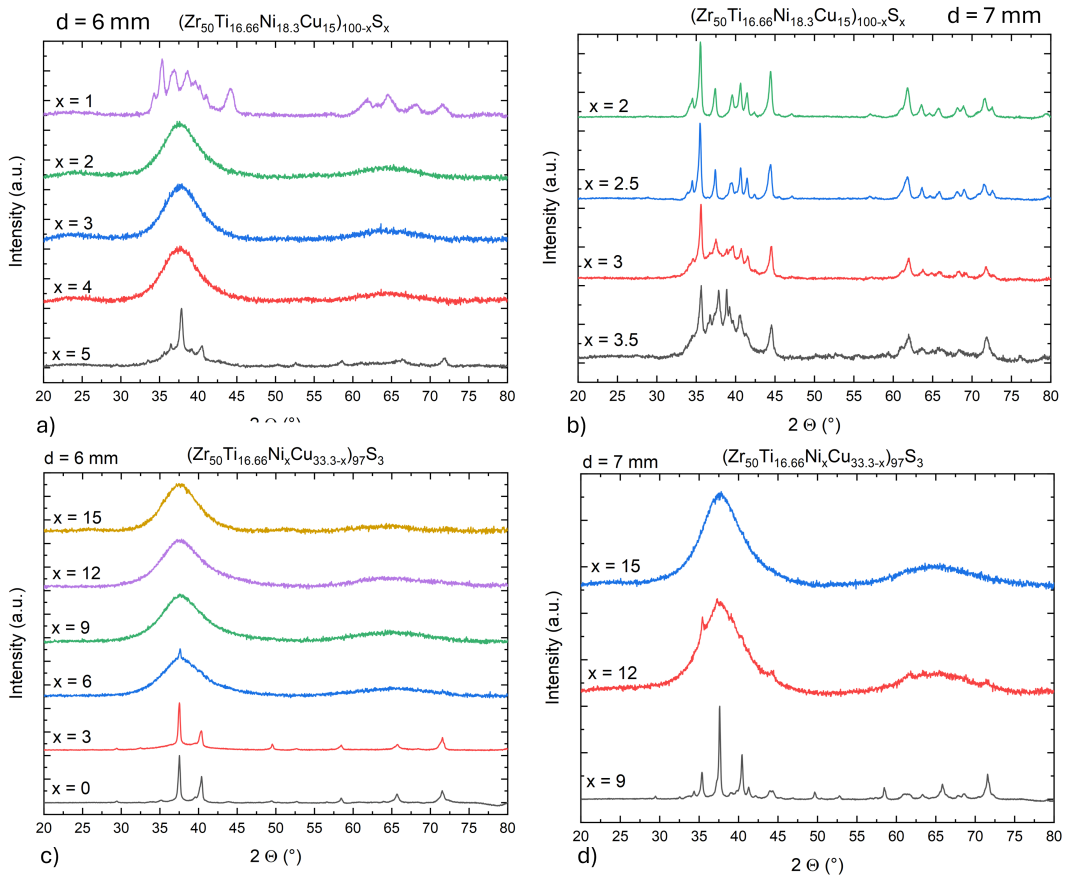

Figure 4.3: a) Regular laboratory XRD diffraction spectra of diameter 6 mm rods that were analyzed over the full cross-section, the rods show diffraction spectra of an amorphous structure for 2 *at*% to 3 *at*% of S addition b) XRD results on the 7 mm diameter cast samples show that none of the samples is amorphous but the 3 *at*% and 3.5 *at*% show a partially crystalline structure signal, marking the 6 mm as critical casting thickness c) Cu-Ni variation also enables a GFA plateau in 6 mm rods and d) even amorphous 7 mm rods with the Cu-Ni exchange, a) and b) published in [22].

The variation of Cu-Ni ratios was performed up to the complete substitution of Ni and the results of the X-ray diffraction are displayed in Figure 4.3, the GFA can be held at 6 mm until an x of 8 $at\%$ which means that the ratio of Cu-Ni is 25.3 $at\%$ to 8 $at\%$ before S addition. On this alloy, the casting size was then increased to 7 mm to probe the most promising Cu-Ni substitutions, and the results can be seen in Figure 4.3 d) - the swap of Cu-Ni at x = 15 $at\%$ enables amorphous castings of 7 mm diameter.

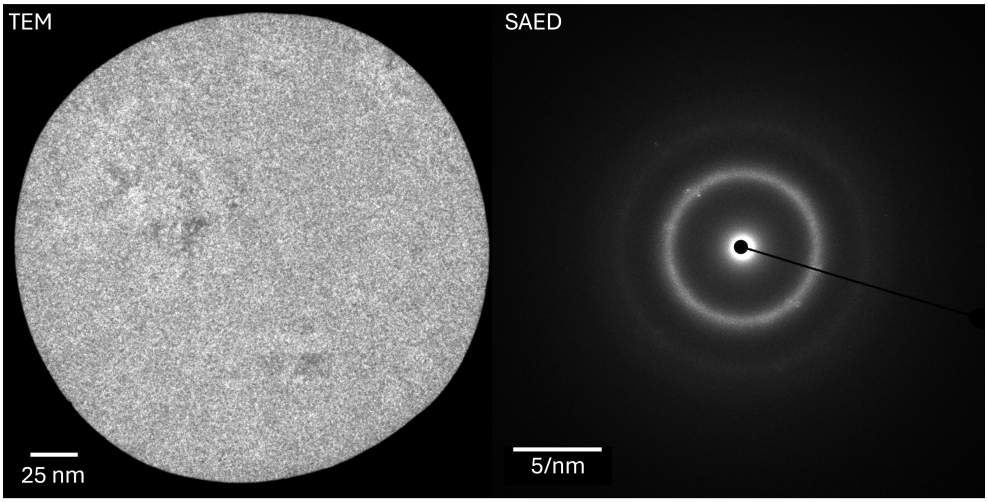

Figure 4.4: TEM image depicting a close up of the microstructure found in the center of an as cast 6 mm rod of $(Zr_{50}Ti_{16.6}Ni_{18.3}Cu_{15})_{97}S_3$ that borders the critical casting thickness and the corresponding SAED image showing a minor crystalline presence taken from [22].

4.1.2 Addition of aluminum and Cu-Ni variation

The alloy was further modified with a rather classical approach of adding Al to the alloy as it is well known from Zr-Ti-Ni-Cu-Al systems like the Vitreloy 105 [14], although the content of Ti in most of these alloys is usually way lower. The results of the $(Zr50)S3$ with aluminum added equally to the alloy in substitution for all other elements simultaneously are displayed in Figure 4.5 a) in the casting size of 8 mm diameter and in b) for 9 mm diameter rods. Here it becomes clear that an addition of 2 $at\%$ to 4 $at\%$ of Al works quite well to achieve a total of 8 mm critical casting thickness for the Al-modified alloy $'((Zr50)S3)Al3'$

$(((Zr_{50}Ti_{16.6}Ni_{18.3}Cu_{15})_{97}S_3)_{97}Al_3)$.
Further developed by employing both the Al addition and the Cu-Ni swap on the $(Zr50)S3$ alloy simultaneously, the GFA can be enhanced to its respective limit for the system, the results are shown in Figure 4.5 c) for a casting size of 9 mm diameter rods.

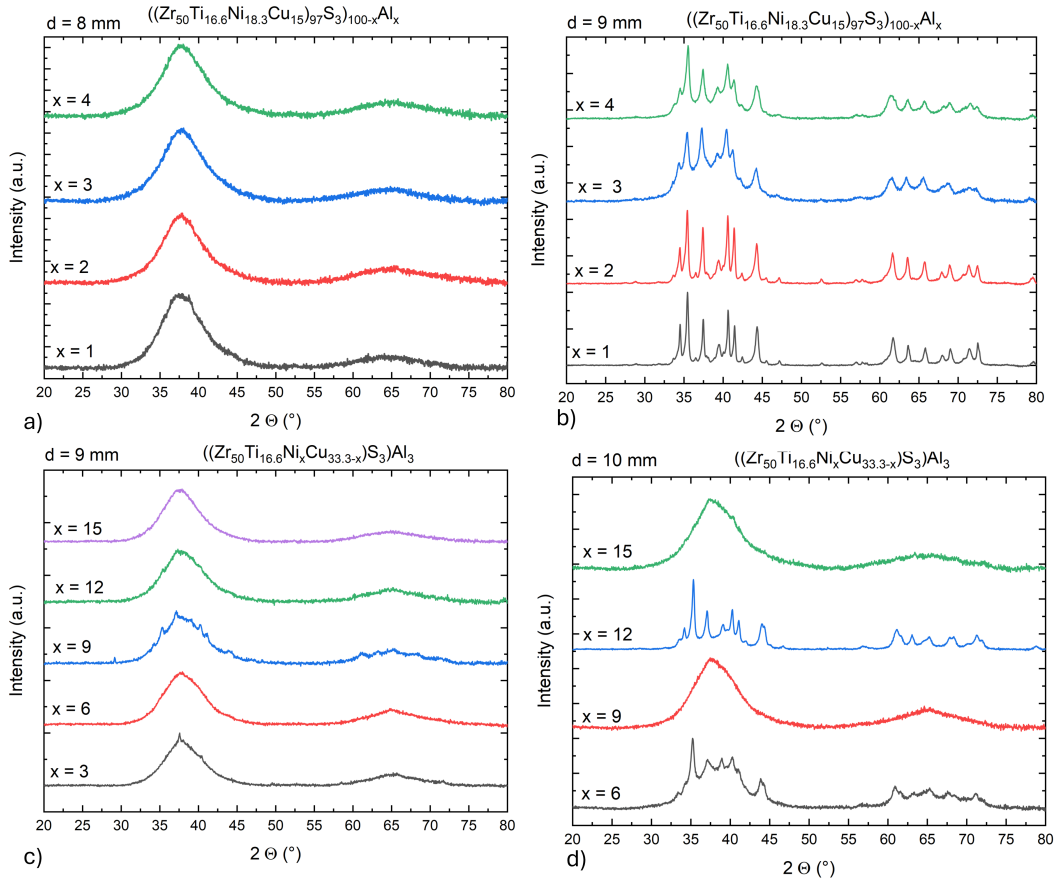

Figure 4.5: XRD results from $(Zr50)S3$ modified with an aluminum addition of 1 $at\%$ to 4 $at\%$ added, where in a) 8 mm rods and in b) 9 mm rods were analyzed. Also in c) the results of 9 mm rods and in d) of 10 mm rods of $(Zr50)S3$ that was modified with both the beneficial effects: Cu-Ni swap and Al-addition.

Where the x = 15 Cu-Ni swap again enhances the GFA up to 9 mm with the 10 mm rod structure being almost amorphous except for a small crystalline presence,

as can be seen in 4.5 d). Overall, the development of the S-infused alloys and their optimization could enhance the glass forming ability in Cu-mold casting from an initial 0.25 mm to 9 mm, which represents more than one order of magnitude in critical casting thickness, resulting in a potent glass forming BMG.

4.2 Thermophysical characterization

4.2.1 Glass transition, super-cooled liquid region and melting behavior

The thermophysical characterization of the $(Zr50)Sx$ alloy series was performed utilizing DSC and DTA as well as TEMPUS and TMA for the characterization of the behavior of the alloys' viscosity in the high-temperature liquid and the supercooled liquid region. The influence of S on the SCLR stability can be seen in Figure 4.6 a), where the DSC curves are shown in dependence of the S content, and a clear trend of increasing SCLR stability and suppression of the first crystallization with increasing S content can be determined.

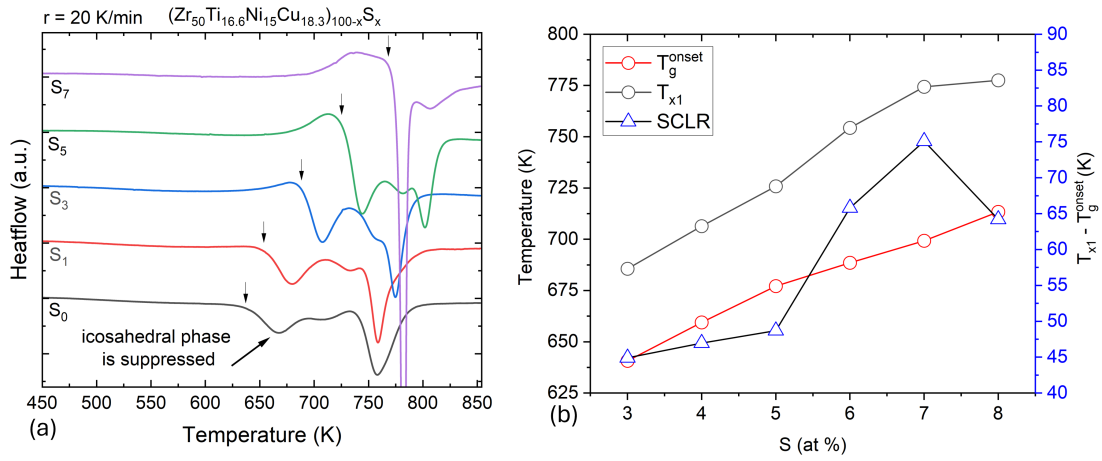

Figure 4.6: a) DSC curves of the $(Zr50)Sx$ development measured with a heating rate of 20 K/s in Al crucibles under Ar protective atmosphere. The content of sulfur was screened with increments of 1 $at\%$ from 0 $at\%$ to 8 $at\%$. b) The derived properties of T_g^{onset}, the onset of the first crystallization stage T_{x1} and the calculated SCLR size as a function of the sulfur content.

The derived onset of glass transition temperature T_g^{onset} and onset of crystallization T_{x1} as well as the SCLR (T_{x1} - T_g^{onset}) are displayed in Figure 4.6 b). The onset of the glass transition could not be determined for the S contents below 3 $at\%$ as the crystallization obscured the glass transition and the tangent method could not

be applied reliably for those alloys. The rise in both glass transition temperature and crystallization temperature appears to be steady under the influence of S, and the crystallization temperature is more susceptible to the S influence as the slope of the increase in temperature is greater. Therefore, the size of the SCLR also rises, although beyond 5 $at\%$ the crystallization temperature increases rapidly, and the shape of the DSC curve shows a full glass transition with no overlap of the crystallization. The $(Zr50)S7$ alloy was found to be the most stable alloy of this development, and only for this alloy, TMA could be measured without the interference of the crystallization.

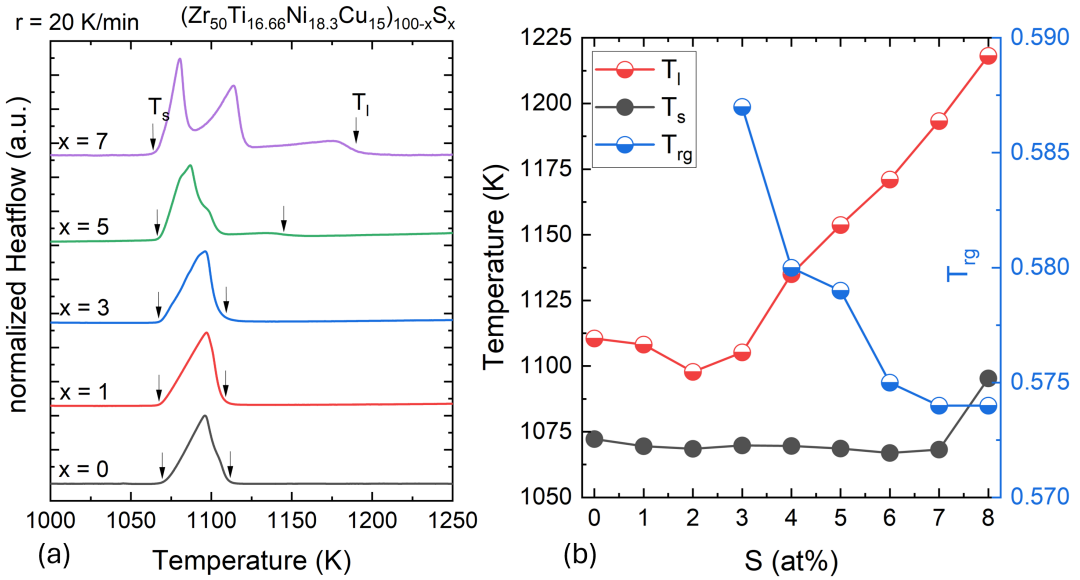

Figure 4.7: a) High temperature DSC curves of the $(Zr50)Sx$ development measured with a heating rate of 20 K/min in C crucibles, coated with Y_2O_3 under Argon protective atmosphere. The content of sulfur was screened with increments of 1 $at\%$ from 0 $at\%$ to 8 $at\%$. b) the derived thermophysical properties of T_l, T_g, and the calculated T_{rg} as a function of the sulfur content.

The alloys were melted in a Netzsch DSC 404 High temperature DSC at the same rate of 20 K/min and the results are displayed in Figure 4.7 a) where the influence of S on the melting behavior of the samples can be seen. The initial alloy displays

almost eutectic melting behavior, that displays a narrow melting interval. With the addition of S into the system however the solidus and liquidus temperatures lower even further with the 2 $at\%$ S addition marking the minimum difference between T_s and T_l with a melting interval of only 29 K. The liquidus temperature rises with further sulfur addition, and the melting curve shows a 'shoulder' on the high-temperature side of the melting event that increases and signifies a multi-phase region. For the S additions beyond 5 $at\%$ the main peak of the melting also begins to split into two separate melting events, as can be seen right away in the curve of the $(Zr50)S7$.

Table 4.1: Results of the Differential Scanning Calorimetry on both the Perkin-Elmer DSC8000 for glass transition as well as crystallization temperatures, and the Netzsch DSC 404 for the solidus and liquidus temperatures on the S-variation of the $(Zr50)Sx$ alloy, all measured with a rate of $20K/s$, $*$: values could not be determined reliavly with tangent method.

Characteristic temperatures						
S $(at\%)$	$T_{\mathbf{g}}^{\mathbf{onset}}$ **(K)**	$T_{\mathbf{x1}}$ **(K)**	$T_{\mathbf{x2}}$ **(K)**	$T_{\mathbf{s}}$ **(K)**	$T_{\mathbf{l}}$	$T_{\mathbf{rg}}$
0	$*$	637	742	1072	1111	
1	$*$	655	748	1070	1108	
2	$*$	676	757	1069	1098	
3	640	686	765	1070	1105	0.587
4	659	706	781	1070	1135	0.581
5	677	726	793	1069	1154	0.579
6	689	754	794	1067	1171	0.575
7	699	774		1068	1193	0.574
8	713	778		1095	1218	0.574

This behavior is unfavorable for direct casting of the materials as the melting is supposed to be narrow, and multiphase regions make the alloys superheating into a fully homogeneous liquid state more difficult. Therefore, the smaller additions of S that show to melt easily with a narrow melting peak are predestined for the casting.

The determined values of T_g^{onset} , T_{x1} , T_s and T_l can be found in Table 4.1. Furthermore, the values of the reduced glass transition temperature were calculated for the heating rate of 20 K/s, which are shown with the high temperature DSC values in Figure 4.7 b). The $(Zr50)S3$ shows the highest value of the reduced glass transition temperature of the system as it possesses a low liquidus temperature. The rising liquidus temperature beyond the 3 $at\%$ of S is responsible for that decrease in T_{rg}, the earlier mentioned glass forming ability mirrors the decay in reduced glass transition temperature.

4.2.2 Crystallization mechanism and kinetics

The initial crystallization of the system during heating from the glass is a quasicrystalline icosahedral phase, which is elaborated in the following section 5.3 in more detail. This phase makes reliable measurements of the glass transition region difficult, as the crystalline phase can form with minimal mobility in the glass structure and therefore forms even before the end of the glass transition temperature is reached.

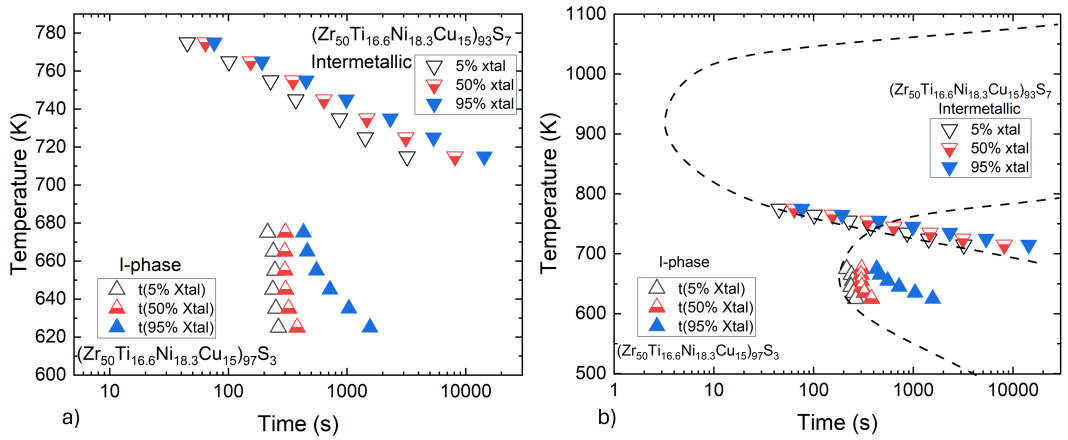

Figure 4.8: a) Isothermal recorded Time-Temperature-Transformation diagram for the significantly different crystallization behaviors of $(Zr50)S3$ and $(Zr50)S7$ alloy and b) with sketched schematic 1% crystallization noses.

This limits especially the capabilities of the DSC method for this system as the

'standard treatment' of heating an amorphous sample into the supercooled liquid and cooling it with the same rate back into the glass is not available that allows the determination of $T_g^{fictive}$ [59, 162]. So pre-treatment cannot be used for the scan measurement nor can the specific heat capacity of the glass phase be measured free from crystallization artifacts in the data.
In Figure 4.8 the isothermal crystallization times for 5 %, 50 % and 95 % are displayed for both the $(Zr50)S3$ alloy as well as the $(Zr50)S7$ alloy, the behavior is quite different as the data from the DSC-scan experiments already suggests, for the $(Zr50)S3$ there is no stable SCLR region, as the crystallization starts almost right after the glass transition has taken place and the mobility in the SCLR phase allows for the clusters to rearrange and form icosahedral quasi-crystalline phases. A similar phenomenon was reported multiple times for Zr-based BMGs, e.g., in $Zr_{65}Al_{7.5}Ni_5Cu_{17.5}Ir_5$, the formation of quasi-crystalline phases from the SCLR could be observed after only 2 min at 743 K, firmly establishing that the icosahedral phase (I-phase) is the precipitating phase later than followed later by intermetallic crystallization, like in that case by an f.c.c. Zr_2Ni phase [163].
The crystallization nose of the icosahedral phase and the intermetallic phase are sketched by extrapolation of the enveloped data in Figure 4.8 in the form of dashed lines, the icosahedral phase seems to intersect the intermetallic crystallization and hints at the thermally stable region of the I-phase. This aligns quite well with the data from the DSC scan experiments since the phase transition of I-phase into the intermetallic compound is situated at a very similar temperature of 765 K of T_{x2} for the $(Zr50)S3$ alloy. The limited stability of the I-phase was reported previously [164] and in contrast to the reported stabilization of the I-phase by oxygen [165], the sulfur appears to completely inhibit the formation of the I-phase in the higher S-additions.

The same I-phase related problem can be concluded for measurements of the low-temperature viscosity utilizing the thermo-mechanical analyzer. The alloys with lower sulfur content are not stable enough to reach the end of the glass transition and the SCLR without interfering crystallization effects that obscure the measurement data of the glass. In Figure 4.9 a) the recorded TMA scan curves for $S = 1, 3, 5, 7\ at\%$ are shown, here the transition glass into supercooled liquid and crystallization cannot be disentangled in the TMA signal as the transition between the two phases appears to be a steady process.

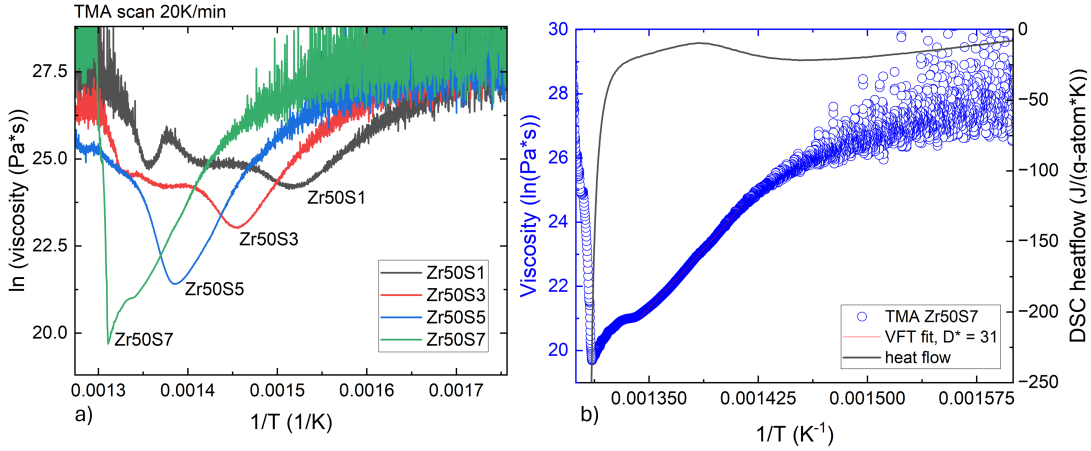

Figure 4.9: a) Non isotherm TMA scans of the $(Zr50)Sx$ alloy set, the curves of $x = 1...5$ are influenced by the crystallization that starts right away, obscuring the SCLR regime in the measurement, only for the $(Zr50)S7$ could the experiment be performed successfully thanks to the high thermal stability of this alloy b) detailed analysis of the TMA scan data from $(Zr50)S3$ that was fitted according to the VFT-model, the fragility parameter was determined to be a $D^*$of 31.2 which makes the alloy a strong BMG at low temperatures.

This is only different for the $(Zr50)S7$ alloy as it reaches the supercooled liquid without interfering crystallization, which ensues only later and has a characteristic feature in the TMA scan. This allows for the measurement of the viscosity of the SCL and the determination of a reasonable fragility parameter $D^\star$ of 31.2 for the $(Zr50)S7$ alloy. The DSC and TMA scans with heating rates of 20 K/min can be seen in Figure 4.9 b) in detail for the $(Zr50)S7$.

4.3 Impact of sulfur on viscosity and surface tension

The parabolic flight campaigns number 41 and 43 carried both the $(Zr50)$ alloy as well as the $(Zr50)S3$ into micro-gravity as part of the proposed TEMPUS experiments. This allows to measure the viscosity and surface tension by the oscillating drop method without the influence of the gravitational field of the Earth. Thanks to the two funded campaigns, the influence of sulfur could be investigated without changing of the remaining element ratios in the alloy, except for the S addition. The results are presented as a comparative plot in Figure 4.10 and highlight the significant impact of sulfur on both the liquid's fragility and surface tension, especially when being directly compared to the initial sulfur-free alloy.

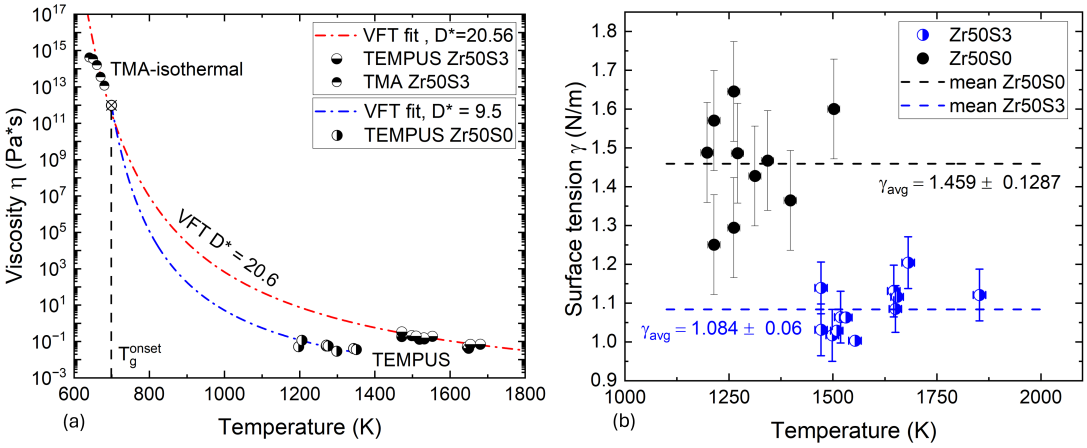

Figure 4.10: Results of the 41^{st} and 43^{rd} parabolic flight campaigns of TEMPUS with added TMA isothermal low temperature viscosity data from the TMA, highlighting the difference between the $Zr50$ and the $(Zr50)S3$ alloy in terms of the liquids behavior at severe superheating above T_l.

The initial composition of $Zr_{50}Ti_{16.6}Ni_{18.3}Cu_{15}$ showed a rather low viscosity at temperatures between 1100 K and 1600 K. Due to the limitations of the oscillating drop method, the upper limit of processable data was situated at about 1450 K, as the oscillations were disturbed by secondary oscillations that were outside of the analyzed damped harmonic mode, like superposed oscillations and rotational oscillations. On the other hand, for the $Zr_{50}S_3$ alloy, the lower end of the temperatures could not be evaluated due to the high viscosity that halted the oscillation

of the droplet before one period of the oscillation could be measured. The fragility was determined with a fit according to the VFT-model and the fragility parameter D^* was determined to be 10.6 for the $Zr50$ as opposed to 20.6 for the $(Zr50)S3$ alloy. This underlines the impact of sulfur, as the fragility parameter doubles for the alloy with sulfur. In absolute viscosity values, this means that a viscosity of 75 $mPa \cdot s$ is reached for the $Zr50$ at 1250 K, whereas the $(Zr50)S3$ needs to be heated to 1650 K to reach the same viscosity.
At a temperature of 1500 K, this results in a factor of 20 difference between the two alloys' viscosity values. A number that was previously encountered in the GFA determination, for this system the 20 fold increase in GFA appears to be directly correlated to the increase in viscosity of the high-temperature liquid, caused by the added S.

The low temperature data from the isothermal TMA experiments are also given in Figure 4.10 a) and can be included in the VFT-model fit, as for the $(Zr50)S3$ it is possible to describe the viscosity well over a range of 12 orders of magnitude. This is quite an uncommon phenomenon and will be discussed later against the state of the art, which differs from this behavior for most Zr-based BMGs. The results of the surface tension is given in Figure 4.10 b), the addition of sulfur reduces the surface tension from an initial 1.459 N/m measured for the $Zr50$ to 1.084 N/m for the $(Zr50)S3$. Both properties are pretty significant for the behavior of the alloy during casting as the filling behavior of molds is coupled directly to the both properties and the data will hopefully allow to expand the basis for casting simulations in the field of Zr-based BMGs.
These results can be directly compared to oxygen as Jonas et al. performed a similar study with AMZ4 alloy, where a high-purity alloy with low oxygen content was compared to an industrial alloy with a high oxygen content [166]. Here, the authors found that oxygen does not significantly alter the viscosity at a level of 1 $at\%$, yet it diminishes the undercooling ability of the AMZ4 [166]. This is quite contrary to the effect of S, as the sulfur strongly impacts the viscosity of the alloy system while the undercooling ability of the system remains comparable to the S-free alloy, and the heightened viscosity and lowered fragility enable good glass formation in the system. The results differ from the effect of S in the

Vit105 alloy that was compared to the Vit105S2 alloy by Bochtler in 2019 [16], here neither a significant increase in GFA nor a significant difference in viscosity or fragility could be found, as the Vit105 and Vit105S2 show 'very similar values' of viscosity at higher temperatures, both behaving fragile with a D^* of 9.9 in the high-temperature region [16]. As Bochtler discussed in his work, both alloy variants of Vit105 behave kinetically fragile in similar to the reported behavior of the Vitreloy 1, which shows a transition from fragile to strong behavior in the liquid state [16, 51]. For the $Zr50$ and $(Zr50)S3$ alloy, there is no such transition observable in the TEMPUS data, as the S-free alloy behaves fragile and the S-infused alloy behaves kinetically strong. The most prominent differences in composition to the Vit 105 alloy is that the alloy is Al-free and contains the 3-fold content of Ti, one of the two being responsible for the significant difference in alloy behavior.

The strong behavior of the S-infused alloy does not come unprecedented, in the $Ti_{60}Zr_{15}Cu_{17}S_8$ alloy Kuball reported results of a successful TEMPUS campaign that also showed high melt viscosity at high temperatures and a strong fragility [59]. A similar fragility value was reported by Ruschel et al. for the $Zr_{56}Ti_{13.3}Ni_{13.6}$ $Cu_{9.6}S_7$ alloy that also showed a high viscosity melt [60] and Wilden et al. reported a similar slow down of melt dynamics due to S for the $Ti_{75}Ni_{25-x}S_x$, where the melt is far less viscous and the fragility parameter indicates a fragile behavior despite a high S addition of 8 $at\%$ [167].
In the case of the $(Zr_{50}Ti_{16.6}Ni_{18.3}Cu_{15})_{97}S_3$ alloy, the slowdown of melt dynamics resulting from the S-addition is accompanied by a significantly different behavior of the viscosity, compared to the S-free alloy. By the addition of the S, systems like Ti-Ni are expected to increase in their efficient melt packing. According to Wilden et al., there is contrary behavior found for the Ti-Ni-S system, where the number density in the liquid decreases for S-additions larger than 5 $at\%$ and indicates covalent interactions [167]. The lower 3 $at\%$ S addition may be situated at a S-content that balances the increase in viscosity and the rise in covalent interactions well, so that bulk glass formation is possible since the intermetallic crystallization is slowed down by the sluggish melt dynamics.
In conclusion, it can be summarized that the S-infused alloy behaves strongly in the low temperature region as well as in the high temperature region due to the

S-addition. A transition of strong to fragile behavior was suppressed in the S-infused alloy, in contrast to the S-free alloy and other known systems of Zr-based BMGs [16, 51, 53]. The increase in viscosity of a factor of 20 in absolute values at 1500 K and a twice as high kinetic fragility parameter D^* can be regarded as a key contributor to the similar rise in glass forming ability that is caused by the addition of 3 $at\%$ S.

5 Structure of amorphous and crystalline phases bearing S

5.1 Structure of the liquid and glass bearing S

The structure of the amorphous phase of the $(Zr50)Sx$ alloys was investigated in detail using the high brilliance of the PETRA III's P21.2 beamline for the full range of the obtained amorphous samples ranging from the base alloy without S up to the maximum amount of 8 $at\%$ S. The sulfur impacts both the obtained total scattering function as well as the reduced pair distribution function.
The total scattering function S(Q) can be seen in Figure 5.1 under the influence of sulfur, especially the first sharp diffraction peak (FSDP) and the second sharp diffraction peak (SSDP) change due to the influence of sulfur. The impact of sulfur becomes clear even when observing just the unmodified S(Q), where the scattering of both FSDP and SSDP is gradually being reduced by the addition of sulfur to the alloy. Except for those two significant changes, the shape of the S(Q) obtained for the different alloys of the set remains largely static. The changes induced by the sulfur addition to the alloy are visualized by the properties of the fitted peaks that are presented in Figure 5.2 a) where the detailed change in the FSDP can be seen, the height of $S(Q_1)$ is being reduced gradually by the added S and the full width at half maximum (FWHM) of the peak increases, indicating that the order of the scattering structural units is being reduced in the glass.

In Figure 5.2 b) the deviation from the ideal icosahedral structural ratios of 1.69 for $Q_{2.1}/Q_1$ and 1.97 for $Q_{2.2}/Q_1$ after Sachdev [168] was calculated as a function of the added sulfur content as well as the averaged deviation from the ideal ratio for both ratios. Initially the ratio of $Q_{2.2}/Q_1$ differs over 5 % from the ideal ratio in the glassy state of the $Zr50$ alloy while the $Q_{2.2}/Q_1$ ratio differs just 1.72 % from the ideal icosahedral ratio.

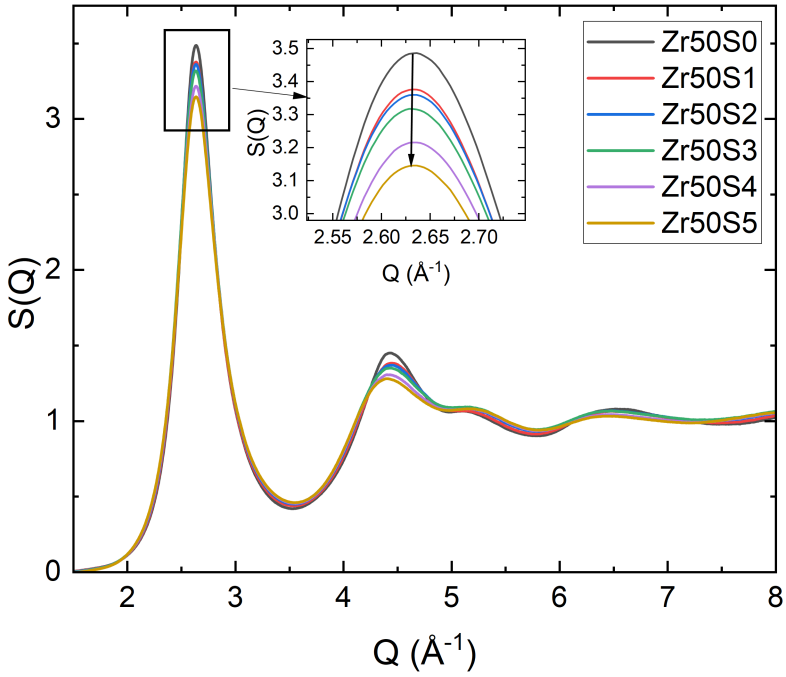

Figure 5.1: Derived total scattering structure function of $(Zr_{50}Ti_{16.6}Ni_{18.3}Cu_{15})_{100-x}S_x$ with x ranging from 0 to 5 $at\%$, the influence of sulfur on the first sharp diffraction peak is quite apparent and can be seen in the magnified inset.

While the ratio of $Q_{2.1}/Q_1$ declines slightly with incorporated sulfur in the structure and rises again for an addition beyond 3 $at\%$, the change in $Q_{2.2}/Q_1$ is more significant, but it follows a similar trend. Overall, the $(Zr50)S3$ alloy shows on average the smallest deviation from the ideal icosahedral ratio, which coincidences inversely with the maximum glass forming ability. From a structural perspective, this explains well why the glass forming ability maximum is found at 3 $at\%$ of S, as the amorphous phase is structurally the most similar to the liquid for this S-addition.

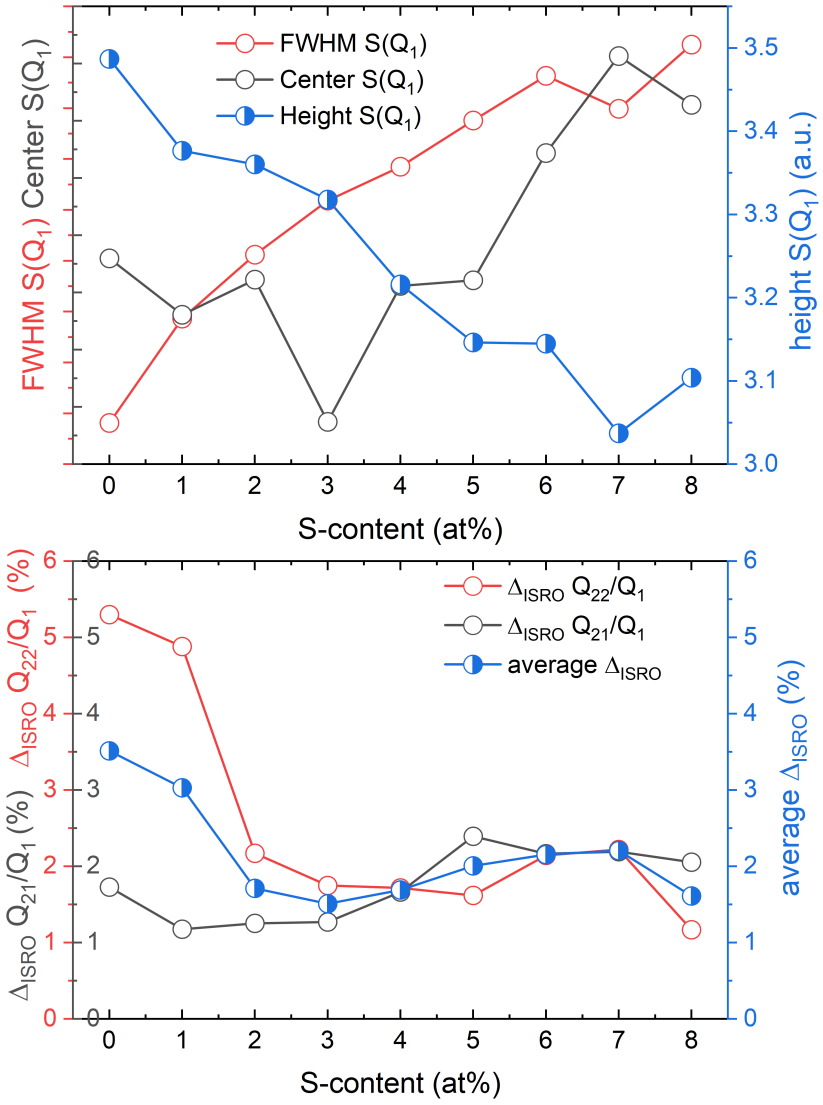

Figure 5.2: a) Derived properties from the fitting of the FSDP, showing the structural changes under the influence of sulfur, b) deviation from the ideal icosahedral ratios, and the averaged deviation of the two ratios.

5.1.1 Structure of the high temperature liquid phase

During the in-situ HE-XRD campaign at beamline P21.1, both the base alloy $Zr50$ as well as the $(Zr50)S3$ alloy were processed in the electrostatic levitation environment, successfully melted and their melt overheated multiple times to achieve the state of the homogeneous high temperature liquid phase. The structure of the liquid was investigated at a temperature of 1275 K, and the total scattering function derived from the achieved diffraction spectra can be seen in Figure 5.3.

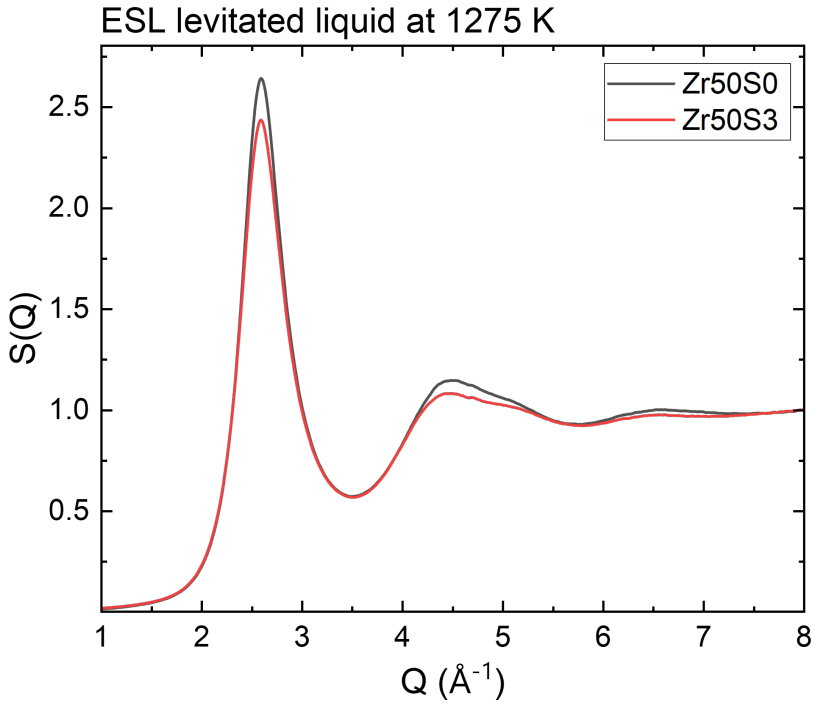

Figure 5.3: S(Q) obtained from in-situ HE-XRD experiments on P21.1, where the structure of ESL processed liquid phase of the base alloy without sulfur, as well as the 3 at % of S added alloy, were investigated, spectra were recorded at 1275 K.

The observed impact of S on the structure of the glass at room temperature can also be observed in the high temperature liquid state, the height of the FSDP is reduced by the sulfur addition as well as the position of the center that is reduced for the S-addition and the FWHM increases due to the sulfur, indicating that

the structural motifs in the liquid contributing to the scattering are diversified and the liquid becomes more disordered under the influence of S. An overview of the derived peak properties is presented in Table 5.1. The order in the high-temperature liquid is thereby also reduced under the influence of the sulfur, as the results from the structural investigation of the glass already suggested, which can be confirmed with this direct experimental evidence of the sulfur's impact on the liquid structure.

Table 5.1: Summary of the derived peak properties from the in-situ ESL processed samples at 1275 K for FWHM, center, and peak height values for $Zr50S0$ alloy and $(Zr50)S3$ alloy.

Zr50S0	**FWHM**	**Center**	**Height**
FSDP	0.355	2.597	2.642
SSDP	0.641	4.535	1.145
Zr50S3	**FWHM**	**Center**	**Height**
FSDP	0.362	2.589	2.436
SSDP	0.535	4.488	1.081

5.1.2 Structure of the as cast amorphous phase

The effect of sulfur on the structure of the amorphous phase was investigated in detail in the real room reduced pair distribution functions (PDF), where G(r) was calculated for all contents of S. In Figure 5.4 a) the PDFs in dependence of the sulfur content can be seen as well as the corresponding scattering weighting factors of the dominant scattering contributions of the atomic pairs Zr-(Zr, Ti) and Zr-(Cu, Ni) and the minor contribution of Zr-S. All remaining atomic pairs and scattering contributions were minor and deemed insignificant due to their contributions being below 5 %.
The detailed scattering behavior of the calculated basic bond pairs can be seen in the Appendix Figure 8.1. The change in the PDFs upon sulfur additions is rather drastic as the total change of $G(r_{1.2})$ is up to - 0.84 $Å^{-2}$ in absolute value and the relative change is accounted for by - 28 %.

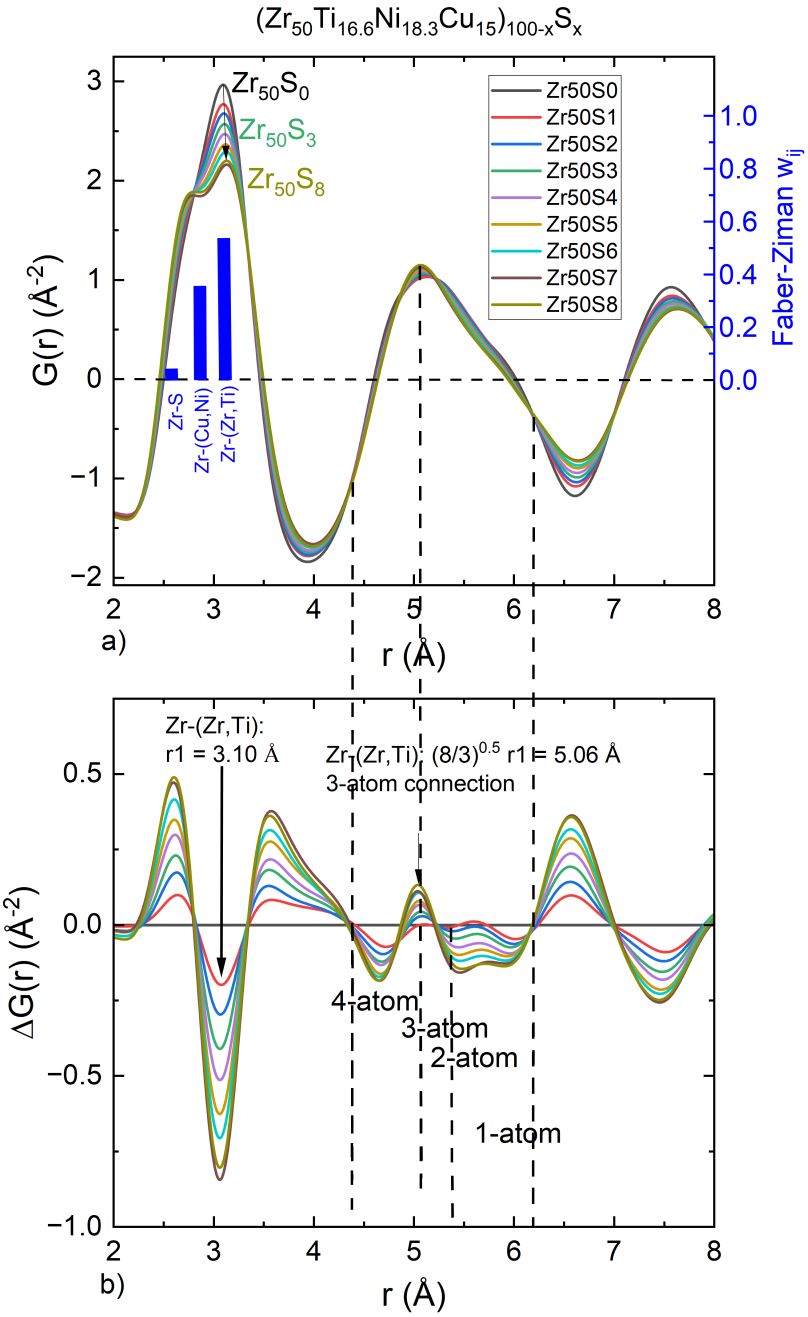

Figure 5.4: a) Results of the synchrotron HE-XRD showing the influence of sulfur on the pair distribution function of the amorphous solid's structure, as well as the weighting factors of the dominant Zr-bonds, b) relative change of the PDF as a function of the sulfur content.

The scattering contribution of $G(r_{1.2})$ situated at 3.1 Å is in this case the most dominant atomic pair of Zr-(Zr,Ti) that experiences the drastic change due to the sulfur addition. The change in the composition of the alloy due to the S-addition in itself cannot reasonably explain the impact on the amorphous structure that is about three times stronger than expected for a direct proportional change in structure related to the change in composition.
The scattering of the Zr-(Cu,Ni) bond pair contributing to $G(r_{1.2})$ at a position of 2.62 Å experiences a total increase of 0.65 $Å^{-2}$ which is a relative increase of 30.5 % at the maximum addition of 8 $at\%$ of S to the alloy. The total contribution of Zr-S increases from 0 % in $Zr50$ to a maximum of 4.5 % in $(Zr50)S8$ which is still negligible in comparison to the two dominant atomic pairs, the change in the Zr-S scattering contribution can be seen in appendix Figure 8.2 where the Faber-Ziman factors as a function of Q are displayed.

The detailed change in the PDF is given as a plot of $\Delta G(r)$ with reference to the structure of $Zr50$ alloy in Figure 5.4 b) so that the graphic displays the relative change in structure due to the added sulfur. Since the Zr-S weighting factors change is only a small contribution to the strong impact on the PDF, it can be assumed that the change in scattering intensity results mainly from the change in local atomic structure. Here, under the assumption of the Zr-(Zr,Ti) pair as the dominant part of the cluster structure, the atomic connections can be calculated according to the ratios of the connection schemes introduced in Section 3.3.6. With the Zr-(Zr,Ti) pair defining r_1, the connection schemes for the 4-atom, 3-atom, 2-atom and 1-atom connections can be calculated as drawn in Figure 5.4, the only atom connection that experiences distinct change due to the influence of S is the 3-atom connection calculated to be located at 5.06 Å which increases gradually in its scattering contribution with the addition of S to the alloy.
The analysis of the PDF as a whole was performed according to the Ornstein-Zernike analysis, where the peak maxima in G(r) are described as a function of exponential decay $f(r) = A{\cdot}exp(-r/\xi)$, where A is an exponential pre-factor and ξ is the correlation length of the structure, where a high value of ξ 'indicates a more ordered/correlated structure' [169, 170]. The result of the peak height analysis as a function of the added sulfur content can be seen in Figure 5.5, the observed

trend is clear as the increase in S leads to a continued disordering/de-correlating of the amorphous structure in the glass. This fits the general trend that is observed for the influence of sulfur in both liquid and solid structure, the two states are compared in Figure 5.6 where the similarity of the structural impact of sulfur becomes clear.

The mismatch in atomic size can be expressed by the atomic size parameter δ that is used to classify the character of the alloy between high entropy alloys with a low δ value and intermetallic or amorphous alloys with a high δ value [171]. The δ parameter for the Zr-Ti-Ni-Cu + S alloy series can be seen in Figure 5.5 b) that can be found in the supplementary file of reference [22].

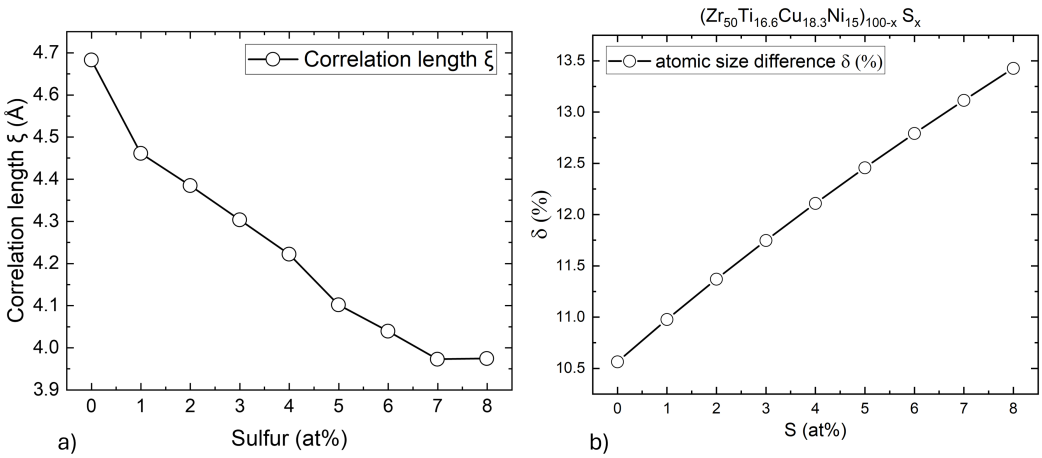

Figure 5.5: a) Results of the Ornstein-Zernike analysis that determines the correlation lengths of the amorphous structure in dependence of the sulfur content in the composition, performed on the PDFs of the $(Zr50)Sx$ alloys in the amorphous solid and b) atomic size mismatch parameter δ as a function of the S content in the alloy.

The alloy possesses a high δ parameter value without S in the alloy already, which confirms the intermetallic character of the alloy based on the assumption of a simple topological consideration, with progressing S-addition however, the value of δ increases even further with its maximum residing at 8 $at\%$ of S-addition to the alloy.

Although the progressing disorder that is being introduced into the alloy does not

continually improve the GFA of the alloy as the confusion principle would predict [22], it can explain why the correlation length of the glass is continually decreasing as the structure of the glass is getting more and more 'confused' by the increase in atomic size mismatch parameter δ.

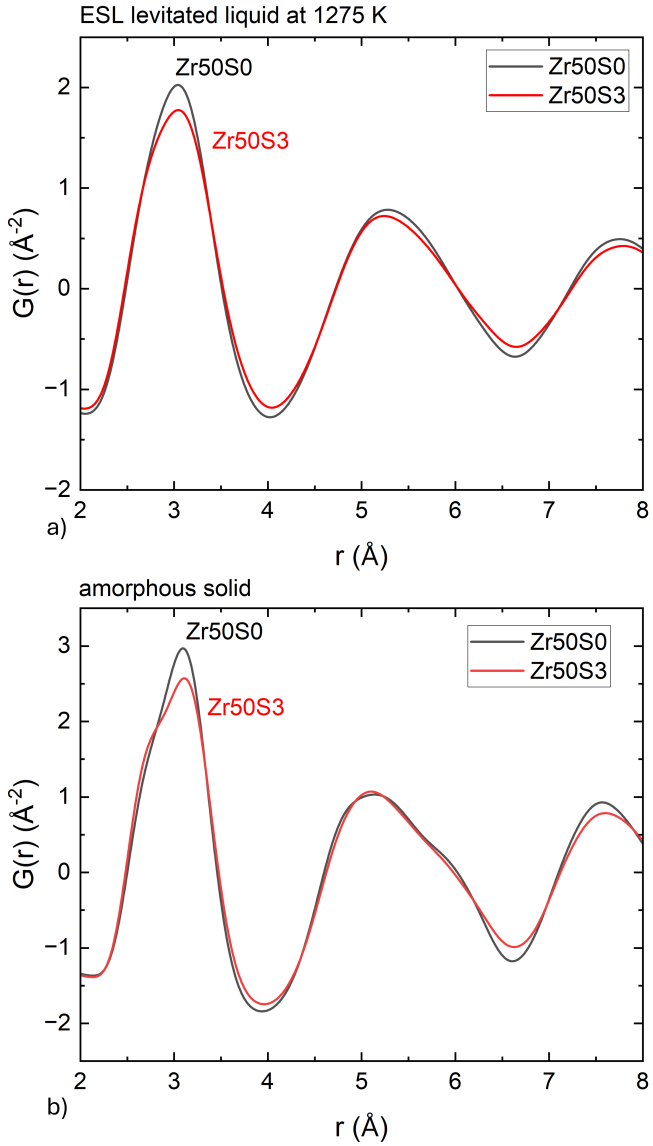

Figure 5.6: a) Results of the synchrotron HE-XRD showing the influence of sulfur on the PDF of the high-temperature liquid's structure. b) comparison of the similar impact of 3 $at\%$ of S in the amorphous solid.

For the $(Zr_{50}Ti_{16.6}Ni_{18.3}Cu_{15})_{100-x}S_x$ this means that the experimentally found GFA is decoupled from the classical confusion principle prediction of the GFA, since the confusion principle is based on a simple model of hard spheres this is not a surprising within this work and falls in line with the previously presented arguments that the chemical contribution of the S outweighs the topological considerations in its importance for the GFA of the alloy.

5.1.3 The structural impact of sulfur

While naturally the liquid structure is more disordered, the solid structure contains a certain degree of ordering in the form of clusters and inter-cluster ordering, where the effect of sulfur can be mainly attributed to the change in Zr-(Zr,Ti) and Zr-(Cu, Ni) bonds. A similar impact on the Zr-Zr bond was reported by Best et al. for O, where the Zr-Zr bond was shifted to longer bond lengths while the Zr-Cu bond remained unchanged [172]. For the S however, the Zr-(Zr,Ti) bond lengths are shifted to longer length scales while the Zr-(Cu,Ni) bonds are shifted to shorter bond lengths under the influence of S, and their contributions to the scattering change significantly in intensity. This implies that the S interacts with the Zr primarily and reduces the scattering contribution of Zr-(Zr,Ti) by increasing the number of Zr-S bonds that scatter only weakly while also influencing the remaining Zr-(Zr,Ti) bonds by diversifying and shifting the contribution to longer length scales.

The deconvoluted first significant peak in G(r) (that represents the SRO) can be seen in Figure 5.7 for the S-bearing alloy as well as the reference alloy in both liquid state and solid state. While in the amorphous solid the S reduces the scattering contribution of the main Zr-(Zr,Ti) bond and increases the scattering contribution of the Zr-(Cu,Ni) bond, it also shifts the center of gravity of Zr-(Zr,Ti) from 3.159 Å without S to 3.165 Å in the alloy bearing S. This differs from the impact of sulfur on the liquid structure, as here the Zr-(Zr,Ti) bond is shifted to to a shorter bond length of 3.068 Å from an initial value of 3.083 Å in the S free alloy, making the SRO in the cluster of (Zr-Zr,Ti) of the liquid denser packed due to the influence of sulfur.

This is accompanied by an increase of the FWHM of the Zr-(Zr,Ti) bond in both

the liquid, as well as the solid state- meaning that more structural motifs of the Zr-(Zr,Ti) bonds are likely existing as the structural order that contributes to the scattering is diversified. The center of gravity of Zr-(Cu,Ni) bond is not shifted in the liquid state and remains at 2.61 Å, while the height of the peak is decreased in the liquid state and increased in the solid state by sulfur, the FWHM however is reduced in both liquid and solid state.

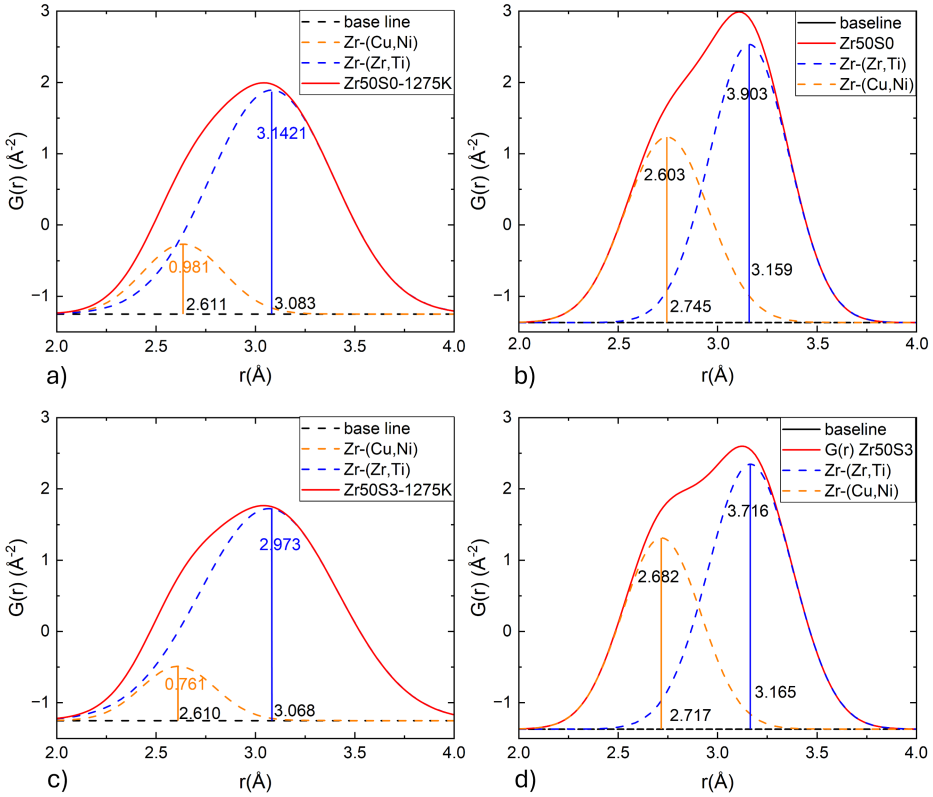

Figure 5.7: Results of the synchrotron HE-XRD showing the first significant peak in G(r) for a) the liquid of the S-free base alloy of $Zr_{50}Ti_{16.6}Ni_{18.3}Cu_{15}$ and b) solid amorphous phase structure and c) comparison of the similar G(r) in $(Zr50)S3$ liquid structure as well as the solid structure of the sulfur bearing alloy, showing the detailed impact of 3 $at\%$ of S on the first significant peak in G(r).

This is unexpected as the decrease in height and FWHM for the liquid state means both a reduction in scattering contribution of the Zr-(Cu,Ni) bond while there are

also less diverse structural motifs contributing to the scattering, implying that the Cu or Ni atoms are not necessarily bonded in clusters with Zr atoms in the liquid state and might possess a higher mobility than the Zr atoms.
An overview of all the derived values from the first significant peak in the pair distribution function can be seen in Table 5.2.

Table 5.2: Summary of the derived peak properties from the in-situ ESL processed samples at 1275 K as well as in the solid state for FWHM, center, and peak height values for $Zr50$ and $(Zr50)S3$.

Zr50S0 $G(r_{1.1})$ & $G(r_{1.2})$	**Height**	**Center Gravity**	**FWHM**
liquid state			
Zr-(Cu,Ni)	0.981	2.611	0.475
Zr-(Zr,Ti)	3.142	3.083	0.737
solid state			
Zr-(Cu,Ni)	2.603	2.745	0.494
Zr-(Zr,Ti)	3.903	3.1589	0.468
Zr50S3 $G(r_{1.1})$ & $G(r_{1.2})$	**Height**	**Center Gravity**	**FWHM**
liquid state			
Zr-(Cu,Ni)	0.761	2.610	0.439
Zr-(Zr,Ti)	2.973	3.068	0.819
solid state			
Zr-(Cu,Ni)	2.682	2.717	0.465
Zr-(Zr,Ti)	3.716	3.165	0.499

The impact of S on the structure of the amorphous phase is far greater than the changes in scattering contributions due to the change in alloy composition would predict. Therefore it is reasonable to conclude that the interaction of S in the alloys structure that enables the significant change in GFA extends beyond the model of hard spheres and the impact of the S is more of a chemical nature that forms extended covalent bonding with the metallic elements of the alloy. A similar finding was reported for the previously investigated system of Ti-Ni-S by Wilden et al., where a decrease in packing fraction in combination with reduced melt

dynamics was attributed to the chemical interactions with the transition metals, as the effect cannot be explained by the dense packing of hard spheres [167].

The changes in the total pair distribution function can be compared well with a previous study of Jiang et al., where the introduction of S into Cu-Zr-Al was described by 'as the sulfur content increases, all peaks broaden and their intensity decreases' [13]. Which was attributed by the authors to the increase in diversity of the chemical bonds [13]. For the $(Zr_{50}Ti_{16.6}Ni_{18.3}Cu_{15})_{100-x}S_x$ system this differs as the behavior of $G(r_{1.2})$ matches the observations of Jiang et al. while the $G(r_{1.1})$ behaves inversely to the effect described by a decrease in intensity accompanied with peak broadening. Therefore, it can be concluded that in the Zr-Ti-Cu-Ni-S system, the structural change of the alloy due to S-addition is more complex than in the Cu-Zr-Al system. The argument of Jiang et al. that the signal corresponding to S-bonds of the metallic elements can be regarded as more or less invisible due to the low scattering contribution and low atomic number of the S in comparison to the metallic elements also applies to the Zr-Ti-Ni-Cu-S system. This means that the out-of-proportion intensity reduction of the $G(r_{1.2})$ scattering contribution can result from Zr-S and Ti-S bonds forming, which are part of S-containing clusters in the amorphous structure that simply do not scatter much due to the aforementioned reasoning.

This is similar to the structural change described for dissolved oxygen in Zr that forms clusters of O coordinated with 6 Zr atoms that form an octahedral configuration can act as a nucleus to f.c.c big cube Zr_2Ni phase [13, 173]. Although the argument of Jiang et al. that the chemical similarity of O and S predicts a similar coordination of S in the amorphous structure is convincing, the effect of S regarding the icosahedral phase and the f.c.c big cube phase is quite different from the effects of O described in the literature as stabilizing the metastable phases and acting as preferential nucleation site [165, 173, 174]. Therefore, it appears reasonable that the configuration of S in the amorphous structure is mainly bonded to Zr and Ti, although not being coordinated in an octahedral configuration around an S atom, since this configuration would lead to the described effects observed for oxygen that is in fact being suppressed instead of stabilized by S-addition according to the results shown previously. In the more recent literature on zirconium

sulfides a study of Kang et al. can be found that investigated arc-melted TM_2Ch alloys where they classify orthorhombic-structured Zr_2S as thermally stable low dimensional electride system, meaning that anionic electrons from the $[Zr_2S]^{2+}$ are located at tetrahedral and octahedral sites of the crystal structure, resulting in a high electron mobility that can lead to exotic physical and chemical properties [175].

The concept for the structure of transition metal rich sulfides is shown in Figure 5.8, where the calculated electronic localization function shows anionic electrons at the tetrahedral and octahedral sites of the Zr_2S crystal [175]. Here the consideration of the possibility that an equivalent effect could exist in the amorphous structure comes to mind, where the anionic electrons of S could occupy both the octahedral or tetrahedral sites in the clusters of a miracle $<$ 12 10 9 $>$ glass structure - depending on the position of S atoms and vacancies in the structure.

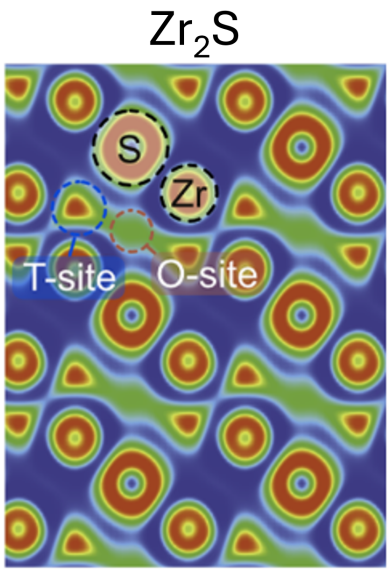

Figure 5.8: 2D layered structure and electronic structures of mono-chalcogenides, positions of Zr and S are denoted by black dashed circles. The tetrahedral-site (T) (blue dashed circles) and octahedral-site (O) (red dashed circles) represent the crystallographic positions of anionic electrons taken from [175].

This could provide a reasonable explanation for the observed increase in the liquid's

viscosity and glass forming ability by the anionic electrons of the Zr-S and Ti-S bonds acting like 'interatomic glue' in the liquid structure, causing the slow down of melt kinetics due to their interaction with the metallic atoms. As will become clear in the next Section 5.2, the local structure of Zr_2S is likely closely related to the structure of the S-infused liquid of $(Zr50)S3$ alloy.

5.2 Crystallization behavior during cooling from the liquid

The change in primary crystalline phase that was encountered in the previous section during alloy development was investigated in more detail in a series of 4 mm cast rods that were analyzed in a measurement campaign with 100 keV at the P21.1 beamline of the PETRA III at the DESY. The resulting spectra are displayed in Figure 5.9 a) as the whole set, and two spectra with their matched main phase are shown separately. The initial crystalline phase that is being encountered in the casting of the $(Zr50)S1$ can be seen in Figure 5.9 b) that matched a crystalline structure of a Zr_2Ni type phase (PDF 00-041-0898 [176]) that is also known as the metastable f.c.c. variant of the Zr_2Ni type. In equilibrium conditions the Zr_2Ni is encountered in a thermally stable tetragonal structure [177]. The Zr_2Ni f.c.c type phase is structurally very similar to the icosahedral-phase as it still contains icosahedral atomic clusters, and was reported to be the crystalline approximant of the icosahedral phase [163].

The supercooled liquid structure of a Zr-based BMG was also reported to function as a template for icosahedral phase nucleation, confirming Frank's hypothesis of the icosahedral structural order in the liquid state that explains the instantaneous nucleation for this phase type well [178, 179]. This leads to the understanding of why this crystallization sequence is not favorable for the GFA of the alloy, as the I-phase can easily nucleate from the undercooled liquid, albeit not being able to grow quickly, which then can transform into the Zr_2Ni f.c.c. type crystalline phase by rearranging the respective Zr- and Ni-clusters inside the icosahedral clusters into octahedrons for the Zr and tetrahedrons for the Ni.

The structure is displayed in a schematic graphic in Figure 5.10, where the connection between the Ni- and Zr-cluster and the icosahedral ordering becomes clear. Both transitions mentioned lack a significant structural barrier for nucleation, hence nucleation is being easier and thereby faster like crystallization via heterogeneous nucleation [163]. Therefore, the suppression of this crystallization pathway is important to achieve bulk glass formation, similar to reports of the importance to suppress the I-phase in Ti-based glassy alloys of Ti-Zr-Ni-Cu-Be [180].

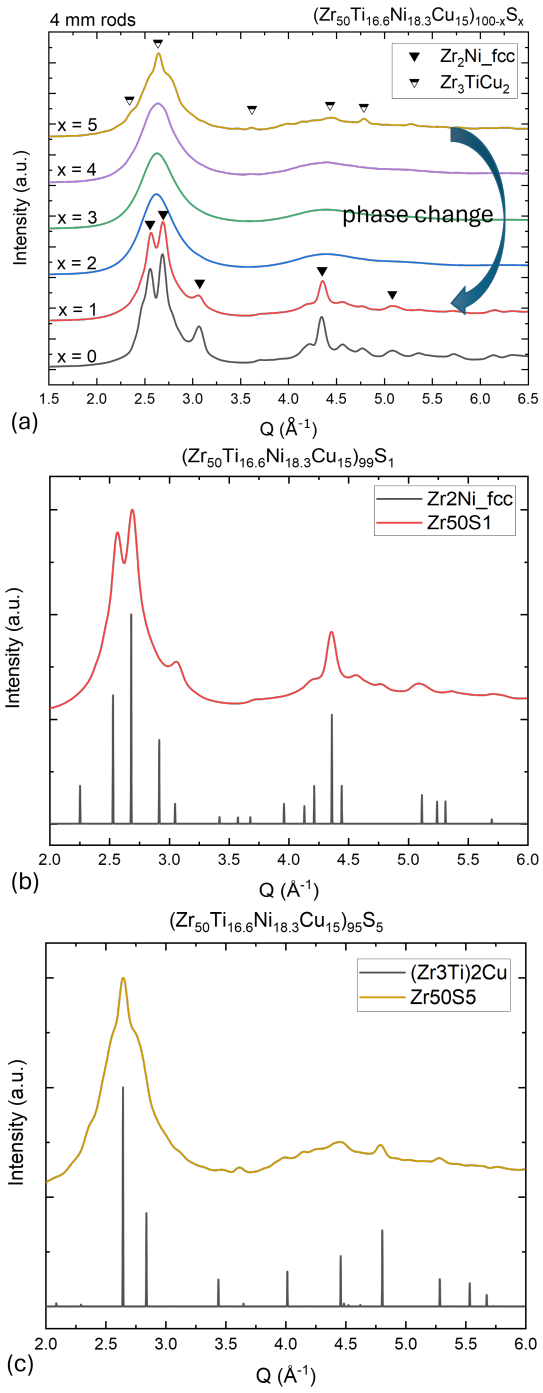

Figure 5.9: a) Synchrotron diffraction spectra of a series of 4 mm rods that were investigated regarding their structure, showing an amorphous structure signal for a content of sulfur from 2 $at\%$ to 3 $at\%$, b) detailed spectrum of the lower sulfur containing $(Zr50)S1$ and c) the detailed spectrum of the high S containing $(Zr50)S5$, redistributed from [22].

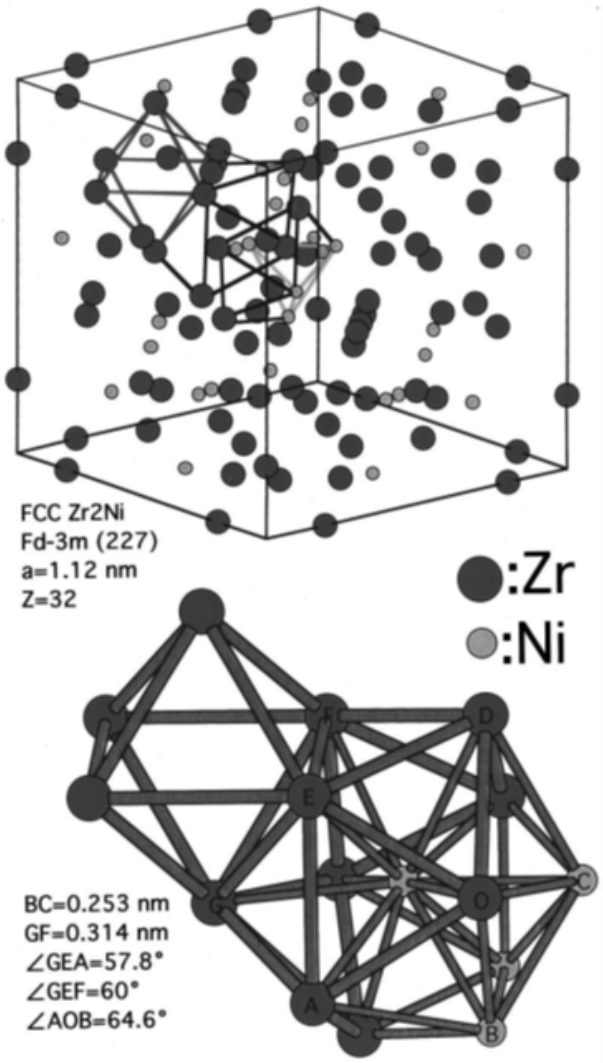

Figure 5.10: Schematic representation of the unit cell for the Zr_2Ni f.c.c. modification with the cluster arrangement of Ni and Zr atoms in the Ni tetrahedron, Zr octahedron, and comprised icosahedron in the large unit cell, taken from [163].

In Figure 5.9 c) the HE-XRD spectrum of $(Zr50)S5$ is displayed that shows a partially crystalline structure with reference data of the identified intermetallic compound type $Zr_3Ti(Cu, Ni)$ (PDF 01-079-3665 [176]), this the stable configuration of the intermetallic compound, therefore the sulfur addition retards the formation of the metastable Zr_2Ni -type that interferes with the glass formation and shifts the intermetallic crystallization to the tetragonal phase. This explains

the rise in GFA well, since the tetragonal phase cannot form polymorphously from the liquid state when sulfur is present in the liquid, thereby delaying the nucleation of this phase significantly and enabling the melt to bypass the crystalline nose at lower cooling rates.
To investigate the microstructure of the different sulfur additions, the sulfur contents of 1 $at\%$, 3 $at\%$ and 5 $at\%$ were compared in the 6 mm casting series. Here the cross-sections of the rods were investigated with the scanning electron microscope and the results of the rods' centers (where the cooling rate is minimal) are shown in Figure 5.11 where in a) the $(Zr50)S1$ in b) the $(Zr50)S3$ and in c) the $(Zr50)S5$. The microstructures differ quite significantly as can be seen directly even at lower magnifications, the small addition of sulfur results in cast microstructure that is dominated by large globular crystals that show less intensity in the BSE contrast of the image and columnar crystals with in the outer zone of those globular crystals with a higher intensity that are likely Zr enriched.
For the $(Zr50)S3$ there is a largely amorphous microstructure to be found with little crystalline inclusion that appear to be enriched in sulfur due to the lower contrast compared to the matrix, although parts of the needle like precipitates has a higher contrast than the matrix in the outer parts of the precipitate, hinting at a multiphase crystalline inclusion in the liquid before amorphous solidification.
For the S-rich $(Zr50)S5$, the resulting microstructure is significantly smaller in overall crystal grain size compared to the low S-containing $(Zr50)S1$. Since there is a lot less BSE contrast between the phases, the microstructure appears to be chemically more homogeneous and, in terms of grain size, significantly finer due to the higher sulfur infusion in those castings. The infusion of the alloy with increasing amounts of sulfur leads to a chemical stabilization of the liquid state that results in a much finer microstructure and, in the case of the $(Zr50)S3$, even a mostly amorphous microstructure can be achieved in a 6 mm casting size. Beyond the 3 $at\%$ addition, however, the degree of crystallinity in the casting increases again rapidly as the sulfide phases and intermetallic phases begin to rival the glass formation during the cooling.

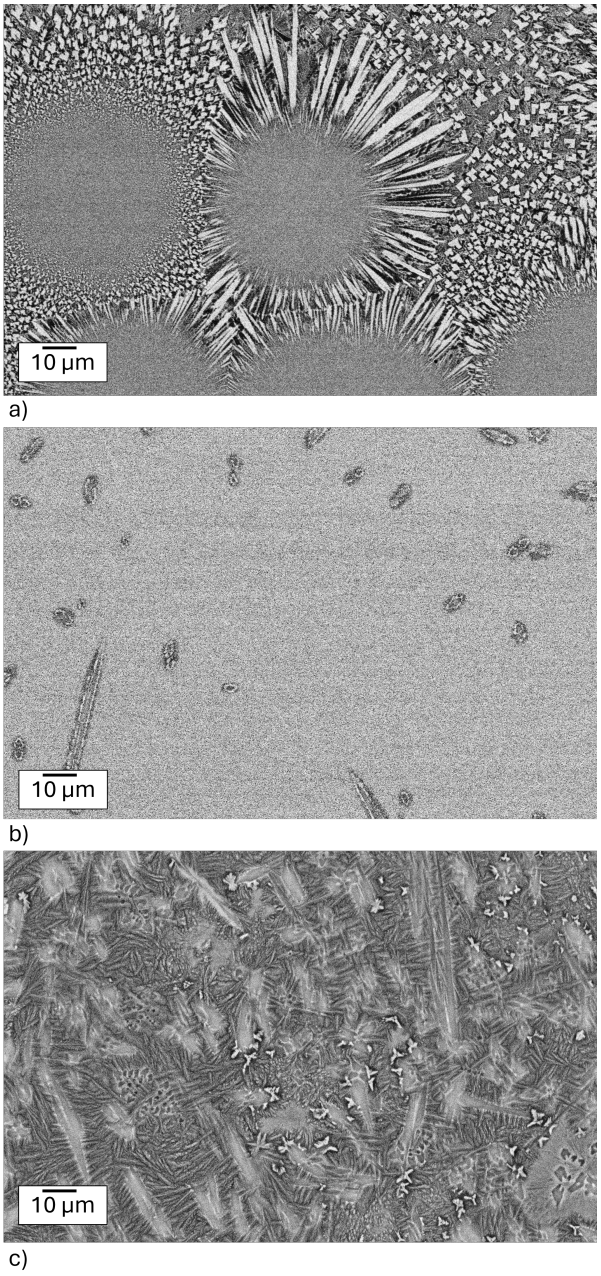

Figure 5.11: a) SEM-BSE images of the microstucture found in a suction cast rod containing 1 $at\%$ of S that shows large spherical crystals with a corona of Zr enriched crystals, b) microstructure of the $(Zr50)S3$ alloy that consists mainly of amorphous matrix, with singular sulfur rich precipitates scattered throughout the volume, c) microstructure of a 6 mm rod containing 5 $at\%$ of S, showing a fine and diverse microstructure.

In the Figure 5.20 the EDS measurements for the 6 mm rods microstructure can be seen where the described trends in chemistry have been verified, however the results are to be understood as general trends since the spatial resolution of the EDS method is not able to resolve the difference in composition between such small crystalline phases with adequate accuracy and the probed volume contains information from multiple phases in this case.

5.2.1 Containerless levitation melting and slow cooling conditions

For the analysis of the primary phases, a more sophisticated approach was the in-situ solidification measurement that could be performed in cooperation with the German Aerospace Center (DLR), utilizing an electrostatic levitation environment that was brought to the P21.1 beamline at PETRA III. Thanks to the containerless melting of the sample in a high vacuum environment, the solidification at a rate of approximately 12.5 K/s was recorded with a temporal resolution of 1 s. The experiments were performed on the base alloy without sulfur and the $(Zr50)S3$ alloy to directly compare the impact of sulfur on the solidification behavior. In Figure 5.12 a), the HE-XRD spectra of the $Zr50$ alloy are depicted as well as the corresponding signal of the pyrometer where the three structural states that were encountered are assigned to their respective temperatures and displayed with the characteristic temperatures of the alloy. For the $Zr50$ alloy a classical behavior of a weak glass former can be observed during the processing of the alloy in the ESL: the alloy is sufficiently overheated and supercools below the liquidus temperature T_l keeping an amorphous structure until just above the solidus temperature T_s where the recalescence starts and the temperature rises again due to the heat released from the crystallization, in total the alloy behaves according to 'textbook' for a weak metallic glass former.
In Figure 5.12 b) the same processing is depicted for the $(Zr50)S3$ alloy where a significant difference in behavior can be seen, the liquid does not supercool below T_l even at a temperature significantly above the liquidus temperature a minor crystalline presence with numerous weakly scattering peaks appears in the HE-XRD spectrum that is labeled 'S-phase', the main crystallization that also causes

a significant recalescence that can be detected in the pyrometer data starts slightly below the solidus temperature T_s.
The strong secondary crystallization gives a diffraction spectrum that resembles a mixture of intermetallic phases that were encountered in the cast rods that exceeded the critical casting thickness of the alloy. The $(Zr50)S3$ alloy appears to possess a slightly larger undercooling regarding the strong crystallization that causes a significant recalescence, however, the undercooling is quite small for the sulfur-infused alloys, albeit their ability to form amorphous castings with significantly larger thickness compared to the alloy without sulfur.
For improved visibility, the data is displayed as a two-dimensional 'heatmap' in Figure 5.13 a) for the $Zr50$ and in b) for the $(Zr50)S3$ alloy. Although the formation of the precipitate can be seen by a slight change of slope in the pyrometer data the formation is barely recognizable in the structural data in contrast to the main crystallization that is clearly detectable. The data also shows that the growth speed of the characteristic crystalline intensity distribution is significantly slower in the S-infused alloy. While it takes the $Zr50$ about 2 s to develop its maximum crystalline intensity profile, the $(Zr50)S3$ alloy takes about 8 s until it displays maximum intensity of the crystalline profile. This fits very well with the viscosity data from the TEMPUS campaign as the viscotiy of the liquid is about 20 times more viscous compared to the S-free alloy.

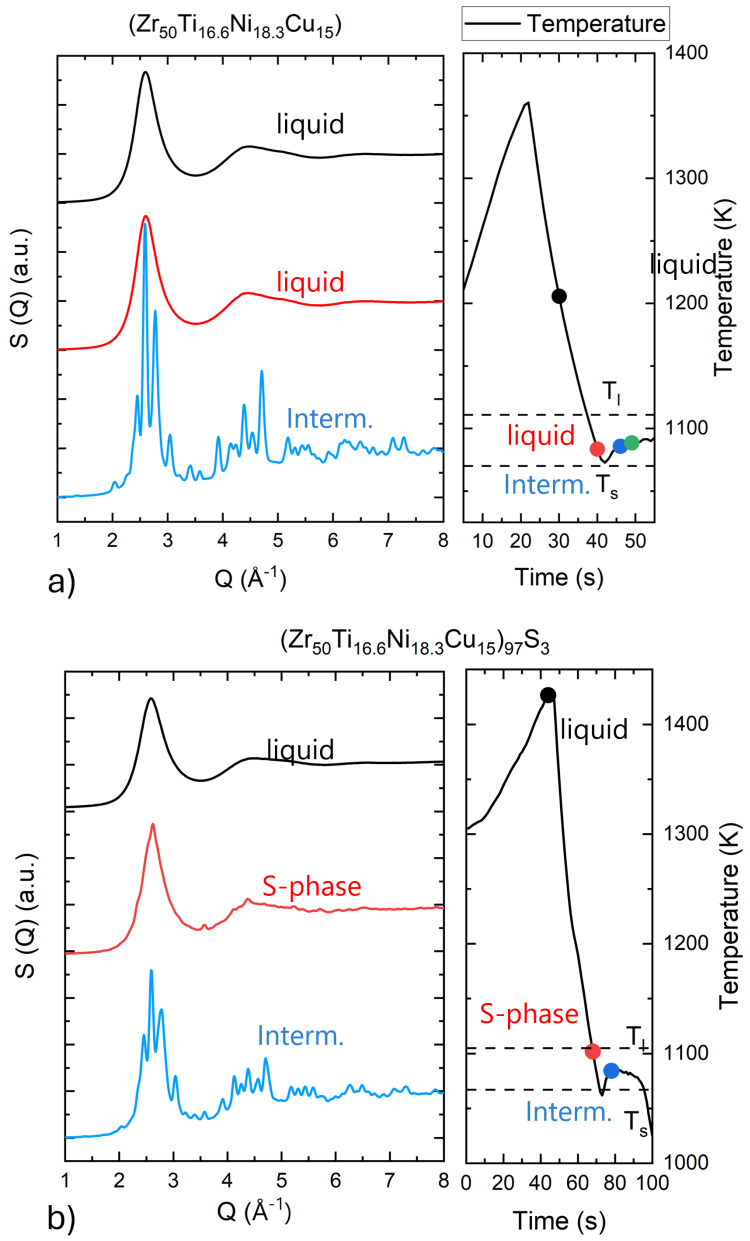

Figure 5.12: Series of total scattering functions from the cooling of an electrostatically levitated and molten sample of a) $Zr50$ showing undercooling and intermetallic crystallization and b) $(Zr50)S3$ alloy that was processed in the ESL showing two different crystalline phases and a lot smaller undercooling than the probed GFA would suggest for the system.

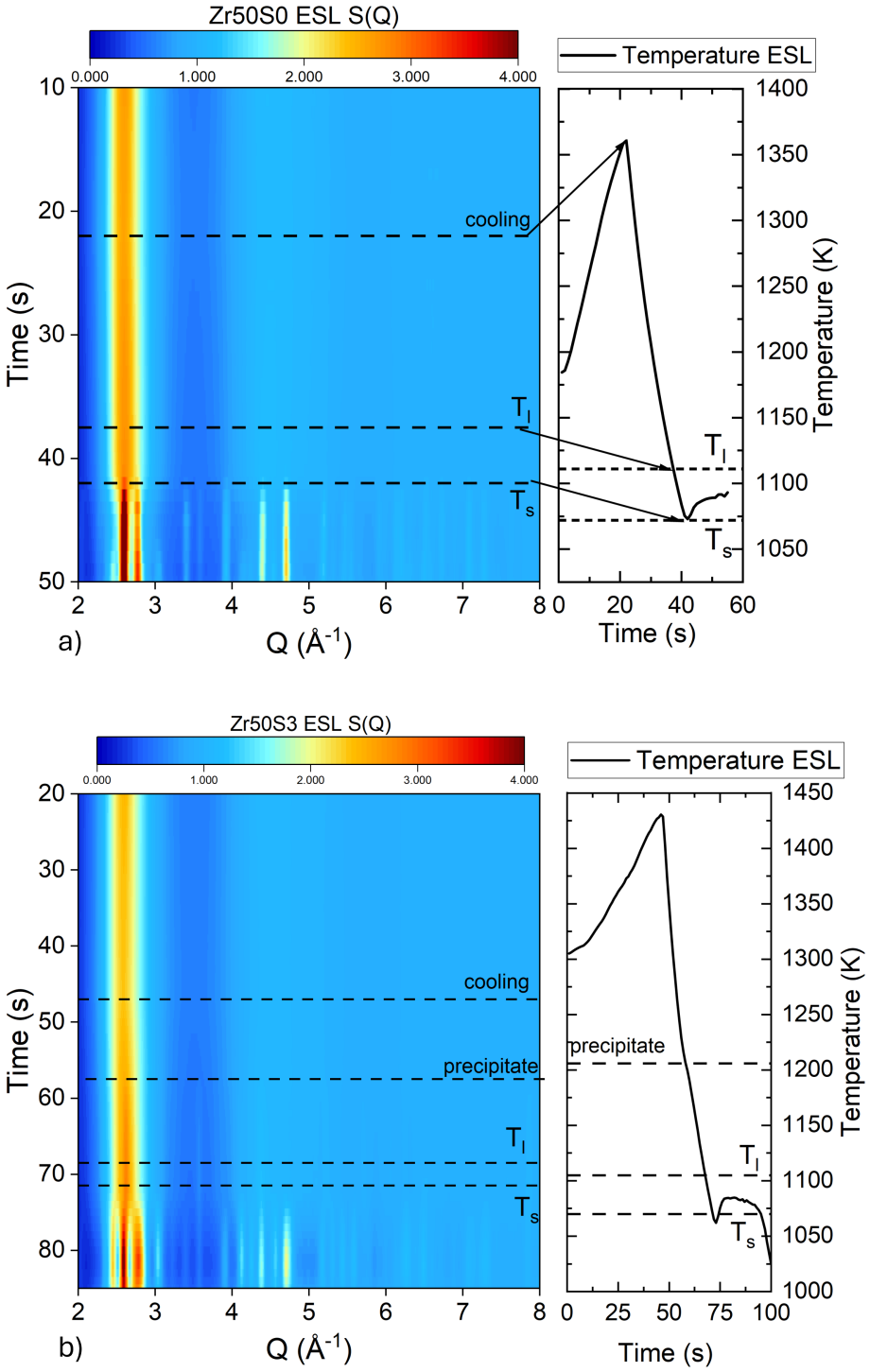

Figure 5.13: 2D graphic displaying the in-situ recorded total scattering structure function of the samples during ESL processing as a function of time, accompanied by the sample temperature recorded by a pyrometer for a) the initial $Zr50$ alloy and in b) the S bearing $(Zr50)S3$.

The singular spectrum of the alloy during cooling from the liquid at 1133 K just above T_l is given in Figure 5.14. It shows the signal of a structure that resembles a nano-crystalline cubic Zr_3Ti within a mixture of more complex phases that scatter with a low intensity.

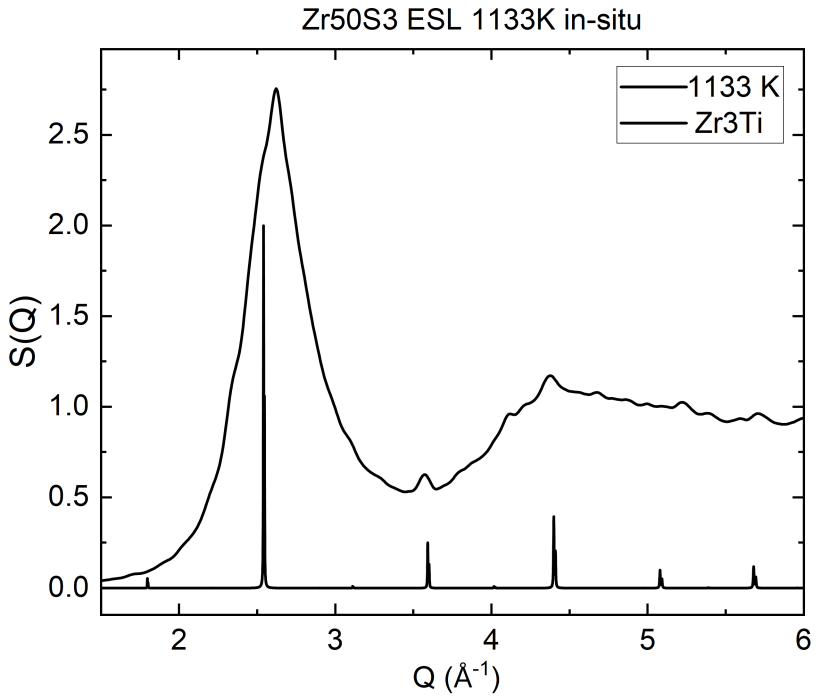

Figure 5.14: Detailed plot of the precipitate's structural signature that was recorded during cooling in the ESL-WAXS setup at PETRA III which shows a nano-crystalline spectrum of which the closest match was a Zr_3Ti cubic phase resulting from the stochiometric mixture of the two basi Zr and Ti phases according to Vegard's law for mixed crystals.

The solidified samples were then investigated by utilizing electron microscopy methods. In Figure 5.15 a) the alloy without sulfur can be seen, and in c) the variant infused with sulfur is displayed. In Figure 5.15 b) and d), the magnified images of the microstructure are displayed, which are presented with EDS results of certain selected phases.

The difference between the two microstructures is quite striking and even greater than the difference seen before in the comparison of the cast microstructures comparing $(Zr50)S1$ and $(Zr50)S5$. In the case of the sulfur-free alloy, the microstructure is dominated by large columnar crystals that easily reach up to 1 mm in size, indicating a high growth rate of the crystalline phase.

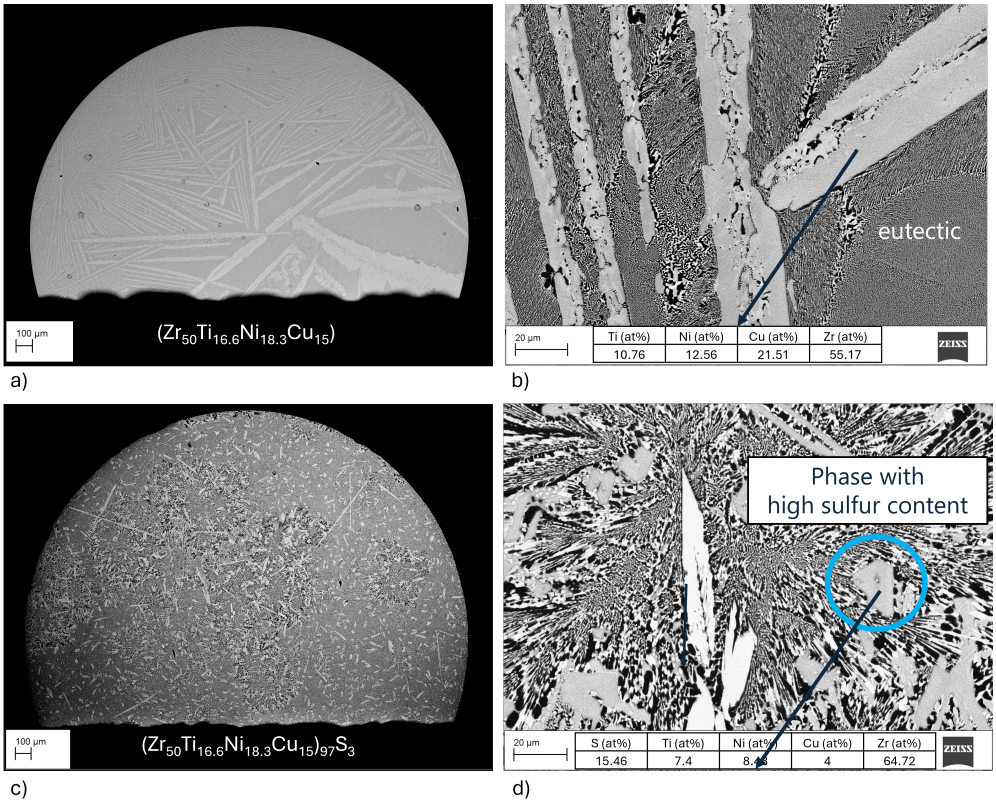

Figure 5.15: SEM BSE images of the in-situ ESL samples after solidification as recorded at the synchrotron a) for the $Zr50$ alloy and c) for the $(Zr50)S3$ alloy, where the difference in micro-structure can be seen right away. Magnified images with EDS analysis are given in b) and d), respectively.

In contrast, a finer, far less orientated and chaotic microstructure is encountered in the S-containing alloy. The EDS results of $Zr50$ alloy specimen show that while the large columnar crystals are slightly enriched in Zr they do not deviate much from the composition of the alloy, which is coherent with the assumption of their rapid growth based on the morphology of the crystals, once the nucleation barrier

has been overcome these crystalline phases of A_2B formalism can form almost polymorphic from the composition that is close to the $Zr50$ liquid.
Upon closer inspection and comparison of the microstructure a key difference can be seen in the amount of encountered phases, for the alloy without sulfur there is one significant columnar phases and in between a very fine eutectic microstructure as can be seen in Figure 5.15 b) whereas the sulfur containing alloy is comprised of at least two more phases. One being highlighted in Figure 5.15 d) that contains a high amount of S and Zr while being depleted in Ti, Ni, and Cu. The amount of S is 5 times higher than the original alloy composition, and the Zr content is also increased by about 15 $at\%$. This indicates that the phase is comprised mainly of Zr-S, however, the phase itself appears not to be pure, as the core in the middle of the sulfide phase differs in Z-contrast. The remaining microstructure of the $(Zr50)S3$ is comprised of eutectic phases and Zr-rich phases located in the center of the image.
The samples were then further prepared for advanced microscopy techniques by ion polishing to remove all mechanical stresses and deformations from the microstructure, where in Figure 5.16 a) the microstructure after ion polishing for the $(Zr50)S3$ ESL sample is shown. It is notable that some of the precipitates now appear to be hollow structures as the material of the core phase is being removed at a faster material removal rate than the surrounding Zr-S phase.
The distribution of elements is displayed in the EDS-maps in Figure 5.16 b). Here, the distribution can be seen easily when comparing the four subfigures, showing that there is an enrichment of Zr and S in the sulfide phases, while the phase is Cu and Ti-depleted. The EDS map also shows that while Cu is distributed quite evenly throughout the sample, this is not the case for Ti and Zr, as there are Ti-enriched and Zr-enriched phases.

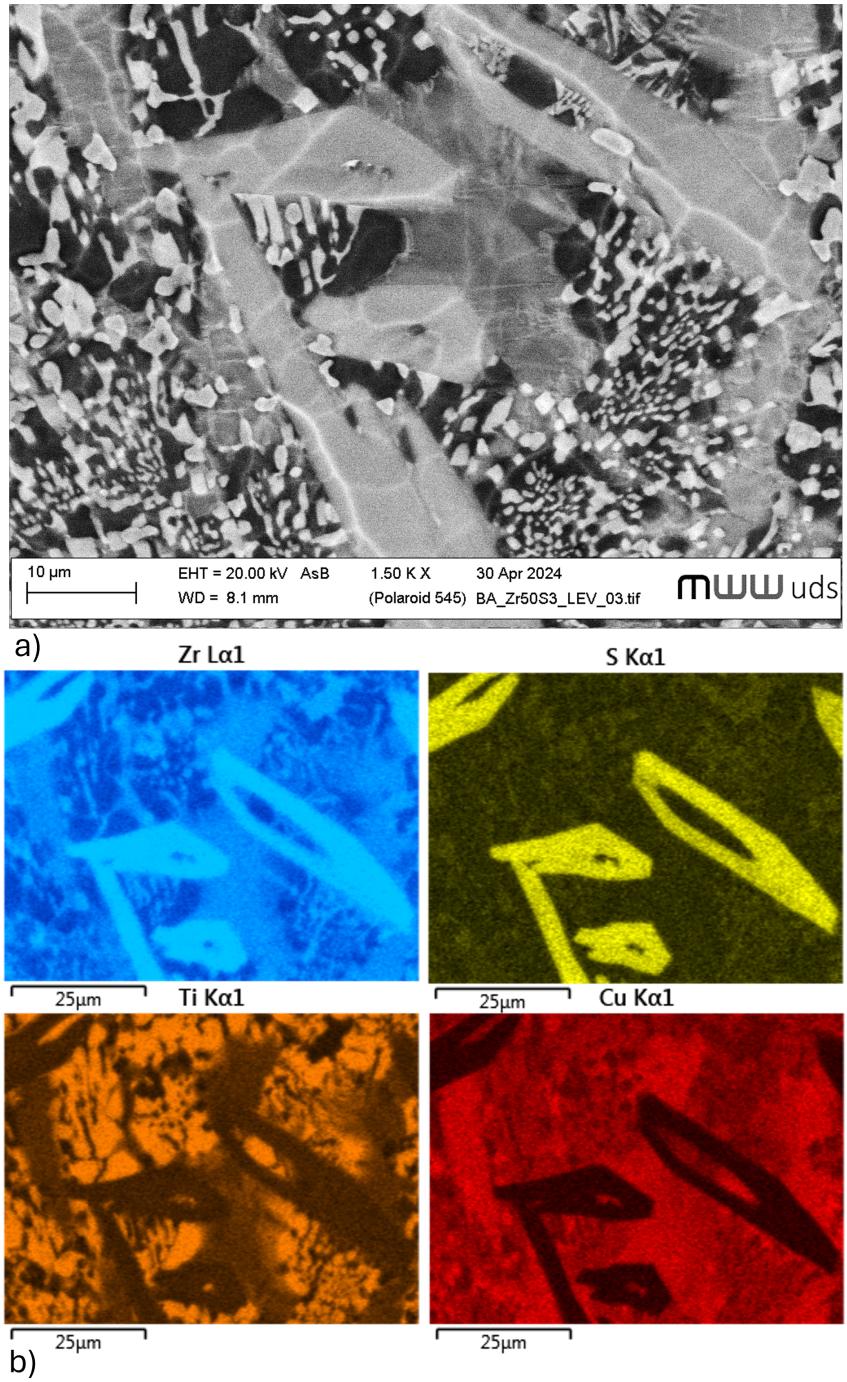

Figure 5.16: a) SEM-BSE image of the in-situ ESL samples after ion polishing of the $Zr_{50}S_3$, focusing on the sulfide phase, b) EDS-maps showing the distribution of Zr, Ti, Cu, and S in the microstructure, highlighting the Zr-S phases as well as Ti-dominated phases.

The FIB preparation was performed on a crystalline sulfide specimen that was oriented with its cross-sectional area parallel to the plane of the metallographic cut. The location of the in-situ lift-out preparation and the resulting TEM lamellae can be seen in Figure 5.17 where the respective phases are shown and the regions of interest are labeled.

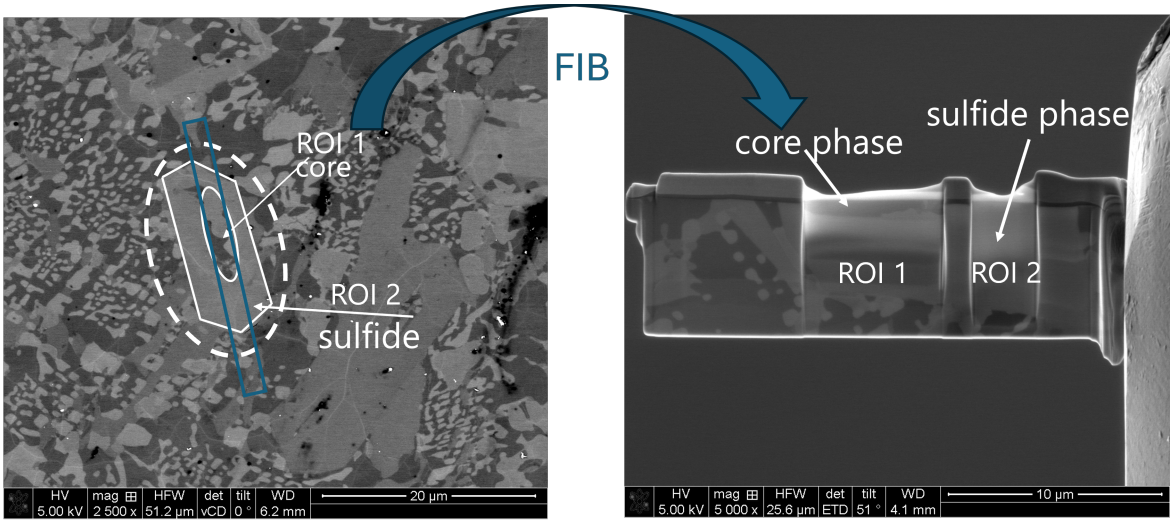

Figure 5.17: a) SEM-BSE image of the chosen sulfide particle with the performed FIB cut outlined in a blue solid line, and b) prepared FIB lamella with two regions of interest, one being the core of the particle and the other being the sulfide phase.

The TEM was used to investigate the structure and composition of both the core phase and the sulfide phase, the results can be seen in Figure 5.18 where the selected area electron diffraction images (SAED) are presented, as well as the TEM-EDS results of the two phases in the form of tables under the corresponding SAED images. The results show no S being present in the core phases and a strong enrichment of Cu and Ni, in the core phase shifting the ratio of (Zr,Ti): (Ni,Cu) from 2:1 to about 5:4. The sulfide phase is highly enriched in Zr and S, the ratio of Zr and S is 11:3 in the sulfide phase compared to a Zr:S ratio of 16:1 in the amorphous phase, whereas the other three elements play no significant role in the sulfide phase.

The initial core phase was assessed with CrystBox software [181] to extract the

d-spacings and their ratios, which are listed in Table 5.3 for the dominant vectors. The data was fitted for different crystallographic phases that were possible according to the phase diagrams of the system, with the best match being the hexagonal Zr reference structure of the materials project database material mp-131 [182].

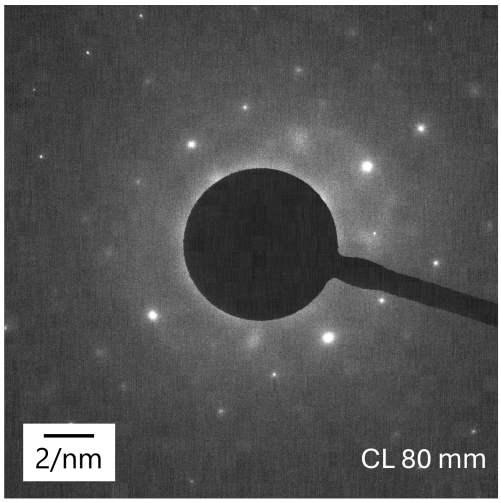

a)

element	Zr	Ti	Ni	Cu	S
at%	31.7	24.5	20.4	23.4	0

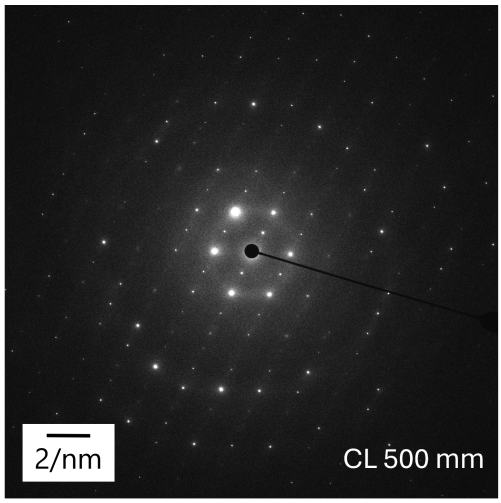

b)

element	Zr	Ti	Ni	Cu	S
at%	55.7	5.7	7.5	15.9	15.1

Figure 5.18: a) Selected area electron diffraction (SAED) image of the ROI 1 with TEM-EDS quantified composition, b) SAED image of the ROI 2, the sulfide phase, with TEM-EDS quantified composition, showing a rather complicated diffraction pattern with intensity variation of the obtained reflexes.

The zone axis was identified as $[0\ -1\ 0]$ with vector A being attributed to the (2 0 0). The lattice parameters were calculated as: $a = 3.283$ Å and $c = 5.156$ Å with a c/a ratio of 1.571 for the core phase. The literature values for a and c are 3.2393 Å and 5.1722 Å respectively meaning the assigned structure deviates 1.4 % from the value of a and - 0.3 % for the value of c.

For the Zr-S phase, the identification of the structure was not as easily available, as no reference structure could be matched with an adequate result. The d-spacings and relative ratios of the d-spacings were extracted and can be seen in the Table 5.4. The sulfides were investigated with EBSD, and the solver matched a reference structure of Zr_9S_2 and Zr_2S, which had the highest agreement with the recorded

Kikuchi pattern. The overall scoring of the obtained solutions was quite poor, however, so that the results could not be interpreted to be more than a hint in the right direction, as the following detailed investigation of the phases revealed.

Table 5.3: Derived d-spacings and d-spacing ratios for the core phase.

d-spacing

	[nm]	**[1/nm]**
A	0.1421	7.0353
B	0.1249	8.0073
C	0.2578	3.8789
D	0.1241	8.0602

d-spacing ratios

	A	B	C	D
A	1	1.1382	0.5513	1.1457
B	0.8786	1	0.4844	1.0066
C	1.8138	2.0643	1	2.0780
D	0.8729	0.9934	0.4812	1

Further investigation utilizing TEM to record the SAED pattern showed that the solution is insufficient, however. The d-spacing values extracted from the SAED pattern gave consistent lattice solutions for Zr_2S, yet the intensity of the spots does not match well with the reported structure as kinematically forbidden reflexes appear in the image, which hints at a breakdown of symmetry into a lower ordered space group or the superposition of a different lattice structure in the investigated sample volume that is similar to the reference structure but lower in symmetry of the space group. The problem can be seen in detail in Figure 5.19 where the formally assigned lattice vectors and the pseudo-indexation of the pattern is shown, here especially the reflexes of the families (0 3 0), (2 2 0) and (2 -1 0) deviate strongly in their intensity and spot size from the rest of the Zr_2S lattice.

5.2.2 Microstructure near the critical cooling conditions

To fully investigate the structure of the Zr-S phase in detail, the slowly cooled ESL sample was found to be inappropriate, and the TEM investigation was additionally performed on the as-cast 6 mm rod sample that contains the early stages of the precipitate formation due to the cooling rate being about 4 times higher than in the ESL. Here, the preparation of the lamella was more challenging due to the size of the crystalline phase being much smaller due to the higher cooling rate, and the number of crystallites oriented perpendicular to the metallographic cut plane being lower plus the residual stresses existing in the cast material.

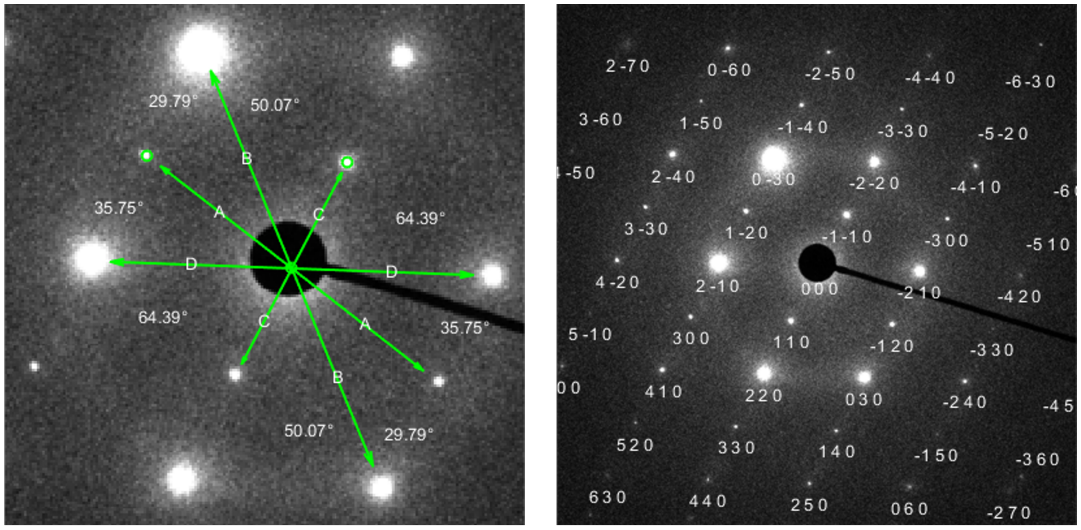

a) b)

Figure 5.19: a) SAED image from the sulfide phase with a close up of the diffraction spots displaying the assigned lattice vectors A to D and relative angles between the vectors b) pseudo-indexation of the Zr_2S pattern displayed along [0 0 1] with the assigned underlying Zr_2S lattice that refers to the small diffraction spots like (1 1 0) and (3 0 0) that is superposed with the big and diffuse spots that do not match the Zr_2S structure like (0 3 0) and (2 -1 0).

Table 5.4: Derived d-spacings and d-spacing ratios for the sulfide phase.

d-spacing

	(nm)	**(1/nm)**
A	0.6302	1.5686
B	0.4909	2.0371
C	0.97259	1.0282
D	0.5774	1.732

d-spacing ratios

	A	B	C	D
A	1	1.2838	0.648	1.0916
B	0.77891	1	0.50473	0.85024
C	1.5432	1.9813 1	1	1.6845
D	0.91611	1.1761	0.59363	1

The initial stage of the precipitate crystallization was therefore investigated in more detail in a 6 mm rod sample that borders the critical casting thickness of the $(Zr50)S3$ alloy. The SEM-BSE image focusing on one of the observable crystalline particles that are embedded in the amorphous matrix phase can be seen in Figure 5.20, where additionally an EDS-linescan is performed along the center

of a larger, 'needle' like crystal that measures about 12 μm in length and 2.5 μm in diameter. The EDS shows that the particle is enriched in Zr and S, while the other elements appear to be depleted, therefore referred to as 'sulfide' in the following description. However, the EDS can only be understood as a trend since the volume excited by the electron beam contains scattering contributions from the underlying matrix phase as well as from the outer part of the sulfide that appears to have a different composition due to the differing BSE-contrast.

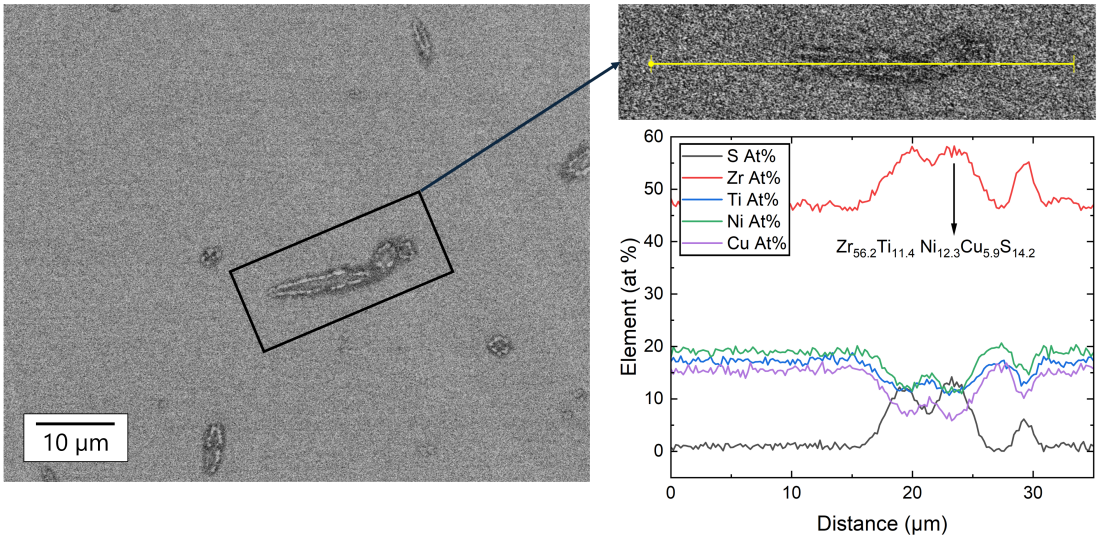

Figure 5.20: SEM-BSE image of a small initial stage precipitate found in a 6 mm rod specimen near the critical cooling rate that was analyzed by a SEM-EDS linescan shown on the right hand side, the particle is enriched in Zr and S while the other elements are depleted in the particle the particle gives an approximate composition of $Zr_{56.2}Ti_{11.4}Ni_{12.3}Cu_{5.9}S_{14.2}$.

From a similar particle to the one analyzed in Figure 5.20 a TEM lamella was prepared from the 6 mm rod of $(Zr50)S3$ by FIB lift out procedure and the sample was attached to a Mo TEM-grid to allow a precise determination of the Cu content in the sample. The sample was further thinned with the help of an ion mill, and the overview picture recorded in STEM mode can be seen in Figure 5.21 where the full complexity of the needle-like crystal becomes visible in 25000 times magnification. The particle is comprised of at least three distinct crystalline

phases that can be distinguished by crystal morphology alone. The corresponding SAED diffraction images on the right-hand side of Figure 5.21 show that the matrix phase's structure is amorphous even close to the crystalline particle. The sulfide in the center of the crystalline particle gives a well-defined diffraction spot pattern, the sample was successfully tilted into two different zone axis positions, which allowed a consistent identification of the sulfide crystal. The same is true for the secondary phase's SAED diffraction image, which is not displayed and was also identified.

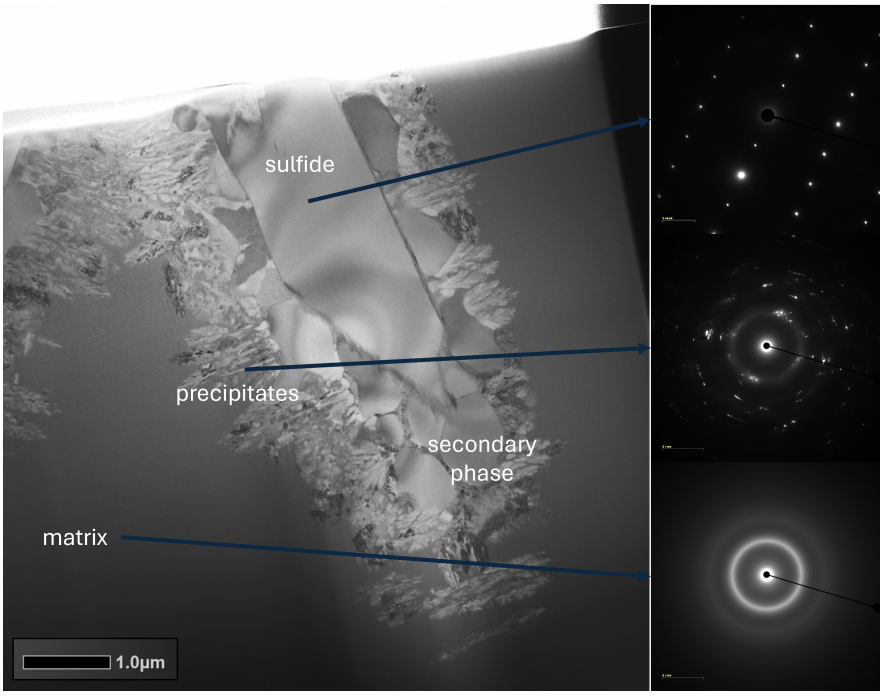

Figure 5.21: STEM bright field image of the local structure of a sulfide precipitate with a magnification of 25000 times. Four different phases can be determined by crystal morphology alone, and with the SAED images on the right-hand side, the structures can be clearly distinguished by their diffraction pattern.

In Figure 5.22 and Figure 5.23, the detailed SAED pattern with its respective indexation is shown for the orthorhombic Zr_2S and the monoclinic $Zr-Cu$ type phase. The measured d-spacing values and their ratios can be found in Table 5.5 and Table 5.6.

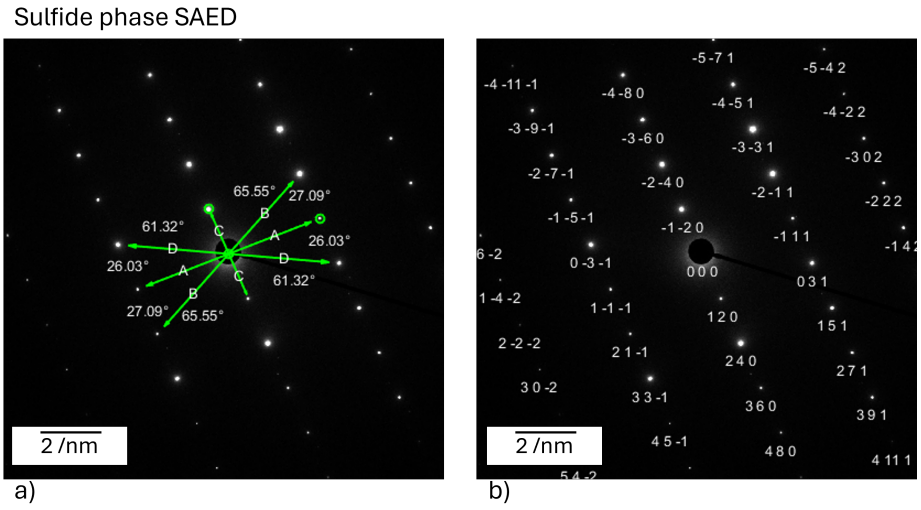

Figure 5.22: a) Diffraction vectors and their relative angles are determined from the diffraction pattern of the sulfide phase. b) successful indexation of the SAED pattern as [2 −1 3] zone axis of the orthorhombic Zr_2S structure.

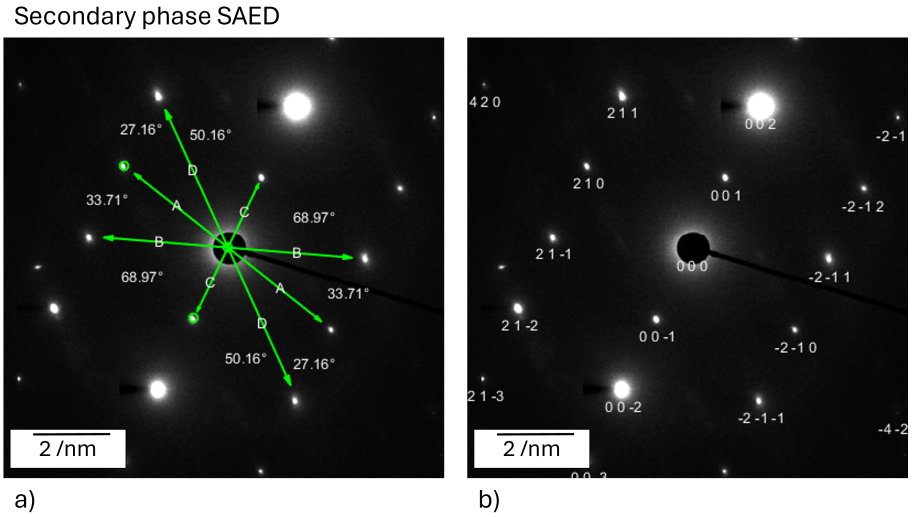

Figure 5.23: a) Diffraction vectors and relative angles, determined from the diffraction pattern of the secondary phase, b) indexation of the SAED pattern as [−1 2 0] zone axis of a monoclinic Zr-Cu type structure.

Table 5.5: Derived d-spacings and d-spacing ratios for the sulfide phase in the as-cast 6 mm rod of $(Zr50)S3$.

	d-spacing	
	[nm]	**[1/nm]**
A	0.32209	3.1047
B	0.29353	3.4069
C	0.64384	1.5532
D	0.28288	3.535

	d-spacing ratios			
	A	B	C	D
A	1.0000	1.0973	0.50026	1.1386
B	0.91131	1.0000	0.45589	1.0376
C	1.9990	2.1935	1.0000	2.2760
D	0.87827	0.96374	0.43937	1.0000

Table 5.6: Derived d-spacings and d-spacing ratios for the secondary Zr-Cu type phase in the as-cast 6 mm rod of $(Zr50)S3$.

	d-spacing	
	[nm]	**[1/nm]**
A	0.29627	3.3753
B	0.28346	3.5279
C	0.49834	2.0067
D	0.23317	4.2887

	d-spacing ratios			
	A	B	C	D
A	1.0000	1.0452	0.59452	1.2706
B	0.95675	1.0000	0.56880	1.2157
C	1.6820	1.7581	1.0000	2.1372
D	0.78702	0.82260	0.46790	1.0000

In contrast, the precipitates give a complex diffraction image with multiple diffraction spots that are 'smeared' out in the angular direction while being defined in the radial direction, resulting from scattering of multiple grains with similar orientations of the nano-crystalline material relative to the electron beam. Additionally, clusters of diffraction spots and streaking of some spots can be observed as a direct influence of the nano-scale microstructure, which contains crystalline features in the size range of about 25 nm.

During the TEM investigation, the TEM-EDS was also recorded as area spectra from the 4 different phases, and the results are displayed in Figure 5.24, where the difference between matrix phase and sulfide as well as the difference in composition between sulfide phase and secondary phase becomes clear.

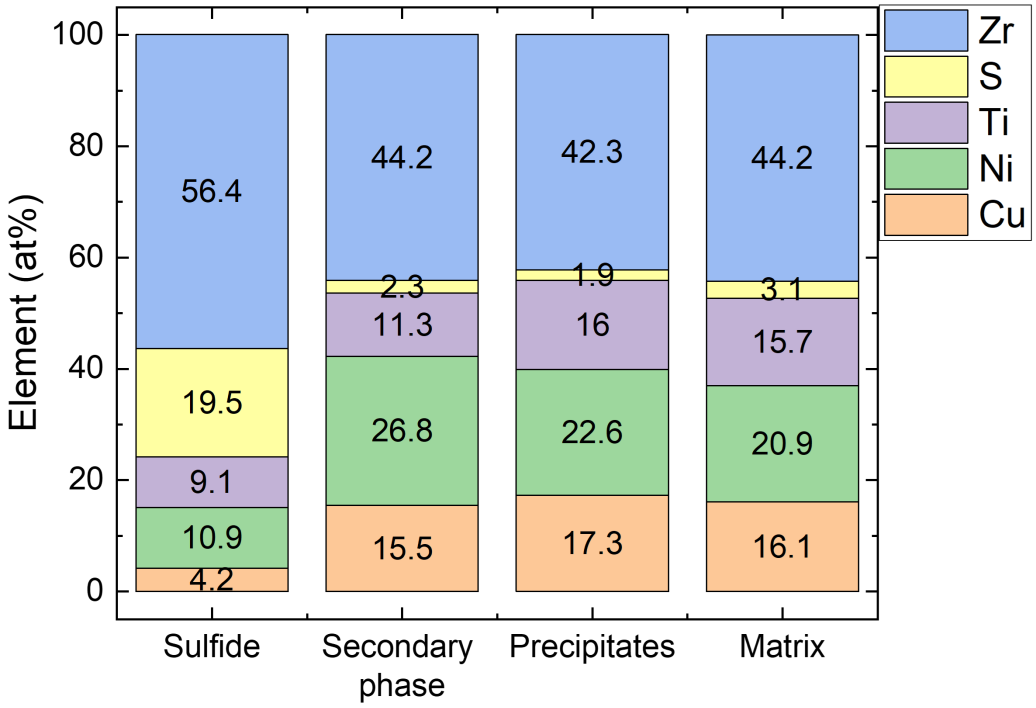

Figure 5.24: Graphic display of TEM-EDS quantification results for the 4 different phases that were encountered in the precipitate specimens of the 6 mm rod sample.

The secondary phase is especially enriched in Ni, and both the fine precipitates as well as the secondary phases show only a low amount of sulfur. The sulfide phase is a lot more enriched in Zr and S than the line scan in the SEM suggested, since Zr-S makes up 76 $at\%$ of the sulfide phase. This is in stark contrast to the secondary phase and the precipitates surrounding the sulfide, as the S-content is almost ten times higher. The results of the TEM-EDS indicate that an S-depleted

zone around the precipitate allows for easier nano-crystallization of the phases that cannot tolerate S in their crystal structure. For those crystal structures to form, the local concentration of the S must be reduced.
To display the distribution of elements and resolve the local concentrations at the phase boundaries better, more detailed STEM EDS-maps with the five-fold standard exposure time per map were recorded. The concentration maps for the individual elements can be seen in Figure 5.25 with an additional high-angle annular dark field image (HAADF). Zr is rather homogeneously distributed throughout the sample with an elevated concentration in the sulfide and a small depletion in the precipitate zone, in contrast to the matrix phase.

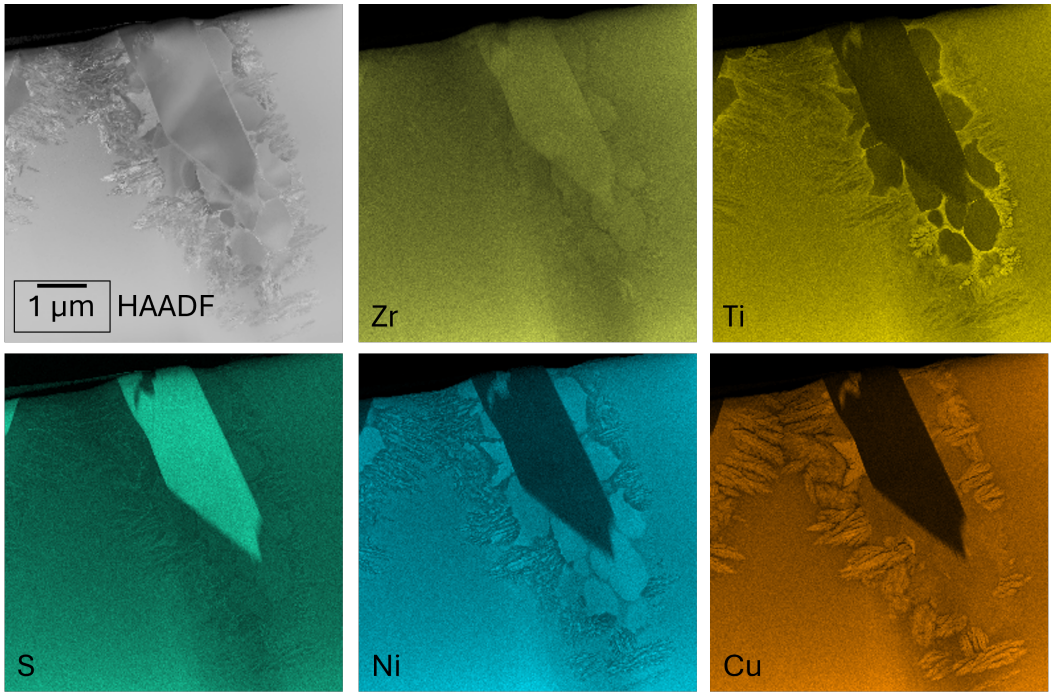

Figure 5.25: STEM-EDS overview map of the precipitate analyzed in the 6 mm rod of $(Zr50)S3$ that shows the distribution of all elements within the sample.

The Ti-EDS-map shows a lot more crystalline features, especially in the tip of the crystalline particle there are multiple very fine Ti-rich structures in between the secondary phases. The Ti is also segregated in alternating concentration areas with higher and lower Ti content that resemble the fine-scale structures observed

in the Ni-map and especially the Cu-map. The Ti appears to behave inversely to the Ni in direct comparison of the two, since the Ni-rich parts of the microstructure appear to be low in Ti and vice versa. Cu behaves similarly in the fine-scale nanocrystalline part of the microstructure and seems to also behave contrary to Ni, except for some distinct smaller crystals that show enrichment in both Ni and Cu.

Table 5.7: Summary of the EDS quantification.

	S ($at\%$)	Ti ($at\%$)	Ni ($at\%$)	Cu ($at\%$)	Zr ($at\%$)
Sulfide	19.47	9.07	10.91	4.15	56.41
Secondary phase	2.25	11.33	26.75	15.47	44.21
Precipitates	1.90	15.97	22.61	17.26	42.27
Matrix	3.14	15.71	20.87	16.07	44.23

5.2.3 Concluding remarks on the crystallization behavior under the influence of sulfur

In conclusion, the nucleation and crystallization behavior can be described as quite a complex sequence of different phases, the findings are summarized in Figure 5.26 in a schematic TTT-diagram. The primary phase that was identified as the core phase of the crystallites is the simple hexagonal structure of α-(Zr,Ti) that is also highest melting phase of the system with a reported melting temperature of 2149 K in the case of pure Zr and a minimum solidus temperature of 1808 K for Ti_2Zr [183]. At the $(Zr50)S3$'s liquidus temperature of 1105 K, the phase is being supercooled over 500 K which gives a reasonable explanation why the nuclei of the phase can be found at the core of the crystallite, their critical nuclei radius is minimal. These results fit to the CALPHAD prediction of Arroyave et al. that in Ti-Zr-Cu 'Close to the liquidus, the b.c.c. phase appears to be present when only the liquid phase is experimentally found. The calculated phase fractions for the b.c.c. phase, however, are below 10^{-2}.' [88]. These b.c.c. nuclei are detrimental to the GFA as they can also act as heterogeneous nucleation site. Further growth of the phase is hindered by the local chemistry coupled with slow diffusion in the very high viscosity melt and the core phase is then 'entrapped' as it serves as heterogeneous

nucleation site for the Zr_2S phase that depletes the surrounding liquid of S and Zr while growing and rejects the remaining solutes of Ni, Cu and Ti into the melt, leading to a local enrichment of these elements around the slowly growing Zr_2S crystal surface. The crystals can grow only slowly as the 'solute atoms must diffuse away' from the interface of the crystal during the growth process [184]. The enriched zone around the Zr_2S then triggers crystallization of multiple phases by constitutional undercooling that is caused by the segregation of the elements being pushed into the remaining liquid by the growing Zr_2S solid/liquid interface.

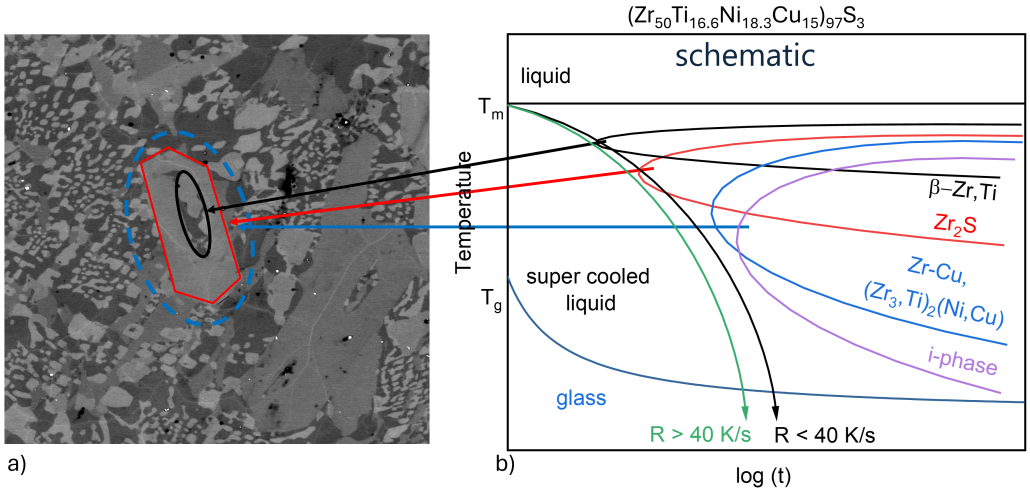

Figure 5.26: a) Microstructure of the ESL processed sample and marked out crystalline phases b) schematic TTT-diagram summarizing the results of the investigation of the solidification products during cooling from the liquid in the S-infused alloy of $(Zr50)S3$.

The main crystallization found in the S-free alloy is changed by the S addition as the metastable f.c.c. Zr_2Ni type phase is suppressed by it, which can be seen clearly in the investigation of the as-cast rods with varying S-content. The main crystallization that causes the recalescence in the ESL processing is the $(Zr_3Ti)_2(Ni,Cu)_1$ tetragonal intermetallic phase that forms from the remaining liquid after supercooling. The formation of the i-phase is sketched in the graphic of Figure 5.26 b)and plays a central part in the devitrification of the alloys.

5.3 Crystallization behavior during heating from the solid

In the alloy set of $(Zr_{50}Ti_{16.6}Ni_{18.3}Cu_{15})_{100-x}S_x$ the structure of amorphous phase, supercooled liquid phase and crystallization stages as well as devitrification behavior were investigated by an in-situ HE-XRD structural analysis at PETRA III's Swedish material science beamline P21.2. The experimental setup with the LINKAM furnace in transmission geometry allowed for scan measurements with $0.33 K/s$ and a temporal resolution of diffraction images of 1 s that were averaged over 5 images, resulting in a resolution of 1.515 K per derived diffraction spectrum.

The results of the S-free alloy and the alloy containing 3 $at\%$ of S are compared side by side in Figure 5.27 a) and b) with their respective DSC curves showing the heatflow on the horizontal axis attached on the right-hand side respectively. The alloys transition from their glassy state through the region of relaxation, which is followed by the onset of the glass transition region into a crystallization process comprised of multiple stages that is explored in the following section.

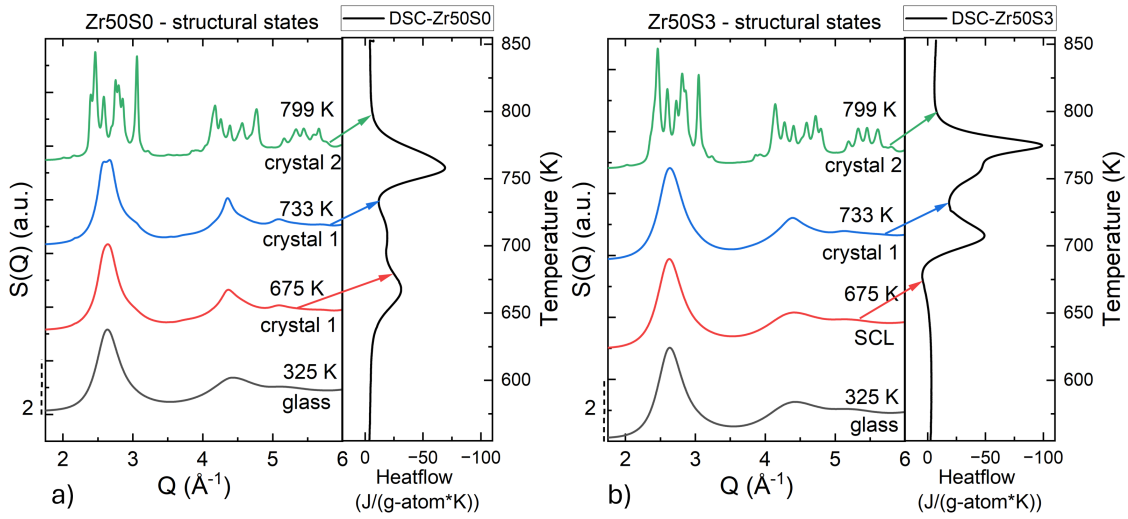

Figure 5.27: Resulting total scattering structure function for different temperature regions, resulting from an in-situ HE-XRD time resolved structural analysis during heating for a) $Zr_{50}Ti_{16.6}Ni_{18.3}Cu_{15}$ and b) $(Zr_{50}Ti_{16.6}Ni_{18.3}Cu_{15})_{97}S_3$.

The difference in supercooled liquid stability that is displayed in the DSC curves and the difference in crystallization kinetic due to the influence of sulfur are also visible in the in-situ measured structural data, the onset temperature of the first crystallization is shifted from 637 K to 686 K. This stage is mostly characterized by a rise in intensity of both the FSDP and SSDP and a reduction of the FWHM, whereas the opposite behavior is encountered for the samples that transition into the SCLR without crystallizing. At 675 K, while the initial crystallization event has already progressed into a significant structural change, the sulfur-induced alloy is still transitioning into the SCLR and displays an amorphous structure. For a higher temperature of 733 K, where the sulfur-free alloy already displays a significant structure in its spectrum that can be assigned to an icosahedral phase, the $(Zr50)S3$ alloy shows a distinguishable increase in intensity on the SSDP, signifying ordering of the clusters in the structure.
The second crystallization shows a very significant structural signal of multiple intermetallic compounds that differ strongly from the crystal 1 and the amorphous structure. The quasicrystalline icosahedral phase is a metastable phase that can form easily from the amorphous phase as soon as sufficient mobility in the structure is available during the initial crystallization stage for the rearrangement of already existing icosahedral clusters in the amorphous state [163].

The experiments were conducted for the full range of sulfur, and the behavior of the alloys changes consistently, which aligns well with the data measured by the DSC, the lower sulfur additions behave quite similarly to the S-free alloy except for the upwards shift in the characteristic temperatures. For the alloy containing 7 $at\%$ of S, however, a differing behavior can be observed as the formation of the crystal phase 1 is neither detectable in the structural data nor the DSC data. The behavior of the alloy set is shown comparatively in Figure 5.28 where in a) to d) the alloys with 1 $at\%$, 3 $at\%$, 5 $at\%$, and 7 $at\%$ are displayed as a two-dimensional scattering structure function maps in dependence of wave vector Q and the temperature, with the corresponding DSC trace and significant temperature marked on the right hand side of the respective sub-figures. The missing first crystallization stage in the $(Zr50)S7$ can be seen clearly when comparing the structural signal to the other alloys of the set, and the transition into the crystal 2 is quite concise in

comparison. Between the onset of the glass transition and the end of the SCLR structure at T_{x2}, no structural or thermal events can be detected, which indicates a stable SCLR structure for the higher S-contents.

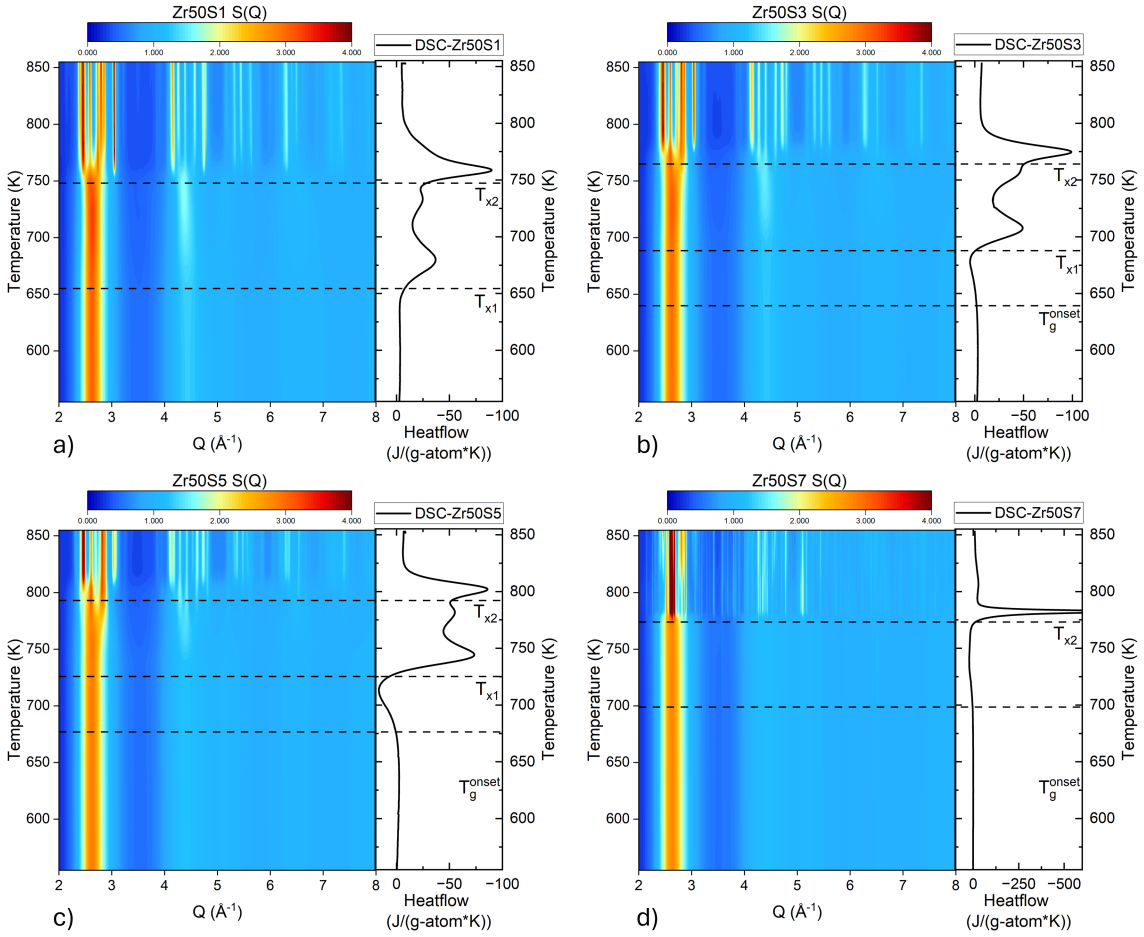

Figure 5.28: Results of in-situ scattering experiments in a LINKAM THMS 600 with a heating rate 20 K/min, the derived total scattering structure function of $(Zr_{50}Ti_{16.6}Ni_{18.3}Cu_{15})_{100-x}S_x$ with x ranging from 1 $at\%$ in a) to 7 $at\%$ in d). It shows the influence of sulfur on the devitrification behavior of the glass, the insets display the DSC data of the recorded heat flow for the four alloys for an identical heating rate applied to both experiments, with characteristic temperatures marked as dashed lines.

Complementary SAXS scattering data can be seen in Figure Figure 5.29 a) and b) as spectra and c), d) as two-dimensional maps. The crystallization behavior can be seen to differ significantly in the SAXS data too, as for the $(Zr50)S3$ alloy an interference peak centered at Q_{max} of 0.0192 $Å^{-1}$ starts to appear in the data at a temperature of about 761 K which is just below the temperature where the DSC data locates the onset of the second crystallization stage.

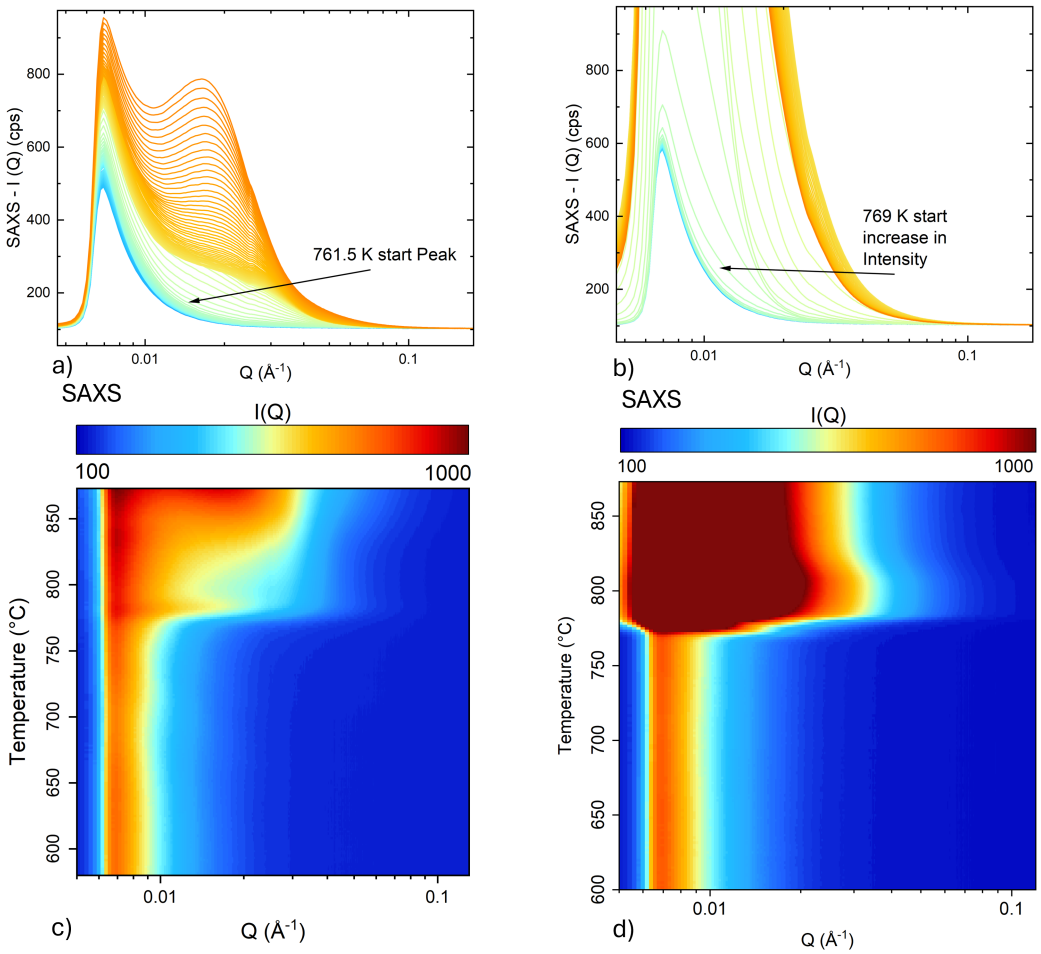

Figure 5.29: Results of in-situ scattering SAXS experiments in a LINKAM THMS 600 with a heating rate 20 K/min, the short-angle scattering intensity of (Zr50)S3 is given in a) as absolute spectra, in c) as 2D map of temperature and wave-vector and analog data is presented in b) and d) for the (Zr50)S7 alloy.

The position of the interference peak's maximum corresponds via $L = 2 \cdot \pi / Q_{max}$ to a correlated domain size of about 33 nm and indicates that 'the interference peaks give evidence for spatially correlated arrangements' in the sample with decomposed regions of different compositions, where L describes the characteristic wavelength after the linearized Cahn theory [185, 186]. For the $(Zr50)S3$ this means that while the glass de-vitrifies into an icosahedral phase during the initial crystallization event there is no significant change in the SAXS intensity, meaning that the local cluster arrangements in the glass reconfigure into the icosahedral phase structure without diffusion and concentration changes. The icosahedral quasi-crystalline phase on the other hand decomposes on a scale of up to 33 nm where then the respective intermetallic compounds start to crystallize. The the peak maximum is also shifting to lower Q-values as the temperature increases, indicating a slow chemical redistribution and growth of the crystalline phase in the domains [185].
For the $(Zr50)S7$ on the other hand there is no interference peak but a sharp increase in scattering intensity and the intensity rises quickly to above 10,000 cps during the crystallization event of the $(Zr50)S7$, indicating a rapid crystallization kinetic that fits to the sharp exothermic event observed in the DSC data.
The difference between the structural states of the $(Zr50)S3$ and the $(Zr50)S7$ is highlighted in Figure 5.30 where the pair distribution functions resulting from the in-situ scan experiment can be seen. The icosahedral phase that appears in the $(Zr50)S3$ alloy at 733 K is structurally very similar to the amorphous phase, although disctinct changes appear in the intensity of the Zr-(Zr,Ti) bond as well as the 1-atom connection and related higher shells of coordination. In Ti-based alloys, Lee et al. reported a similar behavior where the metastable icosahedral phase was found to be much more similar to the local structure of the amorphous than Laves or intermetallic phases [178]. Furthermore, Lee et al. find that the nucleation of such phases that utilize the structure of the SCL itself as 'template' to nucleate cannot be described 'within the one-dimensional kinetic view implicit in the classical theory' [178]. For the Zr-based alloys, the phenomenon of icosahedral phase formation is also well known [163, 187–189].
This is important when considering the description of crystallization by nucleation and growth according to classical theory, as explained in the methodology section

of this work, as the heterogeneous nucleation barrier requires far less energy than the homogeneous nucleation. The similarity in the local structure of metallic glasses and icosahedral crystals was described much earlier by Sachdev et al., who found through density-functional mean-field theory analysis that the icosahedral phase is favored by ISRO order being present in the liquid phase [187].

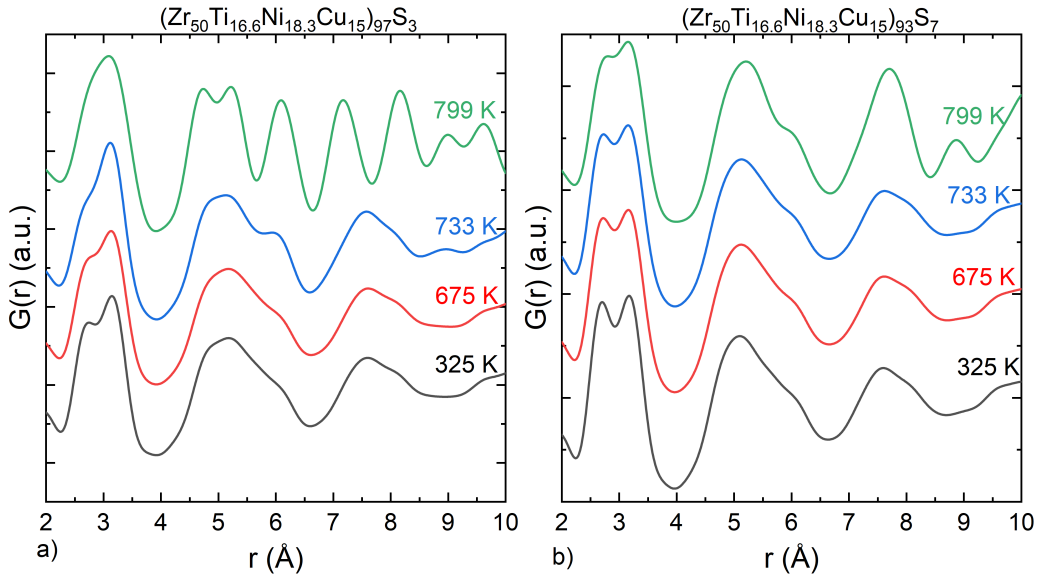

Figure 5.30: Pair distribution function G(r) of the different structural states encountered during the in-situ scanning experiment for a) $(Zr_{50}Ti_{16.6}Ni_{18.3}Cu_{15})_{97}S_3$ and b) $(Zr_{50}Ti_{16.6}Ni_{18.3}Cu_{15})_{93}S_7$ alloy, the structural difference is striking for the high temperature crystal phase at 799 K.

This can be seen as a strong argument as for why the I-phase crystallization appears to behave significantly different in the previously shown TTT-diagram comparing $(Zr50)S3$ and $(Zr50)S7$ alloy, the I-phase possesses a very low energetic barrier due to the similarity of its structure to the SCL structure and the character of the crystallization is more of a heterogeneous nucleation due to the ability to use the SCL structure as a template for nuclei as soon as enough atomic mobility is available due to the increase in temperature.
The $(Zr50)S7$ does not show those icosahedral crystal structures at all, the structure of the supercooled liquid region encountered at 733 K is largely identical with

the amorphous phase at room temperature in comparison. When considering those findings with the deviation of the amorphous structure from the ideal icosahedral ratios as a function of S, shown in Figure 5.2, the increase in S from 3 $at\%$ to 7 $at\%$ increases the deviation from the ideal ISRO making the icosahedral phase less favored for crystallization from the SCLR and thereby stabilizing the liquid structure against the crystallization of metastable icosahedral phases. This allows for the extended stability of the SCL structure until the main crystallization occurs at higher temperatures.

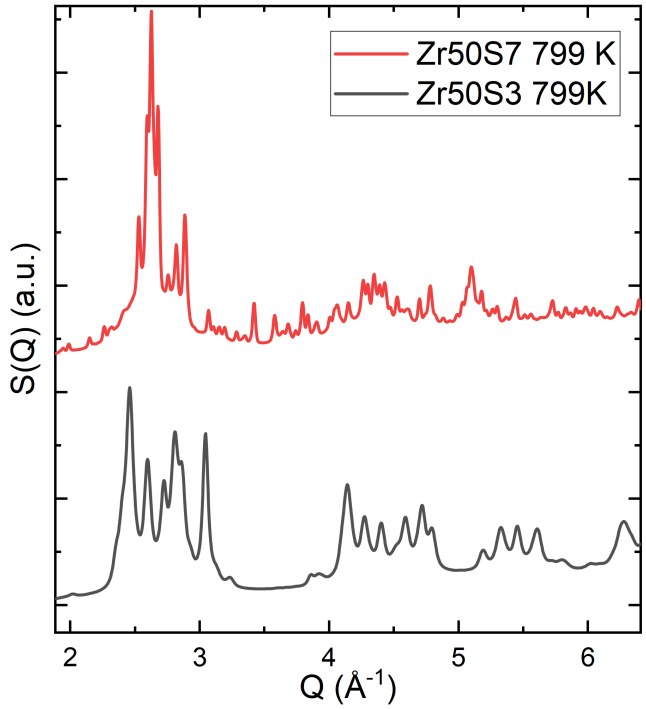

Figure 5.31: Comparison of the total scattering structure functions emerging from the $(Zr50)S3$ and $(Zr50)S7$ alloys at 799 K.

The impact of S becomes also clear when directly comparing the two main crystallization products, the total scattering structure functions are compared in Figure 5.31. Although both are complex mixtures of various crystal phases, the difference in the main crystallization phase can be seen directly when comparing the spectra. The $(Zr50)S3$ shows a mixture of crystalline phases that is very similar to the

crystallization at at larger casting sizes, while the $(Zr50)S7$ alloy shows a more defined intermetallic crystallization accompanied by multiple other minor phases. The difference can be seen more clearly when directly comparing the PDFs of the structures found at 799 K in Figure 5.30. While the SRO atomic arrangement completely changes for the $Zr_{50}S_3$ alloy beyond 4 Å, the opposite is the case for the $(Zr50)S7$ alloy. Here the SRO atomic arrangement stays largely the same up to 6.5 Å. This fits into the picture of the amorphous structure being stabilized in the higher S-content alloys.

6 Mechanical properties of the glass

6.1 Influence of Sulfur

The influence of sulfur manifests not only in the structure and thermophysical properties of the developed alloys, it also alters the mechanical properties of the amorphous phase. The alloys were tested with a Vickers indenter to determine the HV5 hardness, and the results can be seen in Figure 6.1. The addition of S into the alloy leads to a hardening of the amorphous phase as the probed Vickers hardness rises from 480 HV5 to 580 HV5 throughout a 5 $at\%$ of S addition into the alloy. The initial hardness of 480 HV5 lies within the expected range for a Zr-based BMG and is comparable to the hardness of the AMZ4 alloy, for example [190].

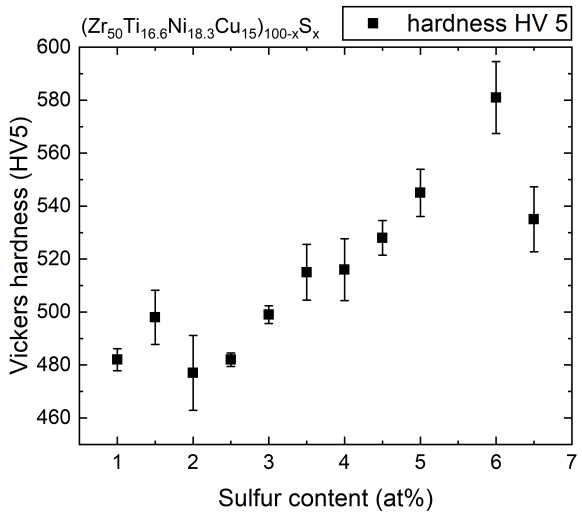

Figure 6.1: Vickers hardness determined on amorphous samples with sulfur additions in the range from 0 to 8 $at\%$, resulting in a near linear correlation between S-content and measured hardness.

The increase in hardness due to the alloying of S is not surprising, as similar

behavior is well reported for the chemically akin oxygen that can significantly influence the hardness of the glass, as reported by Conner et al. where the Vickers hardness of $(Zr_{57}Cu_{15.4}Ni_{12.6}Al_{10}Nb_5)$ increased by 12 % due to a rise of the oxygen level from 410 w-ppm to 1020 w-ppm [191]. The hardening effect of the S is less severe, as the increase of 6 $at\%$ (60.000 a-ppm) only results in a relative increase of 21 % in hardness. The influence of S is therefore considered to be less severe in increasing the hardness compared to the effect of O.

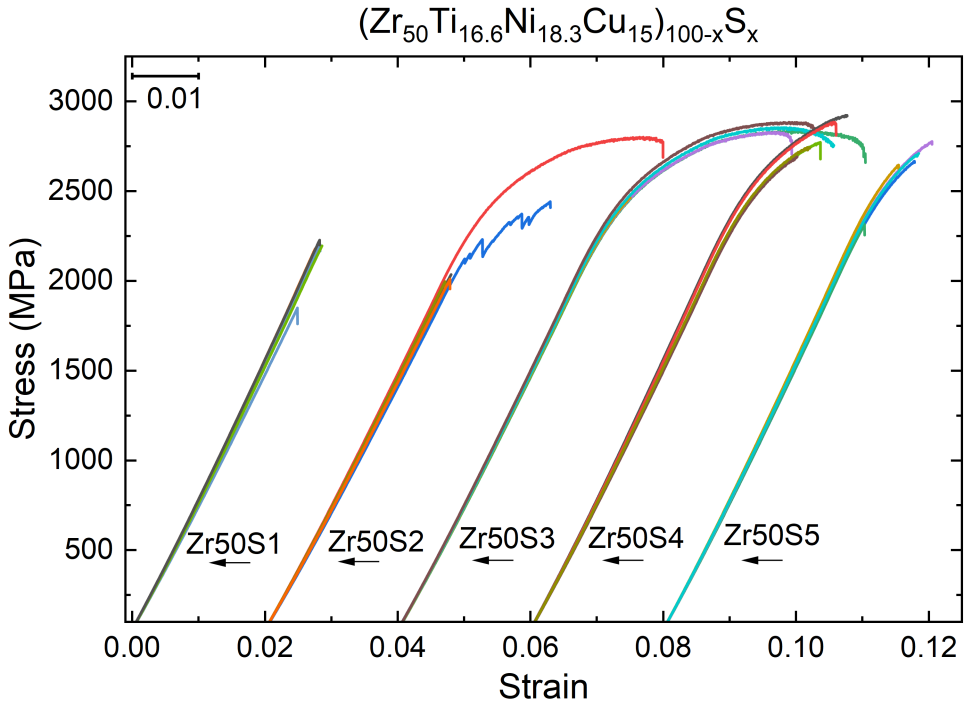

Figure 6.2: Stress-strain curves recorded during the 3-PBB experiments that show different mechanical behaviors in dependence of the S-content, where each measurement contains 5 individual curves.

The influence of sulfur itself on the strength and ductility of the glass was also probed by performing three point beam bending experiments on a series of BMG specimen with varying sulfur content, therefore alloys of $(Zr_{50}Ti_{16.6}Ni_{18.3}Cu_{15})_{100-x}$ S_x with x varying from 1 $at\%$ to 5 $at\%$ were probed. The results of the bending experiments can be seen in the graph of Figure 6.3, where the average of the maxima of stress and strain values for 5 individual measurements each is displayed,

the values are accompanied by their respective standard deviation. The values are also listed in Table 6.1. The curves of the measured data can be seen in the Figure 6.2. The first remarkable property of the series is the consistency, the whole set of 25 samples reaches the elastic yield limit of the samples, which emphasizes the consistent quality of the cast samples.

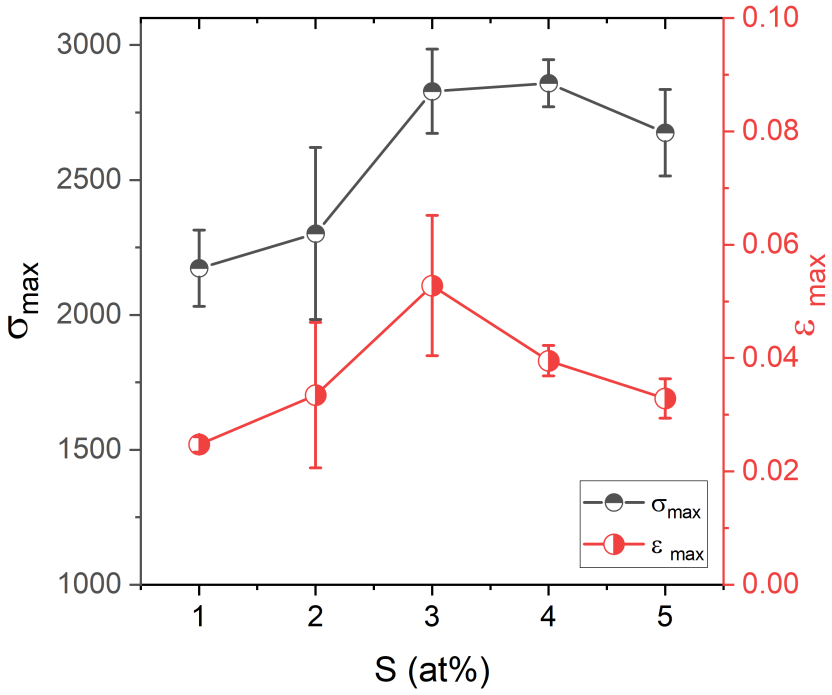

Figure 6.3: Graphic display of the key mechanical properties derived from the 3-PBB experiments as a function of the S-content.

The ductility of the system varies with the sulfur content. In the beginning, there is little plasticity to be observed. The alloy with 1 $at\%$ of sulfur shows no ductility at all, while for the 2 $at\%$ sample, 2 samples show slightly ductile behavior. The $(Zr50)S3$ alloy exhibits the highest ductility of the series, which amounts to 5.2 % total breaking elongation in the 3-PBB testing. This makes the alloy formidable for structural applications that require non-brittle modes of failure.
The maximum stress achieved is higher in the $(Zr50)S4$ alloy, although the alloy shows a reduced total breaking elongation in comparison to the $Zr_{50}S_3$ alloy. The derived Young's modulus E mimics the trend of the liquidus temperature T_l as it is the lowest for $(Zr50)S2$, followed by $(Zr50)S3$, whereas the other alloys show a

higher elastic modulus. This fits with the data from the hardness measurements, as the S-addition leads to an increase in both hardness and stiffness.
This behavior is similar to the reported behavior for the influence of oxygen in BMGs, Wang et al. report that a certain amount of oxygen can be able to increase the plasticity over the base alloy, although the O-addition leads to a certain decrease again upon further addition in BMGs like $Zr_{60}Ni_{25}Al_{15}$, with the explanation given that too much oxygen increases the covalent p-d hybridization in Ni and decrease the plasticity [192].

Table 6.1: Key mechanical properties from 3-PBB experiments in dependence of the S-content, measured with a Zwick Roell universal testing machine.

3-PBB derived data					
S($at\%$)	$\boldsymbol{\sigma_{max}}$	**SD $\boldsymbol{\sigma}$**	$\boldsymbol{\epsilon_{max}}$	**SD $\boldsymbol{\epsilon}$**	**E (GPa)**
1	2173	141.5	0.0247	0.0014	88.4
2	2301	318.7	0.0334	0.013	82.8
3	2828	156.0	0.0527	0.013	85.2
4	2858	86.9	0.0395	0.0027	88.4
5	2675	160.1	0.0328	0.0034	88.8

For the most promising alloys of the alloy development efforts, the mechanical properties were further probed by a series of three-point beam bending experiments on a Shimadzu universal testing machine, with beams measuring 1.8 mm in height and 3 mm in width. The results for the $(Zr50)S3$ alloy can be seen in Figure 6.4 a) as well as for the Cu-Ni swapped alloy and the alloy with added Al, which are also displayed in Figure 6.4 b) and c). The offset yield strength for the $(Zr50)S3$ was determined to be 2.59 GPa, and the other alloy variants result in similar values with 2.7 GPa for the Cu-Ni swapped alloy and 2.75 GPa for the Al addition, and the highest value of 2.83 GPa was achieved for the optimized alloy featuring both the Cu-Ni swap and the Al addition, which can be seen in Figure 6.4 d). The ductility of the alloys appears to be reduced by the Al-addition alone, as the breaking elongation of all other alloy variants is higher in comparison.
An overview of the derived key mechanical properties is given in Table 6.2, where

the values can be easily compared for the alloy development effort. The Cu-Ni swap improves the breaking elongation value slightly to 5.57 % with a standard deviation of only 0.19 %. A significant increase in the breaking elongation, however, is met when both the Cu-Ni ratio in the alloy is swapped and the Al-addition is performed at the same time, due to which the breaking elongation is improved 1.09 % over the base alloy, making the combined effort effective in increasing the ductility.

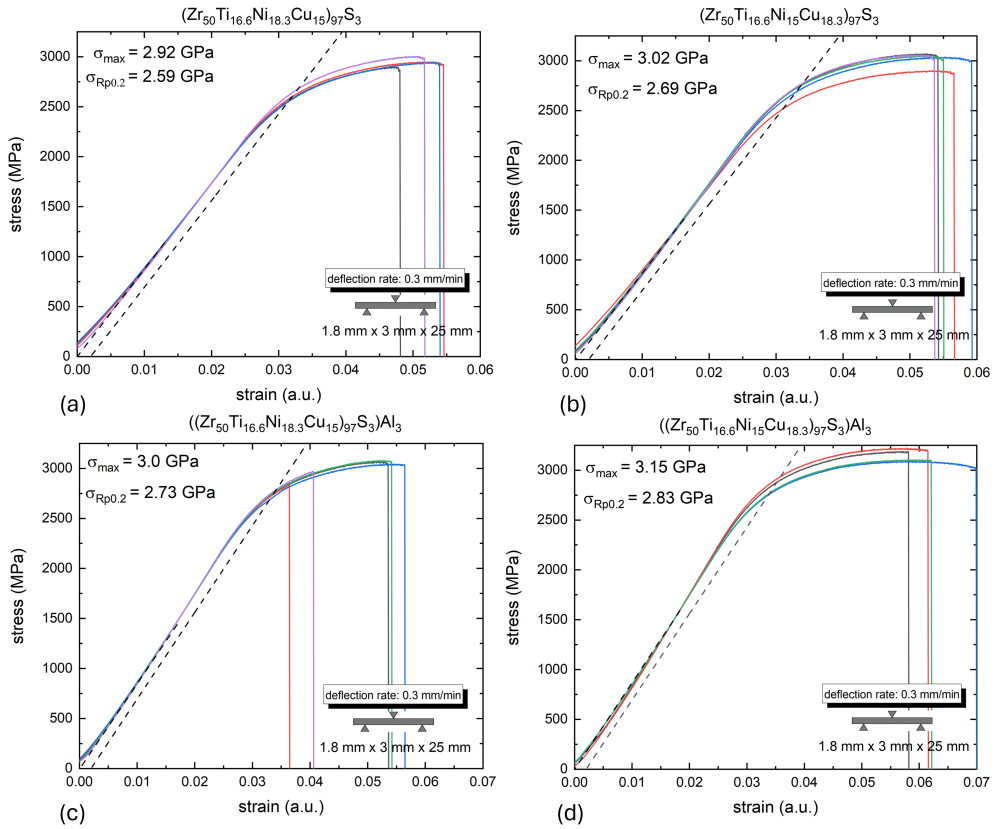

Figure 6.4: Three point beam bending of the $Zr_{50}Ti_{16.6}Ni_{18.3}Cu_{15}S_3$ and b) the Cu-Ni swapped $Zr_{50}Ti_{16.6}Ni_{15}Cu_{18.3}S_3$. The variants of the alloys with added aluminum are displayed in c) and d), respectively.

The results indicate that the combination of both alloy development measures that resulted in the best glass former of the system is also able to successfully enhance the mechanical properties of the alloy even further, and the resulting alloy turns out to possess remarkably good mechanical properties.

Table 6.2: Mechanical properties derived from the 3PBB experiments for the four alloy compositions.

Alloy acronym	σ_{max} **(MPa)**		$\sigma_{0.2}$ **(MPa)**		ε_{break} **(%)**	
	Mean	SD	Mean	SD	Mean	SD
Zr50S3	2950.16	37.72	2598.25	54.02	5.20	0.29
Zr50S3Cu18	3022.51	62.90	2695.40	100.00	5.57	0.19
Zr50S3Al3	2999.28	91.05	2745.20	35.57	4.83	0.81
Zr50S3Al3Cu18	3150.30	54.93	2832.00	75.80	6.29	0.44

6.2 Influence of Oxygen

The glass forming ability and the mechanical properties were also investigated under the influence of a severe oxygen load stemming from the industrial grade material that was deployed in the synthesis of the alloy. For GFA, the structure of multiple casting thicknesses was probed for the $(Zr50)S3$ alloy as well as for two prominent reference alloys that were fabricated in the very same materials quality for comparability. The reference alloys were Vitreloy 105 ($Zr_{52.5}Ti_5Ni_{14.6}Cu_{17.9}Al_{10}$) and AMZ4 ($Zr_{59.3}Cu_{28.8}Al_{10.4}Nb_{1.5}$) which are good bulk glass formers that see industrial application [190, 193]. The glass forming ability for both reference alloys drops significantly when being synthesized from the industrial grade material, as displayed by the XRD results in Figure 6.5 a) and b).
The glass forming ability of the contaminated material reaches 4 mm in the case of the Vitreloy105 and 3 mm in the case of AMZ4. In high-purity material, those alloys usually reach a GFA of about 8 mm in Cu-mold casting [16], making them decent bulk glass formers. The $(Zr50)S3$ alloy reaches a GFA of 5 mm in industrial grade and 6 mm for the Al-added alloy variant, making the Al-addition redundant. The small loss in GFA of the base $(Zr50)S3$ alloy, however, is pretty remarkable as the reference alloys lose half of their GFA under the same materials purity circumstances.
The amount of oxygen both in the raw materials as well as in the final castings was quantified by Chemilytics GmbH via a carrier hot gas extraction procedure. The derived values can be found in Table 6.3. The raw materials of Zr60702 alloy and CP-grade 1 Ti fall within the expected oxygen load according to their respective ASTM norms. The cast parts of industrial grade $(Zr50)S3$ alloy contain 4650 a-ppm of oxygen compared to only 900 a-ppm in the high-purity alloy parts.
The influence of oxygen on the GFA of Zr-based BMG has been studied extensively before by multiple research groups, the effects found for Zr-based BMGs have been reported to be diminishing for the GFA as well as the undercooling ability of the melt [166, 194–196]. The glass forming is commonly found to be negatively impacted, for example, the alloy Vit105 was reported to show drastically reduced GFA at a level of 3000 a-ppm of O in the alloy by Liu et al. [194]. The described phenomena of the oxygen's effect in the alloys vary from the stabiliza-

tion of metastable phases like oxygen-induced oxide particle formation that act as a heterogeneous nucleation site, like Zr_4Ni_2O in the case of Vit105 [194]. On the other hand, oxygen is also able to stabilize metastable icosahedral phases like found in $Zr_{65}Cu_{27.5}Al_{7.5}$ [174] and metastable Zr_2Ni f.c.c. 'big cube' phases like in Vit105 [197]. Furthermore, the addition of O can also lead to partial crystallization due to preferred oxide compound formations like $Zr_7Cu_4Al_3O$ as reported for the $Zr_{55}Cu_{30}Al_{10}Ni_5$ alloy [198].

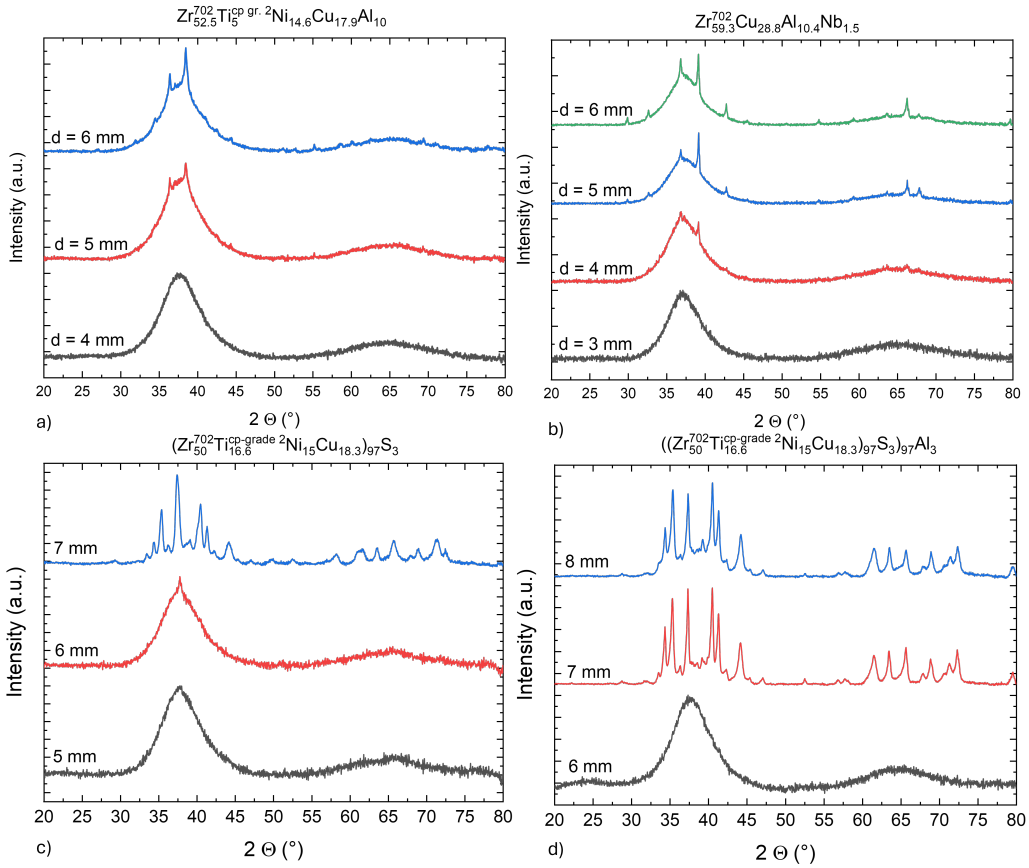

Figure 6.5: XRD spectra of a) 4 mm to 6 mm rods of industrial grade Vitreloy 105 b) the industrial grade AMZ4 for 3 mm to 6 mm rods c) the industrial grade $(Zr50)S3$ alloy for 5 mm to 7 mm rods d) the $((Zr50)S3)Al3$ for 6 to 8 mm rods.

Those effects are detrimental to the glass formation as the stability of the glass is reduced in comparison to the crystalline phases by the oxygen. For S-bearing

alloys, however, this appears not to be the case; in this study, the $(Zr50)S3$ shows only a minor reduction in GFA compared to the high-purity variant.
The complex crystallization sequence that was explored previously in section 5.2 is not necessarily susceptible to the influence of oxygen as the main non-metallic element shaping the local chemistry is the S. This confirms the initial reports of Kuball et al. on the GFA of the $Ti_{40}Zr_{35}Cu_{17}S_8$ alloy [59] and the previously published exploration of the responsible primary phase formation in the system [18]. For the $(Zr50)S3$ alloy, the oxygen appears not to change the primary crystallization of the material significantly, as the effect on the GFA is low.

Table 6.3: Results of the chemical analysis via carrier hot gas extraction for the raw materials of commercial Ti and Zr employed in the synthesis, as well as for the cast parts of the alloy in high purity and industrial purity.

Material	**O (w-ppm)**	**O (a-ppm)**
Zr R60702	1368	7750
Ti cp grade 2	1639	4880
$(Zr_{50}Ti_{16.6}Ni_{15}Cu_{18.3})S_3$ high purity grade	198	900
$(Zr_{50}Ti_{16.6}Ni_{15}Cu_{18.3})S_3$ industrial grade	1026	4650

Throughout the literature, there have been multiple successful alloying additions to Zr-Ti-Ni-Cu BMGs, most prominently Al, as it is known to enhance the GFA of Vit105 or work well as an alloying element in combination with Nb, as in Vit106. In $Zr_{73-x}Cu_{12}Ni_{12}Al_xNb_3$, Tan et al. reported an increase of GFA up to 10 mm by 15 $at\%$ Al addition to the alloy [199], which is exemplary for a good Be-free Zr-based bulk glass former. For the BMG investigated by Tan et al., the Al-addition comes with embrittlement, however, as the dynamic plasticity is reduced drastically [199]. A similar case was reported by Ruschel et al. for the influence of Al on Ti-Zr-Cu, where the alloying of Al increases the glass forming ability of the $Ti_{36}Zr_{33.5}Cu_{24.5}S_6$ while reducing the fracture strength continuously, which is attributed to Al induced increases in the amount of ISRO in the glass [19].
Furthermore, Al acts as an oxygen scavenger as reported by Heinrich et al., which leads to a potential reduction of the Al-additions' effectiveness in industrial grade material due to forming alumina [200]. In this study the $(Zr_{50}S_3)_{97}Al_3$ alloy shows the predicted reduced effectiveness of the Al-addition in the industrial grade ma-

terial as the increase in GFA that the alloy gained from Al in the high purity variant of the alloy is diminished by the oxygen content in the alloy, making the $((Zr50)S3)Al3$ uninteresting for the employment in industrial grade, furthermore the castings of this alloy set behaved very brittle during during handling and XRD sample extraction, hinting at a similar embrittlement effect.
The investigation of the mechanical properties was expanded by performing a comparative study of the industrial and high-purity $(Zr50)S3$ alloy in cooperation with Prof. Jay Kruzic's group at the University of New South Wales. The toughness testing results of the single edge notched beams (SENB) can be seen in Figure 6.6 a) for the high purity alloy and in Figure 6.6 b) for the industrial grade alloy.
The high purity variant reaches a high provisional fracture toughness K_Q of 104.4± 6.9 $MPa\sqrt{m}$, yet it is more astonishing that the industrial grade material despite its severe oxygen load retains a K_Q of 79 ± 5.9 $MPa\sqrt{m}$. Regarding their K_J value however the alloys differ significantly as the high purity variant reaches a K_J of 156.3 ± 36.7 $MPa\sqrt{m}$ while the industrial grade alloy's K_J value is only slightly higher than the K_Q value indicating little plasticity for the SENB 3-PBB experiment.
Compressive testing results for both purities are being presented in Figure 6.6 c) and d). The compression testing data, however, shows no negative impact of the oxygen as both results of the compressive strength are located close to 1.7 GPa and lie within their respective standard deviation intervals. The strain to failure value is even slightly higher for the industrial grade alloy, although both alloy variants reach about 6 % of total strain, which classifies both as adequately ductile materials in compression testing.
The SENB samples were analyzed for casting defects by a micro-X-ray computed tomography, and the result for both the high purity variant can be seen in Figure 6.7. The beams contain singular pores that did not stem from the casting parameters, as they were invariant to parameter optimization and appear to form mainly in the S-infused alloys, as the reference alloys that were cast with the same parameters were porosity-free. The small randomly distributed pores appear not to be necessarily harmful for the mechanical performance of the alloys, owing to

the high fracture toughness of the materials.
Additionally, the hardness of the surface of the sample was investigated by mapping with a Vickers indenter and the HV0.05 testing procedure. The results are given in Figure 6.8 a) for the high purity variant of the $(Zr50)S3$ alloy and in b) for the industrial grade alloy variant.

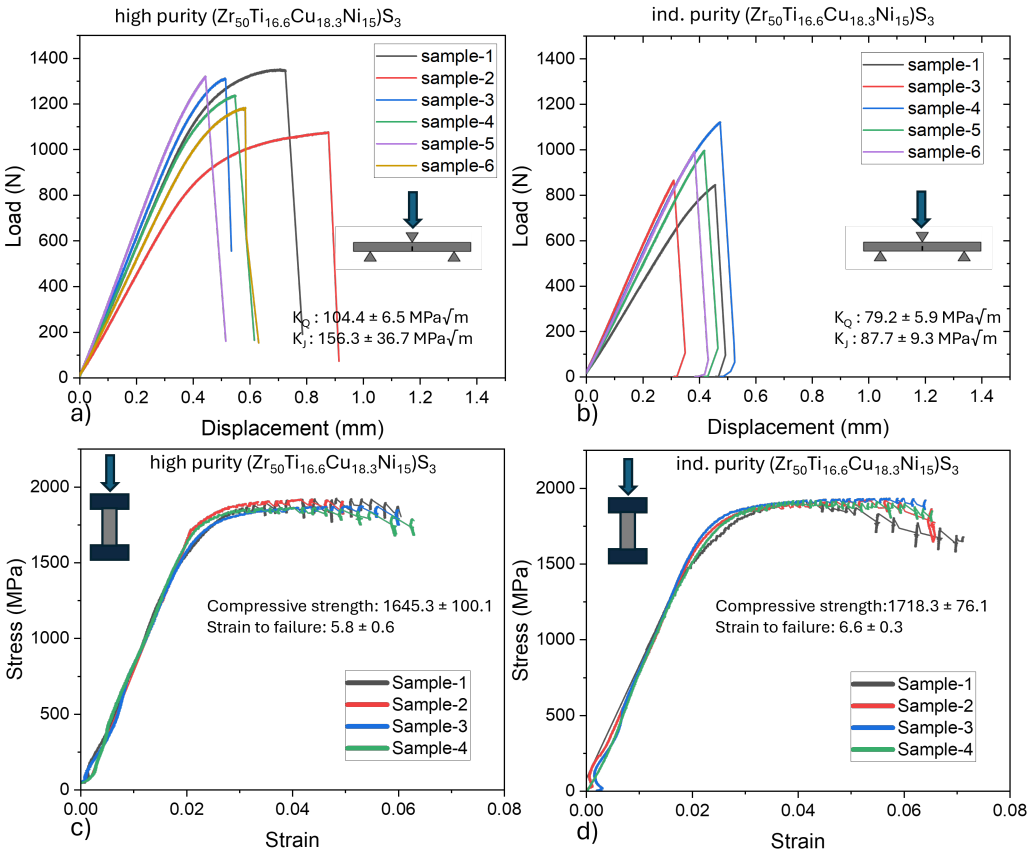

Figure 6.6: Results of the three-point beam bending experiments performed on single-edge notched beam samples of a) high purity $(Zr50)S3$ alloy and b) low purity $(Zr50)S3$. Compressive testing results c) of the high purity alloy and d) the industrial purity alloy

The difference between the alloys is, first, the average hardness that was measured, which increases by 16.2 HV0.05 due to the difference in oxygen content. The distribution of hardness also differs between the alloys can be easily seen from the hardness maps. For the high-purity variant, the average HV0.05 hardness is about

520 HV0.05 with distinct soft spots of a decreased hardness down to 500 HV0.05. Whereas the industrial alloy shows an inverted behavior where the majority of the hardness values are located between 520 and 525 HV0.05, while there are distinct hard spots with a hardness of up to 540 HV0.05 distributed throughout the surface.

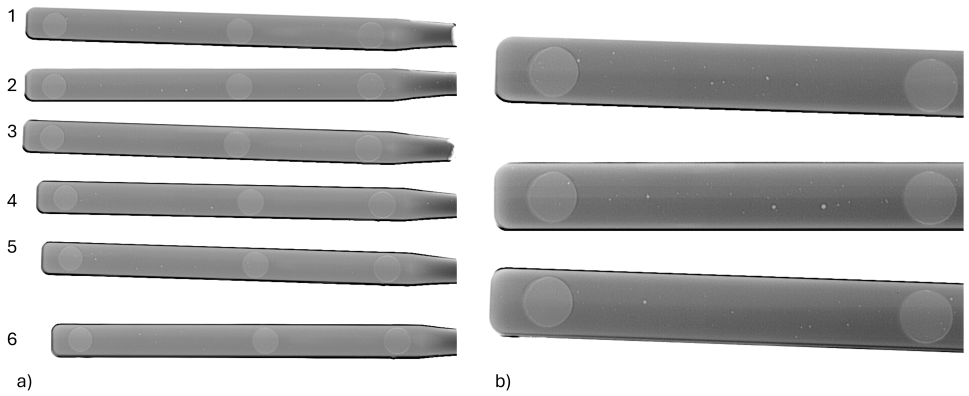

Figure 6.7: a) Micro x-ray computed tomography imaging of the high purity $(Zr50)S3$ alloy and b) higher magnification of beams 1 to 3 that were characterized with fracture toughness testing as well as compression testing.

For the distribution of hardness that can be observed in the HV0.05 indentation maps, the influence of oxygen is quite clear, the distribution of hardness is shifted to higher values on average. The local regions with increased hardness exist likely due to the inhomogeneous distribution of O in the microstructure, which has been reported to change the local structure of Zr-based BMGs increasing the Zr-Zr distances and likely occupying 'interstitial' places in the clusters and 'eliminating local arrangements with the capacity for easy deformation' [172].
The reports in the literature are well aware of the importance of the influence of oxygen in Zr-based metallic glasses, as the dissolution of O in Zr is deemed 'unavoidable' due to the high solubility of O in Zr [201]. Therefore, the effect of oxygen in bulk metallic glasses is well reported within the literature of Zr-based metallic glasses and other susceptible systems of BMGs since the thematic is highly relevant for the industrial application of BMG. In similar alloys like the Vitreloy 106 ($Zr_{57}Cu_{15.4}Ni_{12.6}Al_{10}Nb_5$) Conner et al. reported a study utilizing ZrO_2 in

the alloy synthesis to control the oxygen content in the alloys [191]. They reported a complete loss of ductility in compression and three-point beam bending testing experiments with an addition beyond 410 w-ppm achieved with laboratory grade material [191].

This is in strong contrast to the $(Zr50)S3$ alloy, where the compression testing results remain at a comparable level when comparing laboratory and industrial grade material in compression testing. For one of the best commercial Zr-based BMGs, the Vitreloy 106a alloy ($Zr_{58.5}Cu_{15.6}Ni_{12.8}Al_{10.3}Nb_{2.8}$) a similar study was performed by Teixeira et al. in 2020 where the limit of ductility in three point beam bending testing was located at 900 w-ppm of oxygen in the alloy [202] which is well below the amount of oxygen introduced into the industrial grade $(Zr50)S3$ alloy that retains a breaking elongation of 4.2 %. Here the behavior of the S-bearing alloy differs from the behavior reported for multiple Zr-based BMGs, for example in $Zr_{61}Cu_{25}Al_{12}Ti_2$ BMG Zhou et al. reported the transition from ductile to brittle behavior to be at 3500 $at-ppm$ meaning that the plastic deformation regime in compression testing is less than 2 % with breaking elongation below 4 % in total, the $(Zr50)S3$ industrial alloy contains about 1000 at-ppm more O and retains a total breaking elongation of 6.6 %.

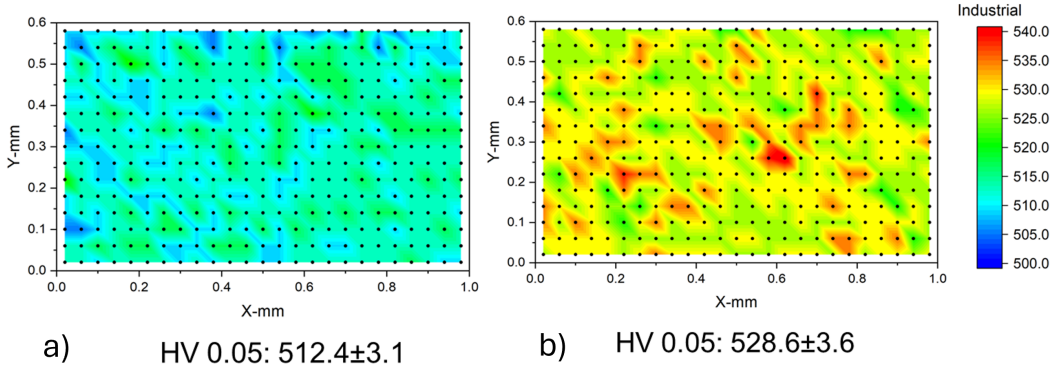

Figure 6.8: Microhardness maps HV0.05 of a) high purity $(Zr50)S3$ alloy and b) low purity $(Zr50)S3$ alloy.

The key values of the characterized mechanical properties are summarized in Table 6.4, where direct comparison between the materials is given for each tested

method, highlighting the difference in material properties due to the oxygen contamination. The reduction of the fracture toughness is also quite small in contrast to the amount of oxygen added to the alloy, as a five times increase of oxygen reduces the fracture toughness only by 25 % in the $(Zr50)S3$ alloy [22]. For another example in the Zr-Cu-Al system, the oxygen embrittlement is much more severe as it occurs already at 2000 at-ppm in $Zr_{50}Cu_{40}Al_{10}$ [203].

Table 6.4: Summary of the mechanical properties determined for both the industrial and high-purity variants of the $(Zr50)S3$ amorphous alloy. $\sigma_{\max}$ refers to the maximum stress, $\varepsilon_{\text{break}}$ to the strain at the breaking elongation, and SD to the standard deviation of the results.

3-PBB	$\sigma_{\max}$	SD	$\sigma_{0.2}$	SD	$\varepsilon_{\text{break}}$	SD
Unit	(MPa)	(MPa)	(MPa)	(MPa)	(%)	(%)
High purity	2932	25	2598	22	5.2	0.29
Industrial	2745	112	2518	84	4.18	0.71
Compression	$\sigma_{\max}$ (MPa)	SD (MPa)	$\varepsilon_{\text{break}}$ (%)	SD (%)		
High purity	1645	100.1	5.8	0.6		
Industrial	1718	76	6.6	0.3		
Hardness	HV0.05	SD				
High purity	512.4	3.1				
Industrial	528.6	3.6				

The same ductility reduction mechanism is common for other BMGs, as the fracture toughness reduction reported in the literature, for example Best et al., which reports the AMZ4's ductility to decrease significantly with O addition to the alloy. The study finds that total embrittlement transition is located at higher oxygen levels beyond at least 1271 w-ppm as no oxide nanocrystals were observed that could embrittle the glass additionally [172], yet the fracture toughness was reduced from a K_Q of 97-138 $MPa\sqrt{m}$ in the low oxygen material down to 25 $MPa\sqrt{m}$ in the high oxygen material. The S-bearing alloy is therefore found to be much more resilient against the influence of oxygen, both in terms of glass forming ability and mechanical properties. This oxygen resilience makes the alloy a promising material for the application in industrial materials quality.

7 Summary and Conclusion

Sulfur as alloying addition

The influence of S on the Zr-Ti-Ni-Cu alloy can be summarized by stating that S is beneficial for both the GFA and the SCLR of the BMG alloys. The maxima of the respective properties do not fall together as the highest GFA is reached at 3 $at\%$ of S, whereas the highest thermal stability for the supercooled liquid is reached at 7 $at\%$. Furthermore, the GFA of the system can be expanded utilizing Al addition and Cu-Ni ratio optimization, which work well independently from each other and can also be applied in combination to increase the GFA by 50 % in high-purity alloy material.

The liquidus temperature of the BMG reduces slightly by adding S to the alloy and increases beyond an addition of 3 $at\%$ which also marks the highest values of T_{rg} in the alloy set. By introducing sulfur the fragility parameter D^* in the high temperature liquid doubles according to the results of the parabolic TEMPUS flight campaign where a strong behavior of the S containing liquid with a D^* of 21 was observed that possesses also significantly increased surface tension compared to the S-free alloy variant.

Influence of Sulfur on the structure of liquid and glass

The structural impact of S on the liquid and amorphous solid phases is pretty significant. It affects especially the short-range order, where distinct changes in Zr-(Zr,Ti) and Zr-(Cu,Ni) bonding length can be easily observed during the pair distribution function analysis of the structural state investigation utilizing HE-XRD. The MRO of the glass is also being affected by the S-addition, the 3-atom connection that embodies face sharing of the clusters, increases continuously. The deviation from both ideal ISRO ratios of FSDP and SSDP correlates well with the GFA in this system, when considering both ratios, the best glass forming alloy also shows the least deviation from the ideal ISRO ratios. The correlation length

determined by Ornstein-Zernike analysis however does not correlate with the GFA and decreases constantly with progressing S addition to the alloy, underlining that although the system is becoming more and more disordered by the S addition as can be seen on the calculated atomic mismatch parameter δ of the alloy, the GFA does not only depend on the amount of disorder but also the changes in primary phases and crystallization sequences during solidification as well as the influence of local chemistry and viscosity.

Influence of Sulfur on crystallization behavior

The crystallization behavior has been explored both from the high-temperature liquid state as well as from the low-temperature glass during crystallization from the SCLR. The primary crystalline phase turns out to be a simple hexagonal (Zr,Ti)-based phase, that is quickly trapped by a Zr_2S phase that binds a lot of the available S in its local environment and within the S depleted regions around the the sulfide a mixture of crystalline phases starts to nucleate and grow. Even above the liquidus temperature of the alloy, precipitates can form, which can only be observed in-situ, container-less ESL during processing with HE-XRD. The crystallization can be reconstructed ex-situ by metallographic analysis of 6 mm rods, where a few small early sulfides and accompanying precipitates are found quenched within the amorphous matrix. Here, TEM samples could be extracted that were successfully identified with SAED indexing of the recorded spot patterns.

The S addition induces a transition of the main crystallization from an icosahedral phase with ensuing Zr_2Ni f.c.c. big cube phase into an intermetallic $Zr_3TiNiCu$ type phase, the region of the high glass forming ability is located near this switchpoint of phases. As Ruschel et al. demonstrated in a previous study, the primary phase and stability of the SCLR shows a correlation with the mechanical properties found in the Ti-based alloys [19], therefore the intermetallic crystallization type is the preferred side of the phase switchpoint, which is conveniently also the point of the highest GFA in the $(Zr50)S3$ alloy.

During heating experiments, the first phase that is encountered remains an icosahedral quasicrystalline phase that obscures the glass transition as it start forming right away as soon as there is enough mobility available in the glass, which is followed by an intermetallic compound type crystallization. This changes for the

alloys above 6 at % of S, where the icosahedral phase is being suppressed and a fast crystallization at higher temperatures is encountered that shows in the heat flow as a narrow and deep exothermic peak in contrast to the wide and shallow icosahedral phase crystallization.

Influence of Sulfur on the mechanical properties

The developed alloy shows excellent yield strength, ductility in compression and three-point bending testing, as well as a high fracture toughness of 104 $MPa\sqrt{m}$, making it a formidable Zr-based BMG in terms of mechanical properties. This is also true for the modifications of the alloy with enhanced GFA by Cu-Ni swap and Al-addition to the alloy, although the usage of the Al-addition is limited to the high-purity alloy variants and does not work well in industrial grade material standards.

Influence of oxygen and industrial purity

The developed $Zr50S_3$ alloy proves to be astonishingly resilient towards oxygen contamination in terms of both GFA as well as mechanical properties, despite the employment of industrial grade material in the synthesis, the alloy only loses about 17 % of GFA and 24 % of fracture toughness due to the high load of 4650 a-ppm oxygen in the alloy. This decrease is less than expected for a Zr-based BMG, whose glass forming and mechanical properties are commonly observed to strongly deteriorate at such high oxygen loads. At the same time, the hardness of the BMG increases, while compressive strength and ductility remain at the level of the high-purity alloy.

This combination of properties enables the application of the alloy in industrial grade material standard, which brings down the materials cost of this BMG alloy compared to the laboratory purity by a significant factor - as the market prices of Zr crystal-bar and Zr grade R60702 differ by a factor of ten in raw materials price due to the high energetic cost of the oxygen removal from Zr.

Concluding remarks Zr-Ti-Ni-Cu-S

Overall the introduction of S into different parts of the Z-Ti-Ni-Cu system yields several BMGs from the $Ti_{40}Zr_{35}Cu_{17}S_8$ [11], over the further refined $Ti_{36}Zr_{33.5}Cu_{24.5}S_6$ [19] up to the most potent glass former $((Zr_{50}Ti_{16.6}Ni_{15}Cu_{18.3})_{97}S_3)_{97}Al_3$ and also some more glass formers of varying importance.

8 Outlook

The bulk metallic glasses that were investigated in this work show promising material properties that make them desirable for the application of structural materials due to their unique combination of elasticity, high hardness, and, in the case of the $(Zr50)S3$ alloy, improved oxygen resilience. This sets the alloy apart from the state of the art in Zr-based BMG materials that are strongly influenced by the oxygen, as their GFA and mechanical properties deteriorate under oxygen load.
Despite the progression and improvement in GFA limits in recent years, the BMGs are suffering from the limitations of the available cooling rates during their manufacturing procedure, especially the injection and suction casting routes have seen little improvement in their fundamental technology. Therefore, the current production technology of the casting route is limited to small parts, manufactured by direct casting or casting with ensuing thermoplastic forming, limiting application in larger scales to niche products of the metallic materials in the industry.
The additive manufacturing route offers a relief from the constrictions of the classic casting route, although it comes with expanded and demanding manufacturing technology challenges. In the atomization and powder-based laser bed fusion, the influence of oxygen contamination is unavoidable and especially important in Zr-based BMGs as reported by Frey et al. [204–206]. The Ti-based BMGs potential for this route has been explored by Schönrath et al. [206], where the first successful laser melting and ensuing amorphous solidification were reported, although the powder production and quality are found to be challenging due to the degree of crystallinity in the powder and high oxygen intake. Here, the $(Zr50)S3$ can provide an alternative with its increased GFA, oxygen resilience, and narrow melting interval. Therefore, the $(Zr50)S3$ alloy is considered to be a promising candidate to explore the research on its feasibility to be processing in commercial powder bed fusion laser melting machines after atomization into powder and advance the

field of BMG applications. Despite being researched for over 60 years, the Bulk Metallic Glasses still offer a lot of potential for scientific research and the industrial applications of tomorrow.

Appendix

Copyright licenses

Table 8.1: Licensing and source information for figures and tables used in this work.

License Number	Figure	Source
6045261443707	Figure 2.11	[50]
6045270274474	Figure 2.12	[58]
6045280188602	Figure 2.17	[88]
1618812-1	Figure 2.18	[20]
6045290275580	Figure 2.19	[21]
6045290675297	Figure 2.21	[98]
6045290924978	Figure 2.22	[8]
6045300203597	Figure 2.23	[106]
6045301004981	Figure 2.24	[108]
6045291439451	Figure 2.25	[106]
6045301331688	Figure 2.26	[110]
CC BY-NC-ND 4.0	Figure 3.8	[123]
1618838-1	Figure 3.16	[127]
CC BY 4.0	Figure 3.26	[140]
CC BY 4.0	Figure 3.31	[155]
CC BY 4.0	Figures 4.2, 4.3, 4.4, 4.6, 4.7, 5.9, 6.1, 6.4, 6.5, 6.6, 6.8	[22]
RNP/25/JUN/092220	Figure 5.10	[163]
CC BY 4.0	Tables 4.1, 6.3	[22]

The calculated scattering contributions of the Zr-Ti-Ni-Cu-S alloy system for the composition of $Zr_{50}S_3$ can be seen in Figure 8.1 where it becomes evident why the scattering contribution of the Zr-S atomic pair is neglible in comparison to the Zr-(Zr,Ti) and Zr-(Cu,Ni) contribution.

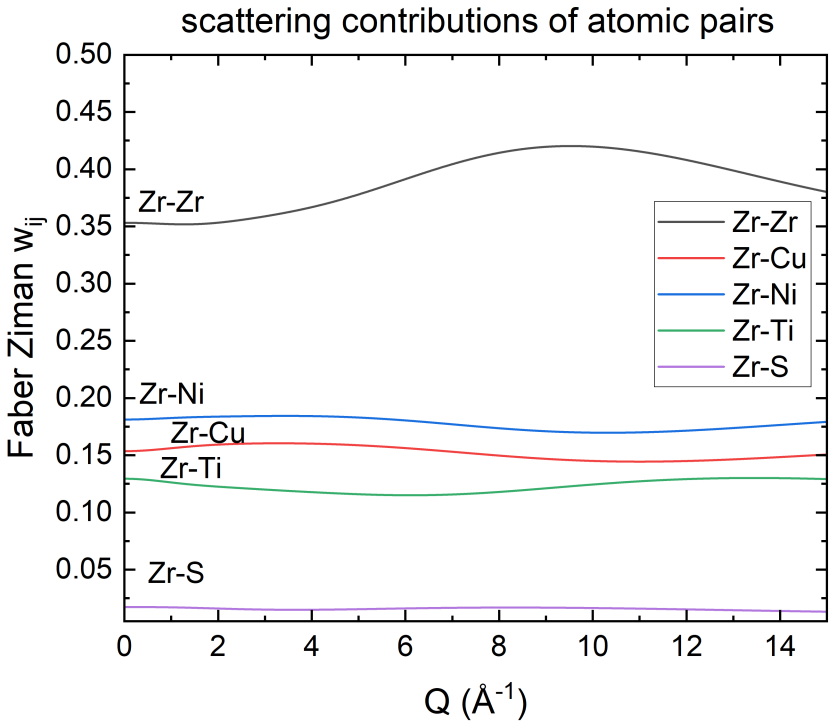

Figure 8.1: Scattering contributions of the relevant atomic pairs, calculated with PDFgetX2 software.

The calculated scattering contributions of the Zr-Ti-Ni-Cu-S alloy system for the Zr-S atomic pair are displayed in Figure 8.2, where the increase in maximum scattering contribution for the $Zr_{50}S_8$ alloy can be determined to be 4.5 %.

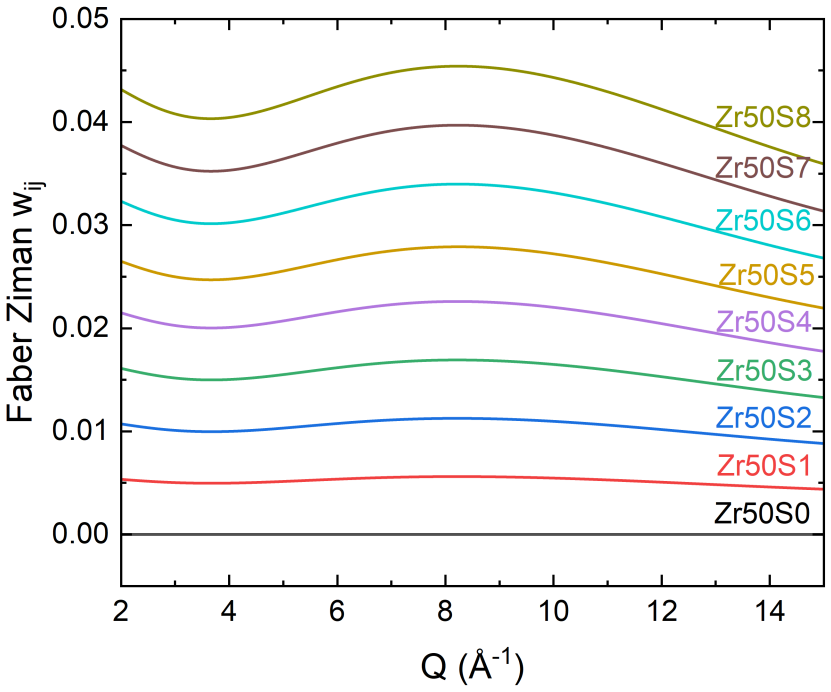

Figure 8.2: Scattering contributions of the Zr-S atomic pair with increasing S addition, calculated with PDFgetX2 software.

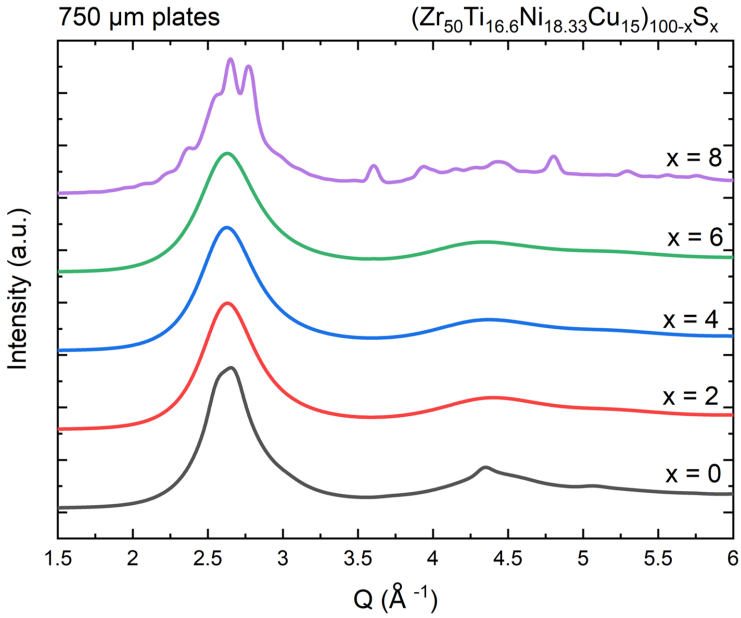

Figure 8.3: HE-XRD of the 0.75 mm casting size for the S-addition of 0,2,4,6, and 8 $at\%$ of S.

Bibliography

[1] B.R.T. Frost. The structure of liquid metals and alloys. *Progress in Metal Physics*, 5(1):96–142. (1954). doi: 10.1179/mtlr.1965.10.1.381.

[2] David Turnbull. Under What Conditions Can A Glass Be Formed? *Contemporary Physics*, 10(5):473–488. (1969). doi: 10.1080/00107516908204405.

[3] W. Klement, R. H. Willens, and Pol Duwez. Non-crystalline structure in solidified Gold-Silicon alloys. *Nature*, 187(4740):869–870. (1960). doi: 10.1038/187869b0.

[4] Li Zhong, Jiangwei Wang, Hongwei Sheng, Ze Zhang, and Scott X Mao. Formation of monatomic metallic glasses through ultrafast liquid quenching. *Nature*, 512(7513):177–180. (2014). doi: 10.1038/nature13617.

[5] Xing Tong, Yue E. Zhang, Bao Shuang Shang, Hua Ping Zhang, Zezhou Li, Yao Zhang, Gang Wang, Yan Hui Liu, Yong Zhao, Bo Zhang, Hai Bo Ke, Jihan Zhou, Hai Yang Bai, and Wei Hua Wang. Breaking the vitrification limitation of monatomic metals. *Nature Materials*, 23(9):1193–1199. (2024). doi: 10.1038/s41563-024-01967-0.

[6] Nobuyuki Nishiyama, Kana Takenaka, Haruko Miura, Noriko Saidoh, Yuqiao Zeng, and Akihisa Inoue. The world's biggest glassy alloy ever made. *Intermetallics*, 30:19–24. (2012). doi: 10.1016/j.intermet.2012.03.020.

[7] A. Peker and W. L. Johnson. A highly processable metallic glass: Zr41.2Ti13.8Cu12.5Ni10.0Be22.5. *Applied Physics Letters*, 63(17):2342–2344. (1993). doi: 10.1063/1.110520.

[8] Mark Telford. The case for bulk metallic glass. *Materials Today*, 7(3):36–43. (2004). doi: 10.1016/S1369-7021(04)00124-5.

[9] Yanglin Li, Shaofan Zhao, Yanhui Liu, Pan Gong, and Jan Schroers. How Many Bulk Metallic Glasses Are There? *ACS Combinatorial Science*, 19 (11):687–693. (2017). doi: 10.1021/acscombsci.7b00048.

[10] Alexander Kuball, Oliver Gross, Benedikt Bochtler, and Ralf Busch. Sulfur-bearing metallic glasses: A new family of bulk glass-forming alloys. *Scripta Materialia*, 146:73–76. (2018). doi: 10.1016/j.scriptamat.2017.11.011.

[11] Alexander Kuball, Oliver Gross, Benedikt Bochtler, Bastian Adam, Lucas Ruschel, Mohammad Zamanzade, and Ralf Busch. Development and characterization of titanium-based bulk metallic glasses. *Journal of Alloys and Compounds*, 790:337–346. (2019). doi: 10.1016/j.jallcom.2019.03.001.

[12] Oliver Gross, Lucas Ruschel, Alexander Kuball, Benedikt Bochtler, Bastian Adam, and Ralf Busch. Bulk metallic glass formation in the (Ti,Zr)–(Ni,Cu)–S system. *Journal of Physics: Condensed Matter*, 32(26): 264003. (2020). doi: 10.1088/1361-648X/ab7c15.

[13] Hao-Ran Jiang, Jing-Yi Hu, Nico Neuber, Benedikt Bochtler, Bastian Adam, Sascha S. Riegler, Maximilian Frey, Lucas Ruschel, Wen-Fei Lu, Ai-Han Feng, Ralf Busch, and Jun Shen. Effect of sulfur on the glass-forming ability, phase transformation, and thermal stability of Cu-Zr-Al bulk metallic glass. *Acta Materialia*, 212:116923. (2021). doi: 10.1016/j.actamat.2021.116923.

[14] Xianghong Lin. *Bulk Glass Formation and Crystallization of Zr-Ti Based Alloys*. Phd, California Institute of Technology, 1997.

[15] X. H. Lin and W. L. Johnson. Formation of Ti-Zr-Cu-Ni bulk metallic glasses. *Journal of Applied Physics*, 78(11):6514–6519. (1995). doi: 10.1063/1.360537.

[16] Benedikt Bochtler. *Thermophysical and Structural Investigations of a CuTi- and a Zr-based Bulk Metallic Glass, the Influence of Minor Additions, and the Relation to Thermoplastic Forming*. PhD thesis, University of Saarland, Saarbrücken, 2019.

[17] Bastian Adam. *Characterization of a novel sulfur bearing titanium based Bulk Metallic Glass*. Masterthesis, Saarland University, 2020.

[18] Bastian Adam, Alexander Kuball, Lucas Matthias Ruschel, Nico Neuber, Maximillian Frey, and Ralf Busch. Sulphuric precipitates in novel titanium-based, sulphur-bearing bulk metallic glass – a BMG composite? *Philosophical Magazine Letters*, 104(1):1–11. (2024). doi: 10.1080/09500839.2024.2376614.

[19] Lucas M. Ruschel, Bastian Adam, Oliver Gross, Nico Neuber, Maximilian Frey, Hans Jürgen Wachter, and Ralf Busch. Development and optimization

of novel sulfur-containing Ti-based bulk metallic glasses and the correlation between primarily crystallizing phases, thermal stability and mechanical properties. *Journal of Alloys and Compounds*, 960:170614. (2023). doi: 10.1016/j.jallcom.2023.170614.

[20] V. V. Molokanov and V. N. Chebotnikov. Glass forming ability, structure and properties of Ti and Zr-intermetallic compound based alloys. In *Mechanical and corrosion properties. Series A, Key engineering materials*, volume 40-41, pages 319–331, 1990. doi: 10.4028/www.scientific.net/kem.40-41.319.

[21] V. V. Molokanov, M. I. Petrzhik, T. N. Mikhailova, T. A. Sviridova, and N. P. Djakonova. Formation of bulk (Zr, Ti)-based metallic glasses. *Journal of Non-Crystalline Solids*, 250-252:560–565. (1999). doi: 10.1016/S0022-3093(99)00132-5.

[22] Bastian Adam, Oliver Kruse, Lucas Matthias Ruschel, Nico Neuber, Maximillian Frey, Oliver Gross, Hao-ran Jiang, Bosong Li, Bernd Gludovatz, Jamie J Kruzic, and Ralf Busch. Introduction of sulfur into an eutectic of the Zr-Ti-Ni-Cu system: Alloy development and characterization of the (Zr50Ti16.6Ni18.3Cu15)100-xSx bulk metallic glasses. *Journal of Alloys and Compounds*, 1025:180307. (2025). doi: 10.1016/j.jallcom.2025.180307.

[23] Max Planck. *Treatise on thermodynamics*. Courier Corporation, 2013.

[24] R Busch, Y J Kim, and W L Johnson. Thermodynamics and kinetics of the undercooled liquid and the glass transition of the Zr41.2Ti13.8Cu12.5Ni10.0Be22.5 alloy. *Journal of Applied Physics*, 77(8): 4039–4043. (1995). doi: 10.1063/1.359485.

[25] Lucas M Ruschel, Sergej Jakovlev, Oliver Gross, Nico Neuber, Bastian Adam, Maximilian Frey, Benedikt Schmidt, Benedikt Bochtler, and Ralf Busch. Unraveling the role of relaxation and rejuvenation on the structure and deformation behavior of the Zr-based bulk metallic glass Vit105. *Materials Today Advances*, 23:100522. (2024). doi: 10.1016/j.mtadv.2024.100522.

[26] D Turnbull. Formation of Crystal Nuclei in Liquid Metals. *Journal of Applied Physics*, 21(10):1022–1028. (1950). doi: 10.1063/1.1699435.

[27] W Kauzmann. *The nature of the glassy state and behaviour of liquid at low temperatures*. PhD thesis, Princeton University, 1948.

[28] O Kubaschewski, C B Alcock, and P J Spencer. *Materials Thermochemistry*. International series on materials science and technology. Pergamon Press, 1993. ISBN 9780080418896.

[29] J. H. Hollomon and D. Turnbull. Solidification of Lead-Tin Alloy Droplets. *Jom*, 3(9):803–805. (1951). doi: 10.1007/bf03397378.

[30] D. Turnbull. Kinetics of Heterogeneous Nucleation. *The Journal of Chemical Physics*, 18(2):198–203. (1950). doi: 10.1063/1.1747588.

[31] X. Y. Liu. Heterogeneous nucleation or homogeneous nucleation? *The Journal of Chemical Physics*, 112(22):9949–9955. (2000). doi: 10.1063/1.481644.

[32] O. Gross. *Precious metal based bulk glass-forming liquids: Development, thermodynamics, kinetics and structure*. PhD thesis, Saarland University, 2018.

[33] K.F. Kelton and A.L. Greer. Interfacial and Thin-Film Reactions. In *Pergamon Materials Series*, volume 15, pages 587–622. Elsevier, 2010. ISBN 1470-1804. doi: 10.1016/S1470-1804(09)01515-6.

[34] Gilles Tarjus and Daniel Kivelson. Breakdown of the Stokes–Einstein relation in supercooled liquids. *The Journal of Chemical Physics*, 103(8):3071–3073. (1995). doi: 10.1063/1.470495.

[35] Marcus T. Cicerone, F. R. Blackburn, and M. D. Ediger. How do molecules move near T g ? Molecular rotation of six probes in o -terphenyl across 14 decades in time. *The Journal of Chemical Physics*, 102(1):471–479. (1995). doi: 10.1063/1.469425.

[36] U. Geyer, W. L. Johnson, S. Schneider, Y. Qiu, T. A. Tombrello, and M.-P. Macht. Small atom diffusion and breakdown of the Stokes–Einstein relation in the supercooled liquid state of the Zr46.7Ti8.3Cu7.5Ni10Be27.5 alloy. *Applied Physics Letters*, 69(17):2492–2494. (1996). doi: 10.1063/1.117716.

[37] J.Q. Wang, Y. Shen, J.H. Perepezko, and M.D. Ediger. Increasing the kinetic stability of bulk metallic glasses. *Acta Materialia*, 104:25–32. (2016). doi: 10.1016/j.actamat.2015.11.048.

[38] Jichao Qiao, Jean-Marc Pelletier, and Riccardo Casalini. Relaxation of Bulk Metallic Glasses Studied by Mechanical Spectroscopy. *The Journal of Physical Chemistry B*, 117(43):13658–13666. (2013). doi: 10.1021/jp4067179.

[39] D. H. Vogel. Das Temperaturabhaengigkeitsgesetz der Viskositaet von Fluessigkeiten. *Physikalische Zeitschrift*, (1921). 22:645.

[40] Gordon S. Fulcher. Analysis of Recent Measurements of the Viscosity of Glasses. *Journal of the American Ceramic Society*, 75(5):1043–1055. (1992). doi: 10.1111/j.1151-2916.1992.tb05536.x.

[41] G. Tammann and W. Hesse. Die Abhängigkeit der Viscosität von der Temperatur bie unterkühlten Flüssigkeiten. *Zeitschrift für anorganische und allgemeine Chemie*, 156(1):245–257. (1926). doi: 10.1002/zaac.19261560121.

[42] Qian Gao, Zengyun Jian, and Junfeng Xu. Correlation between glass transition temperature and Vogel-Fulcher-Tamman temperature in amorphous alloys. *Journal of Alloys and Compounds*, 742:280–283. (2018). doi: 10.1016/j.jallcom.2018.01.193.

[43] Sergej Nemilov. Correlation of Crystallization Character of Glass Melts with the Temperatur dependence of their Viscosity and the Degree of Spatial structural Connectiveness. *Glass Physics and Chemistry*, (1995). 21(2):91–96.

[44] A. Inoue C. Suryanarayana. *Bulk Metallic Glasses, Second Edition*. CRC Press, Boca Raton, 2011. ISBN 9781315153483. doi: 10.1201/9781315153483.

[45] C. A. Angell. Formation of Glasses from Liquids and Biopolymers. *Science*, 267(5206):1924–1935. (1995). doi: 10.1126/science.267.5206.1924.

[46] Gerold Adam and Julian H. Gibbs. On the Temperature Dependence of Cooperative Relaxation Properties in Glass-Forming Liquids. *The Journal of Chemical Physics*, 43(1):139–146. (1965). doi: 10.1063/1.1696442.

[47] Z. P. Lu, Y. Li, and C. T. Liu. Glass-forming tendency of bulk La–Al–Ni–Cu–(Co) metallic glass-forming liquids. *Journal of Applied Physics*, 93(1):286–290. (2003). doi: 10.1063/1.1528297.

[48] Morrel H. Cohen and G. S. Grest. Liquid-glass transition, a free-volume approach. *Physical Review B*, 20(3):1077–1098. (1979). doi: 10.1103/PhysRevB.20.1077.

[49] Roland Böhmer and C. Austen Angell. Correlations of the nonexponentiality and state dependence of mechanical relaxations with bond connectivity in Ge-As-Se supercooled liquids. *Physical Review B*, 45(17):10091–10094. (1992). doi: 10.1103/PhysRevB.45.10091.

[50] Benedikt Bochtler, Oliver Gross, and Ralf Busch. Indications for a fragile-to-strong transition in the high- and low-temperature viscosity of the

Fe43Cr16Mo16C15B10 bulk metallic glass-forming alloy. *Applied Physics Letters*, 111(26). (2017). doi: 10.1063/1.5013108.

[51] Christopher Way, Prashant Wadhwa, and Ralf Busch. The influence of shear rate and temperature on the viscosity and fragility of the Zr41.2Ti13.8Cu12.5Ni10.0Be22.5 metallic-glass-forming liquid. *Acta Materialia*, 55(9):2977–2983. (2007). doi: 10.1016/j.actamat.2006.12.032.

[52] Jong Hyun Na, Marios D. Demetriou, and William L. Johnson. Fragility of iron-based glasses. *Applied Physics Letters*, 99(16):2009–2012. (2011). doi: 10.1063/1.3651763.

[53] Zach Evenson, Tobias Schmitt, Mathias Nicola, Isabella Gallino, and Ralf Busch. High temperature melt viscosity and fragile to strong transition in Zr-Cu-Ni-Al-Nb(Ti) and Cu 47Ti 34Zr 11Ni 8 bulk metallic glasses. *Acta Materialia*, 60(12):4712–4719. (2012). doi: 10.1016/j.actamat.2012.05.019.

[54] Isabella Gallino. On the Fragility of Bulk Metallic Glass Forming Liquids. *Entropy*, 19(9):483. (2017). doi: 10.3390/e19090483.

[55] Julian Pries, Hans Weber, Julia Benke-Jacob, Ivan Kaban, Shuai Wei, Matthias Wuttig, and Pierre Lucas. Fragile-to-Strong Transition in Phase-Change Material Ge3Sb6Te5. *Advanced Functional Materials*, 2202714. (2022). doi: 10.1002/adfm.202202714.

[56] Hajime Tanaka. Two-order-parameter model of the liquid-glass transition. I. Relation between glass transition and crystallization. *Journal of Non-Crystalline Solids*, 351(43-45):3371–3384. (2005). doi: 10.1016/j.jnoncrysol.2005.09.008.

[57] John C. Mauro, Yuanzheng Yue, Adam J. Ellison, Prabhat K. Gupta, and Douglas C. Allan. Viscosity of glass-forming liquids. *Proceedings of the National Academy of Sciences of the United States of America*, 106(47):19780–19784. (2009). doi: 10.1073/pnas.0911705106.

[58] Chunzhi Zhang, Lina Hu, Yuanzheng Yue, and John C. Mauro. Fragile-to-strong transition in metallic glass-forming liquids. *The Journal of Chemical Physics*, 133(1). (2010). doi: 10.1063/1.3457670.

[59] Alexander Kuball. *Development, Characterization and Processing of a novel Family of Bulk Metallic Glasses: Sulfur-containing Bulk Metallic Glasses.* PhD thesis, University of Saarland, 2019.

[60] Lucas Matthias Ruschel, Alexander Kuball, Bastian Adam, Maximilian Frey, and Ralf Busch. Viscosity and surface tension of the Zr56.5Ti13.3Ni13.6Cu9.6S7 bulk metallic glass-forming liquid. *AIP Advances*, 14(3). (2024). doi: 10.1063/5.0192705.

[61] V. I. Motorin. Vitrification kinetics of pure metals. *Physica Status Solidi (a)*, 80(2):447–455. (1983). doi: 10.1002/pssa.2210800206.

[62] Chengbo Li and Dongdong Chen. Investigation on the quench sensitivity of 7085 aluminum alloy with different contents of main alloying elements. *Metals*, 9(9). (2019). doi: 10.3390/met9090965.

[63] Jan Schroers and William L. Johnson. Highly processable bulk metallic glass-forming alloys in the Pt-Co-Ni-Cu-P system. *Applied Physics Letters*, 84(18):3666–3668. (2004). doi: 10.1063/1.1738945.

[64] Yusuke Iguchi, Gábor L. Katona, Csaba Cserháti, Gábor A. Langer, and Zoltán Erdélyi. On the miscibility gap of Cu-Ni system. *Acta Materialia*, 148:49–54. (2018). doi: 10.1016/j.actamat.2018.01.038.

[65] D. M. Lee, J. H. Sun, D. H. Kang, S. Y. Shin, G. Welsch, and C. H. Lee. A deep eutectic point in quaternary Zr-Ti-Ni-Cu system and bulk metallic glass formation near the eutectic point. *Intermetallics*, 21(1):67–74. (2012). doi: 10.1016/j.intermet.2011.09.006.

[66] Byung Joo Park, Hye Jung Chang, Do Hyang Kim, Won Tae Kim, Kamanio Chattopadhyay, T. A. Abinandanan, and Saswata Bhattacharyya. Phase Separating Bulk Metallic Glass: A Hierarchical Composite. *Physical Review Letters*, 96(24):245503. (2006). doi: 10.1103/PhysRevLett.96.245503.

[67] Devinder Singh, Dharmendra Singh, Radhey Shyam Tiwari, Parthiban Ramasamy, and Jürgen Eckert. A brief review on Ce and Zr-based phase-separated metallic glasses. *Journal of Materials Science*, 60(3):1545–1560. (2024). doi: 10.1007/s10853-024-10339-7.

[68] Larry Kaufman and Morris Cohen. Thermodynamics and kinetics of martensitic transformations. *Progress in Metal Physics*, 7(C):165–246. (1958). doi: 10.1016/0502-8205(58)90005-4.

[69] Aurélie Jacob, Erwin Povoden-Karadeniz, Philipp Retzl, and Ernst Kozeschnik. Reassessment of low-temperature Gibbs energies of BCC and FCC in steel for T0-temperature evaluation. *Calphad*, 81:102531. (2023). doi: 10.1016/j.calphad.2023.102531.

[70] David A. Porter, Kenneth E. Easterling, and Mohamed Y. Sherif. *Phase transformations in metals and alloys, third edition.* 2009. ISBN 9781439883570.

[71] Joel H. Hildebrand. The Term 'Regular Solution'. *Nature*, 168(4281):868–868. (1951). doi: 10.1038/168868a0.

[72] J. H. Perepezko. Nucleation-controlled reactions and metastable structures. *Progress in Materials Science*, 49(3-4):263–284. (2004). doi: 10.1016/S0079-6425(03)00028-8.

[73] A. Lindsay Greer. Confusion by design. *Nature*, 366(6453):303–304. (1993). doi: 10.1038/366303a0.

[74] Akihisa INOUE. Stabilization of Supercooled Liquid and Opening-up of Bulk Glassy Alloys. *Proceedings of the Japan Academy, Series B*, 73(2):19–24. (1997). doi: 10.2183/pjab.73.19.

[75] Xuehui Yan, Yu Zou, and Yong Zhang. Properties and processing technologies of high-entropy alloys. *Materials Futures*, 1(2). (2022). doi: 10.1088/2752-5724/ac5e0c.

[76] Daniel B. Miracle. A structural model for metallic glasses-supplementary materials. *Nature Materials*, 3(10):697–702. (2004). doi: 10.1038/nmat1219.

[77] Zhilin Long, Wei Liu, Ming Zhong, Yun Zhang, Mingshengzi Zhao, Guangkai Liao, and Zhuo Chen. A new correlation between the characteristics temperature and glass-forming ability for bulk metallic glasses. *Journal of Thermal Analysis and Calorimetry*, 132(3):1645–1660. (2018). doi: 10.1007/s10973-018-7050-0.

[78] A Inoue, A Kato, T Zhang, S. G. Kim, and T. Masumoto. Mg-Cu-Y Amorphous Alloys with High Mechanical Strengths Produced by a Metallic Mold Casting Method. *Materials Transactions, JIM*, 32(7):609–616. (1991). doi: 10.2320/matertrans1989.32.609.

[79] Z.P. Lu, H. Tan, S.C. Ng, and Y. Li. The correlation between reduced glass transition temperature and glass forming ability of bulk metallic glasses. *Scripta Materialia*, 42(7):667–673. (2000). doi: 10.1016/S1359-6462(99)00417-0.

[80] Z.P. Lu and C.T. Liu. A new glass-forming ability criterion for bulk metallic glasses. *Acta Materialia*, 50(13):3501–3512. (2002). doi: 10.1016/S1359-6454(02)00166-0.

[81] Xueshan Xiao, Fang Shoushi, Wang Guoming, Hua Qin, and Dong Yuanda. Influence of beryllium on thermal stability and glass-forming ability of Zr-Al-Ni-Cu bulk amorphous alloys. *Journal of Alloys and Compounds*, 376 (1-2):145–148. (2004). doi: 10.1016/j.jallcom.2004.01.014.

[82] K. Mondal and B. S. Murty. On the parameters to assess the glass forming ability of liquids. *Journal of Non-Crystalline Solids*, 351(16-17):1366–1371. (2005). doi: 10.1016/j.jnoncrysol.2005.03.006.

[83] Chen Qing-Jun, Shen Jun, Fan Hong-Bo, Sun Jian-Fei, Huang Yong-Jiang, and Mccartney D G. Glass-Forming Ability of an Iron-Based Alloy Enhanced by Co Addition and Evaluated by a New Criterion. *Chinese Physics Letters*, 22(7):1736–1738. (2005). doi: 10.1088/0256-307X/22/7/048.

[84] X H Du, J C Huang, C T Liu, and Z P Lu. New criterion of glass forming ability for bulk metallic glasses. *Journal of Applied Physics*, 101(8):86108. (2007). doi: 10.1063/1.2718286.

[85] G.J. Fan, H. Choo, and P.K. Liaw. A new criterion for the glass-forming ability of liquids. *Journal of Non-Crystalline Solids*, 353(1):102–107. (2007). doi: 10.1016/j.jnoncrysol.2006.08.049.

[86] X. H. Du and J. C. Huang. New criterion in predicting glass forming ability of various glass-forming systems. *Chinese Physics B*, 17(1):249–254. (2008). doi: 10.1088/1674-1056/17/1/043.

[87] D. Wang, Y. Li, B. B. Sun, M. L. Sui, K. Lu, and E. Ma. Bulk metallic glass formation in the binary Cu-Zr system. *Applied Physics Letters*, 84(20): 4029–4031. (2004). doi: 10.1063/1.1751219.

[88] R Arroyave, T.W. Eagar, and L Kaufman. Thermodynamic assessment of the Cu–Ti–Zr system. *Journal of Alloys and Compounds*, 351(1-2):158–170. (2003). doi: 10.1016/S0925-8388(02)01035-6.

[89] Charles C. Hays and William L. Johnson. Undercooling of bulk metallic glasses processed by electrostatic levitation. *Journal of Non-Crystalline Solids*, 250-252:596–600. (1999). doi: 10.1016/S0022-3093(99)00139-8.

[90] S. Mukherjee, Z. Zhou, J. Schroers, W. L. Johnson, and W. K. Rhim. Overheating threshold and its effect on time-temperature-transformation diagrams of zirconium based bulk metallic glasses. *Applied Physics Letters*, 84(24):5010–5012. (2004). doi: 10.1063/1.1763219.

[91] Hao-Ran Jiang, Jing-Yi Hu, Nico Neuber, Maximilian Frey, Lin-zhi Xu, Kang Sun, Yan-Dong Jia, Gang Wang, Ralf Busch, and Jun Shen. Influence of sulfur addition on the glass formation, phase transformation and mechanical properties of Cu50Zr50 alloy. *Acta Materialia*, 255(15):119064. (2023). doi: 10.1016/j.actamat.2023.119064.

[92] Nicolai Grund, Dirk Holland-Moritz, Saba Khademorezaian, Lucas P. Kreuzer, Nico Neuber, Lucas M. Ruschel, Hendrik Voigt, Johanna Wilden, Fan Yang, Soham Banerjee, Malte Blankenburg, Ann-Christin Dippel, Jan Peter Embs, Sergiy Divinski, Ralf Busch, Andreas Meyer, and Gerhard Wilde. Impact of sulfur addition on the structure and dynamics of Ni–Nb alloy melts. *APL Materials*, 12(5):051126. (2024). doi: 10.1063/5.0205058.

[93] Yao Yang, Jihan Zhou, Fan Zhu, Yakun Yuan, Dillan J. Chang, Dennis S. Kim, Minh Pham, Arjun Rana, Xuezeng Tian, Yonggang Yao, Stanley J. Osher, Andreas K. Schmid, Liangbing Hu, Peter Ercius, and Jianwei Miao. Determining the three-dimensional atomic structure of an amorphous solid. *Nature*, 592(7852):60–64. (2021). doi: 10.1038/s41586-021-03354-0.

[94] Kengo Nishio and Anh Khoa Augustin Lu. Unveiling a medium-range structural commonality of amorphous alloys. *Journal of Non-Crystalline Solids*, 624(15):122696. (2024). doi: 10.1016/j.jnoncrysol.2023.122696.

[95] Daniel B. Miracle. A structural model for metallic glasses. *Nature Materials*, 3(10):697–702. (2004). doi: 10.1038/nmat1219.

[96] Neil J. A. Sloane. Kepler's conjecture confirmed. *Nature*, 395(6701):435–436. (1998). doi: 10.1038/26609.

[97] D. B. Miracle. The efficient cluster packing model -An atomic structural model for metallic glasses. *Acta Materialia*, 54:4317–4336. (2006). doi: 10.1016/j.actamat.2006.06.002.

[98] D. B. Miracle, D. V. Louzguine-Luzgin, L. V. Louzguina-Luzgina, and A. Inoue. An assessment of binary metallic glasses: correlations between structure, glass forming ability and stability. *International Materials Reviews*, 55 (4):218–256. (2010). doi: 10.1179/095066010X12646898728200.

[99] K. J. Laws, D. B. Miracle, and M. Ferry. A predictive structural model for bulk metallic glasses. *Nature Communications*, 6(1):8123. (2015). doi: 10.1038/ncomms9123.

[100] Lucas M. Ruschel, Oliver Gross, Benedikt Bochtler, Bosong Li, Bastian Adam, Nico Neuber, Maximilian Frey, Sergej Jakovlev, Fan Yang, Hao Ran

Jiang, Bernd Gludovatz, Jamie J. Kruzic, and Ralf Busch. Ni-Nb-P-based bulk glass-forming alloys: Superior material properties combined in one alloy family. *Acta Materialia*, 253(January):118968. (2023). doi: 10.1016/j.actamat.2023.118968.

[101] Jianfeng Wang, Ran Li, Nengbin Hua, and Tao Zhang. Co-based ternary bulk metallic glasses with ultrahigh strength and plasticity. *Journal of Materials Research*, 26(16):2072–2079. (2011). doi: 10.1557/jmr.2011.187.

[102] Tao Zhang, Akihisa Inoue, and Tsuyoshi Masumoto. Amorphous Zr-Al-TM (TM=Co, Ni, Cu) Alloys with Significant Supercooled Liquid Region of Over 100 K. *Materials Transactions, JIM*, 32(11):1005–1010. (1991). doi: 10.2320/matertrans1989.32.1005.

[103] Ju Wang, Ivan Kaban, Volodymyr Levytskyi, Ran Li, Junhee Han, Mihai Stoica, Roman Gumeniuk, and Kornelius Nielsch. Ultra-high strength Co–Ta–B bulk metallic glasses: Glass formation, thermal stability and crystallization. *Journal of Alloys and Compounds*, 860:158398. (2021). doi: 10.1016/j.jallcom.2020.158398.

[104] A.S Argon. Plastic deformation in metallic glasses. *Acta Metallurgica*, 27 (1):47–58. (1979). doi: 10.1016/0001-6160(79)90055-5.

[105] Frans Spaepen. A microscopic mechanism for steady state inhomogeneous flow in metallic glasses. *Acta Metallurgica*, 25(4):407–415. (1977). doi: 10.1016/0001-6160(77)90232-2.

[106] C Schuh, T Hufnagel, and U Ramamurty. Mechanical behavior of amorphous alloys. *Acta Materialia*, 55(12):4067–4109. (2007). doi: 10.1016/j.actamat.2007.01.052.

[107] Moreel H. Cohen and David Turnbull. Molecular transport in liquids and glasses. *The Journal of Chemical Physics*, 31(5):1164–1169. (1959). doi: 10.1063/1.1730566.

[108] R. D. Conner, W. L. Johnson, N. E. Paton, and W. D. Nix. Shear bands and cracking of metallic glass plates in bending. *Journal of Applied Physics*, 94(2):904–911. (2003). doi: 10.1063/1.1582555.

[109] T. W. Wu and F. Spaepen. Small angle X-ray scattering from an embrittling metallic glass. *Acta Metallurgica*, 33(12):2185–2190. (1985). doi: 10.1016/0001-6160(85)90179-8.

[110] Jan Schroers, Tranquoc Nguyen, Sean O'Keeffe, and Amish Desai. Thermoplastic forming of bulk metallic glass—Applications for MEMS and microstructure fabrication. *Materials Science and Engineering: A*, 449-451: 898–902. (2007). doi: 10.1016/j.msea.2006.02.398.

[111] Golden Kumar, Peter A. Staffier, Jerzy Blawzdziewicz, Udo D. Schwarz, and Jan Schroers. Atomically smooth surfaces through thermoplastic forming of metallic glass. *Applied Physics Letters*, 97(10). (2010). doi: 10.1063/1.3485298.

[112] H.H. Liebermann. The dependence of the Geometry of glassy alloy ribbons on the chill block melt-spinning process parameters. *Materials Science and Engineering*, 43(3):203–210. (1980). doi: 10.1016/0025-5416(80)90103-2.

[113] Victor I Tkatch, Alexander I Limanovskii, Sergey N Denisenko, and Sergey G Rassolov. The effect of the melt-spinning processing parameters on the rate of cooling. *Materials Science and Engineering A*, 323(1-2):91–96. (2002). doi: 10.1016/S0921-5093(01)01346-6.

[114] Yang Min. *Production and characterization of metallic glass ribbons by chill-block melt spinning.* Masterthesis, Saarland University, 2019.

[115] X H Lin and W L Johnson. Formation of Ti–Zr–Cu–Ni bulk metallic glasses. *Journal of Applied Physics*, 78(11):6514–6519. (1995). doi: 10.1063/1.360537.

[116] Tomasz Kozieł, Krzysztof Pajor, and Łukasz Gondek. Cooling rate evaluation during solidification in the suction casting process. *Journal of Materials Research and Technology*, 9(6):13502–13508. (2020). doi: 10.1016/j.jmrt.2020.09.082.

[117] Ralf Busch, Benedikt Bochtler, Oliver Gross, Simon Hechler, and Alexander Kuball. DE 10 2018 115 815 A1: Apparatus and method for producing a cast part formed from amorphous or partially amorphous metal, and cast part, 2020.

[118] Alfred Ludwig, Robert Zarnetta, Sven Hamann, Alan Savan, and Sigurd Thienhaus. Development of multifunctional thin films using high-throughput experimentation methods. *International Journal of Materials Research*, 99 (10):1144–1149. (2008). doi: 10.3139/146.101746.

[119] Peter Tsai and Katharine M. Flores. High-throughput discovery and characterization of multicomponent bulk metallic glass alloys. *Acta Materialia*, 120:426–434. (2016). doi: 10.1016/j.actamat.2016.08.068.

[120] Hai Bin Yu, Yuansu Luo, and Konrad Samwer. Ultrastable metallic glass. *Advanced Materials*, 25(41):5904–5908. (2013). doi: 10.1002/adma.201302700.

[121] N. Chen, R. Frank, N. Asao, D. V. Louzguine-Luzgin, P. Sharma, J. Q. Wang, G. Q. Xie, Y. Ishikawa, N. Hatakeyama, Y. C. Lin, M. Esashi, Y. Yamamoto, and A. Inoue. Formation and properties of Au-based nanograined metallic glasses. *Acta Materialia*, 59(16):6433–6440. (2011). doi: 10.1016/j.actamat.2011.07.007.

[122] TedPella Inc. Abrasive Grit Grading Systems. *webpage*, acc. 14.06. (2025). doi: https://www.tedpella.com/Material-Sciences_html/Abrasive_Grit_Grading_Systems.aspx.

[123] Qinghua Wang, Satoshi Kishimoto, Yoshihisa Tanaka, and Kimiyoshi Naito. Fabrication of nanoscale speckle using broad ion beam milling on polymers for deformation analysis. *Theoretical and Applied Mechanics Letters*, 6(4):157–161. (2016). doi: 10.1016/j.taml.2016.07.001.

[124] PerkinElmer Inc. Technical Specifications Thermal Analysis for the DSC 8000/8500 Differential Scanning Calorimeters. (2009). *SpecificationSheets-DSC8000*.

[125] H. E. HAGY. Experimental Evaluation of Beam-Bending Method of Determining Glass Viscosities in the Range 10 8 to 10 15 Poises. *Journal of the American Ceramic Society*, 46(2):93–97. (1963). doi: 10.1111/j.1151-2916.1963.tb11684.x.

[126] J. C. Phillips. Stretched exponential relaxation in molecular and electronic glasses. *Reports on Progress in Physics*, 59(9):1133–1207. (1996). doi: 10.1088/0034-4885/59/9/003.

[127] Georg Lohöfer. Electrical resistivity measurement of liquid metals. *Measurement Science and Technology*, 16(2):417–425. (2005). doi: 10.1088/0957-0233/16/2/012.

[128] Novespace. Zero G-Parabelflugtechnik. *webpage*, acc. 02.07. (2025). doi: https://www.airzerog.com/de/zero-g-parabelflugtechnik/.

[129] I. Egry, G. Lohöfer, I. Seyhan, S. Schneider, and B. Feuerbacher. Viscosity and surface tension measurements in microgravity. *International Journal of Thermophysics*, 20(4):1005–1015. (1999). doi: 10.1023/A:1022686316437.

[130] R. Willnecker, S. Schneider, F. Münstermann, M. Pütz, and W. Koerver. Digital video system for TEMPUS on parabolic flights. *International Astronautical Federation - 56th International Astronautical Congress 2005*, 1: 460–466. (2005). doi: 10.2514/6.iac-05-a2.5.03.

[131] Bosong Li, Lucas M. Ruschel, Keita Nomoto, Oliver Gross, Bastian Adam, Nico Neuber, Maximilian Frey, Simon P. Ringer, Bernd Gludovatz, Ralf Busch, and Jamie J. Kruzic. Fracture behavior of NiNb and NiNbP bulk metallic glasses. *Journal of Alloys and Compounds*, 1010:177369. (2025). doi: 10.1016/j.jallcom.2024.177369.

[132] A. Mohammed and A. Abdullah. Scanning Electron Microscopy (SEM): A review. *Proceedings of 2018 International Conference on Hydraulics and Pneumatics - HERVEX*, (2018). pages 77–85.

[133] F J Humphreys and I Brough. High resolution electron backscatter diffraction with a field emission gun scanning electron microscope. *Journal of microscopy*, (1999). 195(1):6–9.

[134] T. E. Everhart and R. F. M. Thornley. Wide-band detector for micro-microampere lowenergy electron currents. *J. Sci. Instrum.*, 37(246). (1960). doi: 10.1088/0950-7671/37/7/307.

[135] Íris Carneiro and Sónia Simões. Recent advances in ebsd characterization of metals. *Metals*, 10(8):1–32. (2020). doi: 10.3390/met10081097.

[136] Robert A. Schwarzer, David P. Field, Brent L. Adams, Mukul Kumar, and Adam J. Schwartz. Present State of Electron Backscatter Diffraction and Prospective Developments. In *Electron Backscatter Diffraction in Materials Science*, pages 1–20. Springer US, Boston, MA, 2nd edition, 2009. ISBN 9780387881355. doi: 10.1007/978-0-387-88136-2_1.

[137] Mark Winey, Janet B. Meehl, Eileen T. O'Toole, and Thomas H. Giddings. Conventional transmission electron microscopy. *Molecular Biology of the Cell*, 25(3):319–323. (2014). doi: 10.1091/mbc.e12-12-0863.

[138] David B. Williams and C. Barry Carter. *Transmission electron microscopy*. Elsevier, 1996. ISBN 9780702068874. doi: 10.1016/B978-0-7020-6864-5.00021-9.

[139] H. Franz, O. Leupold, R. Röhlsberger, S.V. Roth, O.H. Seeck, J. Spengler, J. Strempfer, M. Tischer, J. Viefhaus, E. Weckert, and T. Wroblewski. Technical Report: PETRA III: DESY's New High Brilliance Third Generation

Synchrotron Radiation Source. *Synchrotron Radiation News*, 19(6):25–29. (2006). doi: 10.1080/08940880601064984.

[140] DESY. PETRA III. *webpage*, 02 07. (2025). doi: https://photon-science.desy.de/sites/site_photonscience/content/e58/e176720/e270548/image001_eng.jpg.

[141] Christian G. Schroer, Hans Christian Wille, Oliver H. Seeck, Kai Bagschik, Horst Schulte-Schrepping, Markus Tischer, Heinz Graafsma, Wiebke Laasch, Karolin Baev, Stephan Klumpp, Riccardo Bartolini, Harald Reichert, Wim Leemans, and Edgar Weckert. The synchrotron radiation source PETRA III and its future ultra-low-emittance upgrade PETRA IV. *European Physical Journal Plus*, 137(12). (2022). doi: 10.1140/epjp/s13360-022-03517-6.

[142] Giannis Ashiotis, Aurore Deschildre, Zubair Nawaz, Jonathan P. Wright, Dimitrios Karkoulis, Frédéric Emmanuel Picca, and Jérôme Kieffer. The fast azimuthal integration Python library: PyFAI. *Journal of Applied Crystallography*, 48:510–519. (2015). doi: 10.1107/S1600576715004306.

[143] Egami Takeshi and Simon J.L. Billinge. *Underneath the Bragg Peaks Structural Ananlysis of Complex Materials*, volume 7. Elsevier Ltd, 2003. ISBN 0080426980. doi: 10.1016/B978-0-08-097133-9.00013-7.

[144] Xiangyun Qiu, Jeroen W. Thompson, and Simon J. L. Billinge. PDFgetX2 : a GUI-driven program to obtain the pair distribution function from X-ray powder diffraction data. *Journal of Applied Crystallography*, 37(4):678–678. (2004). doi: 10.1107/S0021889804011744.

[145] B E Warren, H Krutter, and O. Morningstar. Fourier Analysis of X-ray Patterns of Vitreous SiO2 and B2O2. *Journal of the American Ceramic Society*, 19(1-12):202–206. (1936). doi: 10.1111/j.1151-2916.1936.tb19822.x.

[146] André Guinier and Gérard Fournet. Small-Angle Scattering of X-Rays. *Physics Today*, 9(8):38–39. (1956). doi: 10.1063/1.3060069.

[147] Lin Li, Mirosław Salamończyk, Sasan Shadpour, Chenhui Zhu, Antal Jákli, and Torsten Hegmann. An unusual type of polymorphism in a liquid crystal. *Nature Communications*, 9(1):3–10. (2018). doi: 10.1038/s41467-018-03160-9.

[148] K. Osamura, K. Shibue, R. Suzuki, and Y. Murakami. SAXS study on the structure and crystallization of amorphous metallic alloys. *Colloid and Polymer Science*, 259(6):677–682. (1981). doi: 10.1007/BF01525038.

[149] Kang-Hua Li, Jia-Cheng Ge, Si-Nan Liu, Shu Fu, Zi-Xuan Yin, Wen-Tao Zhang, Guo-Xing Chen, Shao-Chong Wei, Hua Ji, Tao Feng, Qi Liu, Xun-Li Wang, Xiao-Bing Zuo, Yang Ren, Horst Hahn, and Si Lan. In situ scattering study of multiscale structural evolution during liquid–liquid phase transition in Mg-based metallic glasses. *Rare Metals*. (2021). doi: 10.1007/s12598-021-01767-4.

[150] A. A. Kündig, M. Ohnuma, T. Ohkubo, and K. Hono. Early crystallization stages in a Zr-Cu-Ni-Al-Ti metallic glass. *Acta Materialia*, 53(7):2091–2099. (2005). doi: 10.1016/j.actamat.2005.01.022.

[151] X. J. Liu, X. D. Hui, G. L. Chen, and M. H. Sun. In situ synchrotron SAXS study of nanocrystallization in Zr65Ni25Ti10 metallic glass. *Intermetallics*, 16(1):10–15. (2008). doi: 10.1016/j.intermet.2007.06.014.

[152] Caner Tükel, Semra Ide, Leyla Yildirim, and Mehmet Erbudak. SWAXS analysis on some quasicrystalline alloys: Nanoclusters and nanoaggregates. *Journal of Alloys and Compounds*, 581:860–866. (2013). doi: 10.1016/j.jallcom.2013.07.175.

[153] Jürgen Brillo, Fan Yang, and Dirk Holland-Moritz. *Transport Property Measurement of Liquid Metals and Alloys Using Electromagnetic and Electrostatic Levitation*, volume 45. Springer US, 2024. ISBN 0123456789. doi: 10.1007/s10765-023-03309-9.

[154] T. Kordel, D. Holland-Moritz, F. Yang, J. Peters, T. Unruh, T. Hansen, and A. Meyer. Neutron scattering experiments on liquid droplets using electrostatic levitation. *Physical Review B*, 83(10):104205. (2011). doi: 10.1103/PhysRevB.83.104205.

[155] Jun Ding, Evan Ma, Mark Asta, and Robert O. Ritchie. Second-Nearest-Neighbor Correlations from Connection of Atomic Packing Motifs in Metallic Glasses and Liquids. *Scientific Reports*, 5(1):17429. (2015). doi: 10.1038/srep17429.

[156] S. P. Pan, J. Y. Qin, W. M. Wang, and T. K. Gu. Origin of splitting of the second peak in the pair-distribution function for metallic glasses. *Physical Review B*, 84(9):092201. (2011). doi: 10.1103/PhysRevB.84.092201.

[157] Nico Neuber, Oliver Gross, Maximiliam Frey, Benedikt Bochtler, Alexander Kuball, Simon Hechler, Isabella Gallino, and Ralf Busch. On the thermodynamics and its connection to structure in the Pt-Pd-Cu-Ni-P bulk metallic glass forming system. *Acta Materialia*, 220:117300. (2021). doi: 10.1016/j.actamat.2021.117300.

[158] Oliver Gross, Nico Neuber, Alexander Kuball, Benedikt Bochtler, Simon Hechler, Maximilian Frey, and Ralf Busch. Signatures of structural differences in Pt–P- and Pd–P-based bulk glass-forming liquids. *Communications Physics*, 2(1):83. (2019). doi: 10.1038/s42005-019-0180-2.

[159] Oliver Gross, Nico Neuber, Alexander Kuball, Benedikt Bochtler, Simon Hechler, Maximilian Frey, and Ralf Busch. Signatures of structural differences in Pt–P- and Pd–P-based bulk glass-forming liquids. *Communications Physics*, 2(1). (2019). doi: 10.1038/s42005-019-0180-2.

[160] Jacinta C. Conrad, Param P. Dhillon, Eric R. Weeks, David R. Reichman, and David A. Weitz. Contribution of Slow Clusters to the Bulk Elasticity Near the Colloidal Glass Transition. *Physical Review Letters*, 97(26):265701. (2006). doi: 10.1103/PhysRevLett.97.265701.

[161] Y. Q. Cheng and E. Ma. Atomic-level structure and structure-property relationship in metallic glasses. *Progress in Materials Science*, 56(4):379–473. (2011). doi: 10.1016/j.pmatsci.2010.12.002.

[162] Ralf Busch. The thermophysical properties of bulk metallic glass-forming liquids. *JOM*, 52(7):39–42. (2000). doi: 10.1007/s11837-000-0160-7.

[163] Chunfei Li and Akihisa Inoue. Precipitations of icosahedral quasicrystalline and crystalline approximant phases in Zr-Al-Ni-Cu-Ir metallic glasses. *Physical Review B - Condensed Matter and Materials Physics*, 63(17):63–66. (2001). doi: 10.1103/PhysRevB.63.172201.

[164] W. J. Kim and K. F. Kelton. Icosahedral-phase formation and stability in Ti-Zr-Co alloys. *Philosophical Magazine Letters*, 74(6):439–448. (1996). doi: 10.1080/095008396179977.

[165] J. L. Libbert and K. F. Kelton. The role of oxygen in the formation of titanium-based icosahedral phases and crystal approximants. *Philosophical Magazine Letters*, 71(2):153–159. (1995). doi: 10.1080/09500839508241008.

[166] I. Jonas, W. Hembree, F. Yang, R. Busch, and A. Meyer. Industrial grade versus scientific pure: Influence on melt properties. *Applied Physics Letters*, 112(17):1–5. (2018). doi: 10.1063/1.5021764.

[167] J. Wilden, F. Yang, D. Holland-Moritz, S. Szabó, W. Lohstroh, B. Bochtler, R. Busch, and A. Meyer. Impact of Sulfur on the melt dynamics of glass forming Ti75Ni25-xSx. *Applied Physics Letters*, 117(013702):1–5. (2020). doi: 10.1063/5.0012409.

[168] Subir Sachdev and David R. Nelson. Theory of the Structure Factor of Metallic Glasses. *Physical Review Letters*, 53(20):1947–1950. (1984). doi: 10.1103/PhysRevLett.53.1947.

[169] Hao Ran Jiang, Jochi Tseng, Nico Neuber, Jenifer Barrirero, Bastian Adam, Maximilian Frey, Ann Christin Dippel, Soham Banerjee, Isabella Gallino, Ai Han Feng, Gang Wang, Frank Mücklich, Ralf Busch, and Jun Shen. On the devitrification of Cu–Zr–Al alloys: Solving the apparent contradiction between polymorphic liquid-liquid transition and phase separation. *Acta Materialia*, 226(117668):1–15. (2022). doi: 10.1016/j.actamat.2022.117668.

[170] D. Ma, A. D. Stoica, and X. L. Wang. Power-law scaling and fractal nature of medium-range order in metallic glasses. *Nature Materials*, 8(1):30–34. (2009). doi: 10.1038/nmat2340.

[171] Yaqi Wu, Peter K. Liaw, Ruixuan Li, Weiran Zhang, Guihong Geng, Xuehui Yan, Guiqun Liu, and Yong Zhang. Relationship between the unique microstructures and behaviors of high-entropy alloys. *International Journal of Minerals, Metallurgy and Materials*, 31(6):1350–1363. (2024). doi: 10.1007/s12613-023-2777-4.

[172] James P. Best, Halsey E. Ostergaard, Bosong Li, Moritz Stolpe, Fan Yang, Keita Nomoto, M. Tarik Hasib, Ondrej Muránsky, Ralf Busch, Xiaopeng Li, and Jamie J. Kruzic. Fracture and fatigue behaviour of a laser additive manufactured Zr-based bulk metallic glass. *Additive Manufacturing*, 36(March). (2020). doi: 10.1016/j.addma.2020.101416.

[173] J. Eckert, N. Mattern, M. Zinkevitch, and M. Seidel. Crystallization Behavior and Phase Formation in Zr-Al-Cu-Ni Metallic Glass Containing Oxygen. *Materials Transactions, JIM*, 39(6):623–632. (1998). doi: 10.2320/matertrans1989.39.623.

[174] B. S. Murty, D. H. Ping, K. Hono, and A. Inoue. Direct evidence for oxygen stabilization of icosahedral phase during crystallization of Zr65Cu27.5Al7.5 metallic glass. *Applied Physics Letters*, 76(1):55–57. (2000). doi: 10.1063/1.125654.

[175] Se Hwang Kang, Dinesh Thapa, Binod Regmi, Siyuan Ren, Young Min Kim, Seong Gon Kim, and Sung Wng Kim. Chemically Stable Low-Dimensional Electrides in Transition Metal-Rich Monochalcogenides: Theoretical and Experimental Explorations. *Journal of the American Chemical Society*, 144(10):4496–4506. (2022). doi: 10.1021/jacs.1c12367.

[176] Stacy Gates-Rector and Thomas Blanton. The Powder Diffraction File: a quality materials characterization database. *Powder Diffraction*, 34(4):352–360. (2019). doi: 10.1017/S0885715619000812.

[177] M. Sherif El-Eskandarany and A. Inoue. Mechanically induced cyclic metastable phase transformations of Zr2 Ni alloys. *Physical Review B - Condensed Matter and Materials Physics*, 75(22):1–9. (2007). doi: 10.1103/PhysRevB.75.224109.

[178] G. W. Lee, A. K. Gangopadhyay, T. K. Croat, T. J. Rathz, R. W. Hyers, J. R. Rogers, and K. F. Kelton. Link between liquid structure and the nucleation barrier for icosahedral quasicrystal, polytetrahedral, and simple crystalline phases in Ti-Zr-Ni alloys: Verification of Frank's hypothesis. *Physical Review B - Condensed Matter and Materials Physics*, 72(17):1–10. (2005). doi: 10.1103/PhysRevB.72.174107.

[179] F. C. Frank. Supercooling of liquids. *Proceedings of the Royal Society of London. Series A. Mathematical and Physical Sciences*, 215(1120):43–46. (1952). doi: 10.1098/rspa.1952.0194.

[180] Faqiang Guo, Hsiang Jen Wang, S. Joseph Poon, and Gary J. Shiflet. Ductile titanium-based glassy alloy ingots. *Applied Physics Letters*, 86(9):1–3. (2005). doi: 10.1063/1.1872214.

[181] Miloslav Klinger and Aleš Jäger. Crystallographic Tool Box CrysTBox : automated tools for transmission electron microscopists and crystallographers. *Journal of Applied Crystallography*, 48(6):2012–2018. (2015). doi: 10.1107/S1600576715017252.

[182] Anubhav Jain, Shyue Ping Ong, Geoffroy Hautier, Wei Chen, William Davidson Richards, Stephen Dacek, Shreyas Cholia, Dan Gunter, David Skinner, Gerbrand Ceder, and Kristin A Persson. Commentary: The Materials Project: A materials genome approach to accelerating materials innovation. *APL Materials*, 1(1):11002. (2013). doi: 10.1063/1.4812323.

[183] J. L. Murray. The Ti-Zr (Titanium-Zirconium) system. *Bulletin of Alloy Phase Diagrams*, 2(2):197–201. (1981). doi: 10.1007/BF02881478.

[184] R.E. Smallman and A.H.W. Ngan. Solidification. In *Modern Physical Metallurgy*, pages 93–119. Elsevier, 2014. doi: 10.1016/B978-0-08-098204-5.00003-1.

[185] J. F. Löffler, P. Thiyagarajan, and W. L. Johnson. Concentration and temperature dependence of decomposition in supercooled liquid alloys. *Journal of Applied Crystallography*, 33(3 I):500–503. (2000). doi: 10.1107/S0021889899014867.

[186] E L Huston, John W Cahn, and J E Hilliard. Spinodal decomposition during continuous cooling. *Acta Metallurgica*, 14(9):1053–1062. (1966). doi: https://doi.org/10.1016/0001-6160(66)90193-3.

[187] Subir Sachdev and David R. Nelson. Order in metallic glasses and icosahedral crystals. *Physical Review B*, 32(7):4592–4606. (1985). doi: 10.1103/PhysRevB.32.4592.

[188] Dmitri V. Louzguine and Akihisa Inoue. Formation of a nanoquasicrystalline phase in Zr-Cu-Ti-Ni metallic glass. *Applied Physics Letters*, 78(13):1841–1843. (2001). doi: 10.1063/1.1358362.

[189] U. Kühn, K. Eymann, N. Mattern, J. Eckert, A. Gebert, B. Bartusch, and L. Schultz. Limited quasicrystal formation in Zr-Ti-Cu-Ni-Al bulk metallic glasses. *Acta Materialia*, 54(18):4685–4692. (2006). doi: 10.1016/j.actamat.2006.05.049.

[190] Heraeus AMLOY. Amorphous Alloys made by Heraeus AMLOY. *webpage*, 02 07. (2025). doi: https://www.heraeus-amloy.com/de/amorphous-alloys/.

[191] R. D. Conner, R. E. Maire, and W. L. Johnson. Effect of oxygen concentration upon the ductility of amorphous Zr57Nb5Al10Cu15.4 Ni12.6. *Materials Science and Engineering: A*, 419(1-2):148–152. (2006). doi: 10.1016/j.msea.2005.12.009.

[192] Tuo Wang, Qiqi Hou, Yating Zhou, and Guanting Liu. Tailored plasticity of Zr-based bulk metallic glass by controlling the static holding time of melt before quenching. *Journal of Non-Crystalline Solids*, 650:123380. (2025). doi: 10.1016/j.jnoncrysol.2024.123380.

[193] Jochen Heinrich, Ralf Busch, and Bernd Nonnenmacher. Processing of a bulk metallic glass forming alloy based on industrial grade Zr. *Intermetallics*, 25:1–4. (2012). doi: 10.1016/j.intermet.2012.02.011.

[194] C. T. Liu, M. F. Chisholm, and M. K. Miller. Oxygen impurity and microalloying effect in a Zr-based bulk metallic glass alloy. *Intermetallics*, 10(11-12):1105–1112. (2002). doi: 10.1016/S0966-9795(02)00131-0.

[195] X. H. Lin, W. L. Johnson, and W. K. Rhim. Effect of oxygen impurity on crystallization of an undercooled bulk glass forming Zr-Ti-Cu-Ni-Al alloy. *Materials Transactions, JIM*, 38(5):473–477. (1997). doi: 10.2320/matertrans1989.38.473.

[196] A. Gebert, J. Eckert, and L. Schultz. Effect of oxygen on phase formation and thermal stability of slowly cooled Zr65Al7.5Cu17.5Ni10 metallic glass. *Acta Materialia*, 46(15):5475–5482. (1998). doi: 10.1016/S1359-6454(98)00187-6.

[197] J. J. Wall, J. D. Almer, S. C. Vogel, P. K. Liaw, H. Choo, and C. T. Liu. Synchrotron X-ray scattering investigations of oxygen-induced nucleation in a Zr-based glass-forming alloy. *Scripta Materialia*, 61(3):293–295. (2009). doi: 10.1016/j.scriptamat.2009.04.004.

[198] M. L. Vaillant, T. Gloriant, I. Thibon, A. Guillou, V. Keryvin, T. Rouxel, and D. Ansel. Partial crystallization of as-quenched Zr55Cu 30Al10Ni5 bulk metallic glass induced by oxygen. *Scripta Materialia*, 49(12):1139–1143. (2003). doi: 10.1016/j.scriptamat.2003.08.028.

[199] Y. Tan, Y. W. Wang, X. W. Cheng, Q. Fu, Z. H. Xin, Z. Q. Xu, and H. W. Cheng. Effects of Al replacement on glass forming ability and mechanical properties of Zr-based bulk metallic glasses. *Journal of Non-Crystalline Solids*, 568(May). (2021). doi: 10.1016/j.jnoncrysol.2021.120962.

[200] Jochen Heinrich, Ralf Busch, Frank Müller, Samuel Grandthyll, and Stefan Hüfner. Role of aluminum as an oxygen-scavenger in zirconium based bulk metallic glasses. *Applied Physics Letters*, 100(7):1–4. (2012). doi: 10.1063/1.3685492.

[201] W. H. Zhou, F. H. Duan, Y. H. Meng, C. C. Zheng, H. M. Chen, A. G. Huang, Y. X. Wang, and Y. Li. Effect of alloying oxygen on the microstructure and mechanical properties of Zr-based bulk metallic glass. *Acta Materialia*, 220. (2021). doi: 10.1016/j.actamat.2021.117345.

[202] C. A. Teixeira, R. V. da Silva, L. T. Pereira, and M. F. de Oliveira. Oxygen effect on bending behavior of a zirconium based bulk metallic glass. *Journal of Non-Crystalline Solids*, 535. (2020). doi: 10.1016/j.jnoncrysol.2020.119966.

[203] Yoshihiko Yokoyama, Atsushi Kobayashi, Kenzo Fukaura, and Akihisa Inoue. Oxygen embrittlement and effect of the addition of Ni element in a bulk amorphous Zr-Cu-Al alloy. *Materials Transactions*, 43(3):571–574. (2002). doi: 10.2320/matertrans.43.571.

[204] Maximilian Frey, Jan Wegner, Nico Neuber, Benedikt Reiplinger, Benedikt Bochtler, Bastian Adam, Lucas Ruschel, Sascha Sebastian Riegler, Hao Ran Jiang, Stefan Kleszczynski, Gerd Witt, and Ralf Busch. Thermoplastic forming of additively manufactured Zr-based bulk metallic glass: A processing route for surface finishing of complex structures. *Materials and Design*, 198: 109368. (2021). doi: 10.1016/j.matdes.2020.109368.

[205] Peilei Zhang, Jie Tan, Yingtao Tian, Hua Yan, and Zhishui Yu. Research progress on selective laser melting (SLM) of bulk metallic glasses (BMGs): a review. *International Journal of Advanced Manufacturing Technology*, 118 (7-8):2017–2057. (2022). doi: 10.1007/s00170-021-07990-8.

[206] Hanna Schönrath, Jan Wegner, Maximilian Frey, Martin A. Schroer, Xueze Jin, María Teresa Pérez-Prado, Ralf Busch, and Stefan Kleszczynski. Novel titanium-based sulfur-containing BMG for PBF-LB/M. *Progress in Additive Manufacturing*, 9(3):601–612. (2024). doi: 10.1007/s40964-024-00668-z.